Bioanalytical Tools to Develop Rapid Diagnostics and Study Physiology

Thesis by

Justin Charles Rolando

In Partial Fulfillment of the Requirements for

the degree of

Doctor of Philosophy

CALIFORNIA INSTITUTE OF TECHNOLOGY

Pasadena, California

2019

(Defended 10 May 2019)

Justin Charles Rolando
ORCID: 0000-0001-8948-319X

ACKNOWLEDGEMENTS

There are numerous people who have made this work possible. I express my sincerest gratitude to everyone listed here and many others not mentioned explicitly. Many people could be listed in multiple categories, but I list individuals once and in no particular order:

Those whom I've worked with on published projects: Erik Jue, Nathan Schoepp, Emily S. Savela, Jacob Barlow, Asher Preska-Steinberg, Sujit Datta, Thomas Naragon, Said Bogatyrev

And especially

Tasha Shelby, our group Scientific Editor, who makes my writing articulate, and

Rustem Ismagilov, my research advisor, who helps my ideas sound less foolish.

Those whom I worked with on non-published projects: Daan Witters, Weishan Liu, Shencheng Ge, Stephanie McCalla, Alex Tucker-Schwartz, Travis Schlappi, Alex Persat, Mikhail Karymov, Liang Ma, Stefano Begolo, Bradley Silverman, Joanne Lau, Joong Hwan Bang, Dmitriy Zhukov, Jenia Khorosheva, Tahmineh Khazaei, Annelise Thompson, Heidi Klumpe, Lealia Xiong, Octavio Mandragon-Palomino, and Roberta Poceviciute.

My thesis committee members, for taking time to give me thoughtful feedback on my research: Dave Tirrell, Julie Kornfield, Bob Grubbs, and Jim Heath.

The directors of core facilities that enabled this research:
Nathan Dalleska at Environmental Analysis Center,
David VanderVelde at Liquid Nuclear Magnetic Response Facility,
Andres Collazo at Beckman Institute Biological Imaging Center,
John Van Deusen at Jim Hall Design and Prototyping and Lab.

Administrative staff including: Bridget Samules, Whitney Barlow, Sohee Lee, Joe Drew, Agnes Tong, and Alison Ross.

The many people who have supported me in this journey:

Nolan and Kate Viljoen, Brian Landbloom, Luke Przygocki, Cameron and Elizabeth Robertson, Jessica and Matt Rodgers, Elyse and Isaac Schwartz, and Tony Salem.

My housemates, who have helped to maintain to sanity and reset my perspective: Ana Brown, David Ayala, Rob Usiskin, Roxana Marashi Witters, Jasmin Turner, Oliver Turner, Christine Morrison, Allison Lui, Toni Bauhoffer, Marja Sidel, Phoenix Delman, and Katie Kelsh.

Bruce Eaton and John Vaught, who gave me the first opportunity to be a research scientist,

My extended family. Who believed, encouraged, and supported me since day one. Your unconditional love, support, and continuous encouragement gave me the opportunity to believe, "*You can do whatever you want if you set your mind to it*."

My parents and sister. Who enabled studies throughout my life. Who taught me passion, curiosity, patience, creativity, tolerance, gratitude, and perseverance. My mother, Susie Rolando, who made batteries out of potatoes with me; my father, John Rolando, who helped me build rockets and parabolic listening devices to spy on the neighbors, and my sister, Courtney Rolando, who was undoubtedly the subject of a mischievous older brother's childhood experiments.

In addition to the grants explicitly mentioned at the end of each chapter, my research was funded by:

DTRA (MCDC-18-01-01-007)
BWF (Innovation in Regulatory Science Award)
DARPA-BRICS (HR0011-15-C-0093)
DARPA-CLIPS (HROO 11-17-2-0037)
DARPA-LRS (HR0011-11-2-0006)
DARPA-UW (HROO1 1-17-2-0064) and
The Joseph J. Jacobs Institute for Molecular Engineering for Medicine.

ABSTRACT

This work details the development of bioanalytical tools for use in rapid diagnostics (Chapters 2-4) and in the study of physiology (Chapters 5-6). This research harness the power of real-time, single-molecule microfluidics to study loop-mediated isothermal amplification in urinary tract infections (Chapter 2), chlamydia (Chapter 3), and gonorrhea (Chapter 4). In Chapter 5, non-reactive beads are designed and optimized to study the impact of polymers on murine gastrointestinal mucosa. Chapter 6 details the implementation of a mass spectrometry method to quantify bile acids and investigate their interaction with the microbiota in the murine gastro-intestinal tract.

CONTENT AND CONTRIBUTIONS

Justin C. Rolando, Erik Jue, Nathan G. Schoepp, and Rustem F. Ismagilov. "Real-time, digital LAMP with commercial microfluidic chips reveals the interplay of efficiency, speed, and background amplification as a function of reaction temperature and time." Analytical chemistry. 2018. 91(1):1034–1042. Doi: 10.1021/acs.analchem.8b04324

J.C.R. conceptualized the method, generated and analyzed data. Wrote the paper, constructed figures, and performed all revisions.
E.J. wrote the MATLAB software script for automated analysis of digital LAMP image sequences. Provided minor input to experimental design; and minor edits and inputs to the figures and manuscript.
N.G.S. prepared and quantified nucleic acid stocks. Optimized buffer conditions for *Bst* 2.0. Provided minor input to experimental design and minor edits and inputs to the figures and manuscript.

Justin C. Rolando, Erik Jue, Jacob Barlow, and Rustem F. Ismagilov. "Effect of background DNA on specific and non-specific amplification in LAMP reactions in real-time, digital format with (High Resolution) melting analysis".

J.C.R. conceptualized the method, designed and ran all the experiments, generated and analyzed the data, wrote the paper, and constructed all the figures.
E.J. wrote the MATLAB software script for automated analysis of digital LAMP image sequences.
J.B. Analyzed sequencing data to help predict non-specific LAMP sequences.

Nathan G. Schoepp, Emily S. Savela, Justin C. Rolando, Olusegun O. Soge, and Rustem F. Ismagilov. "Surfactant-enhanced DNA accessibility to nuclease accelerates phenotypic β-lactam antibiotic susceptibility testing of N. gonorrhoeae."

N.G.S. guided initial testing of enhancers and developed two-step nuc-aAST workflow; selected and performed initial testing of surfactant enhancers; optimized sample handling during ABX exposure; performed and analyzed no-enhancer time-course experiments (Fig. 4.2); designed LAMP primers and contributed to the optimization of LAMP conditions for dLAMP experiments (Fig. 4.5); wrote the manuscript and created figures. E.S.S. performed initial enhancer testing experiments;. selected and performed initial testing of osmotic, autolysis, and surfactant enhancers; optimized sample handling prior to ABX exposure; performed and analyzed enhancer testing and nuc-aAST experiments (Figs. 4.3, 4.4, 4.5), and assisted in performing dLAMP experiments (Fig. 4.5); performed data analysis, selected the readout metric of percentage accessibility, and selected optimal conditions for nuc-aAST; contributed to writing the manuscript and figure design and wrote the methods section. N.G.S., E.S.S., and R.F.I. conceived of the project and discussed design and interpretation of experiments. J.C.R. optimized digital LAMP conditions, and performed and analyzed all digital LAMP experiments for Fig. 4.5. O.O.S. provided isolates and guided discussion on gold-standard AST and current

treatment practices for *Ng*, and performed agar-dilution AST. R.F.I. supervised and guided the project, and helped compose the manuscript. All authors read and edited the manuscript.

A. Preska Steinberg, S. S. Datta, T. Naragon, J. C. Rolando, S. R. Bogatyrev, R. F. Ismagilov. "High-molecular-weight polymers from dietary fiber drive aggregation of particulates in the murine small intestine." eLife. 2019. 8:e40387. DOI: 10.7554/eLife.40387

A.P.S. Co-designed all experiments and co-analyzed all experimental results; developed theoretical tools and performed all calculations; co-developed imaging analysis pipeline in ImageJ; developed computational tools for bootstrapping procedure; co-developed microscopy assay for examining luminal contents from mice gavaged particles used in Figure 5.1C and 1D; Co-performed, designed, and analyzed data from experiments involving oral administration of particles in Figure 5.1; performed, designed, and analyzed data from all *ex vivo* aggregation experiments in SI fluid in Figures 5.2, 5.3, 5.5-7, 5.S2, and 5.S5; performed, designed, and analyzed data from all GPC measurements in Figures 5.3, 5.5-7, and Tables 5.S1-7; performed, designed, and analyzed data from all *in vitro* aggregation experiments with PEG solutions in Figure 5.4D, Figure 5.4 – Figure supplements 1-2, and with dietary fiber in Figure 5.7A; developed a computational approach for theoretical calculations in 5.4H and 5.4I and performed all calculations; performed, designed, and analyzed data from Western blots in Figures 5.5E, 5.6E, 5.S3, and 5.S4; helped supervise animal husbandry of MUC2KO colony; performed animal husbandry for WT mice on autoclaved diets in Figure 5.6 and 5.S5; performed animal husbandry for mice on pectin and Fibersol-2 diets in Figure 5.7; performed, designed, and analyzed all zeta potential measurements in Table 5.S8; performed pH measurements on luminal fluid in Figure 5.S2; co-interpreted results; co-wrote the paper.
S.S.D. Conceived and co-planned the project; initially observed the aggregation phenomenon described in this work; co-designed and co-analyzed preliminary experiments; performed preliminary *ex vivo* and *in vitro* aggregation experiments; co-developed microscopy assay for examining luminal contents from mice gavaged particles used in Figure 5.1C and 5.1D; developed *ex vivo/in vitro* aggregation assay used in Figures 5.2-7; co-developed approach to extract liquid fraction of murine intestinal contents; co-developed protocol for NMR measurements on PEG-coated particles; organized transfer and initial set up of MUC2KO colony; co-interpreted results; co-wrote the paper.
T.N. Co-developed imaging analysis pipeline in ImageJ; co-analyzed *ex vivo* aggregation data in Figure 5.2; co-designed and co-analyzed preliminary *ex vivo* aggregation experiments with MUC2KO mice; provided useful advice on design of bootstrapping procedure; co-interpreted results; co-wrote the paper.
J.C.R. Developed protocol for NMR measurements on PEG-coated particles; performed synthesis of particles; performed NMR measurements in Table 5.S8; co-wrote the paper.
S.R.B. Co-performed preliminary experiments; developed fluorescent laser scanning approach for examining luminal contents of mice gavaged with particles appearing in Figure 5.1A and 5.1B; Administered particles to mice in Figure 5.1; co-developed approach to extract liquid fraction of murine intestinal contents; co-organized transfer and initial set up of MUC2KO colony; setup genotyping of MUC2KO mice; helped supervise animal husbandry of MUC2KO colony; helped with interpretation of results; co-wrote the paper.

Said R. Bogatryev, Justin C. Rolando, and Rustem F. Ismagilov. "Quantitative and qualitative changes in the upper gastrointestinal microbiome controlled by self-reinoculation in mice influence the bile acid metabolism and host physiology."

S.R.B. Conception, mouse tail cup development, animal study execution, animal study sample processing for microbial 16S quantification and 16S metagenomic sequencing, 16S quantification and sequencing data analysis, animal study sample processing for metabolomic analysis, bile acid data analysis, plasma ultrasensitive cytokine measurements and data analysis, mouse tissue gene expression quantification and data analysis, manuscript preparation.

J.C.R. Metabolomics method development and validation, animal study sample processing for metabolomic analysis, UPLC-MS instrument setup and sample analysis, chromatographic and mass spectra data analysis.

TABLE OF CONTENTS

LIST OF ILLUSTRATIONS AND TABLES

Chapter 1

AN OVERVIEW

How much?

It's quite obvious to us when we feel ill. Maybe it's sniffling or a cough. Swelling. An itch. A headache. But *how much* are you not well?

Society has a broad need for diagnostics that define and quantify illness. Medicine currently attempts to quantify people relative to the "standard person"—a theoretical person with no interesting features whatsoever other than being completely normal in every way. This standard person is established from averages of the general population and defines a "reference range" of wellness. Of course this person does not exist, and as real humans (not "standard" humans) we have the unfortunate situation of being unique.

That uniqueness starts all the way down at your DNA. Even identical twins sharing identical DNA have unique fingerprints. An old man has roughly the same genome as on the day he was born, yet he appears very different from his youthful self. Fluctuations in physiology are expected as phenotype arises through myriad gene and protein expression networks. In the end, knowing your blueprint (genotype) doesn't tell us what state of health you'll be in at a given time. Your uniqueness is shaped by environmental factors, epigenetics (what your ancestors did), and hysteresis (what you've done until now).

The answer to the question "how much" is determined by how and what is measured, and even what we measure against. Consider the vast variation in concentrations of cortisol and the thyroid hormones as they pass through a diurnal cycle. (When you measure matters!) Or how a sudden arrhythmia in a professional athlete takes heartrate from 40 bpm to an 'abnormally normal' 90 bpm, matching that of the general population. Despite having a 'low' heartrate, that athlete is unhealthy when their measurement agrees with the population average. (Your personal variation matters!) The levels of our individual hormones vary greatly—some measurements vary within a day, others by the day of the month (e.g., female reproductive hormones), others by the time of the year, and others change from year to year. Your individual levels may vary dramatically between you and your friends. Given

these wide fluctuations, it's worth questioning whether we should use the reference of a single "standard" person at all.

My research at Caltech has focused on improving the process of analyzing biology with chemical tools and the understanding of "how much" with regard to diseases that impact human biology and physiology.

This thesis details the development of bioanalytical tools for use in rapid diagnostics (Chapters 2-4).

In my research, I found great use in "digital" microfluidics: a process in which individual molecules can be placed in a small compartment, a reaction run, and the total number of molecules counted by the presence or absence of the reaction product in each compartment. The field calls this "digital" because of the binary (presence or absence) of a molecule within the compartment. By running several thousand compartments in parallel, we can begin to quantify "how much."

These studies also employ a DNA amplification technique that can be run at a single temperature, thus simplifying amplification from the standard process which requires multiple heating and cooling steps. This technique is known as Loop-mediated Amplification (LAMP).

Chapter 2 discusses a process to make the best aspects of digital microfluidics, namely the ability to monitor thousands of single template reactions in parallel with real-time kinetics (measuring "how fast"!) available to anyone with relatively standard laboratory equipment. We demonstrate how the technique can be used to study the impact different conditions have on a LAMP reaction. Finally, we apply the system to an Antibiotic Susceptibility Test (AST) of *E. coli* from clinical Urinary Tract Infections to ask: Which antibiotics will be effective?

Chapter 3 extends the digital LAMP method to incorporate melting temperature—a means to discriminate between true and false amplification based on the underlying DNA product. This additional refinement allows us to know if we are counting the right thing. We use digital LAMP with melting temperature to study the impact of enzyme selection on true and false amplifications, and the implications those choice have on determining the fewest number of molecules that can be counted. We call this version of "how much" the Limit of Detection (LOD). Additionally, we study the impact that a patient's DNA (likely to be present in urine samples and clinical swabs) may have on the detection of the sexually transmitted bacterial infection chlamydia.

Chapter 4 applies the digital LAMP method to quantify the response of gonorrhea to a common class of antibiotics known as β-lactams, and it demonstrates a sum-of-steps for the assay in 30 minutes—demonstrating the potential for using these methods to develop a diagnostic that can be used directly at the point of care.

This thesis also details the development of tools to for the study of physiology (Chapters 5-6), in particular within the murine gastrointestinal tract.

In Chapter 5, I designed and optimized non-reactive beads to study the impact of polymers on murine gastrointestinal mucosa. These beads could be loaded onto murine intestinal mucosa, and the thickness of the mucosa quantified in response to the introduction of different sized polymers, some which occur naturally in the diet. The challenge in developing these beads was that they needed to be chemically inert so that only the physics of the system could be monitored. I developed a process to covalently attach non-reactive PEG polymers to the surface of small polystyrene beads and quantify the amount of non-reactive polymer attached. Because the polymers were non-reactive, I could not run additional reactions to quantify the extent of the polymer attached to the surface and instead selected Nuclear Magnetic Resonance (NMR) to quantify the extent of polymer attached to the surface. Those familiar with NMR will note that magnetic susceptibility changes in the presence of a solid surface like a bead, and can find a *solution* to this problem in the *Materials and Methods* section on page 159. In general, we found that a combination of introducing a linear, high-molecular-weight polymer, "backfilled" by a second low-molecular-weight polymer resulted in the least surface charge (a measurement of possible bead reactivity). These beads have great utility for many additional applications; at the time of the publication of this thesis, the beads have been used in two additional studies that are not detailed in this thesis.

Chapter 6 details the implementation of a mass spectrometry method to quantify bile acids and investigate their interaction with the microbiota in the murine gastrointestinal tract. Bacteria within the gastrointestinal tract are known to chemically modify the natural soaps (bile acids) that our body produces to help digest and absorb food. In the process, the chemical transformation of some of these molecules turns bile acids into signaling molecules, which may impact host physiology. I developed a method using chromatography (a technique to separate molecules by their propensity to partition into oil-like and water-like materials) coupled with their mass to simultaneously quantify *how much* of these 35 different bile acids exist within a given section of the gastrointestinal tract.

In the long term, my hope is that the studies detailed in this thesis, and other studies like them, will enable an improved understanding of human health. Scientifically, we still must understand the variation in genotype and phenotype at the single-cell level and between tissues, and then scale up to see variation among individuals at the organism level. My hope is that longitudinal studies of human health will allow us to begin to define health, instead of malady, and usher in a new era of personalized medicine—medicine that accounts for *your* uniqueness, and not for the standard person. Finally, as devices and the hardware to operate them continue to miniaturize, my hope is that we can improve access to healthcare for all people, regardless of their healthcare system. To me, this is providing access to quality diagnostics, regardless of the location. It's access for a mother at her daughter's gymnastics event, for military personal in the theater of war, for communities in rural Nepal where resources may be limited, to a patient at the doctor's office with an urgent medical question. You will find these concepts echoed throughout the following chapters when I talk about diagnostics for Limited Resources Settings (LRS) and at the Point of Care (POC).

Chapter 2

REAL-TIME, DIGITAL LAMP WITH COMMERCIAL MICROFLUIDIC CHIPS REVEALS THE INTERPLAY OF EFFICIENCY, SPEED, AND BACKGROUND AMPLIFICATION AS A FUNCTION OF REACTION TEMPERATURE AND TIME

Justin C. Rolando, Erik Jue, Nathan G. Schoepp, and Rustem F. Ismagilov. Analytical Chemistry. 2018. 91(1):1034–1042. DOI: 10.1021/acs.analchem.8b04324

ABSTRACT

Real-time, isothermal, digital nucleic acid amplification is emerging as an attractive approach for a multitude of applications including diagnostics, mechanistic studies, and assay optimization. Unfortunately, there is no commercially available and affordable real-time, digital instrument validated for isothermal amplification; thus, most researchers have not been able to apply digital, real-time approaches to isothermal amplification. Here, we generate an approach to real-time digital loop-mediated isothermal amplification (LAMP) using commercially available microfluidic chips and reagents, and open-source components. We demonstrate this approach by testing variables that influence LAMP reaction speed and the probability of detection. By analyzing the interplay of amplification efficiency, background, and speed of amplification, this real-time digital method enabled us to test enzymatic performance over a range of temperatures, generating high-precision kinetic and endpoint measurements. We were able to identify the unique optimal temperature for two polymerase enzymes, while accounting for amplification efficiency, non-specific background, and time to threshold. We validated this digital LAMP assay and pipeline by performing a phenotypic antibiotic susceptibility test on 17 archived clinical urine samples from patients diagnosed with urinary tract infections. We provide all the necessary workflows to perform digital LAMP using standard laboratory equipment and commercially available materials. This real-time digital approach will be useful to others in the future to understand the fundamentals of isothermal chemistries—including which components determine amplification fate, reaction speed, and enzymatic performance. Researchers can also adapt this pipeline, which uses only standard equipment and

commercial components, to quickly study and optimize assays using precise, real-time digital quantification—accelerating development of critically needed diagnostics.

INTRODUCTION

In this paper, we describe a methodology to use commercially available chips, reagents, and microscopes to perform real-time digital LAMP. We use this methodology to perform a mechanistic study of digital isothermal amplification; and apply the lessons learned to perform a phenotypic antibiotic susceptibility test (AST).

Microfluidics-based diagnostics for infectious diseases are advancing as a result of using nucleic acid testing—making them amenable to the point of care (POC) and limited-resource settings where they will have clinical impact. Isothermal amplification methods in particular show promise for simplifying nucleic-acid-based POC diagnostics by circumventing the stringent thermal cycling requirements of PCR.[1] One isothermal method that is being actively pursued in bioanalytical chemistry and the field of diagnostics is loop-mediated isothermal amplification (LAMP).[2-6]

LAMP and other isothermal technologies are fast and sensitive, but when performed in a bulk format in microliter volumes (e.g. in a tube) they provide only semi-quantitative (log-scale) resolution or presence/absence measurements.[7-15] As a result, when optimizing an assay, it is difficult to quantify how small changes in assay conditions (e.g. in primers, reagents, or temperature) impact the reaction's speed and analytical sensitivity. To reliably understand these effects with high precision would require hundreds of bulk experiments per condition.[16] For the field to be able to take full advantage of the capabilities of LAMP, researchers need to be able to optimize reaction conditions by understanding and testing the variables that may influence reaction speed and probability of detection. Furthermore, the semi-quantitative measurements yielded by bulk isothermal methods are insufficient for analyses requiring precise quantification, such as phenotypic antibiotic susceptibility testing.[17,18]

These problems can be solved using "digital" approaches, which partition single target molecules in large numbers of compartments and give a binary (presence/absence) readout for each compartment. These "digital" approaches thus allow determination of the efficiency of the amplification reaction[19] and provide absolute quantification with high resolution.

Digital isothermal measurements have been used to quantify viral load for HCV,[16,20,21] HIV,[19,20] and influenza,[22] perform bacterial enumeration,[23-25] optimize primers,[16] and test for phenotypic antibiotic susceptibility[18] using LAMP[18-28] and RPA.[29]

Real-time digital formats are especially valuable for examining the variables that most affect non-specific amplification and the speed of amplification. Many excellent approaches for end-point[19,20,22-28] and real-time[16,18,21] digital LAMP (dLAMP) have been published. Despite the value that real-time dLAMP can bring to diagnostics, this method is difficult to implement—especially for those without a background in micro-electro-mechanical systems or microfluidics—because there is no commercial system for real-time, digital isothermal amplification. To achieve statistical significance, a meaningful study might require dozens of experiments; such studies are difficult to perform without a commercial source of chips. Consequently, the few LAMP mechanistic studies that have been performed were not done with high precision. Further, those who would most benefit from optimized digital isothermal reactions (e.g. those working on POC diagnostics) cannot efficiently improve them.

Here, we demonstrate how to generate high-precision kinetic and endpoint measurements using a real-time dLAMP assay that is performed completely with commercially available and open-source components (**Figure 2.2.1**). We use this real-time information to investigate dLAMP reactions mechanistically, including the interplay of efficiency, speed, and background amplification as a function of reaction temperature and time on two enzymes. To illustrate one application of using real-time dLAMP to improve a clinically relevant assay, we optimized the assay conditions for a phenotypic AST using the real-time dLAMP pipeline and used the optimized protocol to compare our AST of 17 clinical urine samples to the gold-standard method.

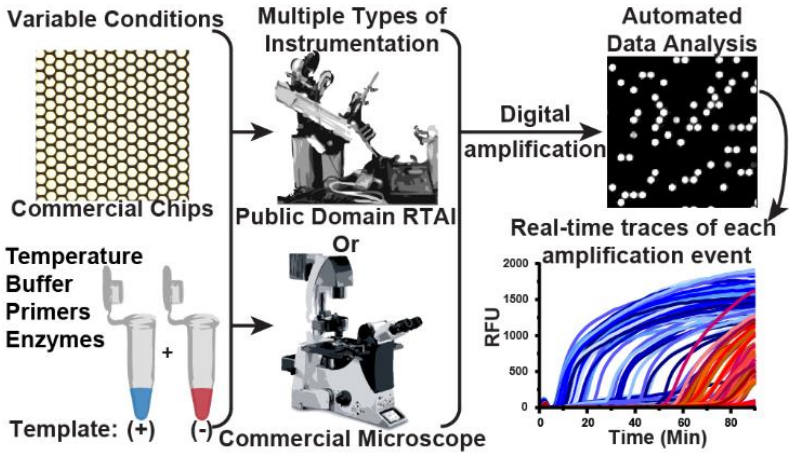

Figure 2.1. A schematic of the pipeline for performing multiplexed, real-time, digital loop-mediated isothermal amplification (LAMP) using only commercially available and/or open source components. Microfluidic chips and reagents (e.g. primers, enzymes, buffer composition) can be purchased commercially. Multiple instrument configurations can be used to capture results. e.g. a customized real-time instrument (instructions for building publicly available[30]) or any commercial microscope. Data analysis is automated using a MATLAB script (Supporting Information, S-I).

EXPERIMENTAL SECTION

Microfluidic chips used in this paper were sourced from Applied Biosystems, Foster City, CA, USA) Ref A26316, "QuantStudio 3D Digital PCR 20k Chip Kit V2."

LAMP reagents

Our amplification target was the *E. coli* 23S ribosomal gene, which we used previously as a target to perform rapid AST on clinical samples.[18] Primers were purchased through Integrated DNA Technologies (San Diego, CA, USA) and were described previously.[18] Final primer concentrations were identical for all experiments: 1.6 µM FIP/BIP, 0.2 µM FOP/BOP, and 0.4 µM LoopF/LoopB.

LAMP experiments using *Bst* 3.0 **(Figure 2.2.2; Figure 2.2.3b d, e, f, h-j; Figure 2.2.4)** contained the following final concentrations, optimized previously[18]: 1x Isothermal Amplification Buffer II (New England BioLabs (NEB), Ipswich, MA, USA; Ref. B0374S;

containing 20 mM Tris-HCl 10 mM $(NH_4)_2SO_4$ 150 mM KCl, 2 mM $MgSO_4$, 0.1% Tween 20 pH 8.8 at 25 °C), 4 mM additional $MgSO_4$ (beyond 2 mM from buffer), 1.4 mM Deoxynucleotide Solution Mix, primers: 1.6 µM FIP/BIP, 0.2 µM FOP/BOP, and 0.4 µM LoopF/LoopB, 1 mg/mL BSA (New England BioLabs, Ref B90005), 320 U/mL *Bst* 3.0, Ambion RNAse cocktail (ThermoFisher, Waltham, MA, USA; Ref AM2286, 5 U/mL RNase A, 400 U/mL TNase T1), 2 µM SYTO 9 (ThermoFisher, Reference S34854), and approximately 660 copies/µL template in Ambion nuclease-free water (ThermoFisher, Ref AM9932).

LAMP experiments using *Bst* 2.0 **(Figure 2.2.3a, c, e, g)** contained the following final concentrations, optimized as shown in **Figure 2.2.S3**: 1x Isothermal Amplification Buffer (New England BioLabs, Ref. B0537S; containing 20 mM Tris-HCl 10 mM $(NH_4)_2SO_4$, 50 mM KCl 2 mM $MgSO_4$ 0.1% Tween 20 pH 8.8 at 25 °C), additional 6 mM $MgSO_4$ (New England BioLabs, Ref. B1003S), 1.4 mM Deoxynucleotide Solution Mix (New England BioLabs, Ref N0447S), primers: 1.6 µM FIP/BIP, 0.2 µM FOP/BOP, and 0.4 µM LoopF/LoopB, 1 mg/mL BSA (New England BioLabs, Ref B90005), 320 U/mL *Bst* 2.0 (New England BioLabs, Ref M0537S), Ambion RNAse cocktail (ThermoFisher, Ref AM2286, 5 U/mL RNase A, 400 U/mL TNase T1), 2 µM SYTO 9 (ThermoFisher, Ref S34854), and approximately 660 copies/µL template in Ambion nuclease-free water (ThermoFisher, Ref AM9932).

Template *E. coli* DNA was extracted from exponential-phase cultures grown in BBL Brain-Heart Infusion media (BD, Franklin Lakes, NJ, USA; Ref. 221813) using QuickExtract DNA Extraction Solution (Lucigen, Middleton, WI, USA; Ref. QE09050) as described previously.[18] Serial 10-fold dilutions were prepared in Tris-EDTA buffer (5 mM Tris-HCl, 0.5 mM EDTA, pH 8.0) containing 2 U/mL RNase A and 80 U/mL RNase T1 (ThermoFisher, Ref AM2286). DNA dilutions were quantified as described previously[18] using the QX200 Droplet Digital PCR (ddPCR) system (Bio-Rad Laboratories, Hercules, CA, USA).

Phenotypic antibiotic susceptibility testing (AST) on clinical samples

For the phenotypic AST, we adopted a workflow described previously,[17,18] and used archived nucleic-acid extractions from a previous study.[18] Briefly, clinical urine samples from patients with urinary tract infections (UTI) were split and diluted into equal volumes of media with or without the presence of an antibiotic. Samples were incubated for 15 min at 37 °C, a nucleic-acid extraction was performed, and these samples were archived at -80 °C until use. LAMP was performed on the archived samples to quantify the number of copies of the *E. coli* 23S ribosomal gene.

We tested our optimized assay on 17 archived clinical UTI samples containing $\geq 5 \times 10^4$ CFU/ml *E. coli* that had been categorized previously using the gold-standard broth microdilution AST (5 ciprofloxacin-susceptible, 5 ciprofloxacin-resistant, 4 nitrofurantoin-susceptible, and 3 nitrofurantoin-resistant).

We assessed samples as phenotypically "resistant" or "susceptible" by calculating the ratio of the concentration of 23S in the control and antibiotic-treated sample, which we call the control:treated (C:T) ratio. The C:T ratio was calculated 10 min after beginning to heat the LAMP reaction. A threshold of 1.1 was established previously,[17,18] so samples with C:T ratios >1.1 indicated that there was DNA replication in the untreated (control) group but not in the antibiotic-treated samples; these samples were identified as susceptible to the antibiotic. Samples with C:T ratios of <1.1 indicated that DNA replication occurred in both the control and antibiotic-treated samples; these samples were identified as resistant to the antibiotic.

RESULTS AND DISCUSSION

Workflow summary of real-time digital LAMP

To evaluate a pipeline for real-time dLAMP experiments, we chose commercially sourced microfluidic chips sold for endpoint digital PCR applications. The chips consist of an array of 20,000 uniform partitions (**Figure 2.2.1**), each 60 μm in diameter and an estimated 0.75 nL internal volume, which is similar to the volumes typically used in dLAMP.[16,18,20-23,25,26,28] These chips are loaded by pipetting the sample mixture (in our case containing the LAMP

reagents: buffer components, enzymes, template, and primers) into the plastic "blade" provided with the chips, and dragging the blade at a 70–80° angle to the chip to load the sample mixture by capillarity. This is followed by drying and evaporation of the surface layer for 20 sec at 40 °C, and application of the immersion fluid. Manual loading requires some skill, though a machine can be purchased to perform the task; typically, we were able to load ~18,000 out of the 20,000 partitions. We performed our evaluation using two different enzyme mixtures, *Bst* 2.0 and *Bst* 3.0 . Our amplification target (**Figure 2.2.1**) was the *E. coli* 23S ribosomal gene that we previously used as a target to perform rapid AST on clinical samples.[18]

The instrumentation requirements for real-time isothermal capabilities include a heater that can hold a stable temperature, and optical components with high spatial resolution that are capable of imaging the fluorescence intensity of the 20,000 individual partitions of the chip over time (**Figure 2.2.2a**). Here, we investigated two approaches: using a standard laboratory microscope (Leicia DMI-6000B), and using the RTAI,[30] which is composed of a thermocycler, optical components, a camera, and a light source.

We generated a custom MATLAB script to analyze the digital real-time data (details in **Supporting Information, S-I**). The software follows the change in fluorescence in individual partitions over time. From these data, we extract each partition's time to a fluorescence intensity threshold and calculate the bulk template concentration. In our demonstration, we loaded the acquired images into FIJI[31] as a time-stack series and manually separated the images of the individual chips to be analyzed separately. To process each chip's image stack, we used the custom MATLAB script that tracks the mean intensity of each partition over the course of each experiment. This script could be run with only minor modifications with images obtained from different instruments.

To calculate the bulk template concentration over time, we (1) identified the partitions that did or did not contain reaction solution, (2) tracked the partitions that met a minimum fluorescence intensity and (3) used the previous information to calculate the concentration of template in the bulk solution.

A summary of the script is as follows: (i) load the images into memory, (ii) count the total number of partitions before heating (iii) identify positive partitions after the conclusion of the experiment, (iv) track the intensity of positive partitions for each image frame, (v) apply

Gaussian smoothing and baseline subtraction, (vi) save the data, and (vii) repeat for each image stack. The output of the script contains: the raw traces of individual partitions over time, baseline corrected traces of individual partitions over time (**Figure 2.2.2b**), the number of partitions exceeding the manually defined minimum fluorescence intensity threshold with time (**Figure 2.2.2f**), and the maximum relative rate in RFU per 30 sec for individual partitions (**Figure 2.2.2d**). These data provide all the necessary information to conduct the analyses detailed in **Figure 2.2.2**.

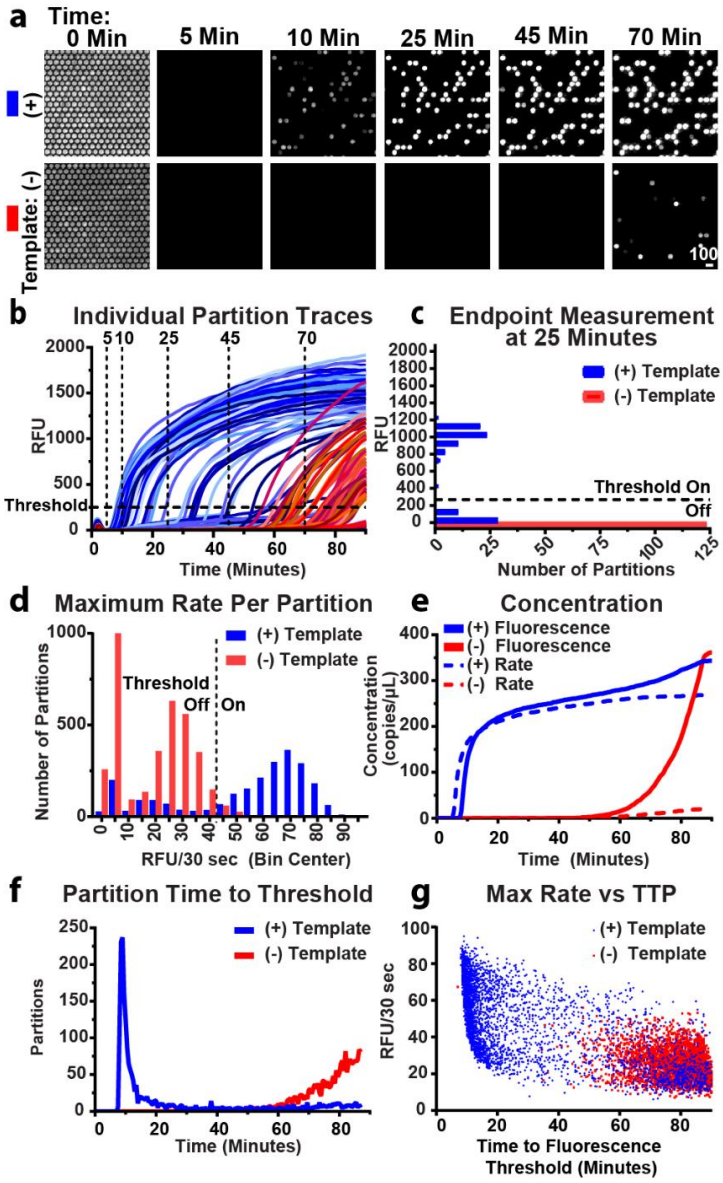

Figure 2.2. Experimental demonstration of the real-time digital LAMP (dLAMP) approach using the commercially available enzyme *Bst* 3.0. Experiments were run at 70 °C and imaged using a commercial microscope.

(a) A time course of fluorescence images from a subset of 350 partitions out of 20,000 partitions undergoing dLAMP reactions. (Intensity range 920-1705 RFU). (b) Fluorescence intensity for a subset of partitions over time. Blue traces indicate partitions containing template; red traces indicate fluorescence in the absence of template (i.e. non-specific amplification). Partitions turn "on" at the time point when the curve passes the threshold at 250 RFU. Vertical traces correspond to time points illustrated in panel (a) and generate endpoint measurements. (c) An "endpoint" measurement taken on a subset of partitions at 25 min. Bin width is 100 RFU. Fluorescence threshold is 250 RFU. (d) A histogram of the maximum observed change in fluorescence of individual partitions using the full chip. Rate threshold is 45 RFU/30 sec. (e) Change in observed bulk concentration over time from the full chip using fluorescence intensity as threshold (solid lines) and rate (dashed lines). (f) Time at which individual partitions in panel (b) cross the fluorescence intensity threshold. (g) Maximum rate per partition plotted by time to fluorescence intensity threshold.

Digital, real-time experiments to quantify LAMP performance

We next sought to experimentally evaluate this pipeline (**Figure 2.2.1**). First, we established whether the fluorescence from LAMP reactions could be reliably measured from individual partitions over time (**Figure 2.2.2a**). We used LAMP reagents for *Bst* 3.0, commercial chips, a resistive heater held at 70 °C, and a commercial microscope. Although the microscope is capable of collecting all 20,000 partitions on one chip in a single image, for simplicity, in **Figure 2.2.2a**, we cropped the image to include only 350 of the 20,000 partitions. Before turning on the heater (t = 0), we measured the autofluorescence from SYTO 9 to quantify the total number of partitions loaded with reaction solution. (To calculate template concentration using the Poisson distribution[32,33], we must know the total number of partitions containing the reaction mixture.) Autofluorescence from SYTO 9 decreases as the chip is heated and is completely eliminated within 3 min. The heater used on the microscope reaches reaction temperature within 120 sec. In less than 10 min, an increase in fluorescence was observed within some of the individual partitions, indicating amplification of individual template molecules inside those partitions. Due to the stochastic nature of amplification initiation, some of the partitions fluoresced later.

In the negative-control (no template) partitions, fluorescence was not observed for the first 45 min. However, we began to observe non-specific amplification after ~60 min. In these experiments, the negative control contains only 0.05x Tris-EDTA buffer in place of template

and represents a best-case scenario. We attribute amplification in the absence of template to primer dimers and other non-specific LAMP products.

Second, we asked if the signal from non-specific amplification was sufficiently delayed to differentiate it from the signal arising from specific amplification in the presence of template. To answer this question, we generated real-time fluorescence curves by plotting the change in fluorescence of individual partitions as a function of time (**Figure 2.2.2b**). We observed specific amplification (blue curves) beginning to initiate at ~7 min and non-specific amplification beginning to initiate at ~50 min (red curves) and concluded that we could discriminate specific and non-specific amplification by time.

Third, we asked whether enzymatic heterogeneity[16,21,34] of specific amplification can be quantified to differentiate specific from non-specific amplification. We plotted the maximum change of fluorescence achieved by each partition of the full chip per 30-sec interval (**Figure 2.2d)**. For the negative-control sample (red bars), we observed non-specific amplification following a bimodal distribution of rates, with a first peak with little to no rate of fluorescence increase and a second peak at ~25 RFU per 30 sec. For the sample containing template (blue bars), rates for specific amplification were heterogeneous and centered around a rate of 70 RFU/30 sec. We note that in PCR, which is gated by temperature cycling, there is no equivalent concept of "rate" as long as replication of DNA occurs faster that the duration of each elongation step. We found in our dLAMP experiments that the rate of specific amplification was greater than non-specific amplification. Hence, tracking amplification in real-time made it possible to distinguish true positives from false positives (non-specific amplification).

Fourth, we asked if the distribution in time to fluorescence threshold is sufficiently narrow to discriminate specific and non-specific amplification. By plotting the number of "on" partitions (i.e. partitions that crossed the fluorescence intensity threshold defined in **Figure 2.2b)** against time, we generated a distribution curve (**Figure 2.2f**) that illustrates the number of partitions that turn on per time point. This is related to the derivative of the change in concentration over time. This plot contains the time to threshold of all partitions within the entire chip, rather than a subset, to minimize sampling bias**.** In the sample containing template (blue curve), most partitions reached the threshold in 7–20 min, whereas the negative-control sample (red curve) had little non-specific amplification until approximately 60 min.

Graphing time to threshold illustrates the overall reaction's speed (defined as the location of the peak or mode time to threshold) and efficiency (proportional to the area under the curve and illustrated in **Figure 2.2f** as the calculated concentration). In our experiment, the peak of the sample containing template was narrow and well separated from the non-specific amplification of the negative control (**Figure 2.2f**), indicating sufficiently low heterogeneity in amplification rate and time to initiation of the reaction.

Fifth, we asked how the calculated bulk concentration changes over time. To answer this question, we generated endpoint-style measurements for each 30-sec time point, and calculated how the concentration changed over time. To demonstrate how to generate a single endpoint-style measurement, we selected one time point (25 min) and plotted RFU as a factor of the number of partitions (**Figure 2.2c**). Partitions were classified as either "on" (>250 RFU threshold) or "off" (<250 RFU threshold). Partitions that are defined as having turned "on" contain a template molecule that amplified, whereas partitions that are "off" either lack a template molecule or have not yet begun amplification. The sum of the partitions passing the threshold out of the total number of partitions with solution was used to determine a precise bulk concentration of template in the sample using the Poisson equation, as has been documented elsewhere.[32,33] We plotted the calculated concentration as it changed over time in **Figure 2.2e** (solid lines).

When the aim is to determine a precise concentration, we need to determine the best time at which to stop the assay. Deciding the best time to end the assay is complicated because each reaction initiates stochastically,[16,21] causing the calculated concentration to asymptotically approach the true concentration (**Figure 2.2e**). It would be ideal for the calculated concentration to rapidly rise to the true bulk concentration and plateau near the true concentration; however, the reaction should be stopped before the rise in non-specific amplification (observed in our example starting at 60 min; red curves, **Figure 2.2e–f**). We tested whether there is heterogeneity in amplification rate (i.e. whether partitions with slow amplification rates take longer to reach the fluorescence intensity threshold than partitions with fast amplification rates) and found that initiation time was stochastic, but the reaction rates for true and false positives were consistent (**Figure 2.2g**). Hence, two molecules could have the same TTP, yet initiate at different moments, resulting in variable amplification rates.

Combining information about the concentration of template (**Figure 2.2e**) and the time it takes for partitions to turn "on" (**Figure 2.2f**) can be used to inform the choice of an optimal assay length for endpoint measurements, for situations where real-time quantification is not feasible. For example, in **Figure 2.2**, the optimal assay length for an endpoint readout would be ~45 min. This approach allows one to balance stochastic initiation of amplification, overcome enzymatic heterogeneity, and reduce the incidence of false positives caused by non-specific amplification.

However, in cases where real-time measurements are desirable, thresholding by rate may be used to separate specific and non-specific amplification. For example, to correct for the observed increase in non-specific amplification (after 45 min), we implemented a threshold (**Figure 2.2d**) on the maximum rate per partition, thus eliminating some of the non-specific amplification in both the presence and absence of template (compare solid and dashed lines in **Figure 2.2e).** For example, the measured value at 60 min is 280 copies per µL (solid line), and the corrected value is 258 copies per µL (dashed line). In the no-template control, at 60 min, the measured value is 16 copies per µL (solid line), whereas the corrected value is 3 copies per µL (dashed line). The correction is more pronounced at 80 min where non-specific amplification is greater. At 80 min, the measured value in the presence of template is 325 copies per µL and the corrected value 266 copies per µL—indicating that almost 20% of the signal could arise from non-specific amplification. In the absence of template, the uncorrected value at 80 min is 187 copies per µL, however if rate is accounted for, then the value can be corrected to 16 copies per µL, thus eliminating the majority of the false positives.

Finally, we note that although we calculated template concentration, the value is precise but could be inaccurate if not all target molecules loaded into the chip undergo amplification (in other words, if efficiency of amplification is not 100%). Thus, we next sought to measure the absolute likelihood of detecting a molecule as a function of reaction condition**.**

Evaluation of the effect of temperature on dLAMP with two different enzymes to analyze the interplay of amplification efficiency, background, and speed of amplification

After establishing a protocol for generating real-time, digital measurements, we evaluated the absolute amplification efficiency of LAMP as a function of temperature for two different enzymes. We selected two commercial polymerases that worked well for us previously. Both enzymes are *in silico* homologues on the *Bacillus* stearothermophilus DNA Polymerase I and Large Fragment. NEB describes *Bst* 3.0 as an improvement of *Bst* 2.0 by adding reverse transcriptase activity, increased amplification speed, and increased thermostability. We sought to understand the differences in performance between these two enzymes at the single template level. For this experiment, we used the previously described RTAI.[30] The field of view for this instrument is larger than a microscope, allowing up to six samples to be observed concurrently. Hence, both the positive and negative controls could be collected in triplicate simultaneously. We expect some differences in measurements made on different instruments as a result of differing camera sensitivities and differences in the heating mechanism. Indeed, when we ran a single-concentration amplification reaction under identical conditions and compared measurements from the microscope and the RTAI, we found that there was significant difference ($P = 0.03$) in amplification efficiency between the two instruments (**Figure 2.S2**), with the RTAI generating higher amplification efficiency. Hence, we performed all enzyme-performance comparisons on a single instrument.

Amplification efficiency

First, we sought to establish the amplification efficiency of dLAMP, i.e. the fraction of template copies loaded that are detected (**Figure 2.3a-b**). We calculated the bulk concentration of template molecules from the digital measurement and plotted the observed template concentration as a fraction of template molecules loaded. To calculate the amplification efficiency, we determined template concentration using ddPCR and assumed all template molecules amplified. Using the real-time component of our measurements, we plotted the percent of copies detected over time compared with ddPCR.

We next asked how temperature impacts amplification efficiency. In general, we observed greater amplification efficiency at longer amplification times, which aligned with our previous observation (**Figure 2.2d–e)**. Second, when observing at a fixed time, increasing temperature increased amplification efficiency to an optimum (green box in **Figure 2.3a-b**) before activity decreased.

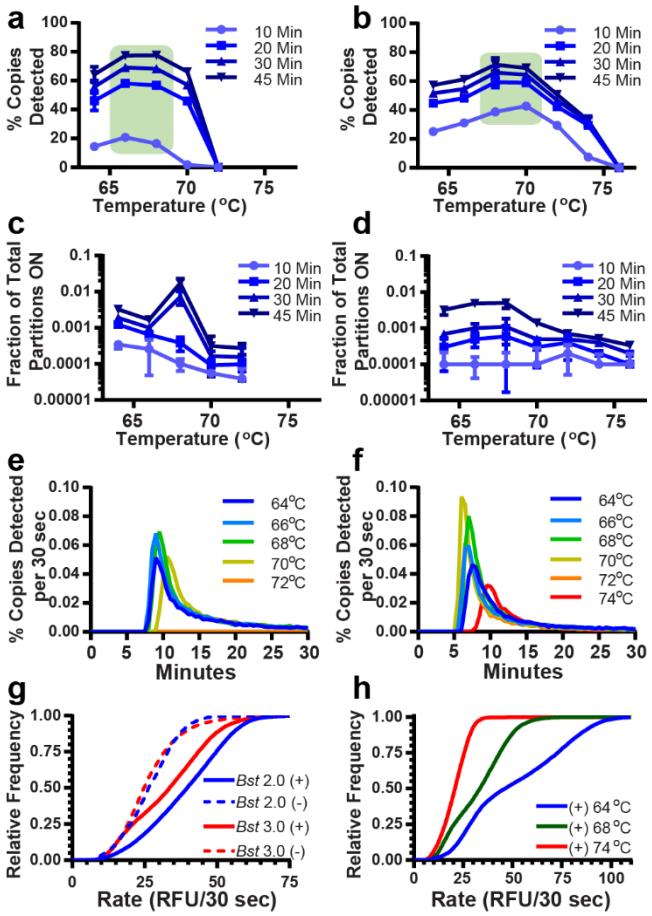

Figure 2.3. Evaluation of reaction conditions (enzymes and temperature) using real-time digital LAMP. (a-b) Amplification efficiency (percent template copies detected out of copies loaded) of *Bst* 2.0 (a) and *Bst* 3.0 (b) as a function of temperature. Green boxes indicate the optimal temperature range for the greatest probability of template detection. (c-d) Non-specific amplification in template-free buffer samples using *Bst* 2.0 (c) and *Bst* 3.0 (d) for conditions matching panels a-b. (e-f) Distribution of time to fluorescence threshold using *Bst* 2.0 (e) and *Bst* 3.0 (f). (g) The fractional cumulative distribution function (CDF) compares the enzymes at their optimal temperatures (68 °C). (h) Fractional CDF plots of *Bst* 3.0 rate at

three temperatures. Error bars are S.D. For all datasets, N = 3 chips (technical replicates). CDF plots are the sum of 3 technical replicates.

Several observations can be made by comparing the results from *Bst* 2.0 and *Bst* 3.0 (**Figure 2.3a-b**). Although *Bst* 2.0 and *Bst* 3.0 have an identical reported optimal incubation temperature in bulk (65°C), we observed they had different optimal temperature ranges for amplification efficiency (*Bst* 2.0 at 66–68 °C; *Bst* 3.0 at 68–70 °C). We detected lower amplification efficiency at higher temperatures with *Bst* 2.0 compared with *Bst* 3.0. *Bst* 2.0 failed to amplify at 72 °C, whereas *Bst* 3.0 continued amplifying until 76 °C. At short amplification times, (such as 10 min), *Bst* 3.0 had greater amplification efficiency than *Bst* 2.0 (42.8% vs 20.8%, respectively). In contrast, at longer amplification times, such as 30 or 45 min, efficiency for the enzymes was similar (77.6% vs 71.5% at 45 min, respectively), though *Bst* 2.0 had slightly greater amplification efficiency than *Bst* 3.0.

We hypothesize that increased temperature improved amplification efficiency (presumably by increasing the breathing of dsDNA and facilitating primer annealing) until, at higher temperatures, a combination of enzyme denaturation or failure of the primers to anneal occurred. Our primers had melting temperatures ranging from 56–61 °C, when excluding the secondary FIP and BIP anealing regions, as calculated using OligoCalc.[35] We found that chip-to-chip variability was extremely low. Relative error for *Bst* 2.0 at optimal temperature (68 °C) and 45 min of amplification was ~2% (**Figure 2.2a**), whereas the predicted Poisson noise for a single chip is 0.7%. Achieving such high precision using bulk measurements would require hundreds of experiments. The low variability among these measurements indicates that we were correctly determining whether a partition contained solution and whether it amplified.

Non-specific background amplification

Next, we quantified the amount of non-specific amplification (**Figure 2.3 c-d)** as a function of time and temperature. We plotted the number of wells that turned "on" in the absence of template relative to the total number of wells filled with LAMP solution. As previously stated, these non-specific amplification reactions included buffer in place of template and represent a best-case scenario. We concluded that at least for these idealized conditions, non-

specific amplification in dLAMP was extremely low. For example, a fraction of 0.001 could correspond to 20 partitions turning on from among a total of 20,000 possible partitions. For both enzymes, we found the maximum fraction of non-specific amplification per total partitions was 0.0012 for times 20 min or less. The highest fraction of non-specific amplification observed was 0.017 at 45 min, corresponding to fewer than 350 non-specific partitions of the 20,000 total (**Figure 2.3c-d**). Furthermore, we observed higher temperatures resulted in lower non-specific amplification (**Figure 2.3c-d**). Finally, at extremely long amplification times (e.g. 60 min amplification, data not shown) *Bst* 2.0 had lower background than *Bst* 3.0.

Variations in speed and amplification efficiency

Third, we quantified the variation in speed and amplification efficiency across partitions in the time to reach fluorescence intensity threshold (**Figure 2.3e-f**). We first plotted the percent copies detected as a function of time for each temperature. As described previously, these curves represent the distribution in the time to threshold across all partitions and thus illustrate the interplay of (i) detecting a molecule (area under the curve from zero to a given time corresponding to the values plotted in **Figure 2.3a-b**), (ii) the speed of the reaction (the time at which the peak reaches a maxima) and (iii) several parameters of peak width summarized in **Table S1**. We hypothesize peak width is related to both the enzyme amplification rate, overall amplification efficiency, and the time at which the reaction initiates. Next, we plotted the peak time to threshold (**Figure 2.S1)**. Images were collected in 30-sec intervals and we report the average of three trials. In some cases, the difference in time to threshold was less than the imaging time interval. For each time point, if fewer than 15 partitions (0.075% of total partitions) were "on," that time point was not included in the calculation of the mode. For these measurements, at the start of the reaction, the heat block was at 25 °C and the time to threshold included the time for the heat block to come to reaction temperature (~70 sec). Hence, there will be minor differences (seconds) in the time for each reaction to reach the fixed temperature. We do not see evidence that this difference manifests in the mode time to positive (TTP) measurements.

In reactions with *Bst* 2.0, below 68 °C, mode TTP was narrowly clustered around 9.5 min. At 70 °C, mode TTP increased, and the reaction failed to amplify beyond 72 °C. In reactions

with *Bst* 3.0, the mode TTP decreased from 8.2 ± 0.3 (mode ± S.D.) min at 64 °C to 6.6 ± 0.3 min at 70 °C, then increased with increasing temperature until amplification failed for all partitions at temperatures ≥76 °C. In the negative controls for both enzymes (**Figure 2.S1**), amplification either failed or started after 75 min.

Several observations can be made by comparing the results from **Figure 2.3e-f.** We found that the optimal temperature for time to threshold corresponded with the optimal temperature for amplification efficiency (**Figure 2.3a-b)**, and that the optimal temperatures also had the smallest tailing factors, Full Width at Half Maximum (FWHM) and asymmetric factor (i.e. narrowest peak widths) **(Figure 2.3e-f; Table S1)**. At optimal efficiency, *Bst 3*.0 was approximately 2 min faster in mode TTP, had much narrower FWHM, smaller tailing factor, and lower asymmetry than *Bst* 2.0. Finally, as efficiency decreases, measurements of peak shape and width increase. To the best of our knowledge, this is the first published quantification that explicitly tests and quantifies the time dependence of LAMP efficiency using these enzymes. Real-time digital enables us to identify the time point at which the observed concentration most closely approximates the true concentration thus optimizing the assay duration.

Rates of amplification (specific and non-specific)

Fourth, we compared the rates of specific and non-specific amplification between *Bst* 2.0 and *Bst* 3.0. The data shown represent the combined rates of three separate trials. We found that non-specific amplification rates were similar for the two enzymes (**Figure 2.3g**, dashed lines), whereas in the presence of template, amplification rates were faster for *Bst* 2.0 than *Bst* 3.0 (**Figure 2.3g**, solid lines), despite lower efficiency at short times. Differences in camera sensitivity between the microscope (used for real-time images in **Figure 2.2**) and the RTAI (used for **Figure 2.3**) result in different apparent amplification rates.

We also examined the relationship between temperature, efficiency, and maximum rate. In the case of *Bst* 3.0, maximum reaction amplification rate does not correspond with optimal efficiency (**Figure 2.3h**). 64 °C had the fastest amplification rates, but suboptimal efficiency (57.3% at 45 min). Optimal amplification efficiency occurs at 68 °C (71.5% at 45 min), but slightly slower amplification rate than 64 °C. At 74 °C, we observed both poor efficiency

(32.7% at 45 min) and slowest reaction rate. We attribute this to a combination of decreased enzymatic velocity and decreased primer annealing. Additionally, we note that different thresholds for amplification rate would be needed for each temperature. This is expected given changes in enzymatic velocity.

Application of the pipeline to a phenotypic antibiotic susceptibility test (AST) using clinical samples

We next asked whether we could apply the output of this digital real-time pipeline to perform a rapid phenotypic AST. Specifically, we aimed to categorically sort clinical samples as phenotypically "susceptible" or "resistant" to an antibiotic in agreement with the gold-standard reference method. This study was constructed as a demonstration of the capability of the microfluidic chips and the value gained from using this digital real-time pipeline to optimize reaction conditions—it was not an assessment of the digital AST (dAST) methodology established previously.[17,18] We selected the optimal dLAMP conditions for *Bst* 3.0 based on the measurements of mode TTP and amplification efficiency established in the previous experiments (**Figure 2.3b**)—70 °C and a reaction time of 10 min. We used archived clinical urine samples from patients diagnosed with urinary tract infections (UTI) containing *E. coli.* These samples had been categorized as phenotypically susceptible or resistant to the antibiotics ciprofloxacin or nitrofurantoin using the gold-standard (broth microdilution) method.[18] We tested exactly 17 samples and observed 100% categorical agreement with the gold-standard method (0 major errors; 0 minor errors). We conclude that the pipeline presented in this paper performs well and could be used, among other applications, to optimize reaction conditions for speed and sensitivity and apply those conditions to a determination of phenotypic antibiotic susceptibility in clinical samples.

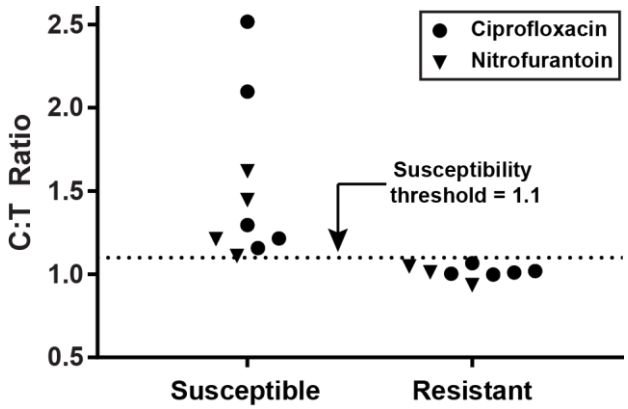

Figure 2.4. Phenotypic antibiotic susceptibility tests of 17 clinical urine samples from patients infected with a urinary tract infection containing *E. coli*. Susceptibility to the antibiotics nitrofurantoin and ciprofloxacin were tested using dLAMP conditions optimized using digital real-time experiments (Figure 2.3). Urine samples were exposed to media without antibiotic (control) or media with an antibiotic (treated) for 15 min and then concentrations of nucleic acids were quantified to calculate a control:treated (C:T) ratio. Samples were categorized by dLAMP as susceptible (above the susceptibility threshold) or resistant (below the threshold). All samples were categorized in agreement with the clinical gold-standard method.

CONCLUSION

We have presented a pipeline to generate real-time, digital isothermal amplification measurements using only commercial and open-source components. We used this pipeline to examine how small changes in reaction conditions influence the interplay of LAMP efficiency, speed, and background by performing 124 real-time dLAMP experiments. As one practical application of this approach, we determined the optimal reaction conditions for a phenotypic test of antibiotic susceptibility using 17 clinical urine samples from patients diagnosed with urinary tract infections. In all cases, the results of the optimized dLAMP assays were in agreement with the clinical gold-standard AST.

These experiments validate that real-time digital measurements enable tests of enzymatic performance in dLAMP. Generally, we found that each enzyme had a unique optimal temperature for amplification efficiency (probability of detecting a target molecule) and for

eliminating non-specific amplification. This “optimal” temperature produced the fastest mode TTP and the narrowest, most symmetrical distribution curves; interestingly, the optimal temperature did not necessarily yield the fastest amplification rate. Together, these data suggest that amplification efficiency is an interplay of enzymatic rate, diffusive transport, and DNA breathing. When reactions are performed away from optimal temperature, the distribution curves broaden and decrease in total area, resulting in reduced overall amplification efficiency and slower mode TTP; whereas amplification rate decreases with increasing temperature. With regard to the specific enzymes in this study, although efficiency was similar at long amplification times (> 20 min), *Bst* 3.0 had a faster mode TTP than *Bst* 2.0 by approximately 2 min, and more narrow and symmetrical distribution curves. However, *Bst* 2.0 had faster amplification rates than *Bst* 3.0, so reactions with *Bst* 2.0 took longer to initiate, but proceeded more rapidly. For both polymerases, non-specific amplification in buffer was extremely low.

In the future, this pipeline can be used to understand the fundamental pieces of LAMP. The field of diagnostics would benefit from a thorough mechanistic study of LAMP asking which components determine amplification fate, and how components, such as primers and heating rate (**Figure 2.S2**), impact reaction and enzymatic speed. This pipeline makes such a mechanistic study possible. For example, in this study we corrected the observed concentration by separating true positives from background amplification using rate and fluorescence, but we did not explore the origins of non-specific amplicons—which deserves its own study and development of more precise tools for studies of non-specific amplification. Finally, this pipeline can be extended to optimize other isothermal amplification chemistries that could be suited to other types of diagnostic assays.

Ultimately, this pipeline will make digital real-time measurements more accessible to researchers, even those who lack microfluidic expertise or specialized equipment. The commercially available chips and reagents used here could be coupled with many combinations of standard laboratory or field equipment, such as a hot plate and a fluorescent stereoscope, or a chemical heater and a cell phone camera. While we believe the general trends found in this manuscript will extend to other primer sets, we hope this pipeline will enable others to study other primer sets and conditions of interest to them.

ACKNOWLEDGMENTS

This research was supported in part by the Burroughs Wellcome Fund Innovation in Regulatory Science Award (to R.F.I.) and a grant from the Jacobs Institute for Molecular Engineering for Medicine. Research reported in this publication was also supported by the Department of Health and Human Services (HHS) Office of the Assistant Secretary for Preparedness and Response (ASPR) and the Wellcome Trust under the CARB-X program (federal award number IDSEP160030-02); the content is solely the responsibility of the authors and does not necessarily represent the official views of the Department of HHS Office of the ASPR. This work is funded in part by CARB-X as a collaboration between Talis Biomedical Corp. and Caltech. This project benefited from the use of instrumentation at the Jim Hall Design and Prototyping Lab at the California Institute of Technology. We thank Travis Schlappi for performing the extractions of the archived clinical samples and Natasha Shelby for contributions to writing and editing this manuscript.

ASSOCIATED CONTENT

Supporting Information:

REFERENCES

(1) Heid, C. A.; Stevens, J.; Livak, K. J.; Williams, P. M. *Genet. Res.* **1996**, *6*, 986-994.

(2) Tanner, N. A.; Zhang, Y.; Evans, T. C. *BioTechniques* **2012**, *53*, 81-89.

(3) Tanner, N. A.; Zhang, Y.; Evans, T. C. *BioTechniques* **2015**, *58*, 59-68.

(4) Notomi, T.; Okayama, H.; Masubuchi, H.; Yonekawa, T.; Watanabe, K.; Amino, N.; Hase, T. *Nucleic Acids Res.* **2000**, *28*, e63-e63.

(5) Tanner, N. A.; Evans, T. C. *Curr. Protoc. Mol. Biol.* **2014**, *105*, 15.14.11-15.14.14.

(6) Becherer, L.; Bakheit, M.; Frischmann, S.; Stinco, S.; Borst, N.; Zengerle, R.; von Stetten, F. *Anal. Chem.* **2018**, *90*, 4741-4748.

(7) Aoi, Y.; Hosogai, M.; Tsuneda, S. *J. Biotechnol.* **2006**, *125*, 484-491.

(8) Drame, P. M.; Fink, D. L.; Kamgno, J.; Herrick, J. A.; Nutman, T. B. *J. Clin. Microbiol.* **2014**, *52*, 2071-2077.

(9) Mori, Y.; Kitao, M.; Tomita, N.; Notomi, T. *J. Biochem. Bioph. Meth.* **2004**, *59*, 145-157.

(10) Ball, C. S.; Light, Y. K.; Koh, C.-Y.; Wheeler, S. S.; Coffey, L. L.; Meagher, R. J. *Anal. Chem.* **2016**, *88*, 3562-3568.

(11) Calvert, A. E.; Biggerstaff, B. J.; Tanner, N. A.; Lauterbach, M.; Lanciotti, R. S. *PLOS One* **2017**, *12*, e0185340.

(12) Poole, C. B.; Ettwiller, L.; Tanner, N. A.; Evans, T. C., Jr.; Wanji, S.; Carlow, C. K. S. *PLOS One* **2015**, *10*, e0139286.

(13) Poole, C. B.; Tanner, N. A.; Zhang, Y.; Evans, T. C., Jr.; Carlow, C. K. S. *PLOS Neglect. Trop. D.* **2012**, *6*, e1948.

(14) Wheeler, S. S.; Ball, C. S.; Langevin, S. A.; Fang, Y.; Coffey, L. L.; Meagher, R. J. *PLOS One* **2016**, *11*, e0147962.

(15) Bhadra, S.; Jiang, Y. S.; Kumar, M. R.; Johnson, R. F.; Hensley, L. E.; Ellington, A. D. *PLoS One* **2015**, *10*, e0123126.

(16) Khorosheva, E. M.; Karymov, M. A.; Selck, D. A.; Ismagilov, R. F. *Nucleic Acids Res.* **2016**, *44*, e10.

(17) Schoepp, N. G.; Khorosheva, E. M.; Schlappi, T. S.; Curtis, M. S.; Humphries, R. M.; Hindler, J. A.; Ismagilov, R. F. *Angew. Chem. Int. Edit.* **2016**, 9557-9561.

(18) Schoepp, N. G.; Schlappi, T. S.; Curtis, M. S.; Butkovich, S. S.; Miller, S.; Humphries, R. M.; Ismagilov, R. F. *Sci. Trans. Med.* **2017**, *9*, eaal3693.

(19) Sun, B.; Shen, F.; McCalla, S. E.; Kreutz, J. E.; Karymov, M. A.; Ismagilov, R. F. *Anal. Chem.* **2013**, *85*, 1540-1546.

(20) Rodriguez-Manzano, J.; Karymov, M. A.; Begolo, S.; Selck, D. A.; Zhukov, D. V.; Jue, E.; Ismagilov, R. F. *ACS Nano* **2016**, *10*, 3102-3113.

(21) Sun, B.; Rodriguez-Manzano, J.; Selck, D. A.; Khorosheva, E.; Karymov, M. A.; Ismagilov, R. F. *Angew. Chem. Int. Edit.* **2014**, *53*, 8088-8092.

(22) Hu, Y.; Xu, P.; Luo, J.; He, H.; Du, W. *Anal. Chem.* **2017**, *89*, 745-750.

(23) Ma, Y.-D.; Chang, W.-H.; Luo, K.; Wang, C.-H.; Liu, S.-Y.; Yen, W.-H.; Lee, G.-B. *Biosens. Bioelectron.* **2018**, *99*, 547-554.

(24) Ma, Y.-D.; Luo, K.; Chang, W.-H.; Lee, G.-B. *Lab Chip* **2018**, *18*, 296-303.

(25) Schuler, F.; Siber, C.; Hin, S.; Wadle, S.; Paust, N.; Zengerle, R.; von Stetten, F. *Anal. Methods-UK* **2016**, *8*, 2750-2755.

(26) Gansen, A.; Herrick, A. M.; Dimov, I. K.; Lee, L. P.; Chiu, D. T. *Lab Chip* **2012**, *12*, 2247-2254.

(27) Rane, T. D.; Chen, L.; Zec, H. C.; Wang, T.-H. *Lab Chip* **2015**, *15*, 776-782.

(28) Zhu, Q.; Gao, Y.; Yu, B.; Ren, H.; Qiu, L.; Han, S.; Jin, W.; Jin, Q.; Mu, Y. *Lab Chip* **2012**, *12*, 4755-4763.

(29) Shen, F.; Davydova, E. K.; Du, W.; Kreutz, J. E.; Piepenburg, O.; Ismagilov, R. F. *Anal. Chem.* **2011**, *83*, 3533-3540.

(30) Selck, D. A.; Ismagilov, R. F. *PLOS One* **2016**, *11*, e0163060.

(31) Schindelin, J.; Arganda-Carreras, I.; Frise, E.; Kaynig, V.; Longair, M.; Pietzsch, T.; Preibisch, S.; Rueden, C.; Saalfeld, S.; Schmid, B.; Tinevez, J.-Y.; White, D. J.; Hartenstein, V.; Eliceiri, K.; Tomancak, P.; Cardona, A. *Nat. Methods* **2012**, *9*, 676.

(32) Kreutz, J. E.; Munson, T.; Huynh, T.; Shen, F.; Du, W.; Ismagilov, R. F. *Anal. Chem.* **2011**, *83*, 8158-8168.

(33) Rissin, D. M.; Walt, D. R. *Nano Lett.* **2006**, *6*, 520-523.

(34) Rojek, M. J.; Walt, D. R. *PLOS One* **2014**, *9*, e86224.

(35) Kibbe, W. A. *Nucleic Acids Res.* **2007**, *35*, W43-W46.

Supporting Information for

REAL-TIME, DIGITAL LAMP WITH COMMERCIAL MICROFLUIDIC CHIPS REVEALS THE INTERPLAY OF EFFICIENCY, SPEED, AND BACKGROUND AMPLIFICATION AS A FUNCTION OF REACTION TEMPERATURE AND TIME

S-I Summary of MATLAB script functions

In order to quantify the reactions on chips using the Poisson distribution, we needed to know the number of partitions that contained solution and the number of partitions that were empty. (It would be naïve to assume that all 20,000 partitions were loaded with solution; visual inspection shows that was rare.) We counted the total number of partitions with solution using the image of the autofluorescence of SYTO 9 dye before heating at time 0 (**Figure 2.2a**). SYTO 9 had uniform autofluorescence independent of template presence, making it easy to count all partitions loaded with solution.

To track the mean fluorescence intensity of each partition over time, we solved two challenges. First, when the microfluidic chip was heated (especially during the first 2 min) the chip moved. As the chip heated, it lost the initial autofluorescence from SYTO 9. Consequently, it was not possible to track this movement with the fluorescence of a single fluorophore. We solved this challenge by creating a mask (using image segmentation) that outlined each detectable partition at the chip's final position using a frame at the end of amplification. An advantage to using only the detectable partitions that met a minimum fluorescence intensity (out of a total of 20,000 partitions per chip) was reduced overall computation time because only a fraction of the total partitions were tracked in real-time.

A second challenge when tracking mean fluorescence intensity of each partition over time using only the detectable partitions is that partitions can appear to be different sizes because of differences in fluorescence intensity (dark partitions can appear artificially smaller and bright partitions can appear artificially larger). To counteract the effect of each partition having a different average intensity, we performed multi-level thresholding with tight restrictions for the area and major axis filters. We set a minimum fluorescence intensity (threshold) for each pixel at a given time and used this information to segment (define the perimeter) each individual partition. This threshold was combined with selection criteria for the area and major axis. The area filter defined the smallest and largest partitions while the major axis filter ensured that detected regions were circular. We repeated this for different threshold values and merged the resulting partitions. This technique restricted partitions to a specific size and shape while enabling detection over many intensity values.

Finally, we used the information from quantifying the number of partitions containing solution and tracking mean fluorescence of each partition over time to calculate the

concentration of template in the bulk solution. To smooth the traces and reduce the noise, we first applied a Gaussian-weighted moving average filter with window length 10 frames to each intensity curve. To ensure all partitions start at zero intensity, we determined the baseline intensity by calculating the average partition intensity for selected frames after heating but prior to detectable amplification (between 2.5 min and 5 min). The baseline intensity was subtracted from all frames. Finally, we manually defined a threshold to determine whether a partition would be counted as a "positive" or "negative." Using the adjusted traces, threshold, and the total number of partitions, we determined the fraction of partitions that were "on" for any given time. Using the fraction of partitions that were "off," we calculated via the Poisson distribution the concentration of template detected in the bulk solution for any given time point. From this measurement of concentration, we can calculate the amplification efficiency by dividing the measured concentration by the known (true) concentration.

The MATLAB script described here has been deposited in the open-access online repository GitHub and may be accessed using the following direct link: https://github.com/IsmagilovLab/Digital_NAAT_Analyzer

S-II Real-time data acquisition parameters

Acquiring real-time data using microscopy

Images were acquired in 30-sec intervals on a Leica DMI-6000B (Leica, Buffalo Grove, IL, USA) with a 1.25x 0.04NA HCX PL FLUOTAR Objective (506215) and 0.55x coupler (Leica C-mount 11541544) using a 1-sec exposure through the L5 (GFP) Nomarski prism and a Hamamatsu ORCA-ER CCD camera (Hamamatsu Photonics K.K., Hamamatsu City, Shizuoka, Japan; Ref. C4742-80-12AG). Heating was performed using an integrated circuit (IC) board prototype for temperature control developed by Green Domain Design (San Diego, CA, USA). The IC board was connected to a DC power supply (Model 3670; Electro Industries, Monticello, MN, USA), a Nichrome wire (12 ohm) attached to a 5 x 25 x 25 mm aluminum block. A thermistor was mounted within the block to measure the temperature of the heating block. When the temperature of the heating block was lower than the set-point

temperature, the IC board supplied current to the Nichrome wire resistive heater. With this setup, heating was achieved to 70.0 ± 2 °C within 2 min. Images obtained on the microscope were processed with our MATLAB script (**Supporting Information, S-I**) using the following parameters: Area Bound [5 40] pixels, Major Axis [2 9] pixels, Threshold [250] Relative Fluorescence Units (RFU), Baseline Smoothing Frames [6 11], Masking Image Frame [175].

Acquiring data using a custom large-format real-time amplification instrument (RTAI)

Images were acquired in 30-sec intervals on a custom-built, public-domain real-time amplification instrument (RTAI), described previously,[30] using the FAM channel with a 15-sec exposure at *f*/5.6. Heating was achieved using the built-in PCT-200 thermocycler, which heats to 70.0 ± 0.3 °C within 70 sec. The temperature of the thermocycler block was held at 25 °C to start all reactions, with the exception of an experiment where the block was preheated to the optimal temperature (**Figure 2.S2b**). We equipped the thermocycler with an aluminum block with two sloped planes (each set at 11°—an angle defined by the microfluidic chip manufacturer's requirements), to segregate bubbles formed during the reaction to a specifically designed bubble trap. It was advantageous to use this instrument to analyze up to six chips in parallel in a single field of view and under a uniform temperature. By running multiple chips on a real-time instrument we achieved "multiplexed" assays (wherein multiple measurements are made simultaneously). Images obtained on the RTAI were processed through our MATLAB script (**Supporting Information, S-I**) using the following parameters: Area Bound [4 12] pixels, Major Axis [2 5] pixels, Threshold [100] RFU, Baseline Smoothing frames [6 11], Masking Image Frame [175].

S-III Limitations of chips used

A limitation of chips that discretize by capillary action is that solution can spread among the partitions. For example, during dLAMP quantification of extractions for three of the clinical samples, we observed spreading of one positive partition to its adjacent partitions. We attribute this spreading to liquid bridges forming among adjacent wells, resulting in transfer of the amplicon among compartments. These bridges could arise from defects in surface coatings of commercial chips or from an excess of surface active molecules present in some

clinical samples. To test whether spreading was due to surface active impurities in the samples, samples were diluted in Tris-EDTA (TE) buffer and in the subsequent test, spreading was eliminated for one sample. For the remaining samples, dilution reduced the spreading enough that quantification at 10 min was not hindered, although some spreading was observed at later times. Quantification of the C:T ratio remained consistent (and the susceptibility call the same) because we use a ratiometric calculation.

S-IV Calculation of Peak width metrics

The average distribution curve (averaged over three trials) was calculated for each temperature and all values normalized to the peak prominence. Time resolution was estimated to the nearest 15 second interval. Calculations were based on: John V. Hinshaw. "How Do Your Peaks Measure Up?" Oct 01, 2013, LCGC Europe, Volume 26, Issue 10, pg 575–582.

Full Width at Half Maximum was calculated at the time difference between the leading at tailing edges at 50% peak prominence.

Asymmetric factor was calculated by dividing the time between the peak prominence and the tailing edge ("$b_{0.1}$") by the time between the peak prominence and the leading edge at 10% peak height ("$f_{0.1}$").

(Eq. S1)

$$Asymmetric\ Factor = \frac{b_{0.1}}{f_{0.1}}$$

Tailing factor was calculated as the total peak width at 5% of the prominence (or the distance from the leading edge to the time of peak prominence ("$f_{0.05}$") plus the distance from the time of peak prominence to the tailing edge ("$b_{0.05}$")) divided by twice the distance from the leading edge to the time of peak prominence.

(Eq. S2)

$$Tailing\ Factor = \frac{f_{0.05} + b_{0.05}}{2f_{0.05}}$$

Table 2.S1. Tabular quantification of the time to threshold distribution curves.

Bst 2.0						*Bst* 3.0					
Temp (ºC)	Efficiency at 45 min (%)	Mode TTP (min)	FWHM (min)	Asymmetric Factor	Tailing Factor	Temp (ºC)	Efficiency at 45 min (%)	Mode TTP (min)	FWHM (min)	Asymmetric Factor	Tailing Factor
64.0	64±8	9.5±0.0	2.5	10.2	14.8	64.0	57±2	8.2±0.3	3.0	8.0	14.2
66.0	78±2	9.3±0.3	2.3	7.6	11.7	66.0	61±2	7.3±0.3	2.3	5.6	11.4
68.0	78±2	9.8±0.3	2.3	7.2	14.3	68.0	71±6	7.6±0.3	2.3	6.0	9.2
70.0	66±1	11.0±0.0	2.8	8.8	9.1	70.0	69±3	6.7±0.3	1.5	7.3	3.7
						72.0	51±3	7.2±0.3	2.0	8.3	4.3
						74.0	33±9	10.2±0.6	2.8	5.7	13.1

S-V **Time to Mode Positive**

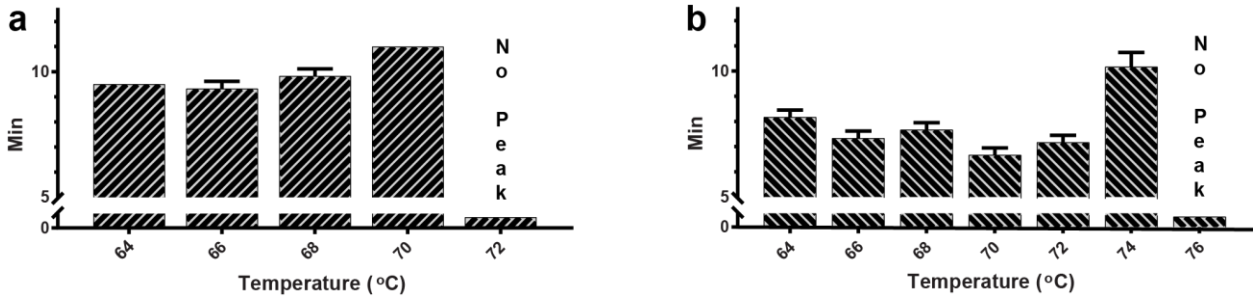

Figure 2.S1. Bar graphs of the time location of the peak of the distribution curve (time to mode positive) using *Bst* 2.0 (a) and *Bst* 3.0 (b). We required 15 or greater partitions turn on at a given time (0.075% of total partitions), to include the time point for the mode. Data are summarized in Table S1 in S-III.

S-VI Hardware and pre-heating considerations

We asked if multiple instrumentation formats could be used to collect the data and if hardware format impacted the amplification efficiency. We used the optimal conditions for *Bst* 3.0. First, we compared the performance of the large-format real-time amplification instrument (RTAI) to a wide-field microscope fitted with a heat block—a set-up that would be accessible to most laboratories. We found that the heater ramp rate was slower on the microscope than the RTAI (120 sec versus 70 sec) resulting in 9.0 ±1.0 min time to mode positive (**Figure 2.S2a)**.

Next, we looked at the effect of pre-heating using the RTAI. We compared the optimal conditions using *Bst* 3.0 and starting from 25 °C (green curve) with the same instrument and heating block already at the optimal reaction temperature of 70 °C (orange curve). When the block is preheated, we observed the mode time to threshold reduced from 6.7 ±0.3 min to 6.0 ±0.0 min (**Figure 2.S2a**).

Next, we asked if differences in hardware configuration and the heating rates between the instruments would also correspond to differences in probability of detection. We observed significant variation in amplification efficiency (RTAI vs RTAI with preheating $P = 0.002$; RTAI vs microscope with heater $P = 0.031$, RTAI with preheating vs microscope with heater $P < 0.001$) and concluded that heating rate may impact probability of amplification (**Figure 2.S2b**). Hence, all comparisons made in this study were instrument specific. Though it remains to be tested, we suspect more precise hardware, with improved heating control, could improve device performance.

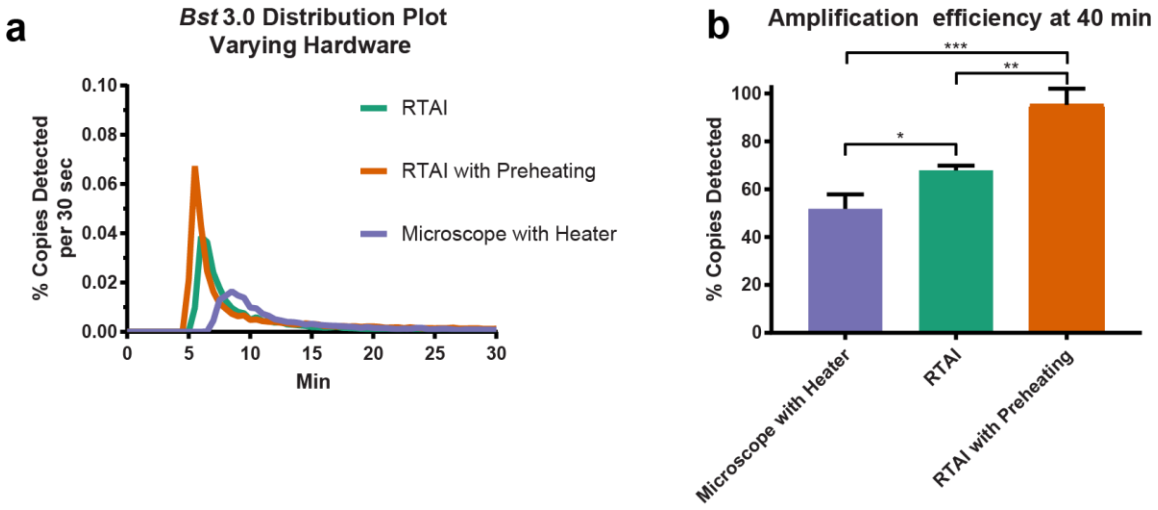

Figure 2.S2. Effect of hardware and heating on (a) the distribution in time to fluorescence threshold and (b) quantification of amplification efficiency (mean percentage copies detected ± S.D.) at 40 min.

S-VII Optimization of *Bst* 2.0 buffer composition

Following the protocol described previously[18], buffer conditions for *Bst* 2.0 were optimized in bulk at 713 copies/µL (e.g. ~4,280 or 0 copies per 6 µL reaction). Optimal buffer composition was selected based on fastest bulk time to positive.

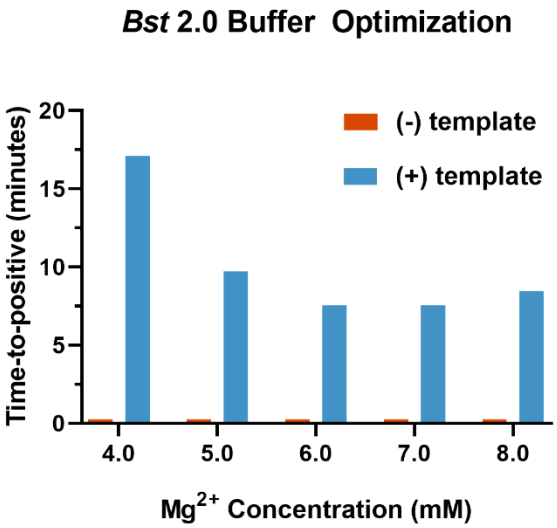

Figure 2.S3. Magnesium optimization for *Bst* 2.0. A value of 0.25 indicates that no amplification was observed. Amplification was performed at 67.5° C. N=1 for all TTP values.

S-VIII Contributions of non-corresponding authors

J.C.R. conceptualized the method, generated and analyzed data. Wrote the paper, constructed figures, and performed all revisions.

E.J. wrote the MATLAB software script for automated analysis of digital LAMP image sequences. Provided minor input to experimental design; and minor edits and inputs to the figures and manuscript.

N.G.S. prepared and quantified nucleic acid stocks. Optimized buffer conditions for *Bst* 2.0. Provided minor input to experimental design and minor edits and inputs to the figures and manuscript.

Chapter 3

REAL-TIME KINETICS AND MELT CURVES IN SINGLE-MOLECULE DIGITAL LAMP DIFFERENTIATE SPECIFIC AND NONSPECIFIC AMPLIFICATION EVENTS TO IMPROVE THE LIMIT OF DETECTION

Justin C. Rolando, Erik Jue, Jacob Barlow, and Rustem F. Ismagilov

ABSTRACT

Isothermal amplification assays, such as LAMP, are showing great utility for the development of rapid diagnostics for infectious diseases because they have high sensitivity, pathogen-specificity, and robustness to high levels of host DNA. However, assay optimization remains constrained by a limited understanding of how assay parameters affect specific and nonspecific amplification. Here, using chlamydia DNA as a clinically relevant target, we develop a real-time digital LAMP (dLAMP) approach to investigate patterns in specific and nonspecific amplification. By incorporating melting temperature (Tm) as a tool to evaluate the impact of thresholds, we show that the digital single-molecule approach can reveal the origins of nonspecific amplification, the role of human DNA, differences among enzymes, and the impact of assay parameters (time, temperature, etc.). By differentiating true and false positives, Tm enables determination of the combination of assay parameters that lead to the lowest limit of detection (LOD) in a digital assay. We predict that this approach of combining melting temperature with real-time dLAMP will be valuable for a wide variety of applications, particularly in the optimization of clinical assays that contain high levels of background DNA and require optimization for low LOD.

INTRODUCTION

Isothermal methods, such as loop-mediated isothermal amplification (LAMP), are attractive for nucleic acid amplification tests (NAATs) in point of care (POC) and limited-resource settings. LAMP in particular shows promise as a less expensive NAAT with fewer hardware requirements compared with PCR. However, despite advancements, optimization of individual LAMP NAATs for a specific target sequence and primer set remains constrained by a limited understanding of how amplification is affected by myriad factors, including temperature, time, and ion concentrations. In particular, nonspecific amplification can be problematic and constrains an assay's limit of detection (LOD). In reactions containing template target molecules, both specific and nonspecific amplification reactions may occur. Unlike PCR, LAMP lacks a temperature-gating mechanism, so nonspecific reactions consume reagents and compete with specific amplification. The presence of nonspecific amplicons therefore adversely impacts both the assay's analytical sensitivity (the fewest template molecules which can be detected) and its analytical specificity (ability to detect the target template in the presence of competing reactions). Separating specific and non-specific amplification would therefore be invaluable both during assay optimization and assay deployment for use in clinical diagnostics.

Substantial research is focused on using isothermal amplification chemistries for diagnosis of infectious disease. For example, chlamydia (caused by the pathogen *Chlamydia trachomatis*, CT*)* is the most common sexually transmitted infection (STI) worldwide, with more than 110 million cases reported annually (1). Diagnosis of CT infections is challenged by a lack of standard symptoms (many infections are asymptomatic) (2) and the presence of mixed flora (particularly in the female reproductive tract) (3). Thus, rapid NAATs with high sensitivity and specificity are critically needed, especially NAATs that can deal with the high levels of host DNA likely to be present in clinical samples such as urine samples and swabs.

To optimize LAMP for CT and other infectious pathogens, a method of separating nonspecific reactions from specific amplification is needed. Reactions run in bulk

(i.e., in a tube) in the absence of template, can be informative to provide information on performance of non-specific amplification. However, in the presence of template, though specific and nonspecific reactions occur simultaneously, they cannot be monitored simultaneously. Thus, bulk reactions have three important limitations with regard to assay optimization: (i) differences in the kinetics of specific and nonspecific reactions cannot be separated, (ii) rare but significant events, such as early but infrequent nonspecific amplification events, cannot be easily characterized; and (iii) bulk cannot provide valuable statistical probabilities without running hundreds of replicate experiments.

To improve analytical specificity and sensitivity, one strategy is to eliminate the detection of non-specific amplification. In bulk LAMP experiments, this has been done by using probes or beacons that show only specific amplification of the target (Cite Meagher, Tilley, others). Although this method improves the assay, this approach doesn't capture nonspecific reactions and thus cannot give insights into the origin of nonspecific amplification or the impact of conditions. Moreover, because the use of probes or beacons does not eliminate nonspecific amplification, it merely prevents the detection of it, nonspecific amplification still competes for reagents and can limit the extent of the signal generated by specific amplification events (4).

In this study, we use digital single-molecule LAMP (dLAMP) to probe the fundamental mechanics of amplification reactions and extract real-time kinetic information to identify reaction conditions and data-processing parameters that minimize nonspecific amplification events. Digital single-molecule methods compartmentalize each reaction into partitions, eliminating interference among individual amplification events, and enable absolute quantification and interrogation of individual reactions. Moreover, by separating individual amplification events into discrete compartments, digital experiments consist of thousands of reactions that run in parallel and thus provide valuable statistical information (5). In this work, we use real-time imaging to monitor the kinetics of tens of thousands of dLAMP reactions per experiment. We hypothesized that high-resolution melting analysis (HRM) could be used to separate specific from nonspecific amplification events and identify

optimal data processing parameters to distinguish specific and non-specific amplification events when assay is deployed without HRM. To test this hypothesis, we use a dLAMP assay with CT DNA as the target to analyze both specific and nonspecific amplification under conditions that include clinically relevant concentrations of background human DNA.

RESULTS

Bulk LAMP studies reveal nonspecific products at high melting temperatures (Tm)

We first wished to test whether melting temperature could be used to separate specific and nonspecific amplification in bulk LAMP. To find the LOD of our CT 23S primers in bulk LAMP, we performed half log dilutions of extracted CT genomic DNA. As CT concentrations approached the LOD, we began to observe nonspecific amplification (Fig 3.1). At target molecule concentrations greater than 10 copies per µL (cp/µL), amplification using *Bst* 2.0 began between 10-11 min (Fig 3.1a) and had uniform melting temperature (Tm; Fig 3.1b). Amplification using *Bst* 3.0 (Fig 3. 2c), also yielded amplification from 10-11 min; however, we also observed a nonspecific amplification at 15 min, defined by having a different Tm than the specific amplification events (Fig 3.1d). We observed that early amplifying products corresponded to specific amplification events, and the later products corresponded to nonspecific amplification, supporting our prediction that we could use melting temperature as a proxy for sequence identity, as is common with PCR.

As the concentration of the target decreased, the amount of nonspecific amplification increased. We reduced the concentration of specific template from 10 cp/µL in half-log intervals. At 3.16 copies/µL (Fig 3.1e,f), only specific amplification occurred (24 replicate wells/plate). However, once template concentrations reached 1 cp/µL (Fig 3.1g,h), nonspecific amplification occurred with greater frequency than specific amplification (18 of 24 replicates produced a false amplification event). Similarly, for 0.316 cp/µL (Fig 3.1 I,J) 15 of 24 reactions generated false positives. We

confirmed the Tm and amplification time of the nonspecific products observed previously, by running amplification in the absence of template (no template control, NTC) (Fig 3.1K,L) and observed 44 of 45 replicates produced amplifications with a Tm of 91°C. While it is possible the reaction generates multiple different non-specific amplification products, even ones with Tm matching to the specific products, we suspect that the single amplicon we observed at 88°C was a cross contaminant.

The melting temperatures of specific amplification differed between the two polymerases tested. Specific amplification for *Bst* 2.0 had a Tm of 85.5°C, while specific amplification using *Bst* 3.0 had a Tm of 88°C, and demonstrated non-specific amplification at Tm of 91°C. The non-specific amplification had identical Tm to amplification in absence of template (Fig 3.1K,L). Despite *Bst* 2.0 and *Bst* 3.0 producing identical specific products (as confirmed by sequencing, see 3.1X) and gel banding patterns (Fig 3.1x), they had different Tm (Fig 3.1b,d respectively). We attribute the difference in Tm to *Bst* 3.0 having 1 mM greater Mg^{2+} than *Bst* 2.0. Magnesium is known to stabilize ssDNA, so we suspect this difference explains the higher observed melting temperature of *Bst* 3.0.

In all instances in bulk, we observed a high Tm nonspecific product. This was surprising because PCR predicts primer dimers to occur at low Tm, however, our bulk amplification failed to produce a nonspecific product with low Tm. Thus, we investigated the sequence identity of the nonspecific product at high melting temperature. We ran the LAMP products on a gel and observed that the characteristic pattern of the specific amplification products differed substantially from the banding pattern seen in the high-Tm non-specific products (Fig 3.1X). To determine the sequence of the high-Tm non-specific products, we performed Next Generation Sequencing (NGS) and identified the product as a mixture of full-length FIP, BIP, and their complements, as well as fragments of these primers. To confirm the sequence identity of the structure, we targeted the FIP region using a restriction endonuclease. Digestion resulted in two bands corresponding to ~40 and 100 bp and confirming the sequence.

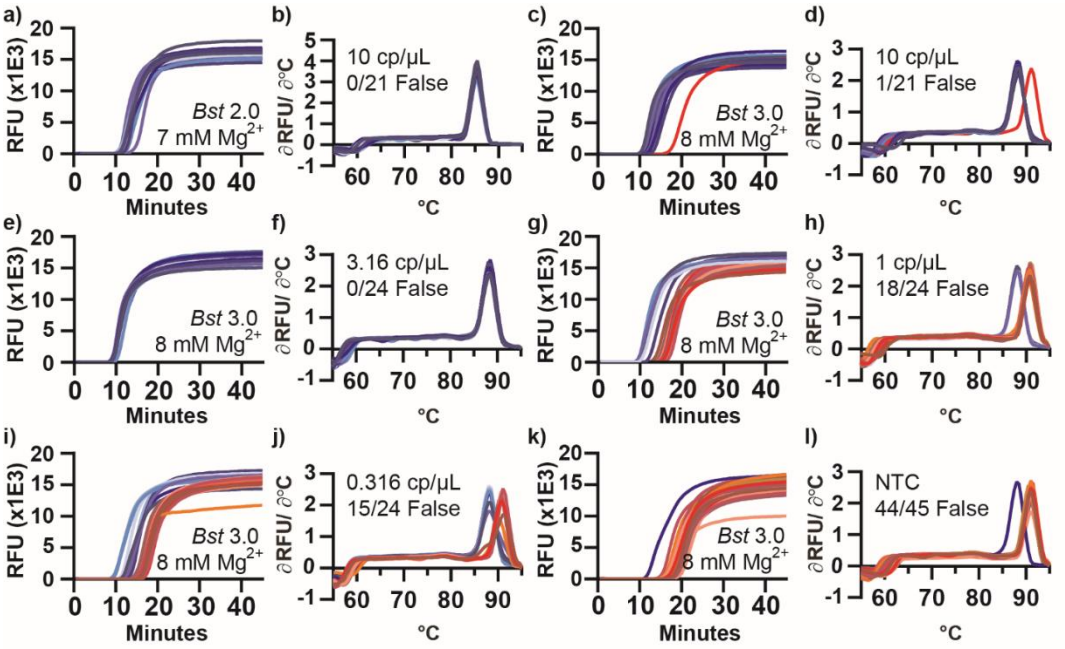

Figure 3.1: Amplification and Melting curves of Chlamydia in a tube produces a high-Tm non-specific product. Plots of fluorescence as a function of time during a LAMP reaction (a,c,e,g,i,k) and the derivative plot of fluorescence as a function of temperature for the corresponding melting curves (b,d,f,h,j,i). Reactions using *Bst* 2.0 at 10 cp/µL (a,b,), *Bst 3.0* at 10 cp/µL (c,d), *Bst 3.0 at* at 3.16 cp/µL (e,f), *Bst* 3.0 at 1 cp/µL (g,h), *Bst 3.0* at 0.316 cp/µL (i,j), and using *Bst* 3.0 without template (k,l). Reactions of specific amplification are colored blue, while non-specific amplification is colored in red.

Melting temperature differentiates specific and nonspecific reactions in dLAMP

To study specific and nonspecific amplification events at the digital single-molecule level, we developed a new approach that enabled high resolution melt analysis (obtaining "melt-curves") to be performed on each partition. We used a commercially available microfluidic chip with 20,000 partitions and a dLAMP method described previously. We improved this approach by incorporating an off-the-shelf thermoelectric unit to both heat and cool the chips, and enhanced our MATLAB script to allow for multicolor tracking. We used the temperature independent fluorophore ROX to track a partition's location and the dsDNA intercalating fluorophore Syto9 to follow amplification and hybridization status. Multi-channel tracking thus enabled determination of the spatial location of a partition, even when

it did not exhibit fluorescence from the intercalating dye (Syto9). This two-channel approach is required to follow a partition through both amplification and the entirety of the melt, when fluorescence from Syto9 is lost. In these experiments, we choose to use a microscope, instead of the custom real-time amplification instrument we used previously, because the microscope, due to its smaller field of view, has superior optical properties (greater pixels per partition and lower exposure time requirements) to access higher temporal resolution and enhanced kinetic measurements.

We first illustrate the capabilities of using real-time digital LAMP to study the kinetic parameters of individual reactions and use melting temperature to classify reaction outcome (Fig 2). In a real-time digital LAMP experiment, we can follow individual partitions as they amplify as a function of time (Fig 2a) and then by temperature as they go through a melt (Fig 2b). Real time imaging of individual partitions enables us to reconstruct the standard amplification curves of intensity of each partition as a function of time (Fig 2c), while plotting the fluorescence intensity as a function of temperature yields a melt trace (Fig 2d), whose derivative plot (Fig 2e) is the standard melt curve. Analogous to bulk measurements, the melt curve classifies the reactions as specific or non-specific. We can use the classification to identify important patterns in the kinetics of each type of amplification (Fig2 f-h).

We used real-time dLAMP with melting temperature to determine whether differences in time to positive (TTP) are due to a difference in amplification initiation or in rate. We expect this information would be valuable for elucidating if the molecules that lead to bulk amplification are the first to initiate or those which initiate with the fastest rates. We found that TTP can be heterogeneous but Tm is constant, indicating that the same product may initiate at different times (Fig 2f). This is consistent with our knowledge of the stochastic initiation of LAMP. Further, we observed some variability in the maximum rate despite consistent melting temperature. This indicates the same product may amplify at different velocities. (Fig 3.2g). In general, we observed that max rate often corresponded to the point where the reaction first begins to amplify. Finally, by plotting Rate as a function of TTP (Fig 3.2h) we observe little fluctuation in rate for very different TTP, indicating that

the difference in TTP is mostly delay in the initiation of amplification rather than rate of amplification.

The use of real-time data revealed heterogeneity in the timing of amplification initiation and the amplification rate, but homogeneity in melting temperature. This indicates the stochasticity of initiation, but lack of heterogeneity in the composition of the product. In some cases, outlier data points for rate occur (Supplement S3.1). These outliers could have several origins, including fluctuations in fluorescence due to scattering of bubbles passing over a partition or random fluctuations in fluorescence due to shot noise. To determine whether removing these points impacted the distribution of enzymatic rates, we performed a non-parametric test (SI S3.1) and found no significant differences in enzymatic rates when these outliers were excluded.

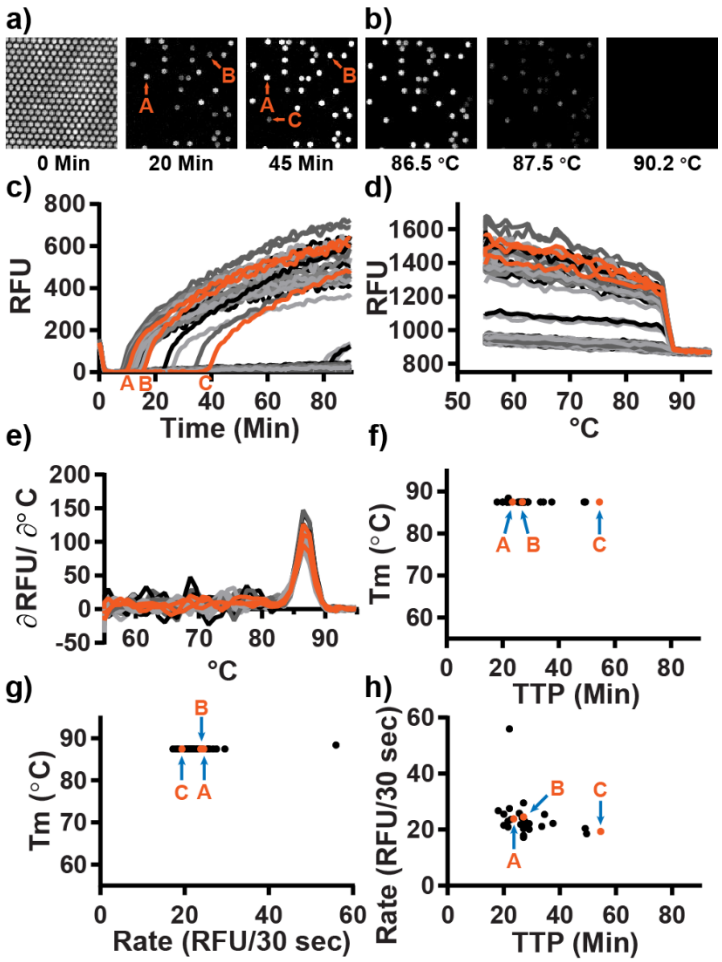

Figure 3.2: Specific amplification in digital single-molecule experiments.
A) Individual partitions are traced over time. For simplicity, we illustrate a subset of 250 of 20,000 possible partitions at three time points (0, 20, and 45 min). Of the 250 partitions in this micrograph, 30 partitions amplified. Partitions A and B are visible at 20 min; partition C becomes visible at 45 min.
B) Fluorescence micrographs of individual partitions during a melting experiment. As the dsDNA in each partition de-hybridizes, the intercalating dye is released and fluorescence decreases. At 86.5 °C, partitions were uniformly bright, they began to decrease in fluorescence at 87.5 °C, and lost fluoresce at 90.2 °C.
C) Plotting the fluorescence intensity as function of time generates the standard amplification traces of individual partitions generated during a 90-min LAMP experiment. Orange curves correspond to partitions A–C from panel a).
D) Traces of fluorescence intensity as a function of temperature of individual partitions during melting experiments. By quantifying real time intensity of individual partitions as the temperature is increased, melting traces are obtained (Fig 3.2D). We collected data with temperature resolution of 1 °C from 55–90 °C, and then at 0.5 °C resolution from 90–95 °C.

E) The derivative plot of panel D generates the standard melting curve. The temperature at which the maximum occurs corresponds to the "melting point" of the LAMP products in the individual partition.
F) Summary data of the individual partitions plotting the time each well reaches a fluorescence intensity of 250 RFU (TTP) against temperature.
G) Summary data of the individual partitions plotting the maximum slope against melting temperature.
H) Summary data of the partition TTP against the maximum rate of individual partitions.

We next asked whether we could observe in dLAMP the same pattern of high-Tm nonspecific amplification and low-Tm specific amplification that we observed in bulk. We performed dLAMP using three chips containing template, and three chips lacking template and observed ~55,000 partitions for each condition. (Details in SI.) Although 60,000 partitions are possible, not all partitions fill nor can all partitions be tracked for the full duration of the experiment. The Tm resolution was 1° C up to 90 °C; and 0.5 °C from 90–95 °C. Due to slight differences in the timing between the heating element and the image collection, some chips were observed at slightly (fractional) different temperatures.

Our approach enabled us to differentiate specific and nonspecific amplification events using Tm. When using *Bst* 2.0 and template (Fig 3.3a blue points), we observed a large band of amplification from 88.5–90.3 °C, in agreement with the Tm observed in Fig 3.2. In contrast, the NTC (Fig 3.3a red points) had very few amplification events in that temperature range. Hence, we defined 88.5–90.3°C as a true positive (specific amplification) event. Partitions having a Tm outside this range were considered to be false positives (nonspecific amplification) events and these appeared in both the NTC and in the presence of template. When using *Bst* 3.0, we observed a large band of amplification from 91.25–92.75 °C in the presence of template (Fig 3.3B, blue points) that did not correspond with amplification in the NTC (Fig 3.3.3D, red points) and defined these as specific amplification events. As with bulk measurements, we attribute the difference in Tm between specific amplification events between *Bst* 2.0 and *Bst* 3.0 to the difference in Mg^{2+} concentrations.

Comparing the performance of the two enzymes, we observed two common themes. First, the Tm for specific amplification events was 2–3 °C lower in digital compared with bulk measurements. We attribute this difference to temperature calibration; the thermocycler is calibrated to the liquid temperature, whereas the thermoelectric element measures the temperature of the heating element.. Second, false positives in the NTC had predominantly high Tm, which we believe corresponds to the nonspecific product we identified in the bulk reactions. We also observed differences between the enzymes. *Bst* 3.0 resulted in substantially more nonspecific amplification than *Bst* 2.0. After 90 min, *Bst* 3.0 yielded 15,200 nonspecific events (out of 54,337 observed paritions), whereas *Bst* 2.0 yielded 74 nonspecific events (out of 51,279). Occasionally, outliers occurred in the NTC and would be misidentified as true positives by Tm. For *Bst* 3.0 this occurred in 29 partitions; for *Bst* 2.0, it occurred in 3.

Next, we asked whether TTP is different for specific and nonspecific amplification. Because LAMP follows a "winner-takes-all" format, frequent and early nonspecific amplification events may dominate bulk amplification. In general, for both *Bst* 2.0 and *Bst* 3.0, specific amplification had earlier TTP than nonspecific amplification, although there was some overlap, mostly at >90.5 °C (Fig 3.3a-b). We were able to cleanly distinguish the clustering of high-Tm nonspecific products separately from specific amplification (Fig 3.3c). We illustrate each partition with only partial opacity so that when false positives in the NTC (red) overlap with false positives in the template-containing sample (blue), the overlap appears purple (Fig 3.3d). Color intensity indicates the abundance of paritions at a given TTP and temperature. To further illustrate how this approach can be used to differentiate specific and nonspecific amplification, we next selected a region where both specific and nonspecific products were observed. For *Bst* 3.0, we were able to distinguish the clustering of nonspecific products separately from specific amplification at high Tm (Fig 3.3e) and we observed better separation of specific and nonspecific amplification than with *Bst* 2.0 (Fig 3.3f). Both enzymes had highly variable TTP, which we have observed previously and attribute to stochastic initiation of LAMP. *Bst* 2.0 had both

earlier specific amplification and later nonspecific amplification than *Bst* 3.0. After removing outliers, *Bst* 2.0 reactions containing template started at 10 min, whereas nonspecific amplification began at ~40 min. In contrast, Bst 3.0 reactions containing template began at 11.5 min and nonspecific amplification began at ~20 min.

Next we asked whether there is a difference between the maximum rates of specific and nonspecific amplification. Previously, we demonstrated that rate could be used to correct for some nonspecific amplification using *E. coli* 23S primers, so we wished to test whether we could use maximum rate as a way to differentiate specific and nonspecific amplification. Generally, specific and nonspecific amplification reactions did not have the same maximum rate. For *Bst* 2.0, nonspecific amplification tended to have a slower max rate than specific amplification, although there was some overlap (Fig 3.3g). At high Tm, the clustering of nonspecific amplification in both the presence of template and in the NTC were observed at > 90.5 °C and below approximately 50 RFU/30 sec (Fig 3.3H). For *Bst* 3.0, although there was substantial overlap, we again observed that nonspecific amplification tended to have slower maximum rate than specific amplification (Fig 3.3I). Examining the high Tm amplification events, nonspecific amplification collects above 92.75 °C and has maximum rate extending out to 75 RFU/30 sec (Fig 3.3J). For both enzymes, overlap between specific and nonspecific amplification was similar and specific amplification tended to be faster. However, the maximum rate of specific amplification between the two enzymes differed; *Bst* 2.0 had a maxium rate of 150 RFU/30 sec, whereas *Bst* 3.0 did not exceed 100 RFU/30 sec. *Bst* 2.0 performing faster than *Bst* 3.0 is consistent with our previous observations using an *E Coli* 23S primer set. Additionally, the maximum rate of non-specific amplification in *Bst* 2.0 tended to be lower than nonspecific amplification in *Bst* 3.0 (50 and 75 RFU/30 sec, respectively). Consequently, the extent of overlap of specific and nonspecific amplification was greater for *Bst* 3.0 than *Bst* 2.0.

During these experiments, we observed an unexpected relationship between the final intensity of each partition and the maximum rate of that partition. After 90 min of amplification, a partition should theoretically reach a fluorescence maxima whereby

all reagents are consumed and amplification plateaus and thus the final intensity would be independent of the maximum rate of amplification. However, surprisingly, we observed a general scaling between the maximum rate and the final intensity of the partition. False positives were generally dimmer and had slower maximum rates than most true-positive events. When examining the brightest partitions, *Bst* 2.0 (Fig 3.3K) and *Bst* 3.0 (Fig 3.3L) exhibit a similar maximal final intensity near 3000 RFU. This maxima is also surprising, considering our 12-bit camera is capable of imaging up to 4096 RFU (the detector was not at saturation). We suspect that this maxima corresponds to consumption of one of the reagents. When contrasting the enzymes, as mentioned previously, their maximum rates differ. Further, the large increase in non-specific amplification for *Bst* 3.0, results in an increase the overlap between false and true positive amplification, not observed in *Bst* 2.0.

We also observed a relationship between maximum rate and TTP in dLAMP. In bulk reactions, the first and fastest amplification event determines the reaction outcome by consuming all of the reagents. Thus, we hypothesized that reaction conditions that promote fast and early amplification in the NTC would lead to a high false-positive rate in bulk. In both *Bst* 2.0 (Fig 3.3m) and *Bst* 3.0 (Fig 3.3n) we observed a general trend of fast amplification events occurring earlier, and slow events occurring later. In *Bst* 2.0, we observed more heterogeneity in TTP and rate than in *Bst* 3.0. Additionally, nonspecific amplicons in the NTC tended to produce slower and later amplification events. Occasional outliers occurred at both fast and early times.

Next, to explicitly test whether fast and early events correspond to specific amplification, as determined using Tm, we analyzed the relationship between a partition's TTP and its maximum rate. In the first 12 min of amplification, we observed six nonspecific amplification events in *Bst* 2.0 (four in the presence of template; two in the NTC; Fig 3.3o), and we observed 13 nonspecific events in *Bst* 3.0 (10 in the presence of template; three in the NTC; Fig 3.3p). For both enzymes, we were able to distinguish the rare, fast and early nonspecific amplicons from true positives. For *Bst* 2.0, these nonspecific amplifications were slower than the fastest true positives, and occurred at similar times. In contrast, for *Bst* 3.0, the earliest

amplification events were false positives and tended to have similar rates to the true positives. We hypothesize that in bulk reactions, the fast and early nonspecific amplification events (as seen in *Bst* 3.0) lead to nonspecific measurements, whereas nonspecific amplification that coincides with specific amplification, but proceeds at a slower rate (as seen in *Bst* 2.0), would still produce specific amplification in bulk.

A complex interplay exists between of TTP, Max Rate, Final Intensity, and melting temperature. All previous plots are merely projections of the four dimensional representations of these interactions. We visualize how the data are related/coupled across four dimensions and examine the interaction for both *Bst* 2.0 and *Bst* 3.0 enzymes (Fig 3.3q-r). We observe clear similarities between *Bst* 2.0 and *Bst* 3.0. For example, all partitions, specific and non-specific alike, earlier and faster amplification tends to be brighter. Additionally, we observe two types of non-specific amplification. First, the traditional "primer-dimer" cloud composed of a low Tm, low final intensity, low max rate and generally late TTP. The second type of non-specific cloud matches only in its High Tm, and spans a variety of rates, TTP, and final intensities. The high Tm non-specific occurs with greater frequency than the low Tm non-specific. The major differences between the enzymes can also be resolved with this visualization. The shear number of non-specific amplification events is much fewer for *Bst* 2.0 than for *Bst* 3.0. Further, these non-specific events in *Bst* 2.0 never achieve same fluorescene intensity or maximum rate as with *Bst* 3.0. We include the 4D representation as part of our MATLAB code, and as videos in the SI.

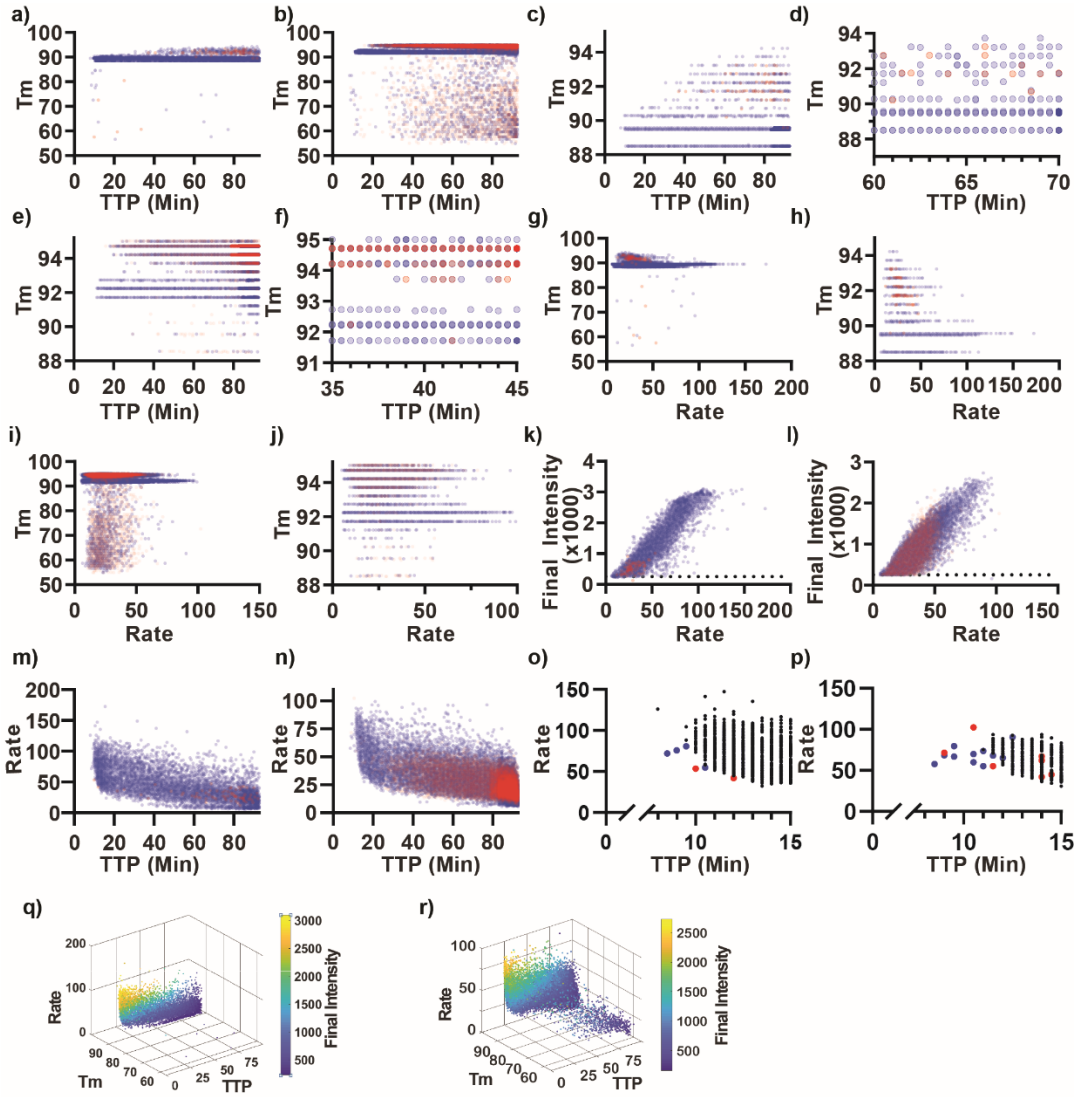

Figure 3.3: **Properties of specific and non-specific amplification using real time kinetics and melting temperature**. True positives can be sorted unequivically using melting temperature (approximaly 90°C using *Bst* 2.0 and 92°C using *Bst* 3.0) Blue amplification events in the presence of template, Red amplification in the absence of template. Partitions in panels a,c,d,g,h,k,n using *Bst* 2.0 are rendered at 20% opacity in the NTC and 20% opacity in the presence of template. Panels b,e,f,I,j,n using *Bst* 3.0 are rendered at 5% opacity in the NTC and 20% opacitity in the presence of template.

a) Plot of the melting temperature of individual amplification events as a function of TTP using *Bst* 2.0.

b) Plot of the melting temperature of individual amplification events as a function of TTP using *Bst* 3.0.

c) Plot of individual partitions with melting temperature between 88 and 95°C as a function of TTP using *Bst* 2.0.

d) Plot of individual partitions with melting temperature between 88 and 95°C and TTP between 60 and 70 min using *Bst* 2.0.
e) Plot of individual partitions with melting temperature between 91 and 95°C as a function of TTP using *Bst* 3.0.
f) Plot of individual partitions with melting temperature between 91 and 95°C and TTP between 35 and 45 min using *Bst* 3.0.
g) Plot of the melting temperature of individual amplification events as a function of maximum rate using *Bst* 2.0.
h) Plot of the melting temperature of individual amplification events between 88 and 95°C as a function of maximum rate using *Bst* 2.0.
i) Plot of the melting temperature of individual amplification events as a function of maximum rate using *Bst* 3.0.
j) Plot of the melting temperature of individual amplification events between 88 and 95°C as a function of maximum rate using *Bst* 3.0.
k) Plot of the final intensity of individual amplification events as a function of maximum rate using *Bst* 2.0. Partitions with final intensity less than 250 RFU (dotted line) were excluded from analysis.
l) Plot of the final intensity of individual amplification events as a function of maximum rate using *Bst* 3.0. Partitions with final intensity less than 250 RFU (dotted line) were excluded from analysis.
m) Plot of the maximum rate of individual amplification events as a function of TTP using *Bst* 2.0.
n) Plot of the maximum rate of individual amplification events as a function of TTP using *Bst* 3.0.
o) Plot of maximum rate from false positive amplifications in NTC (red), false positives amplifications in the presence of template (blue) and true positive amplifications by Tm (black) using *Bst* 2.0 as a function of TTP.
p) Plot of maximum rate from false positive amplifications in NTC (red), false positives amplifications in the presence of template (blue) and true positive amplifications by Tm (black) using *Bst* 3.0 as a function of TTP.
q) Plot comparing maximum rate, melting temperature, TTP, and final intensity of individual partitions using *Bst* 2.0.
r) Plot comparing maximum rate, melting temperature, TTP, and final intensity of individual partitions using *Bst 3*.0.

Reaction classification informs choice of optimal parameters for assay performance

We next asked whether using a combination of digital real-time parameters, in conjunction with Tm, could be used to improve the performance (LOD) of a dLAMP assay. For any given assay, there is a large combination of possible parameter (e.g. amplification rate, TTP, fluorescence intensity). Use of these parameters and selection of a threshold will dictate assay performance (analytical specificity and sensitivity). Assay performance depends on amplification time and the combination of choices of parameters used to process the data impacting LOD, the probability of detecting a molecule (efficiency), and the CLINICAL sensitivity/specificity. Because of the direct relationship between melting temperature, sequence identity, and structure, melting temperature provides new and useful information for dLAMP to explicitly differentiate specific and non-specific amplification, and thus, true from false positive.

We foresee two separate situations of dLAMP analysis using melting temperature. First, where melting temperature is not incorporated in the final assay, but is used during assay development. Second, the ideal situation for quantitative performance, where melting temperature is incorporated into the final assay. We expect the first group of assays to exist because collecting melting temperature data adds additional time to an assay and requires more advanced hardware to run. This may be unideal in situations requiring more rapid diagnostics or LRS/field settings where the hardware may be impractical. Nonetheless, melting temperature is still useful during assay development to select the optimal combination of parameters for end point or real time digital without using Tm. This method allows one to identify the correct combination of assay parameters, and how to analyze the data for best LOD.

In many tests, LOD is the key parameter for clinical utility because for many infectious diseases the pathogen load in the sample is low (e.g. blood infections or asymptomatic sexually transmitted infections). We illustrate the optimization of parameters using improved LOD as the selection criteria. The combination of real time dLAMP with melting temperature can uniquely define LOD (because of the

combination of digital and Tm). Unlike bulk assays which require a concentration titration curve (and are thus dependent on integrated signal intensity and enzymatic turnover), digital assays only require that an event (target molecule) is or is not observed, and can be counted relative to the partition volume. The minimum LOD for any digital assay corresponds to one target or amplification event per partition volume. Hence, we can define LOD from a single concentration point by:

$$LOD = \frac{C_{True}}{[N_{True} - (N_{False} + 3 \times \sqrt{N_{False}})]/NEMCI}$$

Where C_{True} is the concentration of target molecules loaded by ddPCR counts in copies per microliter, N_{True} is the number of True Positive (specific) amplification events observed on a chip, and N_{False} is the number of non-specific amplification events observed on a chip. Note that in this equation, the N_{True} and N_{False} are chip-specific, and take into account the total volume of the chip, the number of partitions, and the volume of partitions. Furthermore, in this equation, amplification efficiency is implicitly taken into account via the N_{True} parameter (in other words, for a less efficient amplification process, a given C_{True} on a given chip would lead to a lower value of N_{True}). Finally, for simplicity, this equation makes the assumption that the measurements are performed at sufficiently low concentrations (as is typical for LOD experiments) that only a very small fraction of occupied partitions contain more than 1 molecule and therefore there is a linear relationship between C_{True} and N_{True}.

The concentration loaded, C_{True}, generates N total counts of both true and false positive events. We can divide this concentration by the minimal number of counts needed to identify a specific amplification event and define this as the LOD.

Using the Poisson equation, one can estimate the desired expected number of molecules that will yield at least 1 detection event/observation for a given CI. We refer to this parameter as NEMCI (number of expected molecules for a confidence interval). If we assume a 95% CI of observe a true positive across an entire chip, the minimum number is of counted events is three. (5% of the time, the expected Poisson loading of 3 target molecules will still measure zero events.) For a 95% confidence

interval, this is three molecules. For a 98% confidence interval, this value would be 4 counts. Hence, all true positive counts in excess of this value may be used to reduce the observed counts to the LOD. For example, if a concentration of 30 cp/µL observes 90 counts, there are 90/3 =30 fold excess counts and the LOD may be inferred to be 30 cp/µL lodaded/30 fold excess = 1 cp/µL.

However, counting only true positives does not account for interference from false positives. In order to meet our minimum counts for detection, our equation must remove those counts which are false. Generally accepted procedure is to assume the counts arising from the background plus three standard deviations of the background. We approximate the variance in the background using the counting error as three times the square root of the number of false positive events counted and subtract those counts from the true positive counts to yield the equation.

This definition of LOD has several limitations. First, this equation fails when number of true positive partitions amplifying (N_{True}) is less than the number of false positive amplification events plus three times the variation in false amplification ($N_{False} + 3 \times \sqrt{N_{False}}$). In this case, it is not possible to conclusively observe a true positive amplification event, and the LOD becomes irrelevant. Second, this equation gives an absolute LOD. The numerator (concentration of template molecules loaded on the chip by PCR) is corrected for the probability of observing a molecule amplify (efficiency) by the True Positive counts. N_{False} accounts for the non-specific amplification, and NEMCI accounts for the Poisson probability associated with loading a target molecule. Third, this equation is be specific to digital assays. We remain optimistic that digital LOD will project to bulk optimal sensitivity and specificity.

We first sought to demonstrate the selection of optimal parameters for situations where Tm is not incorporated into the final assay. Using this process, one can pick any threshold and use Tm to determine the optimal trade off between true and false positives.

We first sought to determine the optimal threshold for Max Rate and Fluorescence Intensity using *Bst* 3.0. In some cases, one parameter may be more important or more accurate for optimizing LOD, in other cases a different parameter may exhibit better utility. We demonstrate optimization of all three parameters, using Tm as the arbiter, to illustrate the utility of our method.

Receiver Operating Characteristic (ROC) curves more commonly used with clinical sensitivity and specificity, can be used to examine the analytical classification performance of a given parameter used for thresholding. These graphs provide a visual representation of the ability to distinguish between a true positive and false positive event, as a function of a given threshold. The graphs plot the true positive fraction against the false positive fraction, where the True Positive Fraction is the number of true positives at a given threshold out of the total number of true positives observed by Tm; and the False Positive Fraction is the number of false positives counted at the given threshold, divided by the total number of false positives observed by Tm. It is generally presented that a perfect classifying test will have the largest True Positive Fraction and smallest False Positive Fraction.

Does the ROC curve clearly indicate the best choice for LOD? ROC curve illustrate tradeoffs between the fraction of true positives detected and the fraction of false positives detected, which are reflections of the analytical specificity and analytical sensitivity, but can be difficult to use for optimal selection of LOD. When plotting the ROC curve for Maximum Rate (Fig 3.4a), we observe that rate initially performs very well for eliminating false positives (False Positive Fraction is very small for very high rates). However, as the rate threshold decreases, a greater number of both false and true positive values are counted. Closer examination of this range of thresholds (Fig 3.4b) emphasizes the Youden Index at 34.6 True Positive Fraction and 4.6 False Positive Fraction as a possible choice for optimum threshold, though the clarity of performance is unclear. The choice for optimal threshold is even less clear with the ROC curve for Final Intensity (Fig 3.4c). In this case, the ROC curves do not give clear indication of the optimal LOD as the curve is a gentle concave slope.

Even relatively high fluorescence thresholds do not give indications of the optimal Cut-Point (Fig 3.4d).

In contrast, filtering using LOD reveals a clear optimum. We plot the total number of events for both true and false positives and LOD as a function of Maximum Rate (Fig 3.4e). In this scenario, the LOD curve reveals a clear minima, corresponding to the optimal cut-point using rate. Selecting the threshold of 49.8 RFU/30 seconds generates a LOD of 2.11 cp/µL. Similarly, plotting LOD against Final Intensity results in a clear minima, despite the cut point in histogram remaining unclear (Fig 3.4f). Using Final Intensity a LOD of 2.14 cp/µL can be achieved at 1393 RFU.

We next sought to determine the optimal threshold using TTP and *Bst* 3.0. In this situation, the ROC curve presents a narrow range of choices around 50% True Positive Fraction and 2 % False Positive Fraction as optimum, though the precise choice is not obvious (Fig 3.4g). To optimize, we plot the LOD and the cumulative counts as a function of Time in both a linear (Fig 3.4h) and logarithmic scale (Fig 3.4i).

Assays employing Tm only during assay development can improve LOD by selecting (making an informed choice of) the optimum threshold. The LOD equation illustrates the optimum filter threshold. The LOD decreases (Blue Curve) as the true positives begin to amplify (Red Dashed). LOD begins to increase, as the false positives amplify (Blue dashed). The minima for this system occurs at 35 minutes and 0.89 cp/µL, striking a balance between allowing many true positives to amplify, and only a small amount of false positives to occur (54.5% True Positive Fraction and 1.7 False Positive Fraction) and is clearly defined using the linear scale (Fig 3.4h). Plotting of LOD on the logarithmic scale (Fig 3.4i) emphasizes improperly selecting a threshold can result in several orders of magnitude loss in assay performance (for example, stopping the assay too early or allowing the assay to run for too long). Though dLAMP is robust to perturbations, precision should still be employed.

In contrast, assays using Tm as part of the final readout can distinguish false positives from the true positives and improve LOD further by removing/ignoring non-specific amplification term. In some instances, a NTC may incorrectly identify partitions as

true positives by Tm (black dashed). We incorporate these events as non-specific amplification in the case Tm is used in the final readout. If non-specific amplification is eliminated, the assay LOD (Fig 3.4h,i, Black solid) continues to improve with time, and is only dependent on the stochastic probability that a true positive will initiate and amplify. In this scenario, there is no penalty allowing the assay to amplify for extended periods of time.

Additionally, there is no limitation on the number of or which combination of parameters are used to select for optimal LOD. Using multiple parameters to filter the data may be useful for individuals not employing Tm in the final assay or in assays only employing endpoint measurement (No real time means rate cannot be measured. E.g. pick best time, pick best fluorescence). For example, we can filter first by optimal TTP, then filtering for the optima of a second parameter. In this case, we select the optimal TTP of 35 minutes, and scan for optimal fluorescence threshold. We plot LOD as a function of fluorescence threshold and determine that the optimal fluorescence threshold at 35 minutes would be 248 RFU and corresponding to a LOD of 0.972 cp/µL (Fig 3.4j).

Do filter parameters exhibit the same LOD minima when using *Bst* 2.0, as they did for *Bst* 3.0? *Bst* 2.0 had much lower non-specific background than *Bst* 3.0, and could behave similarly or may behave differently.

First, does the ROC curve for TTP display a clear optimum? Similar to the TTP ROC for *Bst* 3.0 (Fig 3.4g), the TTP ROC for *Bst* 2.0 has a gentle slope making choice of the optimum a matter of computation (Fig 3.4k). We can visually estimate the balance of True and False Positive Fraction in the range of 50% True and 10% False. Similar curves for Max Rate and Final Intensity could be generated but are not shown here.

Second, Is there an advantage to using Tm in the final assay with *Bst* 2.0? To answer this question, we plot LOD and the cumulative counts of true and false positives as a function of time for *Bst* 2.0 (Fig 3.4L). Similarly to *Bst* 3.0, we observe LOD decrease rapidly as True Positive events are counted. However, unlike *Bst* 3.0, the non-specific amplification events are much fewer and their presence does not have an impact on LOD. Thus, when using *Bst* 2.0, the curves representing LOD with or without Tm in

the final assay overlay and indicate using Tm in the final assay has no additional benefit. Furthermore, the continuously decreasing LOD with time for either case indicates that use of ROC curves to determine an optimum can be misleading. While the ROC implies that an optimum exists, the false positive incidence is rare enough that a TTP optimum selected by LOD does not exist. Assay developers may select assay time based on requirements other than LOD.

We next ask how does the performance of *Bst* 2.0 and *Bst* 3.0 compare with and without Tm? (Fig 3.4M) For both enzymes we observed a similar, rapid decrease in LOD in the initial moments as true positive events are detected. However, we also noticed several differences. *Bst* 2.0 has a lower LOD than *Bst*3 at any amplification time. We attribute this difference to the higher incidence of false positives when using *Bst* 3.0 compared to *Bst* 2.0. An additional consequence of the low false positive incidence using *Bst* 2.0, regardless of the use of Tm in the assay, is the LOD continues to improve with time as additional true positives are counted. In contrast, *Bst* 3.0 benefits greatly from use of Tm in the final assay. If Tm is not included in the assay (Fig 3.4M, red dashed), a clear optimum for LOD occurs at 35 minutes and 0.89 cp/µL at 35 min. However, if Tm is employed in the assay, the LOD more closely resembles the LOD curve for *Bst* 2.0 and improves with increased detection of true positive events.

We made several overarching conclusions regarding improving the LOD of dLAMP using a combination of digital real time parameters and melting temperature. First, filter paramters can be used singly or in combination to improve the performance (LOD) of dLAMP. In certain assays one parameter may perform better than another for this selection. For this primer set, LOD for *Bst* 3.0 was lower when using Time to Positive (0.89 cp/µL) than Max Rate (2.11 cp/µL) or Final Intensity (2.14 cp/µL). Second, incorporation of melting temperature into the final assay readout will benefit some assays more than others. We observed incorporation of melting temperature as a filter/part of the final assay improved the perofmance of *Bst* 3.0 greater than the performance of *Bst* 2.0. This was especially true for long assay times.

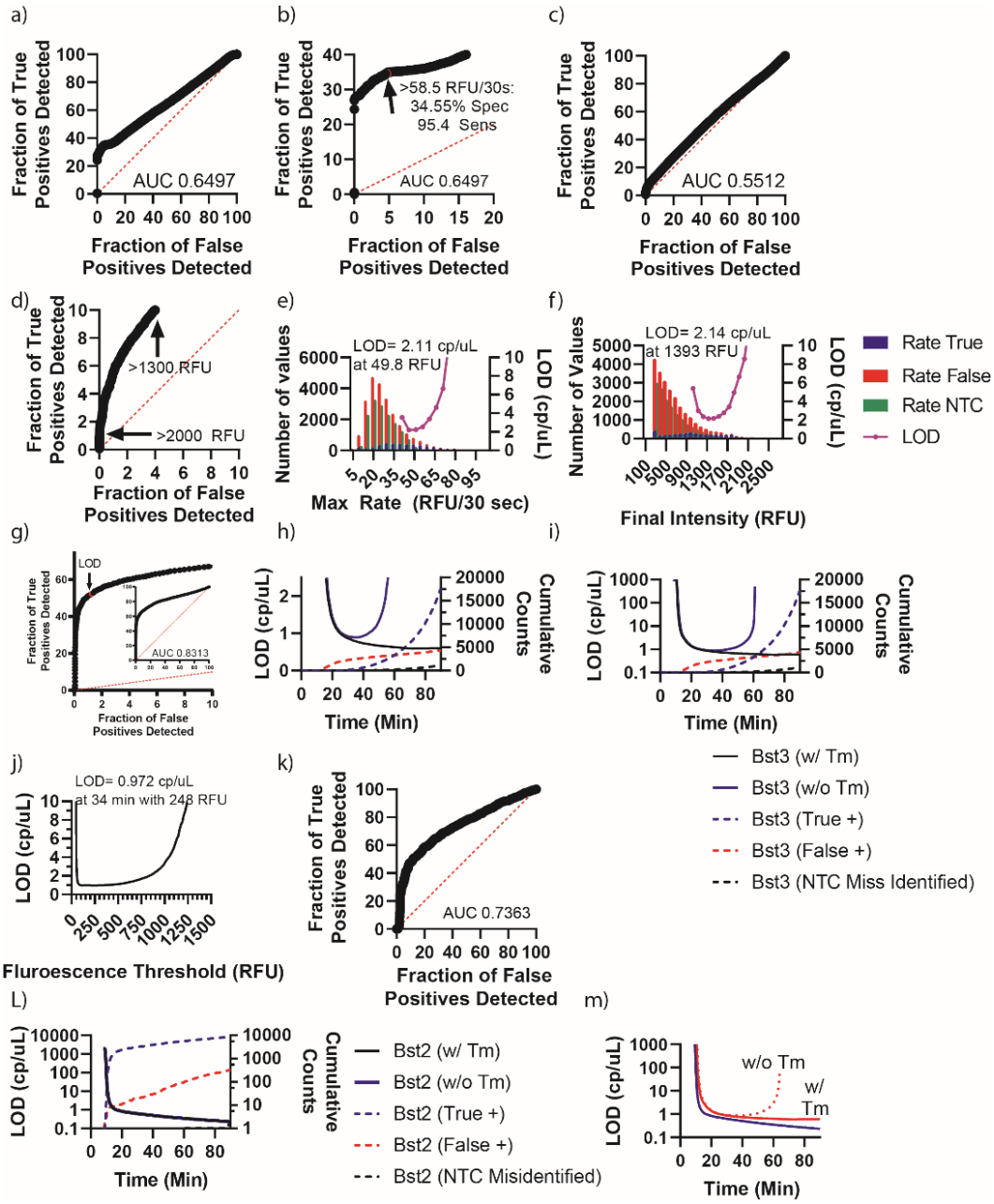

Figure 3.4: Classification of amplification reactions using Tm to determine optimal performance of dLAMP assays.

a) ROC curve using *Bst* 3.0, plotting the fraction of true positives detected versus the fraction of false positives detected using a threshold on Maximum Rate.

b) ROC curve using *Bst* 3.0, plotting the fraction of true positives detected less than 40% versus the fraction of false positives detected less than 20% using a threshold on Maximum Rate. Arrow indicates corresponding LOD.

c) ROC curve using *Bst* 3.0, plotting the fraction of true positives detected versus the fraction of false positives detected using a threshold on Final Intensity of the partition.

d) ROC curve using *Bst* 3.0, plotting the fraction of true positives detected less than 10% versus the fraction of false positives detected less than 10% using a threshold on Final Intensity of the partition. Arrows indicate Final Intensity thresholds of >2000 RFU and >1300 RFU.

e) Histogram of the False Positives identified by Tm within the presence of template (Red), true positives by Tm (blue), and false positives in the NTC (green), binned by Maximum Rate of the partition and a LOD curve plotted as a function of Max Rate using *Bst* 3.0.

f) Histogram of the False Positives identified by Tm within the presence of template (Red), true positives by Tm (blue), and false positives in the NTC (green), binned by Final Intensity of the partition and a LOD curve plotted as a function of Final Intensity using *Bst* 3.0.

g) ROC curve using *Bst* 3.0, plotting the fraction of true positives detected versus the fraction of false positives detected using a threshold on TTP. Arrow indicates LOD.

h) LOD Curves as a function of time without using Tm in the final assay (blue) and using Tm in the final device (Black). Plots of cumulative counts of true positive amplification (Red dashed), False positive counts (blue dashed), and incorrectly identified partitions (black dashed).

i) Logarithmic plot of LOD Curves as a function of time without using Tm in the final assay (blue) and using Tm in the final device (Black). Plots of cumulative counts of true positive amplification (Red dashed), False positive counts (blue dashed), and incorrectly identified partitions (black dashed).

j) LOD plotted as a function of Fluorescence Intensity, when the assay is measured at the optimal TTP of 35 minutes.

k) ROC curve using *Bst* 2.0, plotting the fraction of true positives detected versus the fraction of false positives detected using a threshold on TTP.

l) Logarithmic plot of LOD curves, using *Bst* 2.0, as a function of time without using Tm in the final assay (blue) and using Tm in the final device (Black). The blue and black plots overlay. Plots of cumulative counts of true positive amplification (blue dashed), False positive counts (red dashed), and incorrectly identified partitions (black dashed).

m) Plot of LOD curves as a function of time comparing *Bst* 2.0 (Solid Blue with Tm, Dotted Blue without Tm) and *Bst* 3.0 (Solid Red with Tm, Dotted Red without Tm). Curves for *Bst* 2.0 overlap.

Classification demonstrates host genomic DNA does not alter non-specific background in dLAMP

LAMP assays with high clinical sensitivity and specificity are critically needed. Clinical samples of CT, originating from urine and swabs, pose an intrinsic challenge because they contain variable levels of host DNA (and DNA from other flora) [0 to 100 HHGE/µL or 0 to 3.3E-7 mg/µL]. The analysis of these clinical samples, needs not only to be sensitive (good LOD), but also able to function in the presence of non-specific, potentially amplifiable genomic secondary structures and other possible environmental contaminants, while remaining consistent between samples.

We sought to investigate the impact of host gDNA on non-specific background amplification. We hypothesized that non-specific structures (like hairpins and regulatory elements), may amplify in the presence of LAMP and contribute to non-specific background amplification. We titrated sheared buffy coat gDNA concentrations in 100 fold intervals from a low clinical concentration to a high clinical concentration and observed the impact on specific and non-specific amplification of CT (Fig 3.5). We measured the concentration of gDNA in Human Haploid Genome Equivalents (HHGE) or half the total amount of gDNA in a diploid cell. For each concentration of host DNA and enzyme, we ran three chips in the presence of CT template and three in the absence of template. In total, we observed 862,059 different partitions. At the highest concentration of gDNA, there was 60,600 times more gDNA than bacterial DNA by mass.

We first asked qualitatively how background DNA impacted TTP. We observed for both *Bst 2.0* and *Bst* 3.0 enzymes, specific and non-specific amplification were qualitative similar independent of background DNA concentration. As with previous measurements, *Bst* 2.0 rarely produced low Tm, non-specific events; while *Bst* 3.0 produced both high and low Tm non-specific amplification. Further, both high melting temperature and low melting temperature non-specific amplification events were greater for *Bst* 3.0 than *Bst* 2.0. Increasing the concentrations of gDNA qualitatively appear similar. The Tm of specific amplification remains constant, while quantities of non-specific high and low Tm are similar.

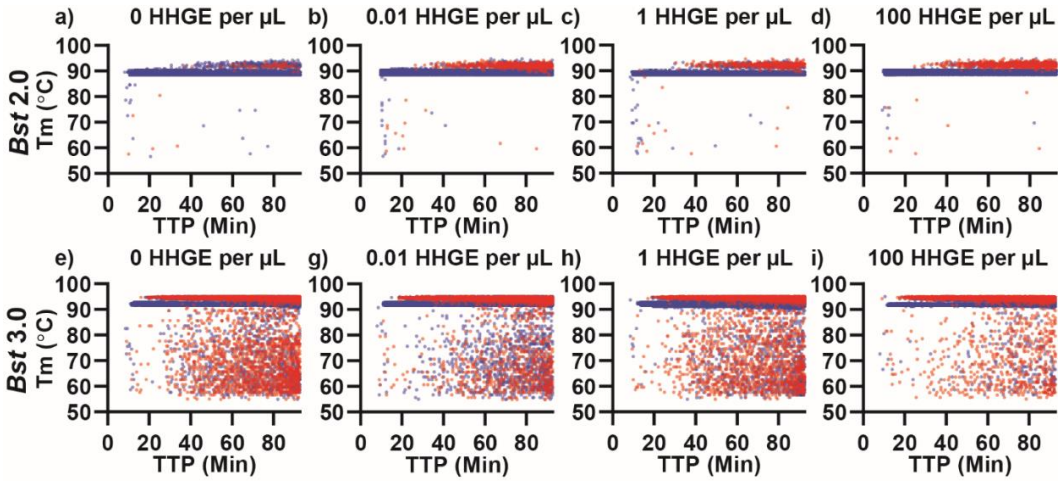

Figure 3.5: Impacts of host gDNA on specific and non-specific amplification. Plots of melting temperature as a function TTP using *Bst* 2.0 at (a) 0 HHGE per µL, (b) 0.01 HHGE per µL, c) 1 HHGE per µL and d) 100 HHGE per µL and using *Bst* 3.0 at (e) 0 HHGE per µL, (g) 0.01 HHGE per µL, h) 1 HHGE per µL and i) 100 HHGE per µL in the presence of template (blue) and NTC (red).

We next asked quantitatively how background gDNA impacts specific and non-specific amplification? We categorized amplification events as specific and non-specific based on melting temperature as previously.

First, we asked is there a relationship between fraction of template molecules amplified and amplification time? We determine the total number of template copies loaded into a chip relative to the copies measured by ddPCR. If amplification initiation is stochastic, as observed in Fig2f and 3ab, does longer assay time increase 'efficiency' and thereby improve LOD (as seen in Fig 3.4h,l)? We observe that for *Bst* 2.0 a large number of partitions amplify in the first 10 min, followed by a second phase near 20 min where additional partitions amplify with lower frequency (Fig6a). For *Bst* 3.0 (Fig7a), we observe a similar trend temporally, though *Bst* 3.0 consistently had few copies detected than *Bst* 2.0 in all phases. This highlights the stochastic nature of amplification using LAMP, and importance in choice of enzyme on sensitivity. In theory, assays could be run until all partitions amplify as either a false or true positive. This would give the highest possible number of copies amplified and lowest possible LOD when using Tm in the final assay.

Second, we asked what is the impact of gDNA on efficiency as a function of time? For both *Bst* 2.0 and 3.0 (Fig6a,7a), we observed that the fraction of copies detected, and the moment the majority of reactions initiate, were indistinguishable regardless of concentration of gDNA.

Third, we asked what is the impact of gDNA and time on non-specific amplification? For *Bst* 2.0, we observed consistent non-specific amplification at high and low Tm, regardless of concentration of gDNA. Single digital partition counts were observed at low Tm non-specific amplification in both the presence of template and the NTC and independent of gDNA concentration (Fig 6b,c). The fraction of wells generating a false positive amplification at low Tm was less infrequent through 40 minutes. For high Tm non-specific amplification, partition counts are in the single digits until around 45 minutes. After 90 minutes, the reaction finishes around 200 counts in 20,000 partitions corresponding to a false positive fraction of 5E-4. One exception is the non-specific high Tm amplification in the absence template and HHGE. This condition appears to have lower non-specific background than other conditions. We collected each replicate on separate days and catch the experimental variability between the presence and absence of template, which might be otherwise lost when using a NTC alone. This experiment emphasizes the advantage of determining non-specific amplification using Tm from the same experiment as specific amplification is counted. At low background rates, such as when using *Bst* 2.0, inherent variability exists in the false positive fraction and can impact LOD. Measuring non-specific amplification from within an experimental measurement eliminates the assumption that the false positive rate remains identical to the NTC or between experimental runs. For *Bst* 3.0, all concentrations of gDNA gave indistinguishable differences in non-specific amplification. At any given time, high Tm non-specific amplification was 5-10x more likely to occur than a low Tm non-specific product. At 40 minutes, low Tm non-specific amplification had a false positive fraction of 5E-4. At the completion of the experiment the majority of partitions have amplified; thus, indicating high rate of non-specific amplification with *Bst* 3.0 may actually suppress efficiency as you eventually runout of partitions.

For this CT primer set, both *Bst* 2.0 and *Bst* 3.0 similarly demonstrate that the presence or absence of template does not impact the probability of non-specific amplification. Furthermore, the presence of gDNA does not impact the likelihood of non-specific amplification occurring. In general, for this primer set and target, we find that *Bst* 2.0 performs significantly better than *Bst* 3.0 as a consequence of having higher probability of detecting a target molecule and low likelihood of generating a non-specific amplification event.

Fourth, we asked is maximum rate impacted by the concentration of gDNA? We hypothesize that background gDNA may compete for the binding site of the polymerase with the target DNA or generate competing amplification events and thus, decrease the maximum observed velocity in a given partition. This phenomena would be challenging to untangle in bulk. We find that maximum rates are similar for a given enzyme, regardless of gDNA concentration (not shown). In general, and echoing the conclusions of Fig 3.3g,i, we observe that *Bst* 2.0 is faster than *Bst* 3.0, regardless of the gDNA concentration.

Cumulatively, these data show background DNA neither alters the probability of detecting a specific molecule (analytical sensitivity), nor the false positive fraction (analytical specificity), nor the maximum rate of amplification. Thus, we conclude background gDNA does not impact LAMP for this primer set. Furthermore, these experiments underscore the value of quantifying non-specific amplification variability, using Tm, from within the same experiment as a target is quantified, means you don’t have to assume the false positive rate remains identical to the NTC or between experimental runs.

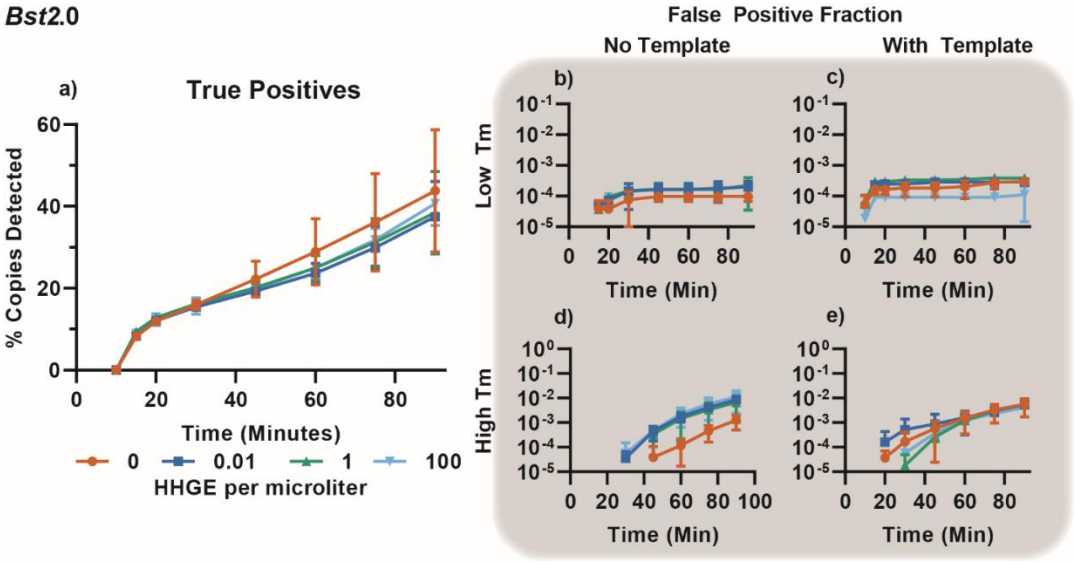

Figure 3.6: Quantification of the impact of gDNA on specific and non-specific amplification using *Bst* 2.0. Sampled temporally at 10,15,20, 35, 45, 60, 75, and 90 minutes. Plot of the % copies detected (specific amplification) as a function of time. A) Plot of the fraction of wells with non-specific amplification with Tm less than the specific amplification in the NTC as a function of time. B) Plot of the fraction of wells with non-specific amplification with Tm less than the specific amplification in the presence of template as a function of time. C)Plot of the fraction of wells with non-specific amplification with Tm greater than the specific amplification in the NTC as a function of time. D) Plot of the fraction of wells with non-specific amplification with Tm greater than the specific amplification in the presence of template as a function of time.

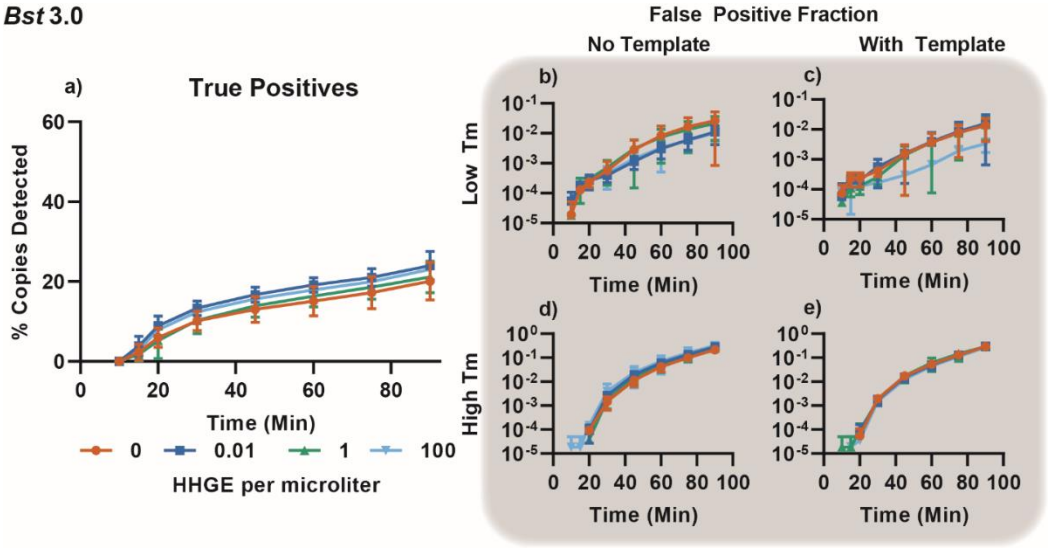

Figure 3.7: Quantification of the impact of gDNA on specific and non-specific amplification using *Bst* 3.0. A) Plot of the % copies detected (specific amplification) as a function of time. B)Plot of the fraction of wells with non-specific amplification with Tm less than the specific amplification in the NTC as a function of time. C)Plot of the fraction of wells with non-specific amplification with Tm less than the specific amplification in the presence of template as a function of time. D) Plot of the fraction of wells with non-specific amplification with Tm greater than the specific amplification in the NTC as a function of time. E) Plot of the fraction of wells with non-specific amplification with Tm greater than the specific amplification in the presence of template as a function of time.

CONCLUSIONS

We predict that the combination of Tm to real-time dLAMP will be invaluable for answering many questions across a wide variety of applications, and thus our approach was designed to be accessible to most standard labs. We employed commercial chips for digitization, a commercial thermoelectric unit for heating and cooling, a commercial microscope for optical analyses, and we made our data-processing script freely available. Our intention was to design an accessible system with readily available components to enable others to access the advantages of digital microfluidics and study and optimize primer sets, enzymes, and reaction conditions of levels of interest to them. We predict these capabilities will be particularly valuable for people working with high background DNA, poorly performing primer sets, or poorly performing enzymes.

We derived four major lessons from this study. First, LAMP can produce nonspecific amplicons with high Tm. The formation of these nonspecific amplicons is likely a result of the interaction of multiple primers. Primer design therefore should be judicious to prevent nonspecific amplification. In addition, incidence of nonspecific amplification differed between enzymes; nonspecific amplification occurred with greater frequency in *Bst* 3.0 than *Bst* 2.0. Digital enabled identification of both high-Tm and low-Tm amplicons, which are not observable in bulk. Others have called these amplicons spurious or suggested the presence of primer dimers. Spurious amplification can also lead to full false positives: we identified these as primer-dimer related.

Second, melting temperature in dLAMP is a useful method for differentiating specific and nonspecific amplification events. Digital experiments measure the fate/rate of each template, in contrast to bulk experiments that only measure early amplification events. Tm allows us to look at many amplification events and determine the nature of that amplification with high statistical probability. Combining these approaches, we can measure nonspecific amplification

experimentally, eliminating assumptions about the incidence of false positives in the NTC or between experimental runs.

Third, by differentiating specific and nonspecific amplification, Tm is helpful in determining the combination of assay parameters that will lead to the lowest LOD in a digital assay. When Tm is incorporated into a dLAMP assay, true and false positive amplification events can easily be separated. LOD is lowered further by elimination of nonspecific background and thus becomes dependent on the number of molecules that amplify (i.e., efficiency or % copies detected), without dependence on the incidence of false positives. In contrast, if Tm were employed in a bulk reaction, the LOD would still be limited by competition (what amplifies first) and would require a high number of trials to achieve sufficient statistical power. Importantly, even when Tm will not be used in the final assay, it can still be incorporated during the assay-development stage to lower the assay's LOD by determining the optimal choice of parameters based on rate, TTP, final intensity, or any combination of these parameters.

Fourth, low-to-moderate levels of non-specific host gDNA do not impact the specificity or sensitivity of dLAMP. We ran our assays up to 100 HHGE per microliter and higher concentrations could be considered, which shows the clinical validity of this approach.

Future efforts should investigate the combination of real-time dLAMP and Tm as a way to increase multiplexing of dLAMP when using a single reporter. In PCR, high-resolution Tm has been used to differentiate among multiple amplification products by looking at differences in melting temperatures. Additionally, we see use of high-resolution Tm for identifying specific products and mutations, such as in SNP detection.

Real-time dLAMP with Tm will also enable the mechanistic optimization of primers. Because it reveals the incidence of nonspecific amplification at high and low Tm, dLAMP with Tm can also be used to investigate approaches that will eliminate different nonspecific products. Fast or early nonspecific events cannot be differentiated from specific events in experiments lacking Tm. Thus, dLAMP with

Tm can be used to design primers that will suppress non-specific amplification in bulk, by generating only nonspecific amplicons that occur at slow rates and late TTP.

SUPPLEMENTAL

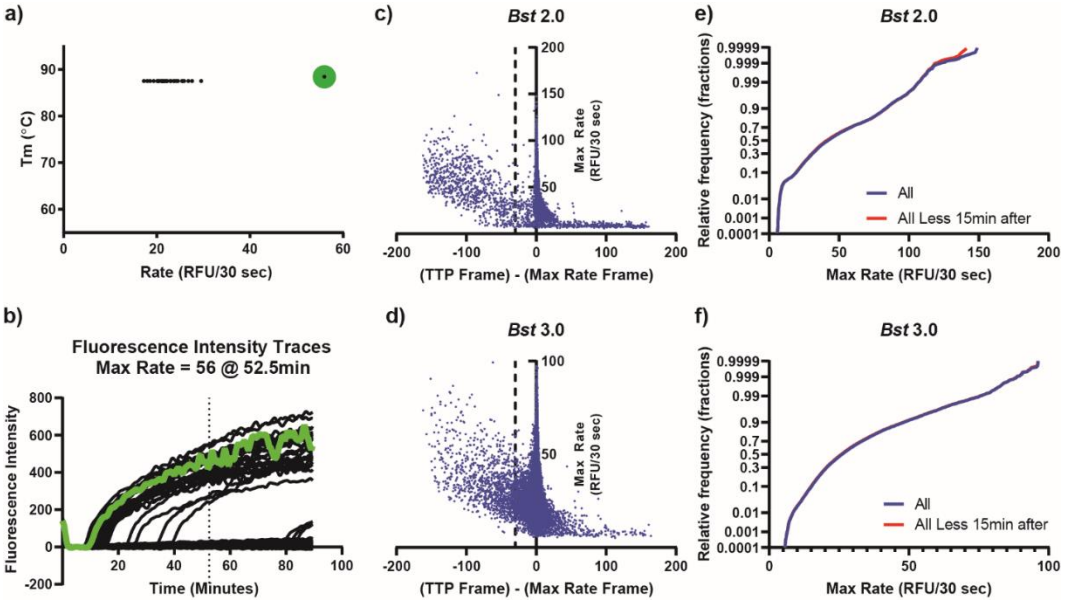

Figure 3.S1 Statistical Analysis of possible outliers by Maximum Rate.

A) We asked what caused one point (Green circle, max Rate 56 RFU) to separate from the majority of the data (20 to 35 RFU/30 sec), if these points were common, and if these points were likely to miss-represent the Max Rate data.

B) Determined the individual trace corresponding to this amplification event. Observed that the maximum rate for this partition was at 52.5 minutes, corresponding to a fluctuation in the plateau phase of amplification (dotted line).

C) We anticipated that the maximum rate should occur at the initial moment of amplification, often slightly before the TTP. To determine this, we determined the frame (2 per minute) where the trace reached the Fluorescence Time to Positive of 250 RFU. From this we subtracted the frame where Maximum Rate was calculated. Values greater than zero represent partitions where the maximum rate occurs before the TTP. Negative values occur when the Max rate occurs after the TTP. We draw a

vertical line separating partitions that occurring more than 15 minutes after the TTP (left), from all other partitions. For the case of *Bst* 2.0, we confirmed that the mode max rate occurs before the fluorescence time to positive of 250 RFU. 9099 total partitions measured, 821 (9.02%) were more than 15 minutes after the TTP. We expect these partitions to have max rate within the noise. Determined that the events of "late" maximum rate are rare.

D) A similar trend was observed for *Bst* 3.0. 24466 positive partitions, 1113 (4.55%) were more than 15 minutes after TTP.

E)We plot the Fractional cumulative distribution function of Max rate for all partitions (blue), and the same fractional CDF removing those points more than 15 minutes after the Fluorescence Intensity based TTP (red). A non-parametric based Kolmogorov-Smirnov test indicated non-significance between the two CDFs (P=0.3255)

F) We plot the Fractional cumulative distribution function of Max rate for all partitions (blue), and the same fractional CDF removing those points more than 15 minutes after the Fluorescence Intensity based TTP (red).A non-parametric based Kolmogorov-Smirnov test indicated non-significance between the two CDFs (P=0.1236). This indicates that removing the partitions more than 15 minutes behind the TTP, does not significantly impact the overall distribution. That removing these points does not impact the distribution.

I tallied up all the samples without HHGE, but containing template for *Bst* 2.0 and 3.0. I ran a non-parametric test comparing the CDF of the Max Rate data with and without those data occurring more than 15 minutes after the TTP by fluorescence intensity ("Kolmogorov-Smirnov Test"). Data coming in this range could be noise in the plateau phase. Removing these data from the distributions did not impact the CDFs, and therefore does not significantly impact our data reported (previously). There is not statistical justification to reprocess the data or assume the max rate data is unrepresentative of truth.

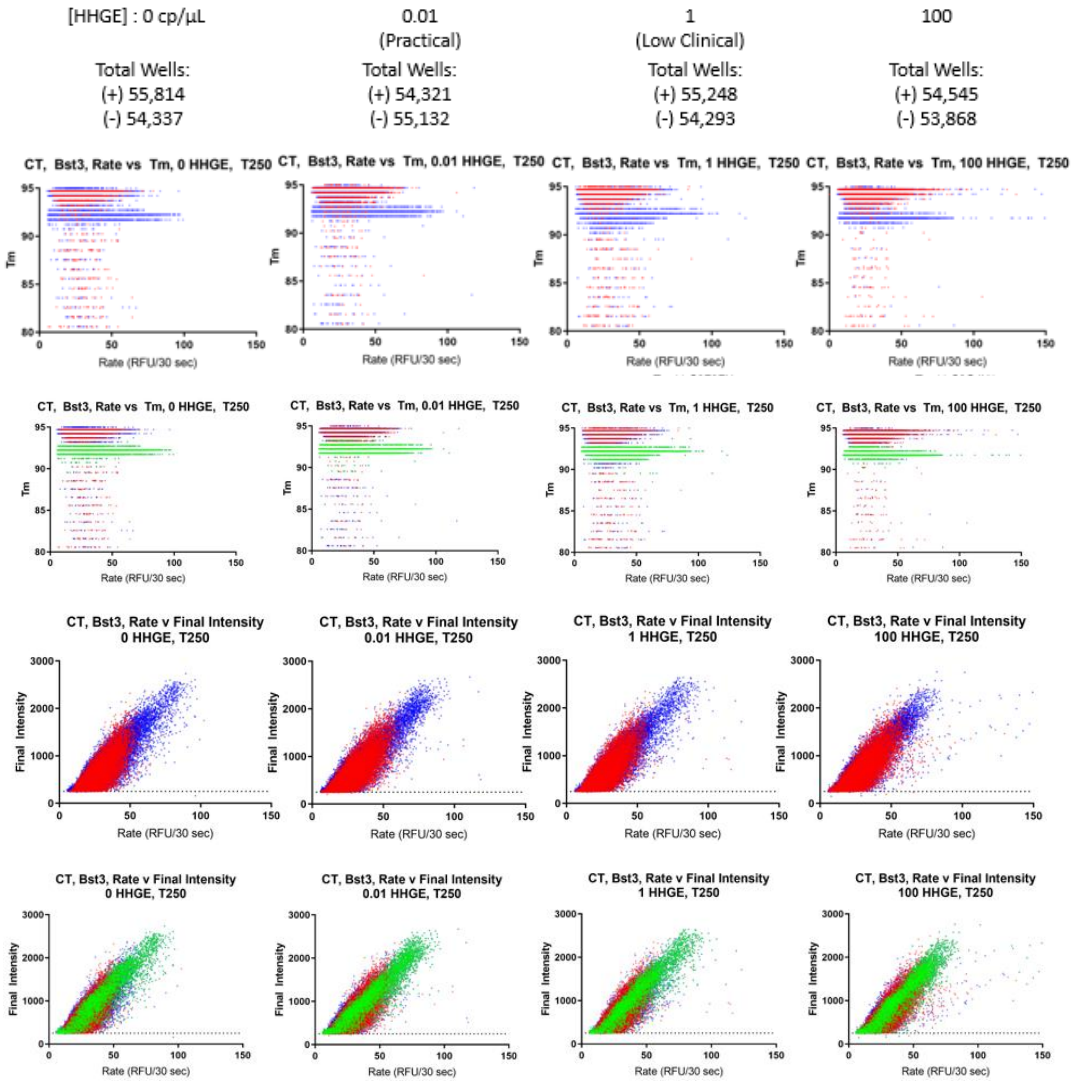

Figure 3.S2: Plots of Rate v Tm, rate, final intensity, for all concentrations of gDNA, using *Bst* 2.0. NTC (red), and presence of template (blue), specific amplification within the presence of template (green).

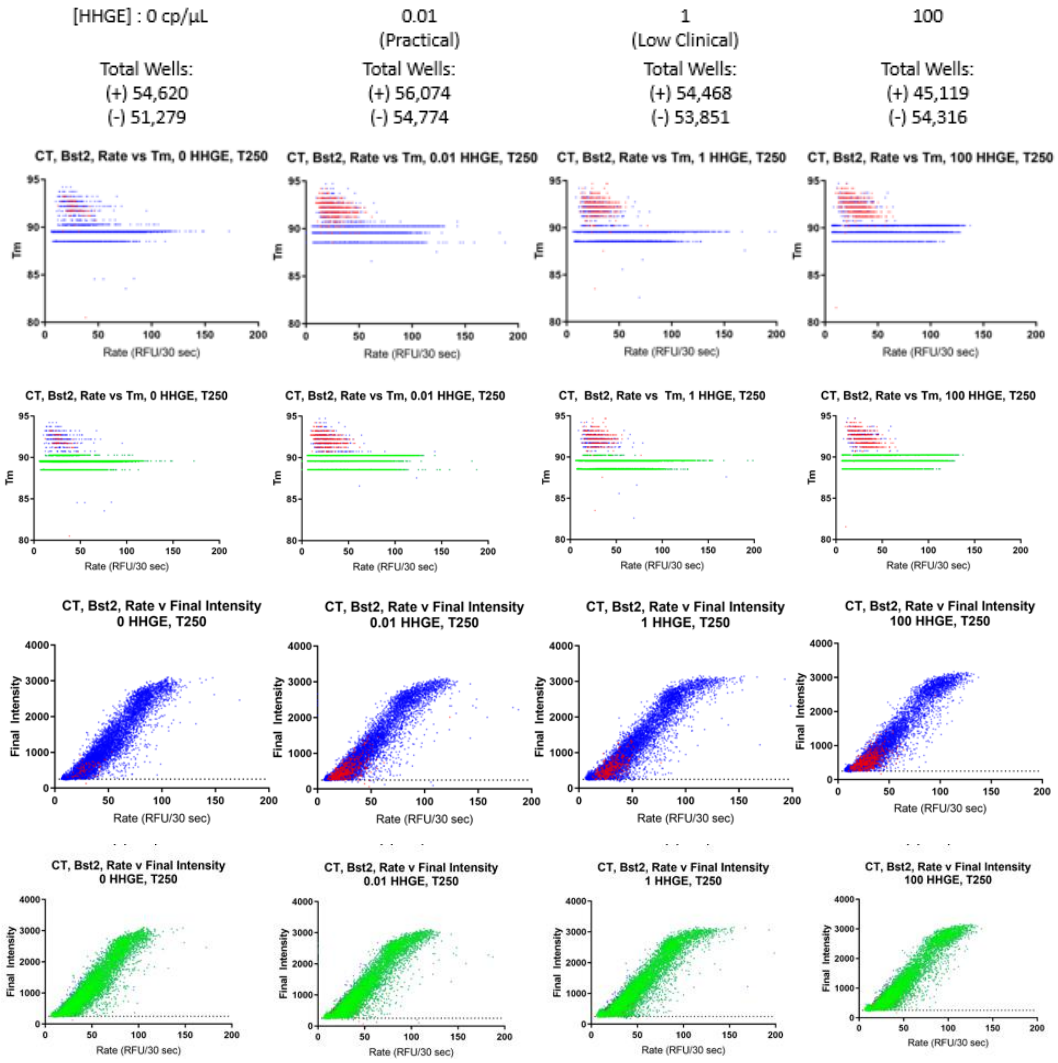

Figure 3.S2: Plots of Rate v Tm, rate, final intensity, for all concentrations of gDNA, using *Bst* 3.0. NTC (red), and presence of template (blue), specific amplification within the presence of template (green).

REFERENCES

1. Somboonna, N., Choopara, I., Arunrut, N., Sukhonpan, K., Sayasathid, J., Dean, D. and Kiatpathomchai, W. (2018) Rapid and sensitive detection of Chlamydia trachomatis sexually transmitted infections in resource-constrained settings in Thailand at the point-of-care. *PLoS neglected tropical diseases*, 12, e0006900-e0006900.
2. Ljubin-Sternak, S. and Meštrović, T. (2014) Chlamydia trachomatis and Genital Mycoplasmas: Pathogens with an Impact on Human Reproductive Health. *Journal of pathogens*, 2014, 183167-183167.
3. Su, W.H., Tsou, T.S., Chen, C.S., Ho, T.Y., Lee, W.L., Yu, Y.Y., Chen, T.J., Tan, C.H. and Wang, P.H. (2011) Diagnosis of Chlamydia infection in women. *Taiwanese journal of obstetrics & gynecology*, 50, 261-267.
4. Wan, L., Chen, T., Gao, J., Dong, C., Wong, A.H.-H., Jia, Y., Mak, P.-I., Deng, C.-X. and Martins, R.P. (2017) A digital microfluidic system for loop-mediated isothermal amplification and sequence specific pathogen detection. *Scientific reports*, 7, 14586-14586.
5. Khorosheva, E.M., Karymov, M.A., Selck, D.A. and Ismagilov, R.F. (2016) Lack of correlation between reaction speed and analytical sensitivity in isothermal amplification reveals the value of digital methods for optimization: validation using digital real-time RT-LAMP. *Nucleic Acids Res*, 44, e10.

Chapter IV

SURFACTANT-ENHANCED DNA ACCESSIBILITY TO NUCLEASE ACCELERATES PHENOTYPIC B-LACTAM ANTIBIOTIC SUSCEPTIBILITY TESTING OF N. GONORRHOEAE[1]

Abstract

Rapid, phenotypic antimicrobial susceptibility testing (AST) for *Neisseria gonorrhoeae* (*Ng*) is critically needed to counter widespread antibiotic resistance. However, rapid phenotypic AST for *Ng* is challenged by the pathogen's slow doubling time and the lack of methods to quickly quantify its response to β-lactams (the largest antibiotic class used to treat *Ng*). Here, we devise an innovative approach for performing a rapid phenotypic AST that measures DNA accessibility to exogenous nucleases after exposure to β-lactams. We show that DNA in antibiotic-susceptible cells has increased accessibility, and that a judiciously chosen surfactant enhanced this effect. We validated our method, termed nuc-aAST (nuclease-accessibility AST) using penicillin, cefixime, and ceftriaxone and showed 100% categorical agreement with gold-standard AST after just 15-30 min of antibiotic exposure. This proof-of-concept provides a pathway toward developing a critically needed phenotypic AST for *Ng* and these innovations can be leveraged to develop ASTs for additional global-health threats.

INTRODUCTION

Gonorrhea, caused by *Neisseria gonorrhoeae* (*Ng*), is the second most common notifiable sexually transmitted infection (STI) in the U.S.(*1*) and the third most common STI globally, affecting 78,000,000 people each year worldwide(*2*). Untreated *Ng* infections can lead to pelvic inflammatory disease, infertility, ectopic pregnancy, and neonatal blindness(*3*), and

[1]This chapter was submitted for publication with authorship belonging to Nathan G. Schoepp, Emily S. Savela, Justin C. Rolando, Olusegun O. Soge, and Rustem F. Ismagilov.

have a significant financial burden on healthcare systems(*4*). Antibiotic resistance in *Ng* emerged quickly and continues to spread unchecked because there is no rapid antibiotic susceptibility test (AST) to guide treatment. Lacking a rapid AST, clinicians are limited to making empiric prescriptions as recommended by the Centers for Disease Control and Prevention (CDC)(*5*) or World Health Organization (WHO)(*6*). When resistance to a particular ABX exceeds 5%, treatment guidelines are updated and the recommended treatment protocol is escalated to the next line of ABX(*7, 8*). As a result, *Ng* strains continue to evolve resistance, including to the last-line (dual treatment with azithromycin/ceftriaxone)(*9-11*). The global prevalence and spread of resistant *Ng* infections has led the CDC to place *Ng* in its highest ("urgent") category of antimicrobial-resistant pathogen threats(*12*) and the WHO to label *Ng* as a high-priority pathogen(*13*). Despite the threat of untreatable *Ng*(*14*) and an international call for rapid diagnostics(*15-17*), no phenotypic AST currently exists that can be performed rapidly enough for the point of care (POC).

Successful and timely treatment of *Ng* infections while providing antibiotic stewardship requires two sequential steps to be performed at the POC. First, an identification (ID) test is run on the patient's sample (typically urine or swab) to confirm that the patient is infected with *Ng*. Then, an AST must be run on the sample to determine whether the infecting strain of *Ng* is susceptible to the available ABX, so that the correct treatment can be prescribed. Substantial efforts (both academic(*18-20*) and commercial(*21, 22*)) are making great progress toward shortening the time required to identify *Ng* infections. However, there is no published path toward development of a rapid phenotypic AST for *Ng*, especially for beta-lactam antibiotics. Thus, even with swift diagnosis of an *Ng* infection, prescription of the correct antibiotics at the POC will remain bottlenecked by the lack of a rapid AST.

AST methods are either genotypic or phenotypic. Genotypic methods predict resistance by screening for the presence of known resistance genes, whereas phenotypic methods determine susceptibly and resistance by directly measuring an organism's response to an antibiotic. Rapid genotypic methods exist for select antibiotic classes such as

quinolones(*23, 24*), but the diverse mechanisms of resistance present in *Ng* would require highly multiplexed assays for most other antibiotic classes(*25, 26*), including β-lactams(*27, 28*), which are the largest class of ABX for *Ng*. For example, hundreds of β-lactamase genes are known(*29*), and new resistance genes continue to emerge, making it challenging to design a comprehensive genotypic AST, even for a single organism. Only phenotypic AST methods provide the ability to directly detect resistance, and susceptibility, regardless of the antibiotic's mechanism of action. The current gold-standard AST for *Ng* is agar dilution, a phenotypic method that takes many days and is only performed in a small number of reference laboratories(*30*). Efforts have been made to shorten the total assay time of culture-based techniques(*31-33*), but these methods still rely on multiple cell divisions and thus require many hours due to the slow doubling time (~60 min) of *Ng*.

A phenotypic AST usable at the POC would be paradigm-shifting for *Ng*(*34*) because it would provide the correct timely treatment of infections, significantly reduce disease burden, and improve global surveillance efforts(*35-37*). Until a POC diagnostic is developed for *Ng*, empiric prescribing of the last-line dual antibiotic therapy of azithromycin/ceftriaxone will likely continue, as it has in the U.S. over the last five years(*38*). Likewise, if informed antibiotic prescriptions cannot be made, resistance will continue to spread, at which point no currently available ABXs will be recommended for treatment of *Ng*. Importantly, a rapid, phenotypic AST would greatly increase treatment options because if clinicians know which ABX will be efficacious for each infection, they can once again treat with ABX that are not prescribed in the current (empiric-based) system because of the risk of resistance. For example, even though cefixime (CFM) is no longer used as a first-line therapy for *Ng*, up to 95% of infections in the U.S. are still susceptible to CFM(*1, 39*). Similarly, up to 77% of *Ng* infections are susceptible to TET(*1*). Therefore, having a POC AST would enable clinicians to once again safely prescribe CFM and other antibiotics(*40*). Several recent cases of *Ng* infections resistant to azithromycin(*41, 42*), or the currently recommended combination of ceftriaxone/azithromycin(*9, 11*) were detected after treatment was administered, highlighting the critical need for faster diagnostics.

For an *Ng* AST to inform treatment decisions at the POC, the total assay time to determine phenotypic susceptibility must be greatly decreased(*43-45*). Quantification of pathogen-specific nucleic acid (NA) concentrations has shown major promise for the rapid determination of susceptibility phenotype(*46-49*). These methods rely on comparing the NA concentrations of control and antibiotic-treated samples, and thus work well for rapidly dividing organisms and for ABX that directly affect NA replication. NA-based phenotypic AST methods also benefit from the high sensitivity of NA amplification, and fast isothermal amplification techniques have led to short total assay times(*46*). For example, by measuring the concentration of *E. coli* DNA, we have shown that the antibiotic-exposure step for phenotypic AST can be shortened to 15 min(*50*). We also were able to achieve a phenotypic AST with a 10-min antibiotic exposure time in *Ng* by measuring changes in RNA concentration after exposure to ciprofloxacin, which directly inhibits DNA replication and downstream translation(*51*). However, for ABX that do not impact DNA replication, such as β-lactams, these NA-based AST techniques have proven difficult; the fastest published method for *Ng* still requires four hours of beta-lactam exposure(*52*). Importantly, of the ABX prescribed for *Ng*, only one, ciprofloxacin(*51*), has been demonstrated to be compatible with this existing NA-based approach.

Here, we describe an innovation that enables a rapid, NA-based phenotypic AST for β-lactams, the largest class of ABX used to treat *Ng*. We hypothesized that cell wall damage caused by exposure to β-lactams could be exploited to determine phenotypic susceptibility faster than cell division. Our method, termed nuc-aAST (nuclease-accessibility AST), measures the accessibility of intracellular *Ng* DNA to exogenously added nucleases after a short antibiotic exposure. We also wished to test whether the total time of the assay could be further decreased by including an enhancement step, defined as a condition that would lead to greater differences in DNA accessibility between resistant (R) and susceptible (S) samples.

We chose to validate this proof-of-concept nuc-aAST using three β-lactams, penicillin (PEN), cefixime (CFM), and ceftriaxone (CRO), that represent first-line treatments at

different points in the history of *Ng* treatment(*6, 53*). Additionally, CRO, in combination with azithromycin, is the current recommended (and last-line) treatment for *Ng*. Determining susceptibility to CRO is thus relevant not only for treatment, but for surveillance efforts. Urine was chosen as the matrix for contrived sample testing because it is one of the primary sample types used for *Ng* diagnosis, especially in males(*5, 6*). We chose to test only categorically S or R isolates, based on EUCAST breakpoints(*54*), because S and R isolates are more useful than intermediate isolates for gaining initial mechanistic insights into nuc-aAST, and because S and R are actionable calls in antibiotic-prescribing scenarios. Lastly, keeping in mind clinical utility, we timed each assay step to determine whether the nuc-aAST could yield a definitive susceptibility call within the time period of a patient's visit, which is usually less than an hour(*44, 45*).

RESULTS

Design and rationale of the nuc-aAST

The nuc-aAST method measures differences in the accessibility of genomic DNA to an exogenous nuclease between control and treated samples following a short antibiotic (ABX) exposure. Like other NA-based AST methods, the nuc-aAST (Fig. 4.1) relies on measuring changes in the quantity of pathogen-specific NAs in response to a treatment with ABX; however, the nuc-aAST differs from existing NA-based ASTs in three aspects. First, in nuc-aAST, exposure of cells to β-lactams is performed in the presence of a DNase enzyme to degrade any DNase-accessible NAs (Fig. 4.1a). DNA is accessible to DNase if it is released from the cells upon cell lysis, or if the action of the antibiotic porates the cells and allows DNase to access the DNA. Second, in nuc-aAST, an enhancement step is introduced to increase accessibility of DNA in cells that have damaged or compromised peptidoglycan caused by β-lactams; DNase is present and active during this enhancement step (Fig. 4.1b). Third, in nuc-aAST, lysis of the sample is performed only after DNase has degraded all accessible DNA (Fig. 4.1c). This lysis step also inactivates the DNase, so that the enzyme does not impact downstream quantification. Following inactivation of DNase

and lysis, DNA remaining in the sample is quantified and the percentage of accessible DNA is used to determine susceptibility (Fig. 4.1d). The percentage of accessible DNA is quantified by subtracting the concentration of inaccessible DNA (DNA not digested) in the treated aliquot from the concentration of DNA in the control aliquot, and dividing this value by the concentration of DNA in the control. Measuring the percentage of accessible DNA is an NA-based metric that enables us to quantify the damage to the cellular envelope induced by ABX targeting cell wall biosynthesis.

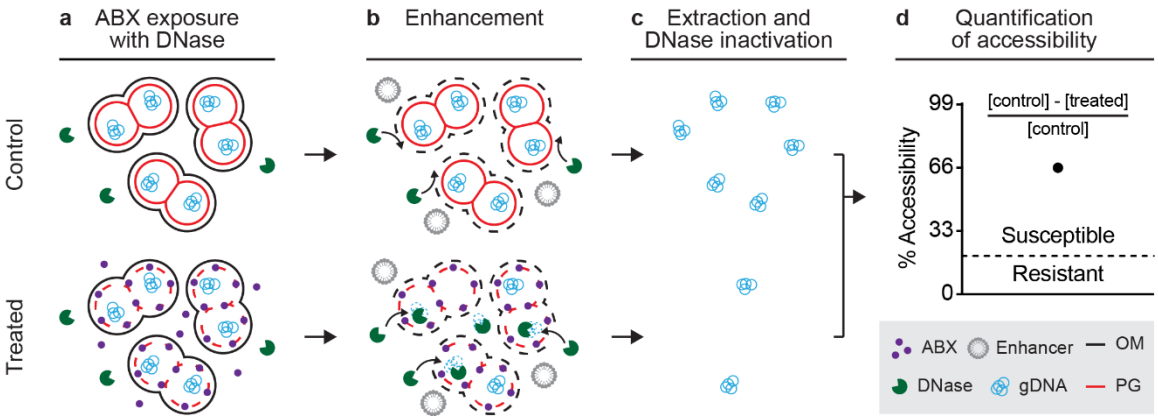

Figure 4.1. The nuc-aAST workflow shown for a sample containing an antibiotic-susceptible pathogen. (a) A sample is split into control and treated aliquots; the treated aliquot is exposed to antibiotics (ABX) in the presence of DNase and any extracellular DNA is digested. ABX compromise peptidoglycan (PG) of cells in the treated aliquot. (b) Accessibility to nucleases is enhanced by the addition of an enhancer, which disrupts the outer membrane (OM). Genomic DNA becomes accessible and is degraded in the treated aliquot. Intact peptidoglycan in control samples (or in treated but resistant samples) prevents degradation. (c) Nucleic acids (NAs) are extracted, and DNase is inactivated. (d) Accessibility is quantified by measuring NA concentrations in the control and treated aliquots and dividing the amount of digested DNA by the amount in the control (to yield percentage accessibility). When the percentage accessibility is greater than the threshold (dashed line), the sample is categorized as susceptible.

β-lactams should primarily affect peptidoglycan(*55*), and should not have a major impact on the outer membrane, which serves as a structural element in Gram-negative bacteria(*56*). Therefore, we expected the primary mechanism behind any increase in accessibility to be cell lysis as a result of exposure to β-lactams, leading to release of genomic DNA to the extracellular environment containing DNase. Additionally, we hypothesized that autolysis, which has been observed as an active stress response in *Ng*(*57*,

58), might accelerate changes in accessibility due to ABX exposure. We tested our hypotheses in a time-course experiment using two penicillin-susceptible (PEN-S) and two penicillin-resistant (PEN-R) *Ng* clinical isolates (Fig. 4.2). We observed a significant difference in the percentage accessibility between susceptible and resistant isolates after 90 min of exposure. This is the shortest incubation time for an *Ng* AST with PEN to date, and faster than existing NA-based methods that rely on DNA replication(*52*). However, the ideal length of an exposure step for an AST used at the POC would be even shorter (15-30 min) to keep the entire workflow within the time period of a patient visit. Thus, we were compelled to further accelerate changes in accessibility of DNA to nuclease as a result of β-lactam exposure in susceptible samples.

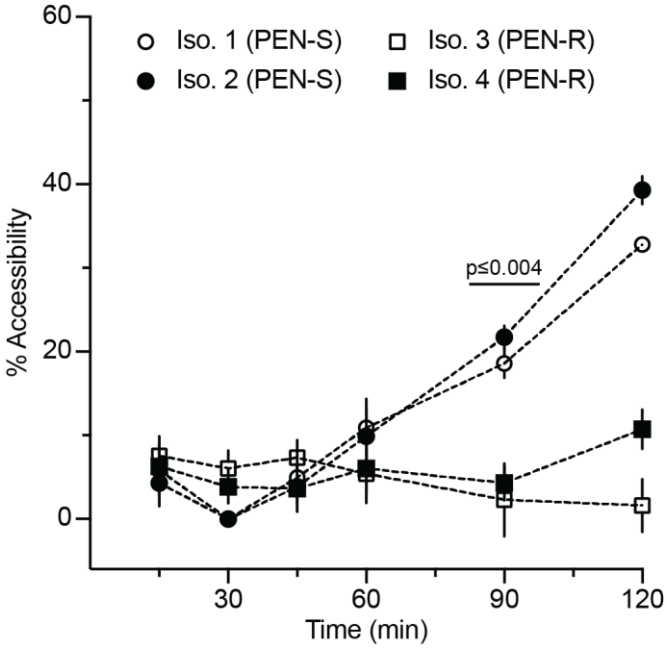

Figure 4.2. Percentage accessibility of DNA over time using the nuc-aAST without the addition of an enhancing step. Two penicillin-susceptible (PEN-S) and two penicillin-resistant (PEN-R) *Ng* isolates were exposed to penicillin in the presence of DNase I. DNA from the control and PEN-treated aliquots was extracted and quantified using qPCR at multiple time points to calculate percentage accessibility. Error bars represent the standard deviation of the PCR triplicates.

Enhancing changes in accessibility

We next hypothesized that the differences in DNA accessibility that we observed between susceptible and resistant isolates exposed to β-lactams could be enhanced using conditions that would modify the permeability of the cell envelope. In Gram-negative organisms like *Ng*, the outer membrane (OM) presents the first, and major, permeability barrier to macromolecules (e.g. nucleases and other enzymes) entering or exiting the cell, typically allowing only small molecules with molecular weights < ~600 Da to pass through(*59, 60*). The peptidoglycan, in contrast to the OM, is a looser barrier that has been estimated to allow macromolecules up to 50 kDa to pass through(*61-63*). We thus suspected that if the OM could be compromised, damage to the peptidoglycan would result in immediate,

measurable changes in accessibility of genomic DNA to DNase, both by allowing DNase to enter and by allowing DNA fragments to exit. Therefore, we hypothesized that we could compromise the OM using an "enhancer" to decrease total assay time.

The ideal enhancer would i) increase DNA accessibility to DNase in cells that have a compromised cell wall as a result of ABX exposure, ii) result in minimal lysis of healthy cells, iii) have a consistent effect on all *Ng* isolates and iv) have no effect on downstream extraction and quantification of NAs. With these parameters in mind, we chose to test hypo-osmotic stress, stimulated autolysis, and four classes of surfactant as potential enhancers.

Hypo-osmotic stress was chosen as a method to enhance lysis of cells with damaged or compromised cell walls because osmotic stress of varying degrees is known to increase release of intracellular contents in Gram-negative bacteria,(*64-66*) although it has never been used to enhance accessibility in the context of AST. We exposed cells to hypo-osmotic conditions by diluting control and treated aliquots 20-fold in water with DNase I and 500 µM $CaCl_2$, resulting in a ~244 mOsm/kg shift from the ABX exposure conditions. Autolysis was chosen as an enhancer with the rationale of leveraging an already existing stress response in *Ng* to enhance changes in accessibility. Autolysis is a natural stress response in *Ng*, and can be accelerated by incubation in high pH conditions (e.g. Tris, pH 8.5)(*67, 68*). We hypothesized that using autolysis as an enhancer might result in large changes in NA accessibility. Surfactants were chosen as potential enhancers as a targeted chemical means of disrupting the bacterial cell membrane. We chose a representative surfactant from each of the four major charge-based classes of surfactants to investigate whether surfactant charge might lead to variability in their effectiveness due to natural variations in the OM of *Ng*. We tested the anionic surfactant sodium dodecyl sulfate (SDS), the cationic surfactant benzalkonium chloride (BAC), the non-ionic surfactant TERGITOL NP (TNP), and the zwitterionic surfactant 3-[(3-Cholamidopropyl)dimethylammonio]-1-propanesulfonate (CHAPS). Each of these surfactant classes, with the exception of zwitterionic surfactants, have been well-studied for their ability to compromise the

integrity of the cell envelope(*69*), but none have been used in the context of AST, or to change DNA accessibility on such short time scales. We chose to include the less well-studied zwitterionic surfactant CHAPS based on the diverse interactions of zwitterionic solutes with the bacterial cell envelope(*70*).

We tested each potential enhancer with respect to i) the degree of lysis caused by incubation with the enhancer alone, ii) the ability to differentiate PEN-S and PEN-R isolates using an enhancement step after exposure to PEN, and iii) the ability to differentiate CRO-S and CRO-R isolates using an enhancement step after exposure to CRO. We chose to use PEN and CRO because we expected that the degree of change in NA accessibility as a result of enhancement would depend on the type of β-lactam used during exposure. CRO and PEN bind and inhibit a different profile of penicillin-binding proteins(*40, 71*) and have different rates of killing(*72*), which we expected would lead to different effects depending on the enhancer. Each enhancer was tested using multiple isolates susceptible or resistant to either PEN or CRO. All enhancers were tested using a 5-min enhancement step after 15 min of ABX exposure. Antibiotic-exposure and enhancement steps were performed separately to decouple their effects on the *Ng* isolates.

Enhancers were first tested for the degree of lysis caused by a 5-min incubation with the enhancer alone (Fig. 4.3a-f). If the enhancement step lyses the majority of cells even without antibiotic exposure, then accessibility will increase in both control and treated aliquots, and any effect of the antibiotic will be diminished. We observed an average of < 50% lysis when testing all potential enhancers except BAC (Fig. 4.3d), which showed an average of 94% lysis across all eight isolates tested. We next measured the percentage accessibility when using each enhancer after a 15 min exposure to PEN. We evaluated the ability to differentiate PEN-S and PEN-R isolates based on the average percentage accessibility in S isolates (which we want to be large), the average percentage accessibility in R isolates (which we want to be small), and the magnitude of separation between those two values. Based on these criteria, Tris (Fig. 4.3h), TNP (Fig. 4.3k), and CHAPS (Fig. 4.3l) were the most promising enhancers for differentiating PEN-S and PEN-R isolates

after 15 min of exposure. However, we observed differences in accessibility in response to CRO compared with PEN depending on the enhancer used (Fig. 4.3m-r). Among CRO-S isolates, enhancement with TNP or CHAPS resulted in the largest average changes in accessibility. We were unable to observe consistently large changes in the seven tested CRO-S isolates using the other two ionic surfactants, SDS (Fig. 4.3i,o) and BAC (Fig. 4.3j,p), regardless of the ABX treatment. Following these tests, we chose CHAPS as the enhancer to use for validation of the nuc-aAST because it resulted in low percentage lysis, large increases in DNA accessibility for PEN-S and CRO-S isolates following exposure, and only small increases in the DNA accessibility of PEN-R and CRO-R isolates.

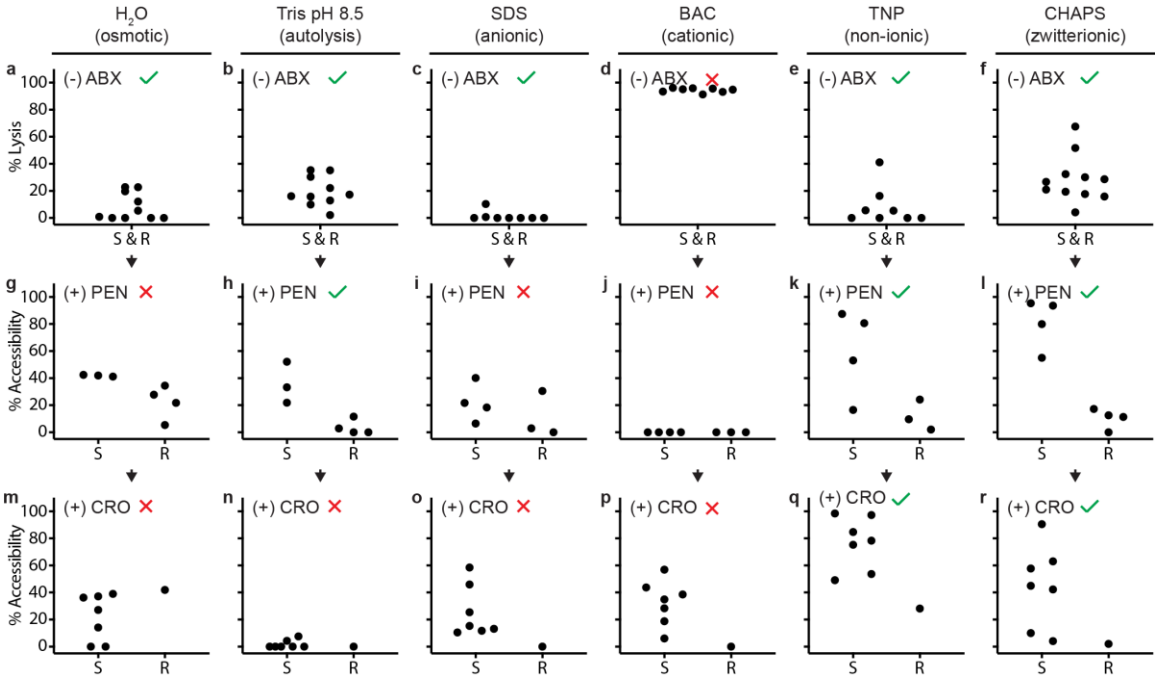

Figure 4.3. Selection of enhancers. Six enhancers were tested for percentage of cell lysis due to enhancer alone (prior to antibiotic [ABX] exposure) (a-f), enhancement after exposure to penicillin (PEN) (g-l), and enhancement after exposure to ceftriaxone (CRO) (m-r). Each point represents the average of all biological replicates run for that condition. Checkmarks indicate enhancers that met our criteria for inclusion in the nuc-aAST; X's indicate enhancers that did not meet our criteria.

Validation using clinical isolates

To validate the nuc-aAST we performed 34 ASTs (with multiple biological replicates each) using 13 clinical isolates of *Ng* exposed individually to PEN, CFM, or CRO for 15 min. We then compared the categorical susceptibility determined using the nuc-aAST to the susceptibility determined using gold-standard agar dilution (Fig. 4.4a-c). Receiver operating characteristic (ROC) plots(*73*) (not shown) were created so that the area under the curve (AUC) could be calculated for each β-lactam tested. After 15 min of exposure we obtained an AUC of 1.000 (PEN), 0.955 (CFM), and 1.000 (CRO). The AUC is determined by scanning a threshold through the ROC plot and measuring the sensitivity and specificity at each theoretical threshold value. This scanning allows one to select the threshold that would differentiate susceptible and resistant organisms with the maximum sensitivity and specificity within the given dataset. For example, an AUC of 1.000 indicates there was a threshold value that perfectly separated susceptible (S) and resistant (R) categories. However, AUC measurements do not consider the experimental noise or the magnitude of separation between S and R samples and should be applied with care to datasets with limited number of measurements, such as ours. For example, in the case of CFM, the difference between the two CFM-R isolates and the CFM-S isolates with the lowest responses (open circles in Fig. 4.4b) was small after 15 min of exposure, so setting the susceptibility threshold between them would be impractical. The same is true of setting a threshold between the single CRO-R isolate that was available to us and two CRO-S isolates with the lowest responses. We therefore set the thresholds for both these ABX at a more conservative 18% even though this threshold generates some errors (Fig. 4.4b,c; open circles) in the CFM and CRO measurements after 15 min of ABX exposure.

We then hypothesized that the differences observed in the magnitude of the response of the susceptible isolates after 15 min of exposure to each antibiotic, including the errors observed when testing CFM and CRO (open points, Fig. 4.4b,c) could be the result of differences in how fast each β-lactam affects *Ng*(*72*). For example, a possible explanation for differences among isolates in their response to ABX could be phylogenetic

differences(*74-76*). If isolates differ in their response times, a longer exposure would result in larger average separation between S and R isolates and potentially better categorical agreement if the S isolates were less-responsive as a result of a delayed response to antibiotic.

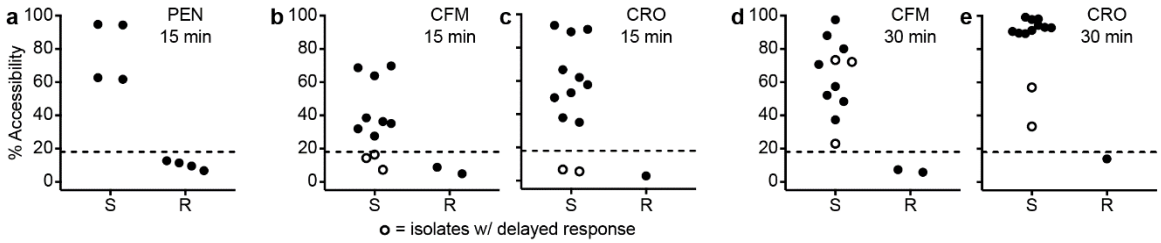

Figure 4.4. Validation of nuc-aAST using clinical isolates. (**a-c**) nuc-aAST results after 15 min of exposure to (**a**) penicillin (PEN), (**b**) cefixime (CFM), and (**c**) ceftriaxone (CRO). (**d-e**) nuc-aAST results after exposure to (**d**) CFM and (**e**) CRO for 30 min. All points represent the average percentage accessibility of single clinical isolates run in (at least) biological triplicate. Open points represent isolates that took longer than 15 min to respond to the β-lactam being tested. The dashed line represents the susceptibility threshold, which was set at 18% accessibility.

To test the hypothesis that there are inherent differences in isolate response time, we performed nuc-aAST using CFM and CRO with 30-min exposure times and, as predicted, we observed a larger average separation between S and R isolates and full categorical agreement with gold-standard agar dilution in all isolates. After 15 min of exposure to CFM and CRO, 73% and 83% of susceptible isolates, respectively, were classified as susceptible using nuc-aAST. After 30 min of exposure to CFM and CRO, 100% categorical agreement was obtained.

Sum-of-steps total time using contrived urine samples

To make a more realistic measure of total assay time, we modified the extraction and quantification steps of the nuc-aAST. The exposure and enhancement steps were performed as described above, but NA quantification was performed using a rapid, chip-based, digital loop-mediated isothermal amplification (dLAMP) method, as described previously(*77*). Additionally, we used a faster, single-step nucleic acid extraction method

based on previous work(*46*). Both modifications made the workflow faster. Additionally, the high precision of digital quantification allowed us to make a susceptibility call as soon as there was a significant difference between the concentration of NAs in the control and treated aliquots.

We measured total assay time based on the sum of the steps of the nuc-aAST using contrived urine samples. Contrived samples mimic clinical urine samples and allowed us to better evaluate how the assay would perform in a clinical setting than assays performed with isolates in media. Samples were created using two PEN-S and two PEN-R isolates; one of the two PEN-R isolates was positive for β-lactamase activity, which we included in order to have PEN-R isolates with different mechanisms of resistance. To perform the AST, samples were first split into control and treated aliquots, and incubated at 37 °C for 15 min. Next the samples were transferred to the enhancement step, and incubated for 5 min in the presence of CHAPS. Samples were then extracted as described above and dLAMP was performed in commercial chips(*77*). Images were obtained in real time using a custom imaging system(*78*). LAMP quantification was performed using an automated data-analysis workflow in MATLAB(*77*) in which images are automatically processed and positive wells counted based on a digitized mask created from the final image (Fig. 4.5b). NA concentrations were used to determine percentage accessibility as soon as the measured NA concentrations in the susceptible sample became significantly different between the control and treated chips. All samples were tested in a total time (measured as the sum-of-steps) of 30 min and agreed with gold-standard agar dilution (Fig. 4.5c).

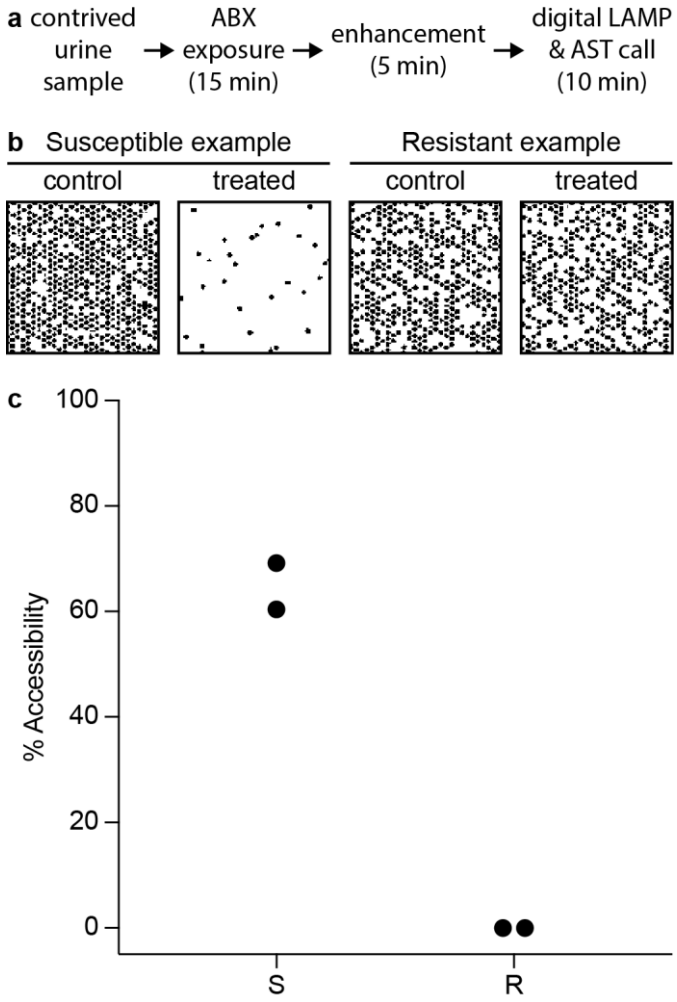

Figure 4.5. The nuc-aAST workflow with each step timed. (a) The nuc-aAST workflow showing the time required for each step. (b) 2x2 mm subsection of masks created from chips used for performing digital LAMP (dLAMP) on control and treated aliquots of susceptible and resistant samples; as an illustration, each mask shows ~625 wells (out of ~20,000 total wells) after 10 min of amplification. Wells that showed amplification of *Ng* DNA appear black. (c) Percentage accessibility determined at earliest significance (<7 minutes of amplification, see Methods) for two susceptible and two resistant samples run using dLAMP. Each step was timed individually and the sum-of-steps of the assay was 30 min for PEN.

DISCUSSION

Here we described a new approach—nuc-aAST—to enable developing a critically needed rapid phenotypic AST for the globally-important pathogen *Neisseria gonorrhoeae*. We show that by measuring the change in the accessibility of DNA after 15 or 30 min β-lactam exposure, the nuc-aAST yields a phenotypic susceptibility readout in less than 1 hour, as opposed to the currently available methods which require hours to days. We further show that the nuc-aAST breaks the current speed limits for nucleic-acid-based phenotypic ASTs using β-lactams (which do not directly impact NAs) by using an innovative approach: coupling cell wall damage to NA readout. The nuc-aAST thus provides a new approach for designing rapid phenotypic ASTs with NA-based readouts for ABX that impact cell envelope integrity. Overall, we envision that leveraging the nuc-aAST and combining it with other creative biological and chemical insights will result in similarly innovative approaches for other important antibiotic classes for *Ng*, such as protein-biosynthesis inhibitors like tetracycline and azithromycin. Existing NA-based approaches, such as those for ciprofloxacin(*23, 51*), can also be combined alongside the nuc-aAST.

We found that phenotypic ASTs that use NA accessibility as a readout benefit from the use of a carefully chosen enhancer. Here, the enhancement step consisted of a surfactant (CHAPS) that enabled detection of cell wall damage faster than cell division. Without the enhancement step, the cell envelope remains intact longer, so measurements of accessibility approximate the timescale of cell division (Fig. 4.2), which, for fastidious organisms such as *Ng*, will be too slow for POC applications. The increase in DNA accessibility in S isolates will differ based on the combination of β-lactam used and enhancer, highlighting the importance of testing multiple β-lactams with the nuc-aAST. Of the surfactants tested as enhancers, the charge-neutral surfactants TNP and CHAPS gave better results than the ionic surfactants SDS and BAC, suggesting that charge may be an important factor when designing an effective enhancement step. We also anticipate organism-specific OM chemistry and general stress responses will play a role in determining which enhancers are optimal in other organisms.

We found that for PEN, susceptibility of *Ng* could be determined after just 15 min of exposure in all isolates tested (Fig. 4.4a). However, for CFM and CRO, a small number of S isolates did not respond after 15 min of exposure but responded after 30 min exposure (Fig. 4.4b-e). We hypothesize that CFM and CRO required a longer exposure than PEN because of their differences in binding kinetics and rates of killing(*71, 72, 79*). Despite these differences, an actionable susceptibility call (i.e. determining that an isolate is susceptible to a particular ABX and therefore can be treated with that ABX) could still be made for most isolates after 15 min of exposure (100% using PEN, 77% using CFM, and 85% of cases using CRO). One approach to balance reducing assay time with minimizing errors is to perform two exposures in parallel for each ABX. The first exposure would be analyzed after 15 minutes. If a response is obtained indicating that the pathogen is susceptible (which should be the case for the majority of patients), the second exposure would be discarded. If no response or if an equivocal response is obtained, then the second exposure (after 30 min total) would be analyzed to provide the definitive susceptibility call. With this approach, the test would provide the answer after 15 min of ABX exposure for the majority of patients, and only a few patients would be delayed by the additional 15 min of ABX exposure.

Several limitations will need to be overcome in order to translate the nuc-aAST approach to an automated and distributable system. First, in this paper we used clinical isolates and contrived urine samples. Although contrived samples are a good proxy for clinical samples and are accepted by the U.S. Food and Drug Administration in certain cases(*80*), the nuc-aAST should be validated with fresh clinical samples. It remains to be tested whether the enhancer chemistry has to be modified to account for the presence of host-derived cells and metabolites that might interfere with the assay. Second, future work should test more *Ng* isolates with diverse phylogeny(*74-76*) as they are made available to researchers and characterized, as well as test isolates with intermediate resistance to PEN, CFM, and CRO. These efforts could also aim to establish a correlation in the magnitude of nuc-aAST response and minimum inhibitory concentration (MIC) of ABX, which would provide even

more detailed information at the POC. Third, in timing the sum-of-steps, we did not include handling time; future work should include optimization of handling steps and timed sample-to-answer experiments. Finally, the nuc-aAST method will need to be translated to a POC device so that larger-scale clinical evaluations can be performed. Devices for multiplexed digital quantification(*81-83*) have been demonstrated and would be useful in performing nuc-aAST for multiple ABX in parallel.

We envision that nuc-aAST would be deployed in combination with two complementary technologies: (i) the pathogen ID technologies that are being developed by others(*18, 19, 21, 22*) to identify *Ng*-positive samples that require an AST, and (ii) rapid genotypic and/or phenotypic ASTs that rely on NA readouts for other ABX used in the treatment of *Ng*, including fluoroquinolones (ciprofloxacin)(*23, 46, 75*) and protein synthesis inhibitors (tetracycline and azithromycin)(*75*). Assuming these two complementary technologies are developed and validated, further development of nuc-aAST would provide the last—and we would argue the most challenging—piece needed for a complete rapid ID/AST workflow for *Ng* based on NA readout. We chose NA readout for the nuc-aAST for two reasons. First, NA readouts will enable easy integration with pathogen ID and other NA-based AST technologies. Second, NA readouts are organism-specific[*46*], and therefore should be effective even for mixed microbial populations potentially present in clinical samples (e.g., *Ng* in the presence of commensals or other pathogens).

Implementation of a rapid phenotypic AST would dramatically improve the antibiotic stewardship of *Ng* infections and therefore impact the health of people who are infected with *Ng*; currently, there are an estimated 78,000,000 global cases of *Ng* every year(*2*). Furthermore, the nuc-aAST approach provides a framework for developing additional accessibility-based AST chemistries for other pathogens that pose global health threats but have been challenging for current phenotypic AST methods. For example, we have shown that quantifying NA accessibility to polymerases can be used to rapidly determine ABX susceptibility in Enterobacteriacea(*84*). Overall, this work highlights the diagnostic capabilities that can be attained by developing innovative NA-based assays for AST;

further expansion and application of these approaches is critically needed to address the crisis posed by antibiotic-resistant bacteria.

MATERIALS AND METHODS

Isolates and agar-dilution MIC testing. Isolates were provided by the University of Washington Neisseria Reference Laboratory. MICs were determined by agar dilution according to the Clinical and Laboratory Standards Institute (CLSI) guidelines(*86*).

Reagents and culture media. BD BBL Chocolate II Agar prepared plated media (GC II Agar, with Hemoglobin and BD IsoVitaleX) was purchased from VWR International LLC (VWR, Radnor, PA, USA). Graver-Wade Medium (GWM) was prepared as described previously(*87*). Cation-adjusted Mueller Hinton II Broth (MHB) (BD, Franklin Lakes, NJ, USA) was prepared according to manufacturer instructions. All sodium bicarbonate ($NaHCO_3$) (Sigma, St. Louis, MO, USA) and calcium chloride ($CaCl_2$) (Fisher Scientific, Hampton, NH, USA) stocks were dissolved in nuclease-free water (NF-H_2O) and sterilized using 0.2-µm filters. DNase I (2000 U/mL) was obtained from New England Biolabs (NEB, Ipswich, MA, USA). Normal urine from pooled human donors was purchased from Lee Biosolutions (Maryland Heights, MO, USA) and filtered through 0.2-µM filters before use.

Antibiotic stocks were prepared and stored as single-use aliquots at -80 °C. Aliquots were thawed once and diluted in NF-H_2O before use. PEN (1 mg/mL) was prepared from penicillin G sodium salt (Sigma, St. Louis, MO, USA) in NF-H_2O. CRO (1 mg/mL) was prepared from ceftriaxone disodium salt hemi(heptahydrate) (Sigma) in NF-H_2O. CFM (5 mg/mL) was prepared from cefixime trihydrate (Sigma) in DMSO.

Unless otherwise noted, enhancer stock solutions were prepared in NF-H_2O and stored at room temperature. Tris buffer (500 mM; pH 8.5 at 37 °C) was prepared according to the Sigma buffer reference tables(*88*) using 0.2-µm filter sterilized stocks of 1 M Tris-HCl

(Sigma) and 1 M Tris base (Fisher Scientific) prepared in milliQ H_2O. TNP HLB 13.1 (100 mM) was prepared by mixing 334 µL 100 mM Tergitol NP-9 (Sigma) + 666 µL 100 mM Tergitol NP-10 (Sigma). CHAPS (200 mM) was prepared from CHAPS solid powder (Sigma). 0.1% sodium dodecyl sulfate (SDS) was prepared by diluting 10% SDS (Invitrogen, Carlsbad, CA, USA). BAC (10%) was prepared from benzalkonium chloride solid powder (MP Biomedicals, Santa Ana, CA, USA).

Nucleic acid quantification. Quantitative PCR (qPCR) was performed using ssoFast EvaGreen Supermix (BioRad, Hercules, CA, USA) in 10 µL reactions with 500 nM primers targeting the *Ng* 16S gene(*89*). DNA template composed 10% of the reaction volume. Cycling conditions consisted of 3.0 min at 95 °C, followed by 35 cycles of 15 sec at 95 °C, 15 sec at 62 °C, and 20 sec at 72 °C. All qPCR was performed on either a Roche LightCycler 96 or BioRad CFX96 instrument. The Cq values obtained from qPCR are used to compute the percentage accessibility and percentage lysis as described in the equations below. Any negative percentages were set to 0 for all analyses.

$$(1)\ \%\ Accessibility\ (control\ and\ treated) = \left((1 - 2^{(Cq_{control} - Cq_{treated})}\right) \times 100$$

$$(2)\ \%\ Lysis\ (no\ enhancer\ and\ enhancer) = \left((1 - 2^{(Cq_{no\ enhancer} - Cq_{enhancer})}\right) \times 100$$

Droplet digital PCR (ddPCR) was performed using QX200 ddPCR Supermix for EvaGreen (BioRad, Hercules, CA, USA) with the same primers and primer concentrations used in qPCR. DNA template composed 10% of the reaction volume. Cycling conditions consisted of 5.0 min at 95 °C, followed by 40 cycles of 30 sec at 95 °C, 30 sec at 60 °C, and 30 sec at 72 °C, followed by a droplet stabilization step of 4 °C for 5 min, and 95 °C for 5 min. Calculations of percentage accessibility and percentage lysis for ddPCR are given the equations below, where λ represents template concentration in copies/µL. The template concentrations are used to compute percentage accessibility and percentage lysis as described in the equations below. Any negative percentages were set to 0 for all analyses.

(3) $\%\ Accessibility\ (control\ and\ treated) = (1 - (\lambda_{treated}/\lambda_{control})) \times 100$

(4) $\%\ Lysis\ (no\ enhancer\ and\ enhancer) = (1 - (\lambda_{enhancer}/\lambda_{no\ enhancer})) \times 100$

A dLAMP assay was performed using a previously published system(*77*). The dLAMP mix consisted of 1 µL NEB Isothermal Amplification Buffer (200 mM Tris-HCl, 20 mM $MgSO_4$, 500 mM KCl, 100 mM $(NH_4)_2SO_4$, 1% Tween 20, pH 8.8), 0.6 µL $MgSO_4$, 0.5 µL BSA (20 mg/mL), 0.4 µL Syto-9 (50 µM, prepared within two weeks of use), 1.4 µL dNTPs (10 mM each), 0.5 µL 20X primer mix, 0.4 µL NEB Bst 2.0 WarmStart, 0.2 µL Ambion RNase cocktail, 4.0 µL NF-H_2O, and 1 µL of template. Primers were designed to target the *Ng* 16S gene, and screened as described previously(*46*). Primer sequences used are as follows, with the final concentration in the amplification mix in parentheses: GCGGTGGATGATGTGGATT (forward outer primer, 0.2 µM), CCGGCAGTCTCATTAGAGTG (backward outer primer, 0.2 µM), CTCCTCCGTCTCCGGAGGATTCaaaaCGATGCAACGCGAAGAAC (forward inner primer, 1.6 µM), TCGTCAGCTCGTGTCGTGAGATttttCCCAACCGAATGATGGCA (backward inner primer, 1.6 µM), CGCACATGTCAAAACCAGG (forward loop primer, 0.4 µM), and GCAACGAGCGCAACCC (reverse loop primer, 0.4 µM). The following equation was used to compute percentage accessibility, where λ represents the template NA concentration in copies/µL as measured by dLAMP.

(5) $\%\ Accessibility\ (control\ and\ treated) = (1 - (\lambda_{treated}/\lambda_{control})) \times 100$

***Ng* culture preparation.** Isolates were streaked from glycerol stocks stored at -80 °C onto BD BBL Chocolate II Agar plates and incubated overnight in a 37 °C incubator with 5% CO_2. Isolates were then passed onto fresh BD BBL Chocolate II Agar plates and grown for 4-7 h at 37 °C with 5% CO_2. In all experiments, cells from plates passed 1-3 times were used. Several colonies were scraped and resuspended in 37 °C GWM to generate a working suspension. Optical density at 600 nm (OD_{600}) was measured, and the working suspension was diluted to create a 2 mL working culture of OD_{600} 0.05 in GWM in 15 mL

polypropylene culture tubes. Cultures were incubated, with 500 rpm shaking, at 37 °C + 5% CO_2 for 3-5 h prior to ABX exposure.

nuc-aAST time-course without enhancing step. Working cultures of *Ng* isolates were prepared as described in "*Ng* culture preparation." Incubation at 37 °C was performed in 100 µL reaction volumes in PCR tube strips on a BioRad C1000 Thermal Cycler. Treated samples consisted of 77.5 µL MHB, 2.5 µL $NaHCO_3$ (200 mM), 5 µL DNase I (2 U/µL), 5 µL PEN (20 µg/mL), and 10 µL working *Ng* isolate culture. PEN was replaced with NF-H_2O in control samples. A 10 µL aliquot of each sample was extracted at 15, 30, 45, 60, 90, and 120 min and diluted 10X in QuickExtract DNA Extraction Solution (Lucigen, Middleton, WI, USA), then heated for 6 min at 65 °C followed by 4 min at 98 °C on a BioRad C1000 Thermal Cycler. All sample handling following antibiotic exposure was performed using a multichannel pipette; qPCR and calculation of % accessibility were performed as described above.

Enhancer use. Working cultures of *Ng* isolates were prepared as described in "*Ng* culture preparation." Initial exposure was performed by incubating 100 µL control and treated samples at 37 °C in PCR tube strips on a BioRad C1000 Thermal Cycler. Treated samples consisted of 75 µL MHB, 5 µL $NaHCO_3$ (100 mM), 5 µL DNase I (2 U/µL), 5 µL PEN or CRO (20 µg/mL), and 10 µL working *Ng* isolate culture. ABX were replaced with NF-H_2O in control samples. After 15 min of incubation, samples were vortexed and quick-spun, and aliquots of all samples were transferred to the enhancement step as described below. After the enhancement step, 5 or 10 µL of all samples were extracted by diluting 10X in QuickExtract DNA Extraction Solution (Lucigen) and heating for 6 min at 65 °C followed by 4 min at 98 °C on a BioRad C1000 Thermal Cycler. All sample handling following ABX exposure was performed using a multichannel pipette; qPCR and calculation of % accessibility was performed as described above.

Osmotic and autolytic enhancing steps were performed in 100 µL volumes. The osmotic enhancing step consisted of 89.75 µL NF-H_2O, 4.75 µL DNase I (2 U/uL), 0.5 µL $CaCl_2$

(100 mM, 0.2-µM filtered), and 5 µL initial exposure samples. The autolytic enhancing step consisted of 75 µL NF-H_2O, 4.75 µL $NaHCO_3$ (100 mM, 0.2-µM filtered), 10 µL Tris pH 8.5 (500 mM), 4.75 µL DNase I (2 U/uL), 0.5 µL $CaCl_2$ (100 mM), and 5 µL of the sample exposed to antibiotic.

All surfactant-enhancing steps were performed in 50 µL volumes with 25 of the 50 µL consisting of initial exposure samples. In the TNP enhancement step, the remaining 25 µL consisted of 1.25 µL DNase I (2 U/uL), 1.25 µL $NaHCO_3$ (100 mM), 20 µL MHB, and 2.5 µL TNP (100 mM). In the CHAPS enhancement step, the remaining 25 µL consisted of 1.25 µL DNase I (2 U/uL), 1.25 µL $NaHCO_3$ (100 mM), 20 µL MHB, and 2.5 µL CHAPS (200 mM). In the SDS and BAC enhancement steps, the remaining 25 µL consisted of 1.25 µL DNase I (2 U/uL), 1.25 µL $NaHCO_3$ (100 mM), 17.5 µL MHB, and either 5 µL SDS (1% w/v) or BAC (1% w/v) respectively.

Nuclease-accessibility AST validation. Working cultures were prepared, exposed to ABX, and enhancing steps performed as described for the CHAPS enhancement step in the "enhancer selection" section above. Extraction was performed as described above. Treated samples in the initial exposure step had a final concentration of 1.0 µg/mL PEN, CFM, or CRO. Samples were excluded if the percent lysis (equation 2) due to CHAPS was > 75%. Three to ten biological replicates were performed for each isolate-antibiotic combination. Biological replicates included separate antibiotic exposure, control exposure, and no-enhancer controls.

Timed sum-of-steps. Working cultures of *Ng* isolates used in Fig. 4.4 were prepared as described in "*Ng* culture preparation" and 1.5 mL of the cultures were pelleted at 2500 g for 2.5 min and resuspended in 150 µL normal human urine (Lee Biosciences) pre-warmed to 37 °C. Initial exposure was performed by incubating 100 µL control and treated samples at 37 °C in PCR tube strips on a BioRad C1000 Thermal Cycler. Treated samples consisted of 65 µL MHB, 5 µL $NaHCO_3$ (100 mM), 5 µL DNase I (2 U/µL), 5 µL PEN (20 µg/mL), and 20 µL *Ng* isolate suspension in urine. NF-H_2O was used in place of PEN in control

samples. A CHAPS enhancing step was performed as described above. After the enhancement step, a 20 µL aliquot from each sample was extracted by diluting 5X in QuickExtract DNA Extraction Solution (Lucigen) and heated for 1 min at 65 °C followed by 1 min at 98 °C on a BioRad C1000 Thermal Cycler. All sample handling following ABX exposure was performed using a multichannel pipette. Amplification was then performed using qPCR, ddPCR, or dLAMP. Extractions were diluted 2.5X in NF-H_2O before use in dLAMP.

Osmolarity measurements. Osmolarity measurements were performed on a Model 3320 Osmometer (Advanced Instruments Inc., Norwood, MA, USA). The instrument was calibrated with reference standards (Advanced Instruments) prior to experiments. Samples identical to the antibiotic-exposure condition (i.e. media, nuclease, etc.) and samples identical to the osmotic enhancing condition were prepared and measured. The volume that would normally be comprised of Ng culture was replaced with media.

Statistical analysis. *P*-values for Fig. 4.2 were calculated using GraphPad Prism 8.0 software from an unpaired, two-tailed t-test comparing the averages of the three replicates of each susceptible sample to each resistant sample. A significance value of 0.02 was used for statistical significance. ROC plots used for setting susceptibility thresholds in Fig. 4.4 were created using GraphPad Prism 8.0 software. Sensitivity was defined as the proportion of gold-standard susceptible samples correctly identified as susceptible by the nuc-aAST. Specificity was defined as the proportion of gold-standard resistant samples correctly identified as resistant by the nuc-aAST. Statistical analyses for Fig. 4.5, (dLAMP measurements) were performed as published previously(*46, 90*). As in our previous publication(*46*), the control and treated concentrations are compared as a ratio for statistical analysis.

$$(6)\ Concentration\ Ratio = \frac{\lambda_{control}}{\lambda_{treated}}$$

This concentration ratio is transformed into a percentage change for visualization purposes, but the ratio is assessed for statistical significance. Poisson statistics were used to calculate the confidence interval of the NA concentration for each measurement(*90*). The error in the concentration ratio, a term used in the calculation of percentage accessibility, is calculated with standard-error propagation methods:

$$(7)\ \sigma_{ratio} = \sqrt{\left(\frac{\sigma_{\lambda_2}}{\lambda_1}\right)^2 + \left(\frac{\lambda_2 \cdot \sigma_{\lambda_1}}{\lambda_1^2}\right)^2}$$

A one-tailed Z-test, assuming a normal distribution, is used to calculate *p*-values for digital NA concentrations. A threshold value for significance is set as a ratio of 1.22, corresponding to a percentage accessibility of 18%.

$$(8)\ Z = \frac{\ln(\lambda_{control}) - \ln(1.22\ \lambda_{treated})}{\sqrt{\sigma^2 \ln(\lambda_{control}) + \sigma^2 \ln(\lambda_{treated})}}$$

A significance value of 0.05 was used for statistical significance. The *p*-values to determine significance in dLAMP experiments were computed using Microsoft Excel's standard normal cumulative distribution function and Z-value.

REFERENCES

1. CDC, Sexually Transmitted Disease Surveillance. (2017) https://www.cdc.gov/std/stats17/default.htm

2. L. Newman, J. Rowley, S. Vander Hoorn, N. S. Wijesooriya, M. Unemo, N. Low, G. Stevens, S. Gottlieb, J. Kiarie, M. Temmerman, Global estimates of the prevalence and incidence of four curable sexually transmitted infections in 2012 based on systematic review and global reporting. *PLoS One* **10**, e0143304 (2015).

3. S. J. Quillin, H. S. Seifert, Neisseria gonorrhoeae host adaptation and pathogenesis. *Nat. Rev. Microbiol.* **16**, 226-240 (2018).

4. H. W. Chesson, R. D. Kirkcaldy, T. L. Gift, K. Owusu-Edusei, Jr., H. S. Weinstock, An illustration of the potential health and economic benefits of combating antibiotic-resistant gonorrhea. *Sex. Transm. Dis.* **45**, 250-253 (2018).

5. CDC, Sexually Transmitted Diseases Treatment Guidelines: Morbidity and Mortality Weekly Report. (2015) https://www.cdc.gov/std/tg2015/tg-2015-print.pdf

6. WHO, WHO Guidelines for the treatment of Neisseria gonorrhoeae. (2016) https://www.who.int/reproductivehealth/publications/rtis/gonorrhoea-treatment-guidelines/en/

7. L. M. Newman, J. S. Moran, K. A. Workowski, Update on the management of gonorrhea in adults in the United States. *Clin. Infect. Dis.* **44 Suppl 3**, S84-101 (2007).

8. WHO, Antimicrobrial Resistance in Neisseria gonorrhoeae. (2001) https://www.who.int/csr/resources/publications/drugresist/Neisseria_gonorrhoeae.pdf

9. H. Fifer, U. Natarajan, L. Jones, S. Alexander, G. Hughes, D. Golparian, M. Unemo, Failure of Dual Antimicrobial Therapy in Treatment of Gonorrhea. *N. Engl. J. Med.* **374**, 2504-2506 (2016).

10. D. M. Whiley, A. Jennison, J. Pearson, M. M. Lahra, Genetic characterisation of Neisseria gonorrhoeae resistant to both ceftriaxone and azithromycin. *Lancet Infect. Dis.* **18**, 717-718 (2018).

11. D. W. Eyre, N. D. Sanderson, E. Lord, N. Regisford-Reimmer, K. Chau, L. Barker, M. Morgan, R. Newnham, D. Golparian, M. Unemo, D. W. Crook, T. E. Peto, G. Hughes, M.

J. Cole, H. Fifer, A. Edwards, M. I. Andersson, Gonorrhoea treatment failure caused by a Neisseria gonorrhoeae strain with combined ceftriaxone and high-level azithromycin resistance, England, February 2018. *Euro Surveill.* **23**, (2018).

12. CDC, Antibiotic Resistance Threats in the United States. (2013) https://www.cdc.gov/drugresistance/pdf/ar-threats-2013-508.pdf

13. WHO, Global Priority List of Antibiotic-resistant Bacteria to Guide Research, Discovery, and Development of New Antibiotics. (2017) https://www.who.int/medicines/publications/global-priority-list-antibiotic-resistant-bacteria/en/

14. G. A. Bolan, P. F. Sparling, J. N. Wasserheit, The emerging threat of untreatable gonococcal infection. *N. Engl. J. Med.* **366**, 485-487 (2012).

15. T. Wi, M. M. Lahra, F. Ndowa, M. Bala, J. R. Dillon, P. Ramon-Pardo, S. R. Eremin, G. Bolan, M. Unemo, Antimicrobial resistance in Neisseria gonorrhoeae: Global surveillance and a call for international collaborative action. *PLoS Med.* **14**, e1002344 (2017).

16. WHO, Global Action Plan to Control the Spread of and Impact of Antimicrobial Resistance in Neisseria gonorrhoeae. (2012) https://www.who.int/reproductivehealth/publications/rtis/9789241503501/en/

17. E. J. Weston, T. Wi, J. Papp, Strengthening Global Surveillance for Antimicrobial Drug-Resistant Neisseria gonorrhoeae through the Enhanced Gonococcal Antimicrobial Surveillance Program. *Emerg. Infect. Dis.* **23**, S47-52 (2017).

18. F. Rahimi, N. Goire, R. Guy, J. M. Kaldor, J. Ward, M. D. Nissen, T. P. Sloots, D. M. Whiley, Direct urine polymerase chain reaction for chlamydia and gonorrhoea: a simple means of bringing high-throughput rapid testing to remote settings? *Sex Health* **10**, 299-304 (2013).

19. S. Cho, T. S. Park, T. G. Nahapetian, J. Y. Yoon, Smartphone-based, sensitive microPAD detection of urinary tract infection and gonorrhea. *Biosens. Bioelectron.* **74**, 601-611 (2015).

20. J. S. Gootenberg, O. O. Abudayyeh, M. J. Kellner, J. Joung, J. J. Collins, F. Zhang, Multiplexed and portable nucleic acid detection platform with Cas13, Cas12a, and Csm6. *Science* **360**, 439-444 (2018).

21. binx, io system for clinical point of care. (2018) https://mybinxhealth.com/clinical-poc/

22. C. A. Gaydos, B. Van Der Pol, M. Jett-Goheen, M. Barnes, N. Quinn, C. Clark, G. E. Daniel, P. B. Dixon, E. W. Hook, 3rd, C. N. S. Group, Performance of the Cepheid CT/NG Xpert Rapid PCR Test for Detection of Chlamydia trachomatis and Neisseria gonorrhoeae. *J. Clin. Microbiol.* **51**, 1666-1672 (2013).

23. L. T. Allan-Blitz, X. Wang, J. D. Klausner, Wild-Type Gyrase A Genotype of Neisseria gonorrhoeae Predicts In Vitro Susceptibility to Ciprofloxacin: A Systematic Review of the Literature and Meta-Analysis. *Sex. Transm. Dis.* **44**, 261-265 (2017).

24. Z. Li, S. Yokoi, Y. Kawamura, S. Maeda, T. Ezaki, T. Deguchi, Rapid detection of quinolone resistance-associated gyrA mutations in Neisseria gonorrhoeae with a LightCycler. *J. Infect. Chemother.* **8**, 145-150 (2002).

25. S. Balashov, E. Mordechai, M. E. Adelson, S. E. Gygax, Multiplex bead suspension array for screening Neisseria gonorrhoeae antibiotic resistance genetic determinants in noncultured clinical samples. *J. Mol. Diagn.* **15**, 116-129 (2013).

26. V. Dona, J. H. Smid, S. Kasraian, D. Egli-Gany, F. Dost, F. Imeri, M. Unemo, N. Low, A. Endimiani, Mismatch Amplification Mutation Assay-Based Real-Time PCR for Rapid Detection of Neisseria gonorrhoeae and Antimicrobial Resistance Determinants in Clinical Specimens. *J. Clin. Microbiol.* **56**, (2018).

27. C. Buckley, E. Trembizki, B. Donovan, M. Chen, K. Freeman, R. Guy, M. M. Lahra, R. L. Kundu, D. G. Regan, H. V. Smith, D. M. Whiley, I. Gonorrhoea Resistance Assessment by Nucleic Acid Detection Study, Real-time PCR detection of Neisseria gonorrhoeae susceptibility to penicillin. *J. Antimicrob. Chemother.* **71**, 3090-3095 (2016).

28. L. K. Wong, P. Hemarajata, O. O. Soge, R. M. Humphries, J. D. Klausner, Real-Time PCR Targeting the penA Mosaic XXXIV Type for Prediction of Extended-Spectrum-Cephalosporin Susceptibility in Clinical Neisseria gonorrhoeae Isolates. *Antimicrob. Agents Chemother.* **61**, (2017).

29. J. Davies, D. Davies, Origins and evolution of antibiotic resistance. *Microbiol. Mol. Biol. Rev.* **74**, 417-433 (2010).

30. CDC, Agar Dilution Antimicrobial Susceptibility Testing. (2013) https://www.cdc.gov/std/gonorrhea/lab/agar.htm

31. S. Foerster, V. Desilvestro, L. J. Hathaway, C. L. Althaus, M. Unemo, A new rapid resazurin-based microdilution assay for antimicrobial susceptibility testing of Neisseria gonorrhoeae. *J. Antimicrob. Chemother*. **72**, 1961-1968 (2017).

32. V. Singh, M. Bala, M. Kakran, V. Ramesh, Comparative assessment of CDS, CLSI disc diffusion and Etest techniques for antimicrobial susceptibility testing of Neisseria gonorrhoeae: a 6-year study. *BMJ Open* **2**, e000969 (2012).

33. M. J. Siedner, M. Pandori, L. Castro, P. Barry, W. L. Whittington, S. Liska, J. D. Klausner, Real-time PCR assay for detection of quinolone-resistant Neisseria gonorrhoeae in urine samples. *J. Clin. Microbiol.* **45**, 1250-1254 (2007).

34. S. T. Sadiq, F. Mazzaferri, M. Unemo, Rapid accurate point-of-care tests combining diagnostics and antimicrobial resistance prediction for Neisseria gonorrhoeae and Mycoplasma genitalium. *Sex. Transm. Infect.* **93**, S65-S68 (2017).

35. S. M. Fingerhuth, N. Low, S. Bonhoeffer, C. L. Althaus, Detection of antibiotic resistance is essential for gonorrhoea point-of-care testing: a mathematical modelling study. *BMC Med.* **15**, 142 (2017).

36. A. R. Tuite, T. L. Gift, H. W. Chesson, K. Hsu, J. A. Salomon, Y. H. Grad, Impact of Rapid Susceptibility Testing and Antibiotic Selection Strategy on the Emergence and Spread of Antibiotic Resistance in Gonorrhea. *J. Infect. Dis.* **216**, 1141-1149 (2017).

37. K. M. Turner, H. Christensen, E. J. Adams, D. McAdams, H. Fifer, A. McDonnell, N. Woodford, Analysis of the potential for point-of-care test to enable individualised treatment of infections caused by antimicrobial-resistant and susceptible strains of Neisseria gonorrhoeae: a modelling study. *BMJ Open* **7**, e015447 (2017).

38. R. D. Kirkcaldy, A. Harvey, J. R. Papp, C. Del Rio, O. O. Soge, K. K. Holmes, E. W. Hook, 3rd, G. Kubin, S. Riedel, J. Zenilman, K. Pettus, T. Sanders, S. Sharpe, E. Torrone, Neisseria gonorrhoeae Antimicrobial Susceptibility Surveillance - The Gonococcal Isolate

Surveillance Project, 27 Sites, United States, 2014. *MMWR Surveill. Summ.* **65**, 1-19 (2016).

39. R. D. Kirkcaldy, M. G. Bartoces, O. O. Soge, S. Riedel, G. Kubin, C. Del Rio, J. R. Papp, E. W. Hook, 3rd, L. A. Hicks, Antimicrobial Drug Prescription and Neisseria gonorrhoeae Susceptibility, United States, 2005-2013. *Emerg. Infect. Dis.* **23**, 1657-1663 (2017).

40. V. G. Allen, L. Mitterni, C. Seah, A. Rebbapragada, I. E. Martin, C. Lee, H. Siebert, L. Towns, R. G. Melano, D. E. Low, Neisseria gonorrhoeae treatment failure and susceptibility to cefixime in Toronto, Canada. *JAMA* **309**, 163-170 (2013).

41. A. R. Katz, A. Y. Komeya, R. D. Kirkcaldy, A. C. Whelen, O. O. Soge, J. R. Papp, E. N. Kersh, G. M. Wasserman, N. P. O'Connor, P. S. O'Brien, D. T. Sato, E. V. Maningas, G. Y. Kunimoto, J. E. Tomas, Cluster of Neisseria gonorrhoeae Isolates With High-level Azithromycin Resistance and Decreased Ceftriaxone Susceptibility, Hawaii, 2016. *Clin. Infect. Dis.* **65**, 918-923 (2017).

42. J. R. Papp, A. J. Abrams, E. Nash, A. R. Katz, R. D. Kirkcaldy, N. P. O'Connor, P. S. O'Brien, D. H. Harauchi, E. V. Maningas, O. O. Soge, E. N. Kersh, A. Komeya, J. E. Tomas, G. M. Wasserman, G. Y. Kunimoto, D. L. Trees, A. C. Whelen, Azithromycin Resistance and Decreased Ceftriaxone Susceptibility in Neisseria gonorrhoeae, Hawaii, USA. *Emerg. Infect. Dis.* **23**, 830-832 (2017).

43. L. J. Piddock, Assess drug-resistance phenotypes, not just genotypes. *Nat Microbiol* **1**, 16120 (2016).

44. J. M. Hicks, R. Haeckel, C. P. Price, K. Lewandrowski, A. H. B. Wu, Recommendations and opinions for the use of point-of-care testing for hospitals and primary care: summary of a 1999 symposium. *Clin. Chim. Acta* **303**, 1-17 (2001).

45. H. D. Marston, D. M. Dixon, J. M. Knisely, T. N. Palmore, A. S. Fauci, Antimicrobial Resistance. *JAMA* **316**, 1193-1204 (2016).

46. N. G. Schoepp, T. S. Schlappi, M. S. Curtis, S. S. Butkovich, S. Miller, R. M. Humphries, R. F. Ismagilov, Rapid pathogen-specific phenotypic antibiotic susceptibility testing using digital LAMP quantification in clinical samples. *Sci. Transl. Med.* **9**, (2017).

47. A. Mezger, E. Gullberg, J. Goransson, A. Zorzet, D. Herthnek, E. Tano, M. Nilsson, D. I. Andersson, A general method for rapid determination of antibiotic susceptibility and species in bacterial infections. *J. Clin. Microbiol.* **53**, 425-432 (2015).

48. K. E. Mach, R. Mohan, E. J. Baron, M. C. Shih, V. Gau, P. K. Wong, J. C. Liao, A biosensor platform for rapid antimicrobial susceptibility testing directly from clinical samples. *J. Urol.* **185**, 148-153 (2011).

49. C. Halford, R. Gonzalez, S. Campuzano, B. Hu, J. T. Babbitt, J. Liu, J. Wang, B. M. Churchill, D. A. Haake, Rapid antimicrobial susceptibility testing by sensitive detection of precursor rRNA using a novel electrochemical biosensing platform. *Antimicrob. Agents Chemother.* **57**, 936-943 (2013).

50. N. G. Schoepp, E. M. Khorosheva, T. S. Schlappi, M. S. Curtis, R. M. Humphries, J. A. Hindler, R. F. Ismagilov, Digital Quantification of DNA Replication and Chromosome Segregation Enables Determination of Antimicrobial Susceptibility after only 15 Minutes of Antibiotic Exposure. *Angew. Chem. Int. Ed. Engl.* **55**, 9557-9561 (2016).

51. T. Khazaei, J. T. Barlow, N. G. Schoepp, R. F. Ismagilov, RNA markers enable phenotypic test of antibiotic susceptibility in Neisseria gonorrhoeae after 10 minutes of ciprofloxacin exposure. *Sci. Rep.* **8**, 11606 (2018).

52. L. Chen, D. J. Shin, S. Zheng, J. H. Melendez, C. A. Gaydos, T. H. Wang, Direct-qPCR Assay for Coupled Identification and Antimicrobial Susceptibility Testing of Neisseria gonorrhoeae. *ACS Infect. Dis.* **4**, 1377-1384 (2018).

53. M. Unemo, W. M. Shafer, Antimicrobial resistance in Neisseria gonorrhoeae in the 21st century: past, evolution, and future. *Clin. Microbiol. Rev.* **27**, 587-613 (2014).

54. EUCAST, European Committee on Antimicrobial Susceptibility Testing: Breakpoint Tables for Interpretation of MICs and Zone Diameters (ver. 7.1). (2017) http://www.eucast.org/clinical_breakpoints/

55. M. A. Kohanski, D. J. Dwyer, J. J. Collins, How antibiotics kill bacteria: from targets to networks. *Nat. Rev. Microbiol.* **8**, 423-435 (2010).

56. E. R. Rojas, G. Billings, P. D. Odermatt, G. K. Auer, L. Zhu, A. Miguel, F. Chang, D. B. Weibel, J. A. Theriot, K. C. Huang, The outer membrane is an essential load-bearing element in Gram-negative bacteria. *Nature* **559**, 617-621 (2018).

57. W. S. Wegener, B. H. Hebeler, S. A. Morse, Cell envelope of Neisseria gonorrhoeae: penicillin enhancement of peptidoglycan hydrolysis. *Infect. Immun.* **18**, 717-725 (1977).

58. J. P. Dillard, H. S. Seifert, A peptidoglycan hydrolase similar to bacteriophage endolysins acts as an autolysin in Neisseria gonorrhoeae. *Mol. Microbiol.* **25**, 893-901 (1997).

59. H. I. Zgurskaya, C. A. Lopez, S. Gnanakaran, Permeability Barrier of Gram-Negative Cell Envelopes and Approaches To Bypass It. *ACS Infect Dis* **1**, 512-522 (2015).

60. T. J. Silhavy, D. Kahne, S. Walker, The bacterial cell envelope. *Cold Spring Harb. Perspect. Biol.* **2**, a000414 (2010).

61. P. Demchick, A. L. Koch, The permeability of the wall fabric of Escherichia coli and Bacillus subtilis. *J. Bacteriol.* **178**, 768-773 (1996).

62. A. J. Dijkstra, W. Keck, Peptidoglycan as a barrier to transenvelope transport. *J. Bacteriol.* **178**, 5555-5562 (1996).

63. D. Pink, J. Moeller, B. Quinn, M. Jericho, T. Beveridge, On the architecture of the gram-negative bacterial murein sacculus. *J. Bacteriol.* **182**, 5925-5930 (2000).

64. S. T. Harrison, Bacterial cell disruption: a key unit operation in the recovery of intracellular products. *Biotechnol. Adv.* **9**, 217-240 (1991).

65. N. Vazquez-Laslop, H. Lee, R. Hu, A. A. Neyfakh, Molecular sieve mechanism of selective release of cytoplasmic proteins by osmotically shocked Escherichia coli. *J. Bacteriol.* **183**, 2399-2404 (2001).

66. G. van den Bogaart, N. Hermans, V. Krasnikov, B. Poolman, Protein mobility and diffusive barriers in Escherichia coli: consequences of osmotic stress. *Mol. Microbiol.* **64**, 858-871 (2007).

67. B. H. Hebeler, F. E. Young, Autolysis of Neisseria gonorrhoeae. *J. Bacteriol.* **122**, 385-392 (1975).

68. W. S. Wegener, B. H. Hebeler, S. A. Morse, Cell envelope of Neisseria gonorrhoeae: relationship between autolysis in buffer and the hydrolysis of peptidoglycan. *Infect. Immun.* **18**, 210-219 (1977).

69. H. Felix, Permeabilized cells. *Anal. Biochem.* **120**, 211-234 (1982).

70. H. Nikaido, Molecular basis of bacterial outer membrane permeability revisited. *Microbiol. Mol. Biol. Rev.* **67**, 593-656 (2003).

71. S. Zhao, M. Duncan, J. Tomberg, C. Davies, M. Unemo, R. A. Nicholas, Genetics of chromosomally mediated intermediate resistance to ceftriaxone and cefixime in Neisseria gonorrhoeae. *Antimicrob. Agents Chemother.* **53**, 3744-3751 (2009).

72. S. Foerster, M. Unemo, L. J. Hathaway, N. Low, C. L. Althaus, Time-kill curve analysis and pharmacodynamic modelling for in vitro evaluation of antimicrobials against Neisseria gonorrhoeae. *BMC Microbiol.* **16**, 216 (2016).

73. K. H. Zou, A. J. O'Malley, L. Mauri, Receiver-operating characteristic analysis for evaluating diagnostic tests and predictive models. *Circulation* **115**, 654-657 (2007).

74. Y. H. Grad, S. R. Harris, R. D. Kirkcaldy, A. G. Green, D. S. Marks, S. D. Bentley, D. Trees, M. Lipsitch, Genomic Epidemiology of Gonococcal Resistance to Extended-Spectrum Cephalosporins, Macrolides, and Fluoroquinolones in the United States, 2000-2013. *J. Infect. Dis.* **214**, 1579-1587 (2016).

75. C. B. Wadsworth, M. R. A. Sater, R. P. Bhattacharyya, Y. H. Grad, Impact of population structure in the design of RNA-based diagnostics for antibiotic resistance in Neisseria gonorrhoeae. *bioRxiv*, (2019).

76. R. A. Gianecini, D. Golparian, S. Zittermann, A. Litvik, S. Gonzalez, C. Oviedo, R. G. Melano, M. Unemo, P. Galarza, G. Gonococcal Antimicrobial Susceptibility Surveillance Programme-Argentina Working, Genome-based epidemiology and antimicrobial resistance determinants of Neisseria gonorrhoeae isolates with decreased susceptibility and resistance to extended-spectrum cephalosporins in Argentina in 2011-16. *J. Antimicrob. Chemother.*, (2019).

77. J. C. Rolando, E. Jue, N. G. Schoepp, R. F. Ismagilov, Real-Time, Digital LAMP with Commercial Microfluidic Chips Reveals the Interplay of Efficiency, Speed, and Background Amplification as a Function of Reaction Temperature and Time. *Anal. Chem.* **91**, 1034–1042 (2018).

78. D. A. Selck, R. F. Ismagilov, Instrument for Real-Time Digital Nucleic Acid Amplification on Custom Microfluidic Devices. *PLoS One* **11**, e0163060 (2016).

79. S. G. Lee, H. Lee, S. H. Jeong, D. Yong, G. T. Chung, Y. S. Lee, Y. Chong, K. Lee, Various penA mutations together with mtrR, porB and ponA mutations in Neisseria gonorrhoeae isolates with reduced susceptibility to cefixime or ceftriaxone. *J. Antimicrob. Chemother*. **65**, 669-675 (2010).

80. FDA, Evaluation of Automatic Class III Designation for T2Candida Panel and T2Dx Instrument. (2014).

81. L. Li, W. Du, R. Ismagilov, User-loaded SlipChip for equipment-free multiplexed nanoliter-scale experiments. *J. Am. Chem. Soc.* **132**, 106-111 (2010).

82. F. Shen, W. Du, E. K. Davydova, M. A. Karymov, J. Pandey, R. F. Ismagilov, Nanoliter multiplex PCR arrays on a SlipChip. *Anal. Chem.* **82**, 4606-4612 (2010).

83. F. Shen, B. Sun, J. E. Kreutz, E. K. Davydova, W. Du, P. L. Reddy, L. J. Joseph, R. F. Ismagilov, Multiplexed quantification of nucleic acids with large dynamic range using multivolume digital RT-PCR on a rotational SlipChip tested with HIV and hepatitis C viral load. *J. Am. Chem. Soc.* **133**, 17705-17712 (2011).

84. N. G. Schoepp, E. J. Liaw, E. S. Savela, R. F. Ismagilov, Differential Accessibility to Polymerase During Isothermal Nucleic Acid Amplification Enables 30-Minute Phenotypic Beta-lactam Antibiotic Susceptibility Testing of Carbapenem-resistant Enterobacteriaceae (CRE). *In Submission*, (2019).

85. S. Banoo, D. Bell, P. Bossuyt, A. Herring, D. Mabey, F. Poole, P. G. Smith, N. Sriram, C. Wongsrichanalai, R. Linke, R. O'Brien, M. Perkins, J. Cunningham, P. Matsoso, C. M. Nathanson, P. Olliaro, R. W. Peeling, A. Ramsay, Evaluation of diagnostic tests for infectious diseases: general principles. *Nat. Rev. Microbiol.* **4**, S21-31 (2006).

86. CLSI, M100-S25 Performance Standards for Antimicrobial Susceptibility Testing. *CLSI* **35**, (2015).

87. J. J. Wade, M. A. Graver, A fully defined, clear and protein-free liquid medium permitting dense growth of Neisseria gonorrhoeae from very low inocula. *FEMS Microbiol. Lett.* **273**, 35-37 (2007).

88. Sigma, Buffer Reference Center. https://www.sigmaaldrich.com/life-science/core-bioreagents/biological-buffers/learning-center/buffer-reference-center.html

89. S. R. Lee, J. M. Chung, Y. G. Kim, Rapid one step detection of pathogenic bacteria in urine with sexually transmitted disease (STD) and prostatitis patient by multiplex PCR assay (mPCR). *J. Microbiol.* **45**, 453-459 (2007).
90. J. E. Kreutz, T. Munson, T. Huynh, F. Shen, W. Du, R. F. Ismagilov, Theoretical design and analysis of multivolume digital assays with wide dynamic range validated experimentally with microfluidic digital PCR. *Anal. Chem.* **83**, 8158-8168 (2011).

ACKNOWLEDGEMENTS

We thank Dr. Jeffrey Klausner at AIDS Healthcare Foundation for invaluable discussions and insight. We thank Peera Hemarajata at the UCLA Clinical Microbiology Laboratory for providing isolates and for discussion of gold-standard practices. We also thank Matthew M. Cooper for assisting in the collection of data contributing to Fig. 4.4, and Natasha Shelby for help with writing and editing this manuscript. **Funding**: This work was funded in part by the Department of Health and Human Services (HHS) Office of the Assistant Secretary for Preparedness and Response (ASPR) and the Wellcome Trust under the CARB-X program (federal award number IDSEP160030-02); the content is solely the responsibility of the authors and does not necessarily represent the official views of the Department of HHS Office of the ASPR. This CARB-X project is a collaboration between Talis Biomedical Corp. and Caltech. This work was also supported by a Burroughs Wellcome Fund Innovation in Regulatory Science Award, an NIH National Research Service Award (NRSA) [5T32GM07616NSF] (to N.G.S.), and a grant from the Joseph J. Jacobs Institute for Molecular Engineering for Medicine. **Author contributions**: N.G.S. guided initial testing of enhancers and developed two-step nuc-aAST workflow; selected and performed initial testing of surfactant enhancers; optimized sample handling during ABX exposure; performed and analyzed no-enhancer time-course experiments (Fig. 4.2); designed LAMP primers and contributed to the optimization of LAMP conditions for dLAMP experiments (Fig. 4.5); wrote the manuscript and created figures. E.S.S. performed initial enhancer testing experiments;. selected and performed initial testing of osmotic, autolysis, and surfactant enhancers; optimized sample handling prior to ABX exposure;

performed and analyzed enhancer testing and nuc-aAST experiments (Figs. 3, 4, 5), and assisted in performing dLAMP experiments (Fig. 4.5); performed data analysis, selected the readout metric of percentage accessibility, and selected optimal conditions for nuc-aAST; contributed to writing the manuscript and figure design and wrote the methods section. N.G.S., E.S.S., and R.F.I. conceived of the project and discussed design and interpretation of experiments. J.C.R. optimized digital LAMP conditions, and performed and analyzed all digital LAMP experiments for Fig. 4.5. O.O.S. provided isolates and guided discussion on gold-standard AST and current treatment practices for *Ng*, and performed agar-dilution AST. R.F.I. supervised and guided the project, and helped compose the manuscript. All authors read and edited the manuscript. **Competing interests**: The technology described in this publication is the subject of a patent application filed by Caltech. R.F.I. has a financial interest in Talis Biomedical Corp. Caltech is a sub-awardee to Talis Biomedical Corp. on the CARB-X grant that partially funded this work. **Data and materials availability**: The authors declare that the data supporting these findings are available within the article. Any raw data for the reported results is available from the corresponding author upon request.

Chapter V

HIGH-MOLECULAR-WEIGHT POLYMERS FROM DIETARY FIBER DRIVE AGGREGATION OF PARTICULATES IN THE MURINE SMALL INTESTINE

A. Preska Steinberg, S. S. Datta, T. Naragon, J. C. Rolando, S. R. Bogatyrev, R. F. Ismagilov. 2019. "High-molecular-weight polymers from dietary fiber drive aggregation of particulates in the murine small intestine." eLife. 8:e40387. DOI: 10.7554/eLife.40387

ABSTRACT

The lumen of the small intestine (SI) is filled with particulates: microbes, therapeutic particles, and food granules. The structure of this particulate suspension could impact uptake of drugs and nutrients and the function of microorganisms; however, little is understood about how this suspension is re-structured as it transits the gut. Here, we demonstrate that particles spontaneously aggregate in SI luminal fluid ex vivo. We find that mucins and immunoglobulins are not required for aggregation. Instead, aggregation can be controlled using polymers from dietary fiber in a manner that is qualitatively consistent with polymer-induced depletion interactions, which do not require specific chemical interactions. Furthermore, we find that aggregation is tunable; by feeding mice dietary fibers of different molecular weights, we can control aggregation in SI luminal fluid. This work suggests that the molecular weight and concentration of dietary polymers play an underappreciated role in shaping the physicochemical environment of the gut.

INTRODUCTION

The small intestine (SI) contains numerous types of solid particles. Some of these particles include microbes, viruses, cell debris, particles for drug delivery, and food granules (1–5). Little is understood about the state of these particles in the small intestine; do these particles exist as a disperse solution or as aggregates? An understanding of how particulate matter is structured as it moves through the SI would contribute to fundamental knowledge on a

host of topics, such as how microbes, including probiotics and pathogens, function in the SI (6–10). Knowledge of how particle suspensions change during transit would also provide insight into how the uptake of drugs and nutrients are affected by the physiochemical properties of the SI environment (3,4). It would also give us better comprehension of how the SI acts to clear potential invaders and harmful debris (2,11).

Polymers abound in the gut in the form of secretions (e.g. mucins and immunoglobulins) and dietary polymers (e.g. dietary fibers and synthetic polymers). It is well known that host-secreted polymers can cause aggregation of particles via chemical interactions; for example, mucins (12–16), immunoglobulins (17–25), and proteins (26) can cause bacteria to aggregate via an agglutination mechanism. However, non-adsorbing polymers can also cause aggregation via purely physical interactions that are dependent on the physical properties of the polymers, such as their molecular weight (MW) and concentration (27–33). Here, we investigate whether these physical interactions play a role in structuring particles in the SI. For this work, we study the interactions between polystyrene particles densely coated with polyethylene glycol (PEG) and the luminal contents of the SI. It has been demonstrated previously that PEG-coated particles have little or no chemical interactions with biopolymers (34,35), so using PEG-coated particles allows us to isolate and investigate only the interactions dominated by physical effects.

RESULTS

PEG-coated particles aggregate in fluid from the murine small intestine

It has been observed that both bacteria (19–21,23,25,26) and particles (3,36–38) aggregate in the gut. Experiments have been performed in which mice are orally co-administered carboxylate-coated nanoparticles, which are mucoadhesive, and PEG-coated nanoparticles, which are mucus-penetrating (3). The carboxylate-coated particles formed large aggregates in the center of the gut lumen. In contrast, PEG-coated particles were sometimes found co-localized with carboxylate-coated particles and also penetrated mucus, distributing across the underlying epithelium of the SI as aggregates and single particles.

To evaluate the distribution of particulate suspensions in the SI, we suspended 1-µm-diameter fluorescent PEG-coated particles (see *Materials and Methods* for synthesis) in buffers isotonic to the SI and orally administered them to mice. We chose 1 µm-diameter particles because of their similarity in size to bacteria. We collected luminal contents after 3 h and confirmed using confocal fluorescence and reflectance microscopy that these particles aggregated with each other and co-aggregated with what appeared to be digesta (**Figure 5.1*C* and *D***; *Materials and Methods*). On separate mice, fluorescent scanning was used to verify that particles do transit the SI after 3 h (**Figure 5.1*A* and *B***; *Materials and Methods*).

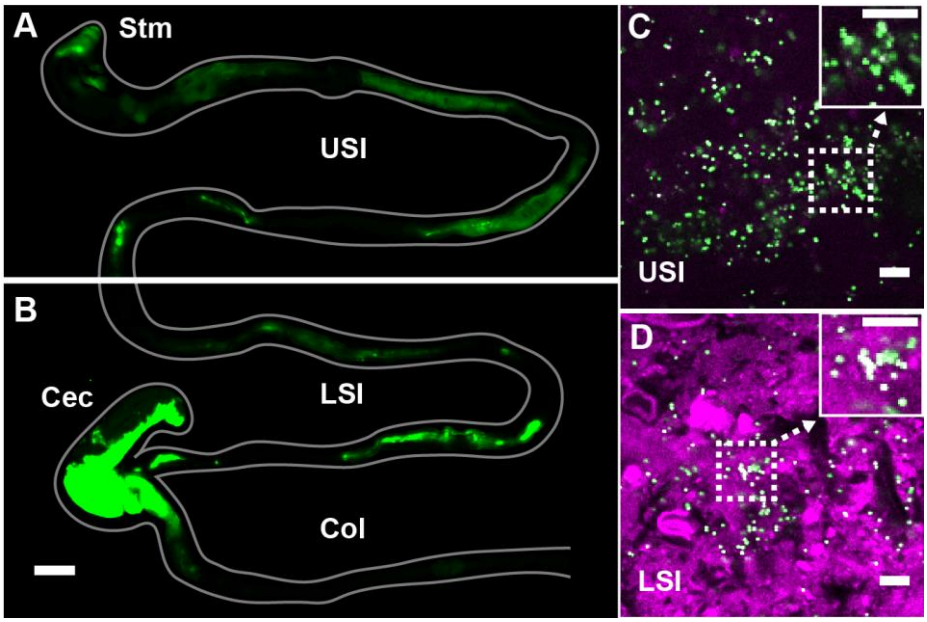

Figure 5.1: PEG-coated particles aggregate in the murine small intestine (SI). (A and B) Fluorescent scanner image of gastrointestinal tract (GIT) from a mouse orally administered a suspension of 1-µm diameter PEG-coated particles (green). Scale bar is 0.5 cm. (see Figure 2-S1 for image processing steps and how contours of gut were outlined). (C and D) Confocal micrographs of luminal contents from the upper (C) and lower (D) SI of a mouse orally gavaged with PEG-coated particles (green) showing scattering from luminal contents (purple). Scale bars are 10 µm. Stm = Stomach; USI = upper SI; LSI = lower SI; Col = colon.

Given the rich complexity of the SI, wherein particles co-aggregate with digesta and bacteria, and are subjected to the mechanical forces of digestion and transit (39), and other phenomena, we developed an *ex vivo* assay to characterize the structure of particles in luminal fluid from the SI of mice. As a simple starting point, we sought to understand

interactions among particles of known chemistry and the luminal fluid of the SI. To minimize chemical interactions with the biopolymers of the SI, we again chose PEG-coated polystyrene particles. PEG coatings have been shown to minimize biochemical interactions between polystyrene particles and biopolymers in a variety of contexts (34,35), and thus PEG-coated particles are commonly used in drug delivery (3,38,40).

To create PEG-coated polystyrene particles for the *ex vivo* experiments, we took 1-μm-diameter carboxylate-coated polystyrene particles and conjugated PEG to the surface (*Materials and Methods*). We used NMR to verify that PEG coated the surface of the particles (see *Materials and Methods* and Table 5.S8). We found that by coating with PEG 5 kDa and then coating again with PEG 1 kDa to backfill the remaining surface sites on the particle allowed us to achieve a lower zeta potential than applying a single coat of PEG 5 kDa (Table 5.S8). We chose these particles for use in our assay. It has been suggested in the literature that a near-zero zeta potential minimizes the interactions particles have in biological environments (35).

To collect luminal fluid from the SI of mice, we excised the SI of adult mice (8-16 weeks old), divided it into an upper and lower section, and gently collected the luminal contents on ice. To separate the liquid and solid phase, we centrifuged the contents and collected the supernatant. To further ensure that any remaining solid material was removed from the fluid phase, we filtered the supernatant through a 30-μm pore size spin column and collected the filtrate (see *Materials and Methods* for more details). We then placed the PEG-coated particles in the SI luminal fluid at a volume fraction of ≈0.001. A low-volume fraction was chosen because bacteria in the healthy SI are found at similarly low-volume fractions (41–43). We found that, despite the PEG coating and low-volume fraction, aggregates of particles formed in 5-10 min (**Figure 5.2*A*-*D***), a timescale much shorter than the transit time for food through the SI, which can be as short as ~80 min in healthy humans (39) and ~60 min in mice (44). On longer timescales, peristaltic mixing could also play a role (39); during fasting, the migrating motor complex (MMC) cycle first consists of a period of quiescence for ~30-70 min, followed by a period of random contractions, then by 5 to 10 minutes in which contractions occur at 11-12 counts per minute (cpm) in the

duodenum and 7-8 cpm in the ileum. After eating, MMC is substituted with intermittent contractions in the SI and waves can occur at a frequency of 19-24 cpm in the distal ileum 1-4 h later. We therefore chose to focus on aggregation at short timescales (~10 min) because we sought to understand the initial formation of aggregates before aggregation is influenced by mechanical forces such as shear due to peristaltic mixing and the transit of food.

To quantify the amount of aggregation in samples of luminal fluid, we developed a method to measure the sizes of all aggregates in solution using confocal microscopy (see *Materials and Methods*). From these datasets, we created volume-weighted empirical cumulative distribution functions (ECDFs) of all the aggregate sizes in a given solution. We used these volume-weighted ECDFs to compare the extent of aggregation in a given sample (**Figure** 5.2*F* and *H*). To test the variability of aggregation in samples collected from groups of mice treated under the same conditions, we compared the extent of aggregation in pooled samples taken from three groups, each consisting of three male mice on a standard chow diet. We plotted the volume-weighted ECDFs of each sample (**Figure** 5.2*F* and *H*) and observed that the variation among the groups under the same conditions appeared to be small compared with the differences between the samples and the control.

To quantify the variability of aggregation among groups using an additional method, we bootstrapped our datasets to create 95% bootstrap confidence intervals (CI) of the volume-weighted average aggregate size of each of the three groups and the control in Hank's balanced salt solution (HBSS) (**Figure** 5.2*G* and *I*; see *Materials and Methods* for complete details of the bootstrapping procedure). All 95% bootstrap CI either overlapped or came close to overlapping, again suggesting there was little variability among pooled samples treated under the same conditions (male mice on a standard chow diet).

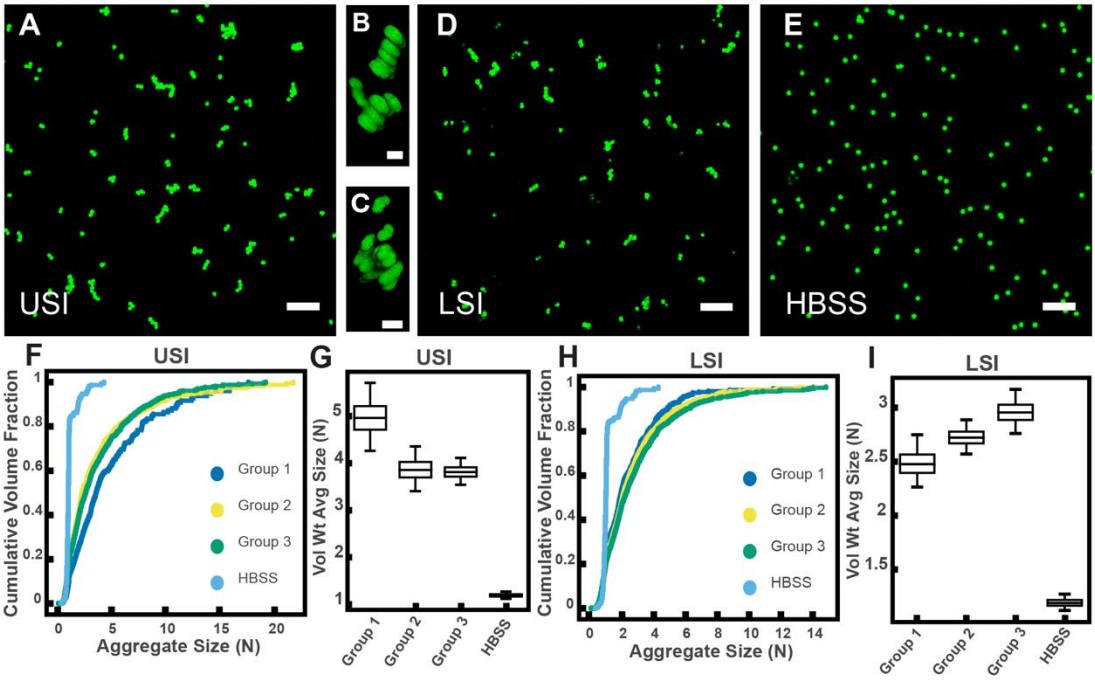

Figure 5.2: PEG-coated particles aggregate in fluid from the murine small intestine (SI) *ex vivo*. The 1-μm-diameter PEG-coated particles form aggregates in fluid collected from the upper (A-C) and lower (D) SI in ~10 min. (A and D) Maximum z-projections of 10 optical slices taken on a confocal microscope. (B and C) 3D renderings of aggregates found in panel A. (E) Maximum z-projection of the same particles in HBSS. Scale bars are 10 μm in 2D images and 2 μm in 3D images. (F and H) Volume-weighted empirical cumulative distribution functions (ECDFs) comparing aggregation of the particles in pooled samples from the upper (F) and lower (H) SI of three separate groups of male chow-fed mice (each group consisted of three mice) and a control (particles suspended in HBSS). The vertical axis is the cumulative volume fraction of the total number of particles in solution in an aggregate of a given size. The horizontal axis (aggregate size) is given as the number of particles per aggregate (N). (G and I) Box plots depicting the 95% empirical bootstrap CI of the volume-weighted average aggregate size (given in number of particles per aggregate, N) in samples from the upper (G) and lower (I) SI (the samples are the same as those from panels F and H). The line bisecting the box is the 50th percentile, the upper and lower edges of the box are the 25th and 75th percentile respectively, and the whiskers are the 2.5th and 97.5th percentiles. USI = upper SI; LSI = lower SI. See *Materials and Methods* for bootstrapping procedure.

Fractionation of SI fluids suggests polymers play a role in aggregation of PEG-coated particles

Given that polymers can aggregate particles and bacteria via several mechanisms (12–33), we hypothesized that biopolymers in SI luminal fluid are involved in the aggregation of our PEG-coated particles. We therefore sought to first quantify the physical properties of the polymers in the luminal fluid of the SI. To do this, we used a 0.45-μm filter to remove additional debris and ran samples from a group of three chow-fed mice on a gel permeation chromatography (GPC) instrument coupled to a refractometer, a dual-angle light scattering (LS) detector, and a viscometer (details in *Materials and Methods*). Chromatography confirmed that polymers were indeed present in the SI fluid (**Figure** 5.3*A* and *D*). Because we do not know the refractive index increment (dn/dc) of the polymers present in these samples and the polymers are extremely polydisperse, we cannot make exact calculations of the physical parameters of these polymers. We can, however, calculate estimated values by assuming the range of the dn/dc values to be about 0.147 for polysaccharides and about 0.185 for proteins and then dividing the sample into different fractions based on retention volume (estimates of concentration and MW of polymers are displayed on **Figure** 5.3*A* and *D*). The estimates suggest that the SI is abundant in polymers with a range of MWs.

To qualitatively test our hypothesis that biopolymers in the SI were involved in the aggregation of our PEG-coated particles, we collected SI luminal fluid from a different group of three male, chow-fed mice. We performed an additional filtration step (0.45-μm) to further ensure the removal of any solid materials. This filtrate was then separated into aliquots and each aliquot was run through a different MW cut-off (MWCO) filter (see *Materials and Methods*). We then collected the eluent of each aliquot and compared the aggregation of our PEG-coated particles in each (**Figure** 5.3*B, C, E,* and *F*). We generally found less aggregation in the fractionated samples compared with the 30- and 0.45-μm filtered samples. When the MWCO was decreased to 3 kDa, the observed aggregation in the eluent matched the extent of aggregation observed for particles in HBSS. Overall, these data supported our hypothesis that polymers were involved in the aggregation of these particles.

Interestingly, in the lower SI, we observed more aggregation in the 0.45-µm filtered sample compared with the 30-µm filtered sample. From handling the samples, we observed that the 30-µm filtered samples appeared to be more viscous than the 0.45-µm filtered samples. We postulate that this increase in viscosity was due to the formation of self-associating polymeric structures, although we did not test this assumption. We attribute this decrease in aggregation in the 30-µm filtered samples to slower aggregation kinetics due to decreased diffusivity of particles in this viscous medium. This decrease in aggregation at high polymer concentrations or viscosities is also observed in solutions of model polymers, as discussed in the next section.

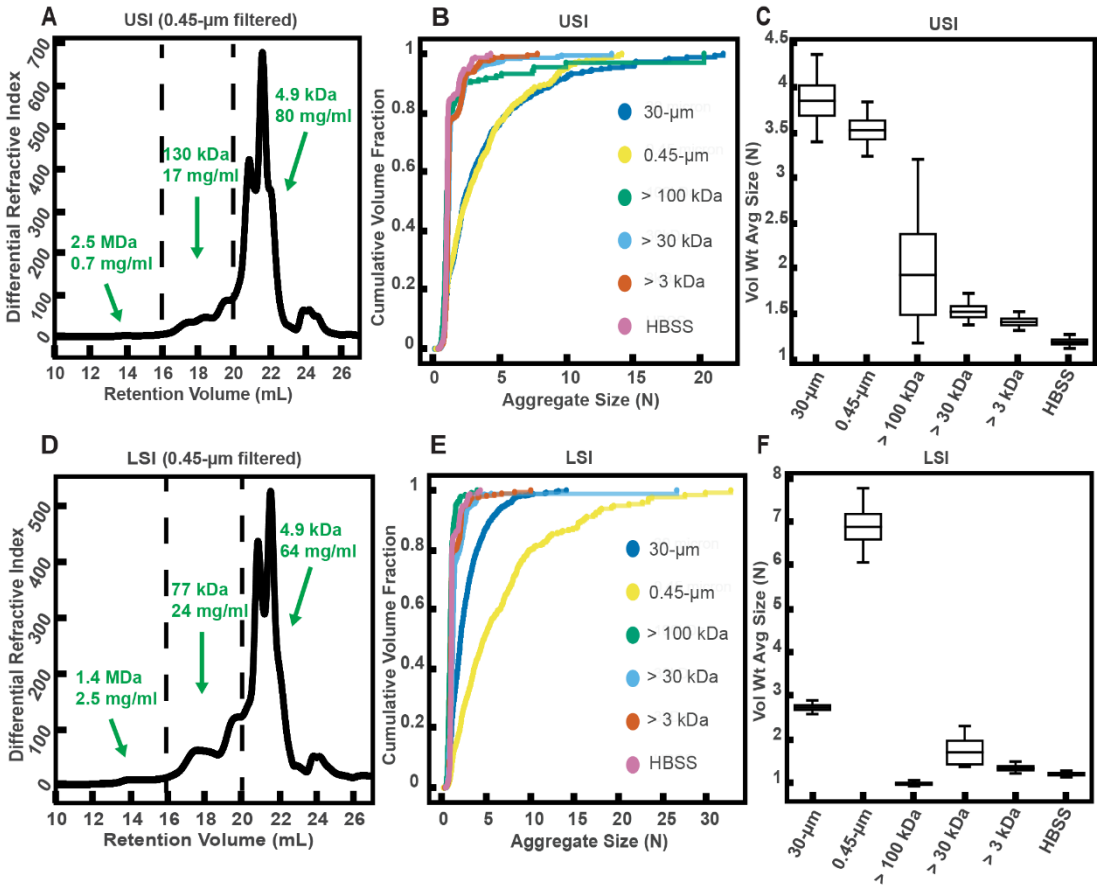

Figure 5.3: Gel permeation chromatography (GPC) of fluid from the small intestine (SI) and aggregation of PEG-coated particles in fractionated fluid from SI. (A and D) Chromatograms of samples from the upper (A) and lower (D) SI from a group of three chow-fed mice. Dashed lines indicate the three retention volumes the chromatograms were divided into for analysis: 11-16 mL, 16-20 mL, and >20 mL. Estimated concentrations and molecular weight (MW) are reported in green on the chromatograms for each retention volume. (B and E) Volume-weighted empirical cumulative distribution functions (ECDFs) of aggregate sizes in the upper (B) and lower (E) SI liquid fractions of chow-fed mice which have been run through MW cut-off (MWCO) filters with different MWCOs. As a control, aggregate sizes were also measured for particles placed in HBSS. The vertical axis is the cumulative volume fraction of the total number of particles in solution in an aggregate of a given size. The horizontal axis is aggregate size (number of particles per aggregate, N). (C and F) Box plots depict the 95% empirical bootstrap CI of the volume-weighted average aggregate size (given in number of particles per aggregate, N) in the samples from panels B and E, respectively (see *Materials and Methods* for bootstrapping procedure). The line bisecting the box is the 50th percentile, the upper and lower edges of the box are the 25th and 75th percentile respectively, and the whiskers are the 2.5th and 97.5th percentiles.

Aggregation of PEG-coated particles in model polymer solutions shows complex dependence on the concentration and MW of polymers.

Before exploring the complex environment of the SI further, we sought to first understand how our PEG-coated particles behaved in simple, well-characterized polymer solutions with similar MW and concentrations to those polymers we found in the SI in the previous experiments (**Figure** 5.3*A* and *D*). It has been demonstrated that the aggregation of colloids and bacteria can be controlled by altering the concentration and size of the non-adsorbing polymers to which particles are exposed (27–33). In these controlled settings, particles aggregate due to what are known as depletion interactions (27–29). Many groups have focused on depletion interactions with hard-sphere-like colloids; they often use polymethylmethacrylate particles sterically stabilized with polyhydroxystearic acid, because these particles closely approximate hard-sphere-like behavior (45,46). In these scenarios, depletion interactions are often described as forces that arise when particles get close enough to exclude polymers from the space between them, resulting in a difference in osmotic pressure between the solution and the exclusion region, leading to a net attractive force (27–31). Others have instead chosen to describe the phase behavior of the colloid/polymer mixture in terms of the free energy of the entire system (33,47). Short-range attractions (polymer radius is ten-fold less than particle radius) between hard-sphere colloids induced by polymers have been described successfully in the language of equilibrium liquid–gas phase separation (48,49).

Some groups have explicitly accounted for the effects of the grafted polymer layer used to sterically stabilize colloids when studying interactions between polymer solutions and colloids (50–58); this includes groups studying mixtures of polystyrene particles sterically stabilized with grafted layers of PEG (MWs of 750 Da and 2 kDa) and aqueous solutions of free PEG polymer (MW from 200 Da to 300 kDa) (51,52). It has been found experimentally that in mixtures of polymers and sterically stabilized colloids, the colloids form aggregates above a threshold polymer concentration. At even higher concentrations, as the characteristic polymer size shrinks, the colloids cease to aggregate, a phenomenon referred to as “depletion stabilization.”

To test whether our PEG-coated particles behave similarly to what has been previously found in mixtures of polymers and sterically stabilized particles, we created polymer solutions with PEG at a range of polymer concentrations and MWs and measured the extent of aggregation in these polymer/particle mixtures (**Figure** 5.4*A*-*D*). We chose PEGs that have MWs similar to the MW of polymers we found naturally occurring in the SI (**Figure** 2.3*A*, *D*): 1 MDa, 100 kDa, and 3350 Da. Using PEGs with similar physical properties (i.e. MW, concentration) as a simple model of polymers found in the SI allows us to focus solely on physical interactions between the particles and polymers. We created PEG solutions in HBSS at mass concentrations similar to those measured for polymers in the SI (**Figure** 2.3*A* and *D*) and imaged the polymer/particle mixtures after ~10 min. HBSS was chosen because it has a similar pH and ionic strength to that of the SI (59,60). At the high ionic strengths of these buffered aqueous solutions (~170 mM), any electrostatic repulsions that can occur between particles should be screened to length scales of order the Debye screening length ~0.7 nm (61,62), nearly an order of magnitude smaller than the estimated length of the surface PEG brush (~6.4 nm; see *Materials and Methods* for more details). We again chose to look at aggregation on short timescales (after ~10 min) because we sought to understand the initial formation of aggregates; in the SI, on longer timescales, aggregation will likely also be influenced by mechanical forces such as shear due to peristaltic mixing and the transit of food.

For PEG 1 MDa and 100 kDa solutions we found aggregates of similar sizes to those observed in the SI luminal fluid (**Figure** 5.4*A*-*D*). We did not detect any aggregation for the PEG 3350 Da solutions (**Figure** 5.4*D*). Because the pH is known to vary across different sections of the gastrointestinal tract and this could affect the observed aggregation behavior, we measured the pH in luminal fluid from the upper and lower small intestine (see ***Figure*** *2-S2* and *Materials and Methods*). We found that the upper small intestine (USI) luminal fluid was $pH = 6.0 \pm 0.1$ and for the lower small intestine (LSI) $pH = 7.5 \pm 0.3$. For the HBSS used, $pH = 7.6 \pm 0.1$ (See *Materials and Methods*), which matches that of the LSI but not the USI. We therefore conducted the same *in vitro* experiment for PEG 1 MDa in phosphate buffered saline with $pH = 6.0 \pm 0.1$ (*Materials*

and Methods and **Figure** 5.4 – **Figure** supplement 1). We found some differences in the aggregation, but the overall trends were similar to before.

Overall, though our system is not at equilibrium at these short timescales, we found trends consistent with what has been observed in the literature for depletion interactions with sterically stabilized particles (50–58). At dilute polymer concentrations, the extent of aggregation increased with concentration. At higher polymer concentrations, the extent of aggregation began to decrease as the solutions begin to "re-stabilize." Additionally, the extent of aggregation was greater for longer polymers. Interestingly, we found that the curves for the long polymers in **Figure** 5.4D could be collapsed by normalizing the polymer concentration by the overlap concentration (which denotes the transition between the dilute to semi-dilute polymer concentration regimes) for each respective polymer solution (**Figure** 5.4 – **Figure** supplement 2). We next sought to describe the inter-particle potential using theory that combines depletion interactions with steric interactions.

We applied previously established theoretical frameworks that combine depletion interactions with steric interactions to better understand our system (50,54,58). To account for the depletion attractions between colloids we used the Asakura–Oosawa (AO) potential (U_{dep}) (27–29):

$$U_{dep}(r) = \begin{cases} +\infty \; for \; r \leq 0 \\ -2\pi\Pi_P a\left(R_P - \frac{r}{2}\right)^2 \; for \; 0 < r < 2R_P \\ 0 \; for \; r > 2R_P \end{cases} \qquad (Eq. 2.1)$$

Where U_{dep} is given in joules, Π_P is the polymer osmotic pressure (in Pa), a is the radius of the colloid (in m), R_P is the characteristic polymer size (in m), and r is the separation distance between bare particle surfaces (in m). This form of the depletion potential equation assumes that $a >> R_P$, a condition satisfied for 1 μm particles we used. For the polymer osmotic pressure, we used the following crossover equation for a polymer in a good solvent (63,64):

$$\Pi_P = \frac{N_{Avo} kT}{MW} c_P \left(1 + \left(\frac{c_P}{c_P^*}\right)^{1.3}\right) \qquad (Eq. 5.2)$$

Where Π_P is given in pascals, N_{Avo} is Avogadro's number, k is the Boltzmann constant, T is the temperature (in kelvins), MW is the molecular weight of the polymer (in Da), c_P is the polymer mass concentration (in kg/m^3), and c_P^* is the polymer overlap concentration (in kg/m^3). This equation describes the polymer osmotic pressure well in both the dilute and semi-dilute regime.

For the characteristic polymer size, we used the concentration-dependent radius of gyration (31,65). This can be written as:

$$R_P(c_P) = R_g(0) \left(\frac{Mw}{N_{Avo} kT} \frac{d\Pi_P}{dc_P}\right)^{-\frac{1}{2}} \qquad (Eq. 5.3)$$

Where $R_P(c_P)$ is the concentration-dependent radius of gyration or the characteristic polymer size given in meters, $R_g(0)$ is the radius of gyration (in m) at dilute concentrations and Π_P is given by equation 5.2. The characteristic polymer size is given by the dilute radius of gyration at low concentration and is close to the correlation length of the polymer solution, or the average distance between monomers, in the semi-dilute regime. Therefore, using equations 5.2 and 5.3, we acquire the correct limits for the depletion potential; the Asakura–Oosawa potential in the dilute regime and the depletion potential described by Joanny, Liebler, and de Gennes in the semi-dilute regime (66). Similar crossover equations have been found to adequately describe experimentally observed depletion aggregation in polymer-colloid mixtures where the polymer concentration spans the dilute and semi-dilute regimes (67). Using literature values for the hydrodynamic radii of the PEGs (68) and the Kirkwood-Riseman relation, which relates the hydrodynamic radius to the radius of gyration (68–70), we estimated $R_g(0)$ for each polymer. We estimated $R_g(0) \approx 62.6$, 16.7, 2.9 nm for PEG 1 MDa, 100 kDa, and 3350 Da, respectively. Using both the estimates of $R_g(0)$ and the MW of each polymer, we then estimated c_p^* for each polymer (63,71). We

estimated c_p^* = 1.6, 8.6, and 52.6 mg/mL for PEG 1 MDa, 100 kDa, and 3350 Da, respectively.

To account for steric interactions between the two grafted layers upon close inter-particle separations, we used equation 5.4 (50,52). For inter-particle separation distances between *L* and 2*L*, where *L* is the length of the grafted layer, the steric interactions between the two grafted layers can be described using the Flory–Huggins free energy of mixing:

$$U_{s,mix}(r) = \frac{4\pi akT}{v_1}\left(\overline{\phi_2^a}\right)^2\left(\frac{1}{2}-\chi\right)\left(L-\frac{r}{2}\right)^2 \qquad (Eq.\,5.4)$$

Where $U_{s,mix}$ is the steric interaction energy due to mixing (given in joules), *a* is the particle radius (in m), v_1 is the volume of a water molecule (in m^3), $\overline{\phi_2^a}$ is the average volume fraction of the grafted polymer (unitless), χ is the Flory–Huggins interaction parameter for the grafted polymer and the solvent (unitless), and *L* is the length of the grafted layer (in m). For PEG in aqueous solvents, $\chi = 0.45$ (72). Our NMR measurements (see *Materials and Methods* for details) suggest that the grafting density of PEG is within the brush regime. We therefore use the Alexander–de Gennes approximation (63) and our NMR measurements to estimate the length of the grafted layer (*L*) as *L* ~ 6.4 nm and the average volume fraction to be $\overline{\phi_2^a} \sim 0.43$.

For inter-particle separations closer than *L*, one needs to account for elastic deformations of the grafted layers (50,57). This is far greater in magnitude than U_{dep}, so one can simply assume that at this point the potential is extremely repulsive. For inter-particle separations greater than *L*:

$$U(r) = \begin{cases} U_{s,mix} + U_{dep}\ for\ L < r < 2L \\ U_{dep}\ for\ r \geq 2L \end{cases} \qquad (Eq.\,5.5)$$

Using this theoretical framework, we can build a physical intuition for the system **(Figure** 5.4*E-G***)**. Long polymers have depletion layers that extend out past the brush layer and overlap, inducing attractions between the particles (**Figure** 5.4*E*). For short polymers ($R_P < L$), the depletion attractions are buried within the steric repulsions induced by the brush

and there are effectively no attractions among the particles (**Figure** 5.4*F*). We can use this crossover to estimate the magnitudes of the minima in the inter-particle potentials for the three PEG solutions **(Figure** 5.4*H***)**. It should be noted that we have made several simplifications; for example, we do not consider interactions between free polymers and the grafted layer, which could lead to partial penetration of free polymers into the grafted layer or possible compression of the grafted layer by the free polymers (50,56,57). Despite such simplifications, we find that the calculated minima display similar concentration trends to the trends seen in the average aggregate sizes **(Figure** 5.4*D***).** These calculations offer an explanation for why there is no aggregation of PEG-coated particles in solutions of PEG 3350.

Another factor that needs to be considered at the short timescales and low-volume fractions we are working at is aggregation kinetics (73–75). The probability that particles collide in solution is directly related to the diffusion coefficient and the volume fraction of the particles. As we increase the polymer concentration we increase the viscosity of the solution and decrease the diffusivity of the particles. In **Figure** 5.4*I*, we plot theoretical estimates of the diffusion coefficients of the particles against the concentrations of the PEG solutions. These diffusion coefficients were estimated using literature measurements, the Stokes–Einstein–Sutherland equation, and the Huggins equation for viscosity (63,68).

Because our system has not reached equilibrium, in this case the non-monotonic dependence of aggregation on polymer concentration for long polymers is due to a complex interplay between thermodynamics and kinetics (which we have not untangled). However, both the dependence of diffusivity (**Figure** 5.4*I***)** and the equilibrium prediction of inter-particle minima **(Figure** 5.4*H***)** on polymer concentration suggest that we should expect a decrease in aggregation at high polymer concentrations. The inter-particle minima also suggests that we should not expect short polymers to induce aggregation. Both trends are consistent with what we observe. Understanding how our PEG-coated particles behave in these so-called “simple” polymer solutions with similar physical properties to the intestinal polymers we detected (**Figure** 5.3*A* and *D*) informs the interpretation of the results of the next sections.

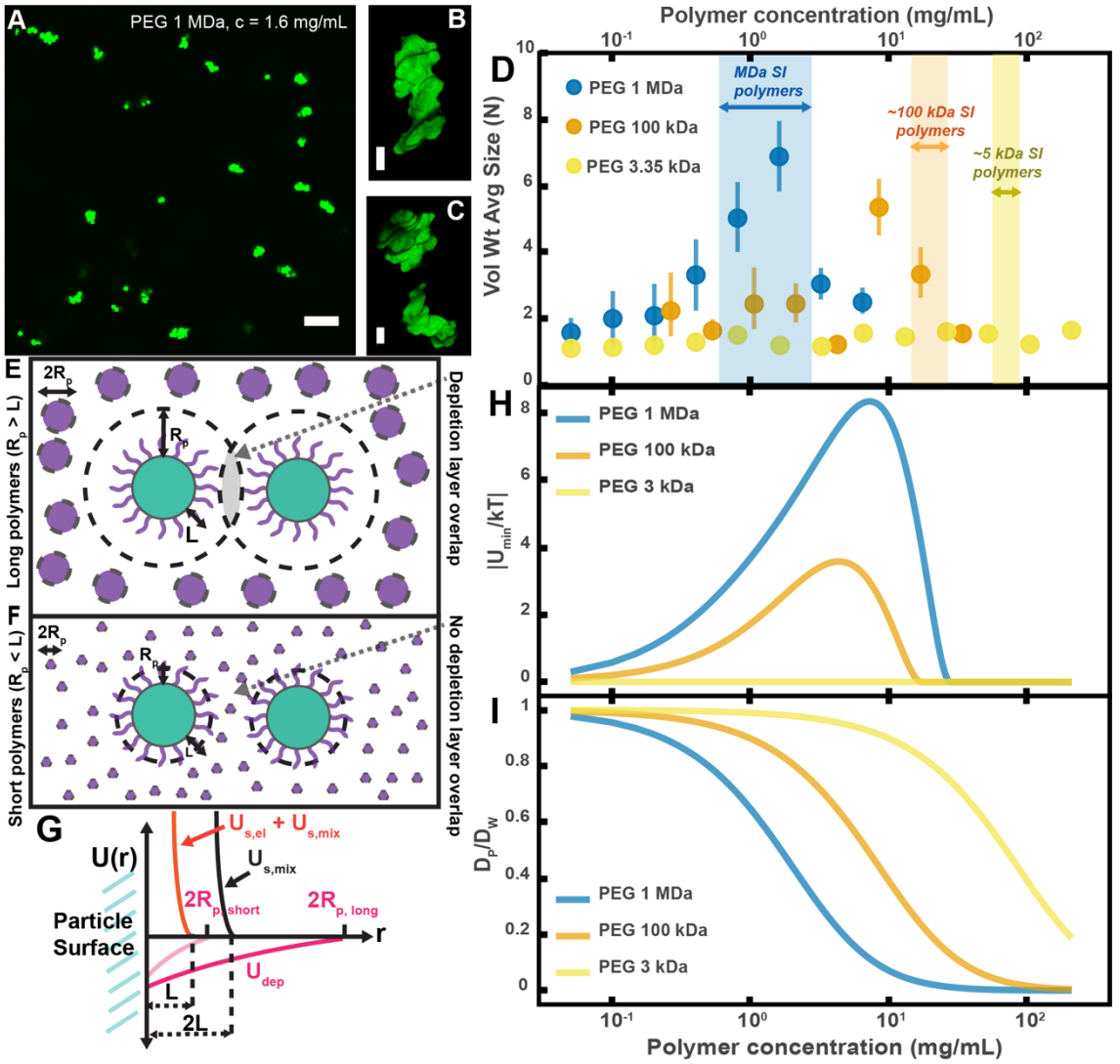

Figure 5.4: Aggregation of PEG-coated particles in model polymer solutions shows complex dependence on molecular weight (MW) and concentration of PEG. **(A)** Aggregates of 1 µm diameter PEG-coated particles in a 1 MDa PEG solution with a polymer concentration (c) of 1.6 mg/mL. Image is a maximum z-projection of 10 optical slices taken on a confocal microscope. Scale bar is 10 µm. **(B** and **C**) 3D renders of aggregates found in panel A. Scale bars are 2 µm. **(D)** Volume-weighted average sizes for serial dilutions of PEG solutions of three MW (1 MDa, 100 kDa, and 3350 Da). Volume-weighted average sizes are plotted on the vertical axis in terms of number of particles per aggregate (N) against polymer mass concentration (c_p) in mg/mL. The vertical error bars are 95% empirical bootstrap CI (see *Materials and Methods* for bootstrapping procedure). Shaded regions indicate the concentration ranges of detected intestinal polymers of similar MW. **(E)** Schematic depicting depletion interactions induced by "long polymers" (polymer radius (R_P) > length of the brush, L). Free polymers are depicted as purple spheres. Colloids are depicted in green with the grafted brush layer in purple. The depletion layer around each colloid is depicted by dotted lines. The overlap region between the two depletion

layers is indicated in grey. **(F)** Schematic depicting depletion interactions induced by "short polymers" (R_p < L). The depletion zone does not extend past the length of the brush and there is effectively no overlap in the depletion layers; the depletion attractions are "buried" within the steric layer. (**G**) Schematic depicting the different contributions to the inter-particle potential (U(r)) against inter-particle separation distance (r). The hard surfaces of the particles are in contact at r = 0. U_{dep} depicts the depletion potential for a short polymer ($R_{P,short}$) and a long polymer ($R_{P,long}$). $U_{s,mix}$ shows the contribution to the steric potential due to mixing. $U_{s,el}$ + $U_{s,mix}$ shows the contribution due to elastic deformations and mixing at close inter-particle separations. **(H)** The magnitude of the minima of the inter-particle potential (U_{min}/kT) plotted against polymer concentration for the three PEG solutions in (D). **(I)** Diffusion coefficients estimated from the Stokes–Einstein–Sutherland equation for 1 µm particles in the PEG solutions used in (D). Diffusion coefficients of particles in polymer solutions (D_P) are normalized by the diffusion coefficients in water (D_W) and plotted against polymer concentration. **Figure supplement 1** shows the dilution series for PEG 1 MDa at pH = 6.0 compared to pH = 7.6. **Figure supplement 2** shows the dilution series displayed in **Figure** 5.4D where the polymer concentration has been normalized by the overlap concentration of each polymer solution.

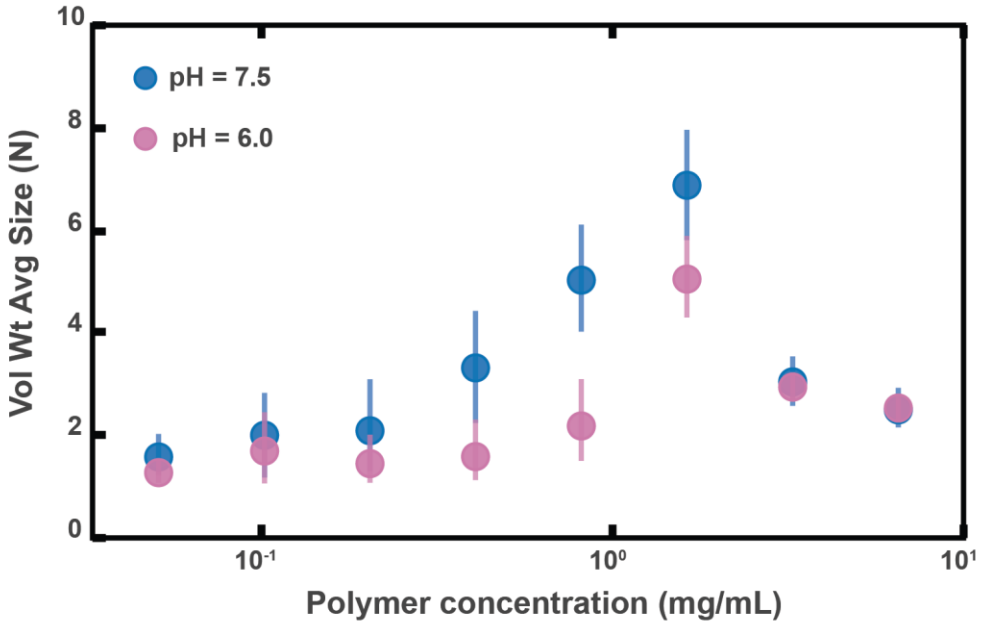

Figure 5.4 – Figure supplement 1: Aggregation of PEG-coated particles in model polymer solutions with different pH**. (A)** Volume-weighted average sizes for serial dilutions of 1 MDa PEG solutions in a phosphate buffered saline solution with $pH = 6.0 \pm 0.1$ (labeled pH = 6.0) and in Hank's balanced salt solution (HBSS) with $pH = 7.6 \pm 0.1$ (same data from **Figure** 5.4D). Volume-weighted average sizes are plotted on the vertical axis in terms of number of particles per aggregate (N) against polymer mass concentration (c_p) in mg/mL. The vertical error bars are 95% empirical bootstrap CI (see *Materials and Methods* for bootstrapping procedure).

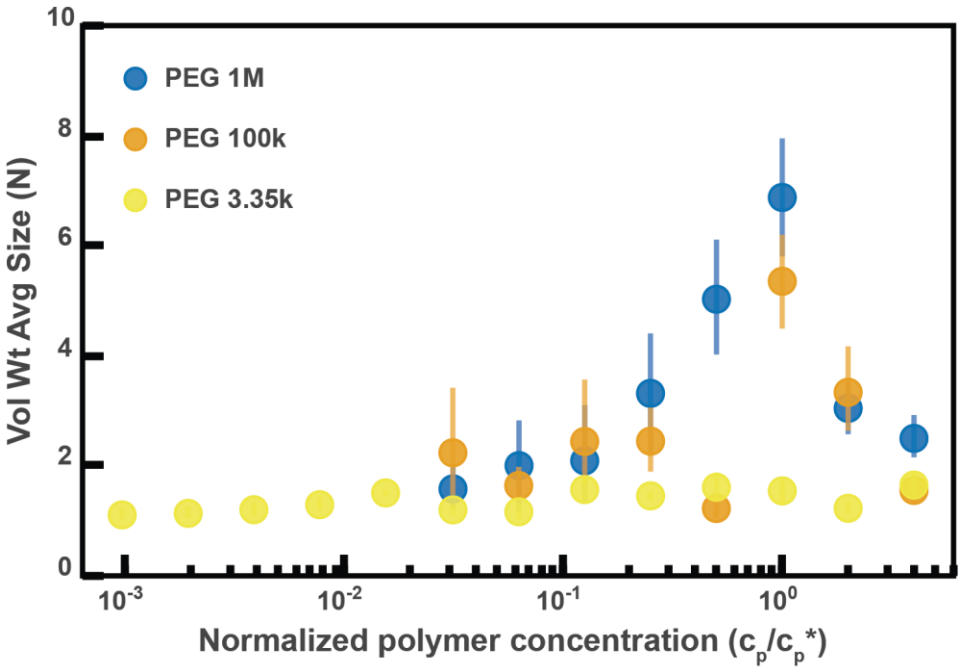

Figure 5.4 – **Figure** supplement 2: Aggregation of PEG-coated particles in model polymer solutions from **Figure** 4D normalized by polymer overlap concentration. Volume-weighted average sizes for serial dilutions of 1 MDa PEG solutions in Hank's balanced salt solution (HBSS). Volume-weighted average sizes are plotted on the vertical axis in units of number of particles per aggregate (N) against the "normalized polymer concentration." The normalized polymer concentration is the polymer mass concentration (c_p) in mg/mL divided by the overlap concentration of each polymer solution (c_p^*) in mg/mL. The overlap concentrations for PEG 1 MDa, 100 kDa, and 3350 Da are c_p^* = 1.6, 8.6, and 52.6 mg/mL, respectively. The vertical error bars are 95% empirical bootstrap CI (see *Materials and Methods* for bootstrapping procedure).

MUC2 may play a role in the aggregation of PEG-coated particles, but is not required for aggregation to occur

It has been demonstrated that mucins can aggregate and bind to bacteria *in vitro* (12–16); thus, we wanted to test whether mucins, such as Mucin 2 (MUC2), which is the primary mucin secreted in the SI (76,77), drive the aggregation of PEG-coated particles in SI fluid. It is known that in the presence of Ca^{2+} and at $pH \leq 6.2$, MUC2 can form aggregates or precipitate out, but it is soluble without Ca^{2+} or at higher pH (78). Our measurements of the pH throughout the SI suggest that it is possible that MUC2 precipitates out in the upper

small intestine; however, because it is unclear how much Ca^{2+} is in the lumen of the upper small intestine, there could be soluble MUC2 in the upper small intestine. Additionally, the literature suggests that, based on the pH, there should be soluble MUC2 in the lower small intestine. We therefore tested if MUC2 drives aggregation in both the upper and lower small intestine. To do this, we compared the aggregation of our PEG-coated particles in samples from MUC2 knockout (MUC2KO) mice to samples from wild-type (WT) mice. To carefully preserve the native composition of the SI fluid, we used a protease-inhibitor cocktail when collecting the samples (see *Materials and Methods*). We confirmed mouse MUC2KO status via genotyping and Western blot (**Figure** 5.5*E*; *Materials and Methods*). The Western blot detected MUC2 in the colons of WT mice and not MUC2KO mice, as expected, however it did not detect a signal for MUC2 in the SI of either the WT or MUC2KO mice. We speculate that the lack of MUC2 signal in the SI of WT mice may be due to low levels of MUC2 present in the luminal contents of the SI.

We observed aggregation in samples from both the MUC2KO and WT mice (**Figure** 5.5*A-B*). To test the strength of the aggregation effect in the different samples, we serially diluted the samples and measured the average aggregate size to see when the effect disappeared (**Figure** 5.5*C-D*). As explained in the previous section, we do not necessarily expect to see a linear decrease in aggregation with dilution. For simplicity, we will refer to the dilution factor at which aggregation begins to disappear as the "aggregation threshold." We found differences in the aggregation threshold in the samples from MUC2KO and WT mice **(Figure** 5.5*C-D*), suggesting that although MUC2 is not required for aggregation to occur, it could play a role in the aggregation of PEG-coated particles.

We wanted to test differences in the MW distribution of the polymers found in these samples, so we 0.45-μm-filtered our samples and analyzed them by GPC (see *Materials and Methods*). The chromatograms from the refractometer (**Figure** 5.5*F-G*) suggest that the polymer composition of MUC2KO and WT samples were qualitatively similar. Following the same methods in **Figure** 5.3, we made estimates of the physical parameters of the detected polymers. These estimates are summarized in Tables 5.S1–S2 for both the

upper and lower SI of MUC2KO and WT mice. We find that these estimates suggest there are some differences in the polymeric composition of the SI of these two groups.

To test whether these measured differences in polymeric composition are reflected in differences in aggregation, we looked at aggregation in the 0.45-μm-filtered samples. We found that the undiluted samples from both groups displayed aggregation (**Figure** 5.S3*A-B*). We then created serial dilutions of the samples and found different aggregation thresholds for the samples (**Figure** 5.S3*C-D*). These results further confirm our conclusion that although MUC2 may play a role in particle aggregation, it is not required for aggregation to occur.

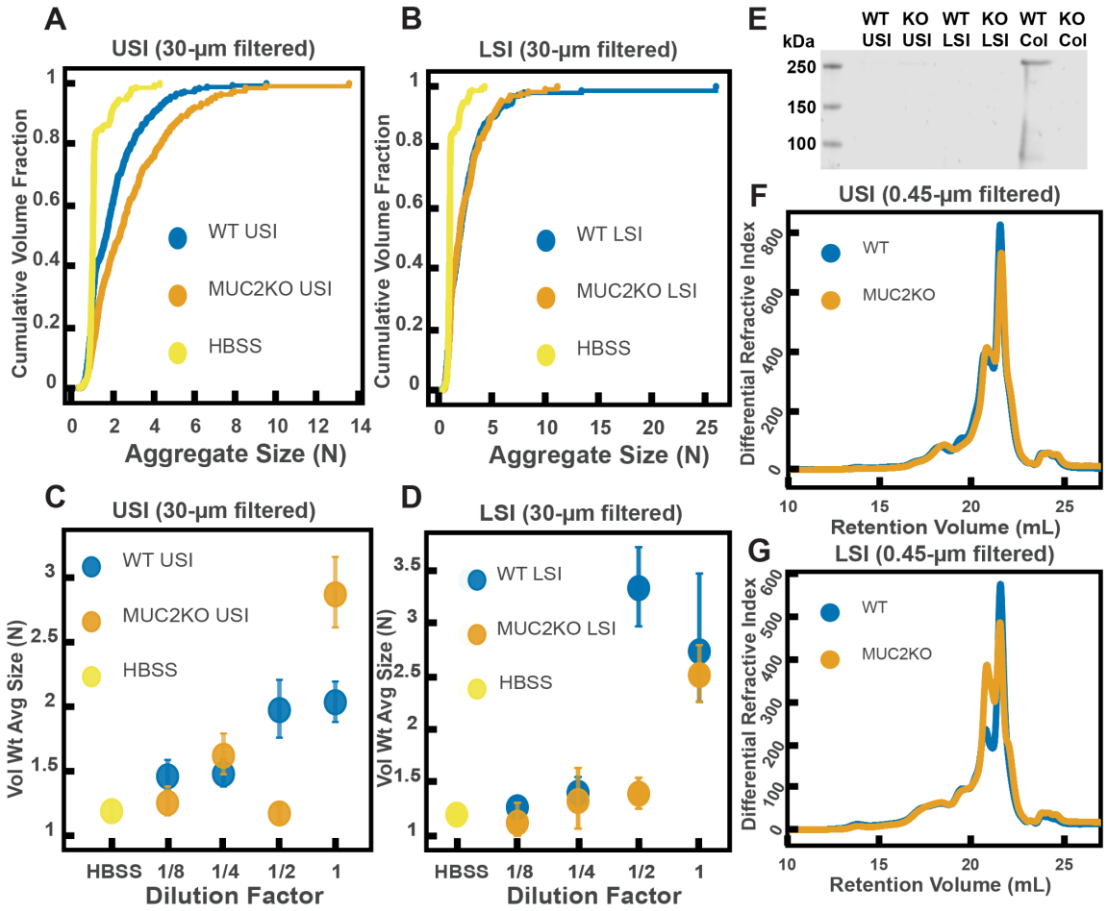

Figure 5.5: Quantification of the aggregation of particles in the small intestine (SI) in MUC2 knockout (MUC2KO) and wild-type (WT) mice. (A and B) Volume-weighted empirical cumulative distribution functions (ECDFs) comparing aggregation of the particles in undiluted, 30-µm filtered samples from the upper (A) and lower (B) SI of two separate groups of wild-type (WT) and MUC2-knockout (MUC2KO) mice to the control (particles suspended in HBSS). The vertical axis is the cumulative volume fraction of the total number of particles in solution in an aggregate of a given size; the horizontal axis is aggregate size in number of particles per aggregate (N). (C and D). Volume-weighted average aggregate sizes (Vol Wt Avg Size) for serial dilutions of 30-µm-filtered samples from the upper (C) and lower (D) SI of two separate groups of WT and MUC2KO mice. The dilution factor is plotted on the horizontal axis; a dilution factor of 1 is undiluted, ½ is a two-fold dilution. The vertical error bars are 95% empirical bootstrap CI (see *Materials and Methods*). (E) Western blots of 30-µm filtered samples from the SI and the colon of WT and MUC2KO mice. WT USI = WT upper SI; KO USI = KO lower SI; WT LSI = WT lower SI; KO USI = KO upper SI; WT Col = WT colon; KO Col = KO colon (F and G). Chromatograms of samples from the upper (F) and lower (G) SI of groups of WT and MUC2KO mice.

Immunoglobulins may play a role in aggregation, but are not required for aggregation to occur

It has also been demonstrated that immunoglobulins can bind to bacteria and induce them to aggregate (17–25). We therefore wanted to test the hypothesis that immunoglobulins drive the aggregation of PEG-coated particles in the SI. To do this, we compared the aggregation of our PEG-coated particles in samples from groups of mutant mice that do not produce immunoglobulins (Rag1KO), to samples from groups of WT mice. Again, to carefully preserve the native composition of the SI fluid, we used a protease-inhibitor cocktail when collecting the samples (see *Materials and Methods*). Because Rag1KO mice are immunocompromised, they need be fed an autoclaved chow diet. To control any potential differences in diet, both the Rag1KO and WT mice were fed an autoclaved chow diet for 48 h before samples were collected.

The mice were confirmed to be Rag1KO via genotyping and Western blot (**Figure** 5.6*E*). According to the literature, IgA is abundant in the SI (79). As expected, we saw a signal for IgA in the upper and lower SI of WT mice. We also tested for less abundant immunoglobulins such as IgG and IgM (**Figure** 5.S4 and **Figure** 5.S5, respectively), but did not detect their presence in the luminal contents of either WT or KO mice.

We observed aggregation in 30-μm-filtered samples from Rag1KO and WT mice (**Figure** 5.6*A* and *B*). To test the strength of the aggregation effect in the different samples, we serially diluted the samples and compared the volume-weighted average aggregate sizes at each dilution (**Figure** 5.6*C* and *D*). We found differences in the amount of aggregation between the Rag1KO and WT samples at different dilutions, suggesting that although immunoglobulins are not required for aggregation to occur, they could play a role in the aggregation of PEG-coated particles.

We wanted to test differences in the MW distribution of the polymers found in these samples, so we 0.45-μm-filtered our samples and analyzed them by GPC (see *Materials and Methods*). The chromatograms from the refractometer (**Figure** 5.6*F* and *G*) suggested that the Rag1KO and WT samples were visually similar. We again made estimates of the

physical parameters of the polymers in these samples (summarized in Tables 5.S3–S4). These estimates suggest that there are some differences in the polymeric composition of the SI of these two groups of mice.

To test whether these measured differences in polymeric composition correspond with differences in aggregation, we quantified aggregation in the 0.45-μm-filtered samples. We found that the undiluted samples for both groups displayed aggregation (**Figure** 5.S6*A* and *B*). When we created serial dilutions of the samples we found that the levels of aggregation were similar (**Figure** 5.S6*C* and *D*). Taken together, the results suggest that immunoglobulins may play some role in aggregation, but the presence of immunoglobulins are not required for aggregation to occur.

Interestingly, there are some differences in the levels of aggregation in WT mice fed the autoclaved diet compared with the standard chow diet. The two diets are nutritionally the same, only the processing is different. When samples from the WT mice in the MUC2KO experiments are compared with samples from the WT mice in the Rag1KO experiments are compared, it is apparent that, compared with WT mice fed the normal chow diet, samples from WT mice fed the autoclaved diet had (i) a lower average concentration of polymers and (ii) polymers of lower overall MW (see "WT" samples in Tables 5.S1–S4). These observations suggested two hypotheses: (1) dietary polymers may play a role in aggregation and (2) aggregation may be controlled by changing the polymer composition of the diet. We tested these hypotheses next.

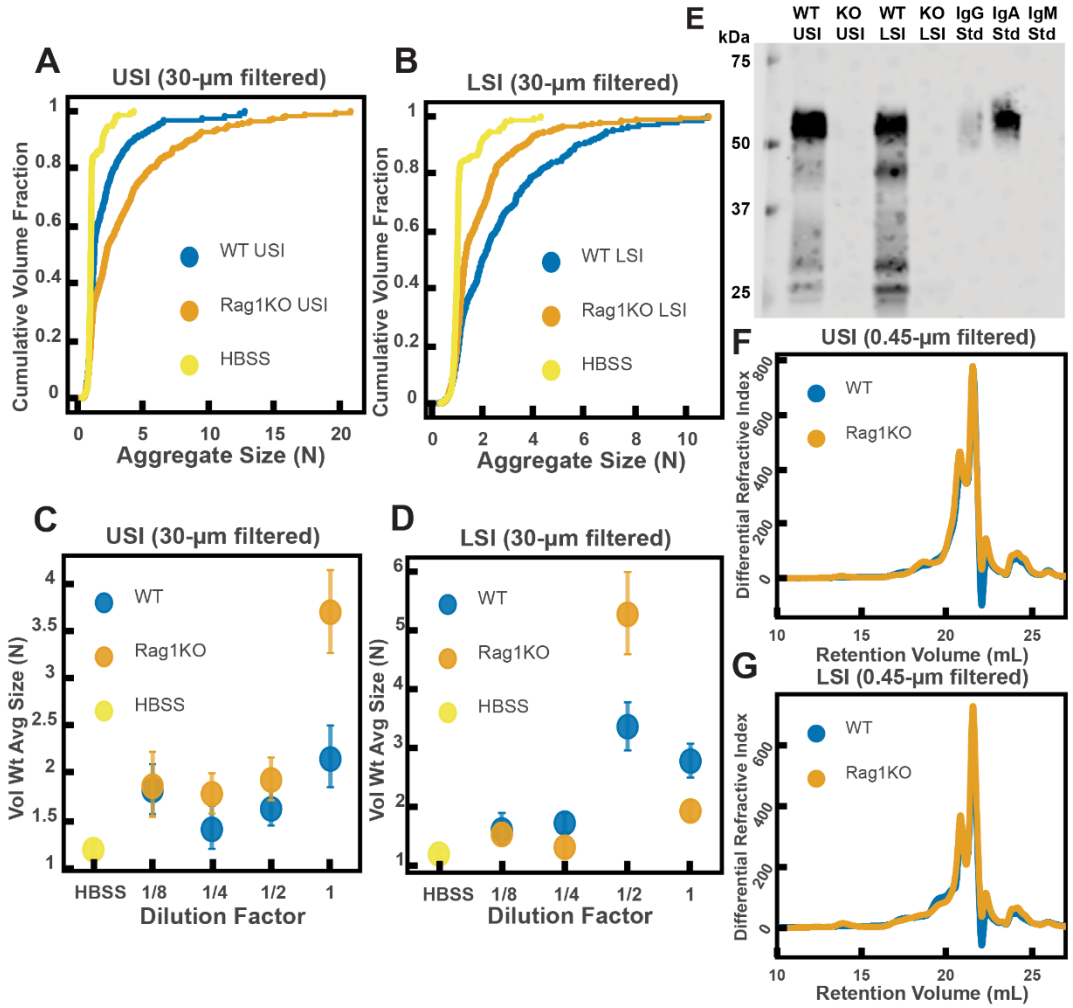

Figure 5.6: Quantification of the aggregation of particles in the small intestine (SI) in Immunoglobulin-deficient (Rag1KO) and wild-type (WT) mice. (A and B) Volume-weighted empirical cumulative distribution functions (ECDFs) comparing aggregation of the particles in undiluted, 30-µm filtered samples from the upper (A) and lower (B) SI of two separate groups of wild-type (WT) and immunoglobulin-deficient (Rag1KO) mice to the control (particles suspended in HBSS). Plotted on the vertical axis is the cumulative volume fraction of the total number of particles in solution in an aggregate of a given size. Plotted on the horizontal axis are aggregate sizes in number of particles. (C and D). Volume-weighted average aggregate sizes (Vol Wt Avg Size) for serial dilutions of 30-µm filtered samples from the upper (C) and lower (D) SI of two separate groups of WT and Rag1KO mice. The dilution factor is plotted on the horizontal axis, where a dilution factor of 1 is undiluted, ½ is a two-fold dilution, and so on. The vertical error bars are 95% empirical bootstrap CI using the bootstrapping procedure described in *Materials and Methods*. (E) Western blots of 30-µm filtered samples from the SI of WT and Rag1KO mice. WT USI = WT upper SI; KO USI = KO lower SI; WT LSI = WT lower SI; KO USI = KO upper SI. (F and G) Chromatograms of samples from the upper (F) and lower (G) SI of groups of WT and Rag1KO mice.

Polymers in the diet control aggregation of PEG-coated particles in a manner consistent with depletion-type interactions

As described in **Figure** 5.4, the extent of aggregation can be controlled by altering the polymer size and concentration of the polymer solution. Furthermore, as pointed out above, SI fluid from mice fed autoclaved and non-autoclaved diets induced different levels of aggregation. We hypothesized that aggregation behavior would differ between mice fed polymers of different sizes—even if the polymers were composed of similar chemical monomers and were present at the same polymer mass concentration. We hypothesized that mice fed short polymers would exhibit less aggregation in the SI (i.e. short polymers reduce the strength of the effect because depletion attractions are reduced). We predicted that the converse would be true for long polymers (i.e. long polymers increase the strength of the effect because depletion attractions are increased).

We first identified two candidate dietary carbohydrate polymers; Fibersol-2, a "resistant maltodextrin" composed of D-glucose monomers (80,81), with a MW of ~3500 Da (see Table 5.S5) and apple pectin, composed of D-galacturonic acid and D-galacturonic acid methyl ester monomers (82,83), with a MW of ~230 kDa (Table 5.S5). Before feeding mice these polymers, we first tested their effects on aggregation *in vitro* at various concentrations in buffer (**Figure** 5.7*A*). We found similar trends to the PEG solutions in **Figure** 5.4. Pectin at low (~0.05 to ~1 mg/mL) and very high mass concentrations showed little aggregation (~7 mg/mL) and showed the most aggregation at an intermediate concentration (~1.5 to ~3 mg/mL). Fibersol-2 did not induce much aggregation up to a mass concentration of ~240 mg/mL.

To test our hypothesis that we could use polymer size to control aggregation, we devised a simple experiment. One group of mice was fed a solution of Fibersol-2 and a second group was fed a solution of apple pectin for 24 h. The mass concentrations of the fibers in the two solutions were matched at 2% w/v and 5% w/v sucrose was added to each to ensure the mice consumed the solutions. Mesh-bottom cages were used to ensure that the mice did not re-ingest polymers from fecal matter via coprophagy. According to the literature,

neither of these two polymers should be broken down in the SI (81,84,85). As before, all samples were collected with a protease-inhibitor cocktail.

As before, we created serial dilutions of the small intestinal luminal fluid and looked at the extent of aggregation in each sample. In the 30-µm-filtered samples from the upper SI we observed more aggregation in the pectin-fed mice compared with the Fibersol-2 fed mice (**Figure** 5.7*E*). For the undiluted 30-µm-filtered lower SI sample, the pectin-fed mice samples formed a gel-like material which we were unable to pipette and therefore could not use for aggregation experiments. This gelation is not too surprising considering that pectin can form a gel in certain contexts (83,86). We were able to dilute this gel four-fold and then compare the aggregation in serial dilutions of the pectin-fed LSI to the Fibersol-2-fed LSI. We found, again, more aggregation in the pectin-fed mice than the Fibersol-2-fed mice (**Figure** 5.7*G*).

We again 0.45-µm-filtered these samples and ran them on GPC to test differences in the MW and size distributions of the polymers in these samples. The chromatograms from the refractometer (**Figure** 5.7*C* and *D*) suggest that there are differences in the polymeric distribution in the two groups of mice. **Figure** 7*B* shows chromatograms of just Fibersol-2 and pectin in buffer. We see that pectin elutes between 14-18 min, which is where we see an enhancement of the concentration of high-MW polymers in the samples from the SIs of the group fed pectin. We also see that Fibersol-2 elutes between 18-22 min, which is where we see an enhancement in the concentration of low-MW polymers in the samples from the SI of the group fed Fibersol-2. We again made estimates of the physical parameters of the polymers in these samples which are summarized in Tables 5.S6 and 5.S7**.** The estimates also suggest that there are differences in the polymeric composition of the SI of the two groups. Overall, the data from GPC suggests that the pectin-fed mice have more high-MW polymers than the Fibersol-2-fed mice. Low-MW polymers appear to be more abundant in Fibersol-2 fed mice compared with pectin-fed mice. We observed visually that the SI contents of the pectin-fed mice formed a gel and pectin is also known to self-associate to form a gel or aggregates in solution (83,86). We note, therefore that by 0.45-µm-filtering

these samples we may be removing these structures and decreasing the concentration of pectin in our samples.

To test that these measured differences in polymeric composition are reflected in differences in aggregation, we tested aggregation in the 0.45-μm-filtered samples. We found that in both the upper and lower SI samples, the samples from the pectin-fed group showed more aggregation than the samples from the group fed Fibersol-2 (**Figure** 5.7*F* and *H*). When we created serial dilutions of these samples, we found that the samples from the mice fed Fibersol-2 showed almost no aggregation at any concentration whereas the samples from pectin-fed mice showed aggregation. We also observed that we needed to dilute the 30-μm-filtered samples more to achieve the greatest extent of aggregation (**Figure** 5.7*E* and *G*). We speculate that this shift in the aggregation behavior between the 30-μm-filtered and 0.45-μm-filtered samples is due to some of the polymers being lost when 0.45-μm-filtering the samples as a result of the aforementioned self-association of pectin.

These data taken together lead us to conclude that polymers in the diet can be used to control the aggregation of PEG-coated particles. This data further suggests that feeding higher MW polymers at the same mass concentration as lower MW polymers leads to an enhancement in aggregation. Due to the high polydispersity and complex chemical composition of SI luminal fluid as measured by GPC, it is unfeasible to apply the same theoretical analysis as was done in **Figure** 5.4 to these data. We can, however, note that visually the behavior is qualitatively consistent with the depletion-type interactions found in simple PEG solutions in **Figure** 5.4.

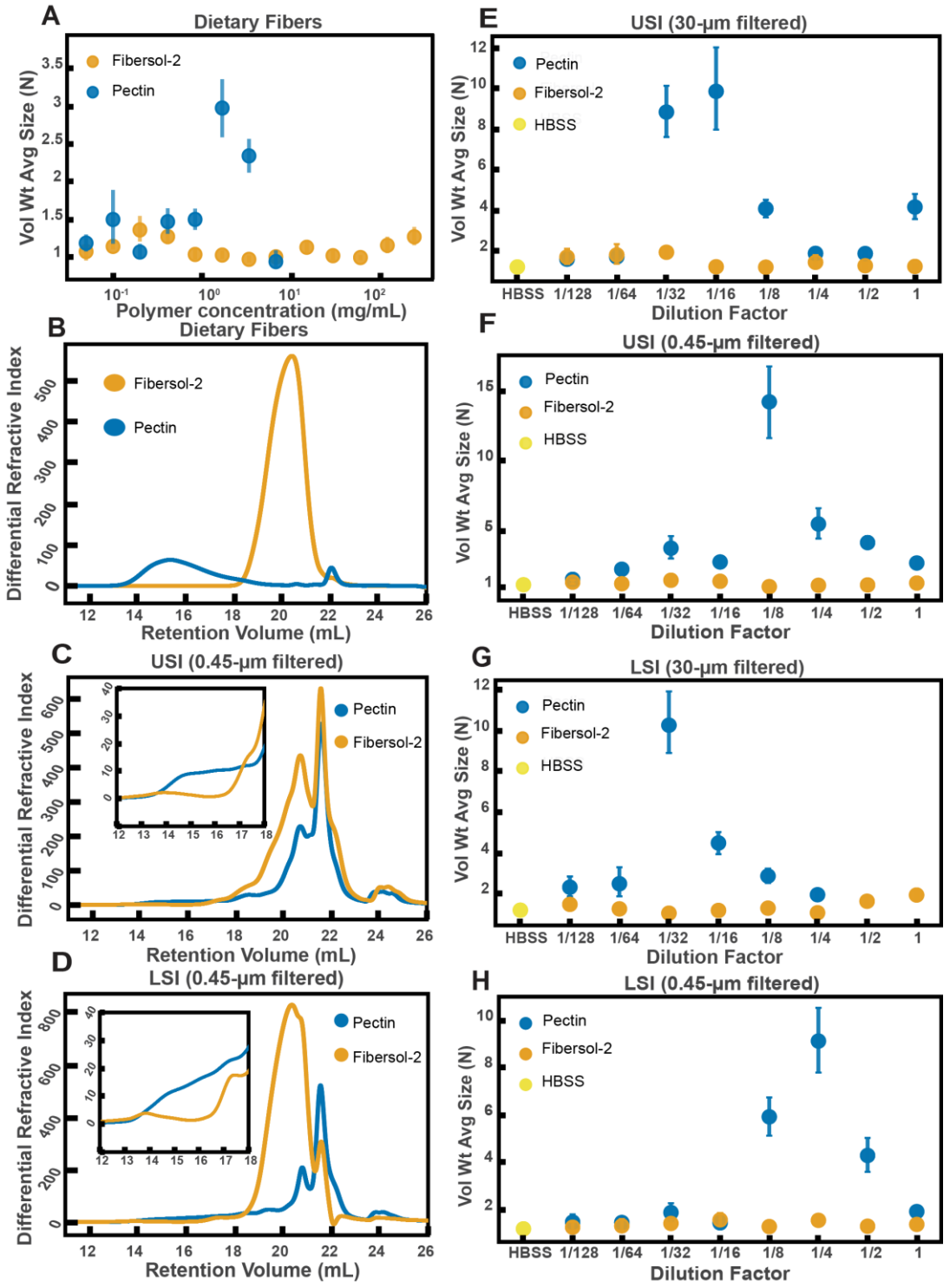

Figure 5.7: Quantification of aggregation of PEG-coated particles in the small intestine (SI) of mice fed different polymers from dietary fiber. **(A)** Volume-weighted average aggregate sizes (Vol Wt Avg Size) for serial dilutions of apple pectin and Fibersol-2. Volume-weighted average sizes are plotted on the vertical axis in terms of number of particles per aggregate (N) against polymer concentration (mg/mL). The vertical error bars

are 95% empirical bootstrap CI using the bootstrapping procedure described in *Materials and Methods.* **(B)** Chromatograms of apple pectin and Fibersol-2 in buffer. (**C and D)** Chromatograms of samples from the upper (E) and lower (F) SI of two separate groups of mice (fed pectin or Fibersol-2). **(E-H)** Volume-weighted average aggregate sizes (Vol Wt Avg Size) for serial dilutions of 30-μm-filtered samples from the upper (E) and lower (G) SI of two separate groups of mice (fed pectin or Fibersol-2) to the control (particles suspended in HBSS). (**F and H**) Serial dilutions of 0.45-μm-filtered samples from the same groups. The dilution factor is plotted on the horizontal axis, where a dilution factor of 1 is undiluted, and ½ is a two-fold dilution. The vertical error bars are 95% empirical bootstrap CI using the bootstrapping procedure described in *Materials and Methods*.

DISCUSSION

This work shows that even PEG-coated particles, which have minimal biochemical interactions, form aggregates in the luminal fluid of the SI. It reveals a previously unknown way in which dietary polymers can impact, and be used to control, the structure of particles in the SI. We speculate that this phenomenon may play a role in the aggregation of other particles in the SI such as microbes, viruses, nanoparticles for drug delivery, and food granules. In these systems, other factors will also inevitably affect the formation of these aggregates (e.g. interactions with mucins and immunoglobulins); thus, it will be important to explore the interplay among all these factors. Another important next step is to investigate how mixing in the SI and the co-aggregation of different types of particles may affect aggregation. We speculate that the aggregation of particles in the SI could also have functional consequences, such as promoting colonization by microbes, affecting infection by pathogens, and altering clearance of microbes (2,6–8,10,11). Aggregation will also need to be considered when designing nanoparticles for drug delivery (3,4).

We found that MUC2 and immunoglobulins, which have been found to aggregate microbes both *in vivo* and *in vitro* (12–25), are not required for the aggregation of PEG-coated particles. Instead, we found that by feeding mice dietary polymers with similar chemistry but very different sizes we could tune the extent of aggregation in the SI. These polymers (pectin and Fibersol-2) are forms of fiber commonly found in the human diet. We found that feeding long polymers induced aggregation, whereas short polymers did not. More work needs to be done to understand the underlying mechanism, but surprisingly the

observed aggregation behavior in the SI luminal fluid from mice fed dietary polymers of different sizes is qualitatively consistent with the aggregation behavior in simple PEG solutions, where aggregation is driven by depletion interactions. Overall, this suggests a simple dietary method for controlling aggregation in the gut. It will be important to extend this work to microbes and other particles commonly found in the gut and to measure the relative contributions of polymer-driven aggregation and chemical-driven aggregation. We note that mucins and immunoglobulins are polymers that can also self-associate into structures of very high MW (78,87,88), suggesting that they could cause aggregation via both physical and chemical mechanisms. Interestingly, during the review of this manuscript, a study was published with *in vitro* work done using model buffer solutions of mucins, DNA, and other biopolymers further implying that aggregation of bacteria by host-polymers can be depletion-mediated (89). *In vivo*, it will also be important to consider the effects of flow, as it has been shown that flow in non-Newtonian fluids can induce particle aggregation (90–92). In particular, studies have suggested that the combination of flow and polymer elasticity can lead to aggregation (93) and that shear thinning viscosity can influence aggregation as well (94). In our work, we neglected flow effects for simplicity and thus our findings are most applicable to the initial formation of aggregates before aggregation is influenced by mechanical forces due to peristaltic mixing and the transit of food. A rudimentary estimate of the Weissenberg number (see *Materials and Methods)*, which weighs the contributions of elastic and viscous forces, yields $\mathrm{Wi} \sim 0.3$ to 10, suggesting that elasticity-induced effects may play a role in the SI and will be an important direction to pursue in follow-up studies. If flow-induced clustering does occur *in vivo*, the literature suggests it would aid in the process, perhaps enhancing particle aggregation.

We note that current dietary guidelines do not differentiate between fibers of low and high MW (95,96). Our work implies that the MW of fiber, and the subsequent degradation of a high-MW fiber into a low-MW component (97), which we have discussed previously in the context of mucus compression, is important in defining the physicochemical environment of the gut. Further studies will be required to understand the effects of industrial food processing on MW of the dietary polymers present in foods, and which

processing methods preserve or produce high-MW polymers that impact mucus compression (97) and particle aggregation in the gut.

MATERIALS AND METHODS

Table 5.1: Key Resources Table

Reagent type (species) or resource	Designation	Source or reference	Identifiers	Additional information
MUC2KO, C57BL/6 mice (female)	MUC2KO	Eugene Chang Lab provided initial breeding pairs which were provided to them from Leonard H. Augenlicht at the Department of Oncology of Albert Einstein Cancer Center		Genotyping was performed by Transnetyx Inc.; Western blot was done to confirm lack of MUC2 (See Fig. 5.5E)
Rag1KO, C57BL/6 mice (male)	Rag1KO	Provided by Mazmanian Lab at Caltech		Western blot was done to confirm lack of IgA as explained in the text (See Fig. 5.6E)
C57BL/6 mice (all male except for WT controls in MUC2KO experiments in **Figure** 5 and S3)	WT	The Jackson Laboratory		
antibody	MUC2 polyclonal antibody (rabbit host)	Biomatik	Cat No: CAU27315	

antibody	Li-Cor IRDye 800CW Goat Anti-Rabbit IgG	Li-Cor	P/N 925-32211	
antibody	Li-Cor IRDye 800 CW Goat Anti-Mouse IgG	Li-Cor	P/N 925-32210	
antibody	Li-Cor IRDye 800 CW Goat Anti-Mouse IgM	Li-Cor	P/N 925-32280	
antibody	Goat Anti-Mouse IgA-unlabeled	SouthernBiotech	Cat No: 1040-01	
antibody	Li-Cor IRDye 800 CW Donkey Anti-Goat IgG	Li-Cor	P/N 925-32214	
chemical compound, drug	apple pectin	Solgar Inc.	"Apple pectin powder"; SOLGB7012000B	
chemical compound, drug	Fibersol-2	Archer Daniels Midland/Matsutani LLC	Product code: 013100, Lot #: CY4P28540	
chemical compound, drug	USP grade sucrose	Sigma-Aldrich		
chemical compound, drug	Protease inhibitor cocktail	Roche cOmplete, Mini, EDTA-free Protease-Inhibitor cocktail, Roche		
chemical compound, drug	PEG 100kDa	Dow	POLYOX WSR N-10	
chemical compound, drug	PEG 1 MDa	Dow	POLYOX WSR N-12K	

chemical compound, drug	PEG 3350	Bayer	MiraLAX	
chemical compound, drug	Hanks' Balanced Salt Solution (without calcium, magnesium, phenol red)	GE Healthcare Life Sciences	Product code: SH30588.02	
software, algorithm	3D aggregate analysis pipeline	This paper; source code available through Dryad		Description in Materials and Methods; source code provided on Dryad
other	mesh-bottom (or wire-bottom) floors	Lab Products, Inc.	P/N: 75016	
other	1-µm diameter PEG 5kDa-coated polysytrene beads	This paper		Description of synthesis in Materials and Methods
other	1-µm diameter PEG 5kDa-coated polysytrene beads with PEG 1 kDa "back-filling"	This paper		Description of synthesis in Materials and Methods
other	standard chow diet	PicoLab	PicoLab Rodent Diet 20; Product #5053	
other	autoclaved chow diet	PicoLab	Laboratory Autoclavable Rodent Diet 5010	

Details of animals used

All mice were male or female specific pathogen free (SPF) C57BL/6 mice between 8-16 weeks old. Mice on a standard, solid chow diet were given food and water *ad libitum.* Immunoglobulin-deficient (Rag1KO) mice were maintained on an autoclaved chow diet due to their immunocompromised status. The control group of WT mice used as a comparison to this group was maintained on the same autoclaved chow diet for 48 h before euthanasia. Genotyping of MUC2 deficient (MUC2KO) and Rag1KO mice was done by Transnetyx (Transnetyx, Inc., Cordova, TN, USA). Mice given only apple pectin (Solgar, Inc., Leonia, NJ, USA) with sucrose (USP grade, Sigma-Aldrich, St. Louis, MO, USA) or Fibersol-2 (Archer Daniels Midland/Matsutani LLC, Chicago, IL, USA) with sucrose were first raised on a standard chow diet and given water *ad libitum,* then were maintained on a restricted diet consisting of only 2% apple pectin + 5% sucrose or 2% Fibersol-2 + 5% sucrose for 24 h. For those 24 h, these mice were kept on mesh-bottom cages to prevent the re-ingestion of polymers from the standard chow diet via coprophagy. The MUC2KO colony was raised and maintained by the Ismagilov Lab. The Rag1KO mice were provided by the Mazmanian lab (Caltech). All other mice were from Jackson Labs (The Jackson Laboratory, Bar Harbor, ME, USA). All animal experiments were approved by the California Institute of Technology (Caltech) Institutional Animal Care and Use Committee (IACUC) and the U.S. Army's Animal Care and Use Review Office (ACURO). Mice were euthanized via CO_2 inhalation as approved by the Caltech IACUC in accordance with the American Veterinary Medical Association Guidelines on Euthanasia (98).

Oral administration of particles

Particles were gavaged at a concentration of 0.1–2% w/v in either 1x HBSS or 1x PBS. We used small fluid volumes (50 µL) to minimize volume-related artifacts (3). We chose buffers isotonic to the SI because it has been shown that the isotonicity of the delivery medium can greatly affect the *in vivo* particle distribution (38). In some experiments, animals were food-restricted for 4 h prior to administration of particles. It has been

previously demonstrated though that food-restriction has minimal effects on the *in vivo* distribution of PEG-coated particles (3). In all experiments animals were euthanized 3 h after administration of particles.

Fluorescent scanner experiments

Gastrointestinal tracts (GIT) were excised and laid out flat on petri dishes on ice. Drops of saline were then placed around the GIT and the petri dishes were sealed with parafilm. Samples were then immediately brought to the fluorescent laser scanner (Typhoon FLA 9000) for imaging. Samples were scanned with an excitation wavelength of 473 nm and a 530 nm bandpass filter.

Imaging of luminal contents from mice orally administered particles

Immediately after euthanization the small intestines of the mice were excised and divided into an upper and lower section. The luminal contents were collected by gently squeezing the intestines with tweezers. They were placed directly onto a glass slide and encircled by a ring of vacuum grease that did not touch the contents. A coverslip was then immediately placed on top to create an air-tight chamber. Samples were kept on ice during the collection process. The samples were then immediately taken for imaging. All imaging was performed using a Zeiss LSM 800 or a Leica DMI6000, using either bright-field microscopy, epifluorescence microscopy (GFP, L5 Nomarski prism), confocal fluorescence microscopy (488 nm excitation and 490-540 nm detection), or confocal reflectance microscopy (561 nm excitation and 540-700 nm detection).

Collection of intestinal luminal fluid

Immediately after euthanasia, the SI of each mouse was excised and divided into an upper and lower section. If luminal fluid was collected from the colon, then the colon was also excised. The luminal contents were then collected from each section in separate tubes and kept on ice. The luminal contents from an individual mouse was insufficient in volume to perform all the required analyses (i.e. *ex vivo* aggregation, GPC, and sometimes Western

blot), so contents were pooled from a group of three mice of the same age that were co-housed. These pooled samples, kept divided by section, were then spun down at 17 kG at 4 °C for 1 h to separate the liquid and solid portions of the contents. The supernatant of each sample was collected and then placed on 30 µm filters (Pierce Spin Columns – Snap Cap, Thermo Fisher Scientific, Waltham, MA, USA) and spun down at 17 kG at 4 °C for 1 h. Part of the filtrates of each sample were then collected, divided into aliquots, and frozen at -20 °C for future experiments. The remaining portion of the filtrates was then taken and placed on 0.45 µm centrifugal filters (Corning Costar Spin-X centrifuge tube filters; cellulose acetate membrane, pore size 0.45 µm, sterile) and spun down at 5 kG at 4 °C for 1 h. For experiments in which a protease-inhibitor cocktail (Roche cOmplete, Mini, EDTA-free Protease-Inhibitor Cocktail, Roche, Indianapolis, IN, USA) was used, a 100x concentrated stock solution was prepared in HBSS (without calcium, magnesium, and phenol red; GE Healthcare Life Sciences, Marlborough, MA, USA). The same procedure as detailed above was followed for the collection of luminal fluid, except immediately after the luminal contents were brought back from the animal facility on ice, 10 µL of the 100x protease-inhibitor cocktail was added to each tube. The mixtures were then vortexed briefly to mix. The contents were then spun down at 17kG at 4 °C as described above to separate the solid from liquid contents. The liquid fraction collected from each group before 30 and 0.45 µm filtration was usually ~200–300 mL, so the additional 10 µL of protease-inhibitor cocktail only diluted the samples by ~5% at most.

Ex vivo and in vitro aggregation assays

We took 1-µm diameter PEG 5 kDa-coated polystyrene beads (with PEG 1 kDa “back-filling”) and suspended them at 10 mg/mL in deionized water. Before use, they were vortexed to re-suspend in solution and then sonicated for 1 min. The particle solution was then added to the polymer solution or small intestinal luminal fluid at a ratio of 1:10. After addition of particles, the mixture was vortexed for 10 seconds. Then, 2 µL of the mixture was then immediately pipetted into an imaging chamber created with a SecureSeal imaging spacer (0.12 mm depth and 9 mm diameter, Electron Microscopy Sciences, Hatfield, PA, USA) and a glass slide. The top of the imaging chamber was immediately sealed with a

#1.5 coverslip. The samples were then imaged approximately 10 min later. In PEG solution experiments and serial dilution experiments, HBSS (without calcium, magnesium, phenol red; GE Healthcare Life Sciences) was used to dilute.

In the 1 MDa PEG experiments conducted in phosphate buffered saline (PBS) with pH = 6 (**Figure** 4 – **Figure** supplement 1) the PBS solution was initially prepared with 138 mM sodium chloride, 7.5 mM monosodium phosphate dihydrate, 1.1 mM disodium phosphate heptahydrate, and deionized (DI) water (Milli-Q). The sodium chloride was added to ensure that the ionic strength matched that of Hank's balanced salt solution. The pH was then measured using an Orion 2-Star Benchtop pH Meter (Thermo Scientific) with an Orion 9110DJWP Double Junction pH electrode (Thermo Fisher Scientific) after first calibrating the instrument using the following reference standard buffers: pH = 10 (VWR BDH5078-500 mL), pH = 7 (VWR BDH5046-500 mL), and pH = 4 (VWR BDH5024-500 mL). The pH of the solution was then adjusted to pH = 6 using 1 M NaOH in DI water.

Microscopy for ex vitro and in vitro aggregation assays

All imaging was performed using a Zeiss LSM 800, using confocal fluorescence microscopy (488 nm excitation, detection at 490-540 nm). We collected 3D stacks which were 200 x 200 x 40 µm in volume. 3D renders of aggregates were created using Imaris software from Bitplane, an Oxford Instruments Company.

Imaging analysis

All image analysis was done in FIJI (ImageJ 2.0.0) using an ImageJ macro written using the ImageJ macro scripting language. These macros are available in Dryad. Z-stacks were saved as 16 bit .czi files and were subsequently loaded into FIJI. Each z-stack extended ~40 µm deep into each sample in the z-direction and was composed of 113 slices. As a result of the depth of the stacks in the z-direction, we observed a significant drop-off in measured aggregate fluorescence between the first slice and the last slice, likely due to scattering from the intestinal fluid and the particles themselves. To ensure that aggregates throughout a given stack had a similar brightness, which is important for the 3D Object

Counter plugin, the median pixel intensity for aggregates in every slice was set as the maximum pixel intensity value for every slice. To achieve this, first the 10^{th} slice and the 10^{th} to last slice of the z-stack were selected and thresholded using the Otsu method (99), creating a binary image of the aggregates in the two slices. The binary images were used as masks to measure the median pixel intensity of each aggregate in the two slices as well as the mean and max pixel intensity values for the background of both images. The drop-off in intensity was assumed to be approximately linear, so the median pixel intensity for aggregates in each slice was determined by interpolating between the median aggregate pixel intensity values from the 10^{th} slice and 10^{th} to last slice. The minimum pixel intensity value for each slice was determined by adding 1/3 of the mean background pixel intensity to 2/3 of the maximum background pixel intensity for the 10^{th} and 10^{th} to last slices (this was necessary to deal with the challenge determining background pixel intensities) and then interpolating to calculate the minimum for all other slices. The process of intentionally introducing image clipping in the z-stacks was justified by the manner in which aggregates were identified; aggregates were first measured by total volume instead of by particle count, thus being able to discern individual particles inside of each aggregate was unnecessary.

The 3D Objects Counter plugin in FIJI was used to measure various parameters, including the volume of each aggregate. The plugin initially thresholds all slices in a stack using a single thresholding value, which requires objects in every slice of a stack to be roughly the same intensity (hence, the thresholding procedure described previously). The plugin takes the resulting now-binary z-stack and determines the number of voxels occupied by each aggregate and converts voxel volume to metric volume using metadata in each .czi file. A second macro was used to determine the average size of a singlet (single particle) for each z-stack. In this macro, we identified 10 singlets by visually inspecting the sample to determine the average size of a singlet. This was then used to normalize differences in measured aggregate volume between samples by converting to a particle count per aggregate. This normalization step was necessary due to variations in the average measured singlet size between samples. It also helped account for any differences in the thresholding procedure from sample to sample.

The accuracy of this method for determining aggregate sizes was validated by comparing empirical cumulative distribution functions (ECDFs) of the cross-sectional area of the aggregates in a given z-stack determined by the ImageJ macro to ECDFs generated by visually inspecting the samples to measure the cross-sectional areas of aggregates. This comparison was done for at least three separate z-stacks. ImageJ macros will be made available upon request.

Quantification of aggregate sizes

The sizes of aggregates in solution were quantified in two ways. One was by comparing the volume-weighted empirical cumulative distribution functions (ECDFs) of the aggregate sizes of each sample to each other. The volume-weighted ECDF, $\hat{F}$, as follows (100):

$$\hat{F}(N) = \frac{1}{\sum N_i} \sum_{i=1}^{n} I(N_i \leq N) \qquad (Eq. 5.6)$$

$$I(N_i \leq N) = \begin{cases} N_i \; if \; N_i \leq N \\ 0 \; if \; N_i > N \end{cases} \qquad (Eq. 5.7)$$

Where N_i is the number of particles per aggregate and n is the total number of aggregates in solutions (where single particles also count as aggregates).

The other way in which the extent of aggregation was quantified was by creating bootstrap replicates of the ECDFs of the aggregate distributions of each sample and computing the volume-weighted average aggregate size ($\langle N \rangle$; given in number of particles per aggregate) for each bootstrap replicate. The volume-weighted average aggregate size is given by the following equation in units of "number of particles per aggregate":

$$\langle N \rangle = \frac{\sum_{i=1}^{n} N_i^2}{\sum_{i=1}^{n} N_i} \qquad (Eq. 5.8)$$

This allowed us to calculate 95% empirical bootstrap CI on the volume-weighted average aggregate size. We generated 10,000 bootstrap replicates from the original ECDF of each sample to generate these. The advantage of this approach is that we do not need to assume anything about the underlying probability distribution; it is non-parametric (100). The original ECDFs, from which the replicates were generated, each contained at least 300 aggregates, in many cases containing ~1000 or more aggregates. The codes used for the analyses (volume-weighted ECDFs and 95% empirical bootstrap CIs) were written in Python 3.6.4 and are available on Dryad.

Filtration with MW cut-off filters

Small intestinal luminal fluid was collected and 0.45 µm-filtered as described in "Collection of Luminal Fluid". It was then divided up and placed on MWCO filters (Pierce Protein Concentrators, Thermo Fisher Scientific) of with the following MWCOs: 100 kDa, 30 kDa, and 3 kDa. The samples were then centrifuged at 15 kG at 4 °C for 2 h, checking every 15 min for the first hour if additional volume had flowed through. After the eluent from each was collected, they were diluted back to their original volumes with HBSS.

pH measurements of luminal fluid

Pooled samples of luminal fluid were collected from each section (stomach, upper small intestine, lower small intestine, cecum, and colon) and 30 µm-filtered as described in "Collection of Luminal fluid" (with use of the same protease inhibitor cocktail). Samples were collected from two separate groups of 2-month old B6 male mice on a standard chow diet. Each group had three mice. Because there was only ~25 µL of luminal fluid from the colons of each group we did not 30 µm-filter the colonic fluid as there was concern all the fluid would be retained by the filter. The colonic contents were simply spun down at 17 kG at 4 °C for 1 h to separate the liquid and solid portions of the contents. Then the supernatant (luminal fluid) was collected. Measurements were done using an Orion 2-Star Benchtop pH Meter. The instrument was first calibrated with three reference standard buffers: pH = 10 (VWR BDH5078-500 mL), pH = 7 (VWR BDH5046-500 mL), and pH = 4 (VWR BDH5024-500 mL). Measurements were conducted at T = 25 °C. There was at

least 100 µL of sample from each section except for the stomach sample from one group of mice and from colon samples from both groups. Measurements were conducted with both a standard pH electrode (Orion 9110DJWP Double Junction pH Electrode) and a micro pH electrode (Orion 9810BN Micro pH Electrode, Thermo Fisher Scientific). This was done because the standard electrode is only accurate for samples with volumes of 200 µL whereas the micro electrode is accurate for samples as small as 0.5 µL in volume. The results are consistent with other results for rodents (101,102) with the exception of a study conducted with mice of a different gender, strain, and fed an 18% protein diet (103).

For the pH measurement of HBSS, the pH was measured with both the standard and micro pH electrodes, and three technical replicates were done with each probe. The value for the pH reported in the main text is the average of all six measurements.

Estimation of coverage and length of grafted PEG layer

Based on our NMR measurements (see section NMR of PEG-coated particles with "backfill") the grafting density (Γ) of the PEG polymer on our PEG 5 kDa-coated particles with PEG 1 kDa backfill should be approximately: $\Gamma = 0.48\ \text{chains/nm}^2$ (to estimate this we assume that all of the PEG on the surface is PEG 5 kDa). One can estimate the grafting density at which the grafted chains transition from separate coils to overlapping coils or the brush regime by calculating the grafting density at which coils would just begin to overlap (104). This can be estimated as:

$$\Gamma^* \sim \frac{1}{\pi R_g^2} \qquad (Eq.\,5.9)$$

Where R_g is the radius of gyration of the grafted polymer. Using literature measurements of the hydrodynamic radius of PEG 5 kDa and the Kirkwood-Riseman relation, this can be estimated as $R_g \sim 3.45$ nm. We therefore estimate that $\frac{\Gamma}{\Gamma^*} \sim 5$, meaning that the grafting density is such that the polymer coils on the surface should be overlapping and within the brush regime. To estimate the length and average volume fraction of the layer, we therefore made the assumption that the grafted polymer layer behaved as a brush and used the

Alexander-deGennes brush approximation (63,105). This theory was originally developed for high-MW polymer coils, but has also been found, surprisingly, to quantitatively capture forces for grafted layers only a few segments long (105). We estimated the length (L) of the brush as (63):(62,95). This theory was originally developed for high-MW polymer coils, but has also been found, surprisingly, to quantitatively capture forces for grafted layers only a few segments long . We estimated the length (L) of the brush as :

$$L \sim N\Gamma^{\frac{1-\nu}{2\nu}} b^{\frac{1}{\nu}} \qquad (Eq.5.10)$$

Where N is the number of monomers per grafted chain, ν is the Flory exponent, and b is the Kuhn length of the grafted polymer. We used b = 0.76 nm based on literature measurements (106) and took $\nu \cong 0.588$, because aqueous salt solutions are good solvents for PEG (107). Lastly, we estimated the number of monomers per chain by assuming the number of monomers is approximately equation to the number of Kuhn segments and the relationship between the radius of gyration, the Kuhn length and the number of Kuhn segments (63): $N \sim \left(\frac{R_g}{b}\right)^{\frac{1}{0.588}} \sim 13$. We therefore estimate that $L \sim 6.4\ nm$.

The Alexander–de Gennes approximation assumes a step profile for the volume fraction of the grafted polymer (ϕ). We can estimate this using the following equation (63):

$$\phi \approx \begin{cases} (\Gamma b^2)^{\frac{3\nu-1}{2\nu}} \ for\ z < L \\ 0 \ for\ z > L \end{cases} \qquad (Eq.5.11)$$

Where z is the distance from the bare particle surface. Using the same approximations as above we find $\phi \approx 0.43$.

Western blot of luminal contents

30-µm filtered small intestinal luminal fluid was reduced in sample buffer with 100 mM dithiotreitol DTT at 95 °C for 5 min (the luminal fluid was diluted 10-fold in the sample buffer). Gel electrophoresis was then run on 4–15% SDS/PAGE gels. The transfer was performed using wet electroblotting to a nitrocellulose membrane. For detection of MUC2,

the primary antibody was diluted 1:1,000 (MUC2 polyclonal antibody, rabbit host, Biomatik, Wilmington, DE, USA) as a 1:10,000 in Odyssey blocking buffer (Li-Cor, Lincoln, NE, USA) with 0.2% Tween 20. The secondary antibody (Li-Cor IRDye 800CW Goat Anti-Rabbit IgG, Li-Cor) was diluted 1:10,000. For the detection of IgG and IgM, 1:10,000 dilutions of Li-Cor IRDye 800 CW Goat Anti-Mouse IgG and Li-Cor IRDye 800CW Goat Anti-Mouse IgM were used respectively. For detection of IgA, a 1:10,000 dilution of SouthernBiotech Goat Anti-Mouse IgA-unlabeled was used as the primary and a 1:10,000 dilution of Li-Cor IRDye 800CW Donkey Anti-Goat IgG was used as the secondary. All membranes were visualized using a Li-Cor Odyssey scanner.

Gel permeation chromatography

We used a Malvern OMNISEC RESOLVE connected to two Malvern A6000M columns (Malvern, Westborough, MA, USA) equilibrated with 1x PBS with 0.02% sodium azide, flow rate: 0.75 mL/min. For detection of the polymers, the OMNISEC REVEAL was used with a refractometer, UV detector, dual-angle light scattering detector, and a capillary viscometer. Luminal contents were 0.45-µm filtered as described above, then diluted 10-fold in the running buffer (1x PBS with 0.02% sodium azide) before injection into the system. Prior to injection, samples were kept on the autosampler at 4 °C.

Synthesis of PEG-coated particles

We amended a previously published protocol (3) to synthesize PEG-coated particles; briefly, 2 mL of 1-µm fluorescent carboxylic-acid-terminated polystyrene beads (FluoroSpheres, Invitrogen, Thermo Fisher Scientific) at 2% v/v with 2 mM NaN_3 were rinsed at 3900g for 40 min using a centrifugal filter (Millipore Amicon Ultra-4 mL 100 K MWCO). Particles were removed from the filter using 4 mL of a solution of 15 mg/mL 1-Ethyl-3-(3-dimethylaminopropyl)carbodiimide (EDC, Sigma-Aldrich) and 15 mg/mL N-hydrosuccinimide (NHS, Aldrich), an excess concentration of NH_2-PEG-OMe (5 kDa, Creative PEGworks, Chapel Hill, NC, USA) in 1 mL increments using 100 mM borate buffer, pH 8.4. By an excess concentration of NH_2-PEG-OMe we mean ten-fold the concentration of PEG required to enter the polymer brush regime (see “Estimation of

coverage and length of grafted PEG layer" section for details of calculation). This solution was tumbled on a rotary tumbler for 4 h at room temperature in a 15 mL falcon tube. Particles were washed three times to remove starting materials with 4 mL Milli-Q water in a centrifugal filter and re-suspended in 2 mL in Milli-Q water.

Synthesis of PEG-coated particles with "backfill."

12 mL of 1-µm fluorescent carboxylic-acid-terminated polystyrene beads at 2% v/v with 2 mM NaN_3 (FluoroSpheres 1-µm; 505/515, Invitrogen) were centrifuged to a pellet at 12,000g for 10 min. Beads were pelleted and rinsed three times with Milli-Q water. To the final pellet of particles, 12 mL of a solution of 6 mM EDC (10 mg/mL; Sigma-Aldrich) and 5 mM Sulfo-NHS (1.08 mg/mL, ThermoFisher), with 50x excess of the number of chains needed to enter the brush regime (see "Estimation of coverage and length of grafted PEG layer" for details of calculation) of NH_2-PEG-OMe (mPEG-Amine 2kDa; mPEG-Amine 5kDa; Creative PEGWorks) in 10x PBS, pH 7.4 (100 mM), was added. This solution was tumbled on a rotary tumbler for 4 h at room temperature. Tubes were vented every 30 min to release gas produced by the reaction. Particles were then pelleted and rinsed three times with Milli-Q water. The 12 mL sample was divided into four 3 mL aliquots for the remaining conditions. For condition without backfill, beads were quenched with 50 mM Tris pH 7.4 overnight at room temperature with slow tilt rotation prepared from 10x Tris-buffered saline with Tween 20, pH 7.5 (Sigma-Aldrich). For particles with backfill, the 3-mL aliquot was re-suspended in with 50x excess of the number of chains needed to enter the brush regime (see "Estimation of coverage and length of grafted PEG layer" for details of calculation) of NH_2-PEG-OMe (mPEG-Amine 350; mPEG-Amine 1 kDa; mPEG-Amine 5kDa, Creative PEGWorks) in 100 mM PBS, pH 7.4 containing 6 mM EDC and 5 mM Sulfo-NHS for 4 h before quenching overnight with 50 mM TRIS buffered Saline with Tween 20, pH 7.5. All beads were washed three times with Milli-Q water before suspending in 3 mL sterile filtered PBS, pH7.4 with 1% BSA for storage.

NMR of PEG-coated particles with "backfill."

We took 400 µl of 2% w/v samples and lyophilized (~8 mg), then dissolved in deuterated chloroform (Cambridge Isotope Laboratories, Tewksbury, MA, USA) with 0.01% tetramethylsilane (Aldrich) immediately before measurement. Data were collected on a Varian Innova 600 MHz spectrometer without spinning, using a 45^{o} pulse width and 1 sec relaxation delay between scans. The concentration of PEG in each sample was determined by integrating the singlet at 3.64 pm and normalizing the integral to TMS internal standard at 0.0 ppm.

Zeta potential measurements on PEG-coated particles with "backfill."

Each particle solution was 0.1 mg/mL of particles in 1 mM KCl. Measurements were done on a Brookhaven NanoBrook ZetaPALS Potential Analyzer (Brookhaven Instruments Corporation, Holtsville, NY, USA). Three trials were done where each trial was 10 runs each and each run was 10 cycles. Values reported are the average zeta potential for the 30 runs.

Estimate of Weissenberg number for small intestine

The Weissenberg number (Wi), which weighs the relative contributions of elastic and viscous forces, can be written as (108):

$$Wi = \dot{\gamma}\lambda \qquad (Eq. 5.12)$$

Where $\dot{\gamma}$ is the shear rate (in s^{-1}) and λ is the fluid relaxation time (in *s*). The shear rate in the human small intestine during peristaltic contractions has been estimated as $\dot{\gamma} \sim 29\ s^{-1}$ (109). For dilute aqueous polymeric solutions of polyacrylamide with MWs ranging from 10^4 to 10^7 Da, it has been found that $\lambda = 0.009$ to 0.45 s, with the relaxation time increasing with MW as $\lambda\, \alpha\, MW^{2/3}$(110). Using these values, we can estimate the Weissenberg number to be Wi ~ 0.3 to 10.

Author contributions

APS, SSD, and RFI designed the research; APS, SSD, JCR, SRB performed the research; APS, SSD, TN, JCR, SRB contributed new reagents/analytic tools; APS analyzed the data. All authors wrote the paper.

Acknowledgements

This work was supported in part by DARPA Biological Robustness in Complex Settings (BRICS) contract HR0011-15-C-0093, Army Research Office (ARO) Multidisciplinary University Research Initiative (MURI) contract #W911NF-17-1-0402, the Jacobs Institute for Molecular Engineering for Medicine, and an NSF Graduate Research Fellowship DGE-144469 (to APS). We acknowledge Michael Porter, Joong Hwan Bahng, Jacob Barlow, Zhen-Gang Wang, Julia Kornfield, David Tirrell, Justin Bois, and Greg Donaldson for useful discussions; the Beckman Institute Biological Imaging Facility, the Broad Animal Facility, and the Church Animal Facility for experimental resources; Jennifer Costanza, Taren Thron, the Caltech Office of Laboratory Animal Resources, and the veterinary technicians at the California Institute of Technology for technical support; Joanne Lau for assistance with Western blot measurements; Emily Wyatt for assistance with zeta potential measurements; the Mazmanian laboratory for providing Rag1KO mice; the Eugene Chang Lab (University of Chicago) for providing the initial breeding pairs for the MUC2KO colony and Leonard H. Augenlicht at the Department of Oncology of Albert Einstein Cancer Center for providing the original MUC2KO line to them; and Natasha Shelby for contributions to writing and editing this manuscript.

Competing interests

The technology described in this publication is the subject of a patent application filed by Caltech.

Data availability statement

All source data and data codes are available from the Dryad Digital Repository: https://doi.org/10.5061/dryad.kd1qt0p.

References

1. Donaldson GP, Lee SM, Mazmanian SK. Gut biogeography of the bacterial microbiota. Nat Rev Microbiol [Internet]. 2015;14(1):20–32. Available from: http://www.nature.com/doifinder/10.1038/nrmicro3552

2. McGuckin MA, Lindén SK, Sutton P, Florin TH. Mucin dynamics and enteric pathogens. Nat Rev Microbiol [Internet]. 2011;9(4):265–78. Available from: http://dx.doi.org/10.1038/nrmicro2538

3. Maisel K, Ensign L, Reddy M, Cone R, Hanes J. Effect of surface chemistry on nanoparticle interaction with gastrointestinal mucus and distribution in the gastrointestinal tract following oral and rectal administration in the mouse. J Control Release. 2015;40(6):1301–15.

4. Goldberg M, Gomez-Orellana I. Challenges for the oral delivery of macromolecules. Nat Rev Drug Discov [Internet]. 2003;2(4):289–95. Available from: http://www.nature.com/doifinder/10.1038/nrd1067

5. Faisant N, Gallant DJ, Bouchet B, Champ M. Banana starch breakdown in the human small intestine studied by electron microscopy. Eur J Clin Nutr [Internet]. 1995;49(2):98–104. Available from: http://europepmc.org/abstract/MED/7743990

6. Millet YA, Alvarez D, Ringgaard S, von Andrian UH, Davis BM, Waldor MK. Insights into Vibrio cholerae intestinal colonization from monitoring fluorescently labeled bacteria. PLoS Pathog. 2014;10(10).

7. Lukic J, Strahinic I, Milenkovic M, Nikolic M, Tolinacki M, Kojic M, et al. Aggregation factor as an inhibitor of bacterial binding to gut mucosa. Microb Ecol. 2014;68(3):633–44.

8. Del Re B, Busetto A, Vignola G, Sgorbati B, Palenzona D. Autoaggregation and adhesion ability in a Bifidobacterium suis strain. Lett Appl Microbiol. 1998;27:307–10.

9. Kos B, Šušković J, Vuković S, Šimpraga M, Frece J, Matošić S. Adhesion and aggregation ability of probiotic strain Lactobacillus acidophilus M92. J Appl Microbiol [Internet]. 2003;94(6):981–7. Available from: http://doi.wiley.com/10.1046/j.1365-2672.2003.01915.x

10. Tzipori S, Montanaro J, Robins-Browne RM, Vial P, Gibson R, Levine MM. Studies with enteroaggregative Escherichia coli in the gnotobiotic piglet gastroenteritis model. Infect Immun. 1992;60(12):5302–6.

11. Howe SE, Lickteig DJ, Plunkett KN, Ryerse JS, Konjufca V. The uptake of soluble and particulate antigens by epithelial cells in the mouse small intestine. PLoS One [Internet]. 2014;9(1):e86656. Available from: http://www.ncbi.nlm.nih.gov/pubmed/24475164

12. Puri S, Friedman J, Saraswat D, Kumar R, Li R, Ruszaj D, et al. Candida albicans shed Msb2 and gost mucins affect the Candidacidal activity of salivary Hst 5. Pathogens [Internet]. 2015;4(4):752–63. Available from: http://www.mdpi.com/2076-0817/4/4/752/

13. Laux DC, McSweegan EF, Williams TJ, Wadolkowski E a, Cohen PS. Identification and characterization of mouse small intestine mucosal receptors for Escherichia coli K-12(K88ab). Infect Immun [Internet]. 1986;52(1):18–25. Available from: http://www.pubmedcentral.nih.gov/articlerender.fcgi?artid=262191&tool=pmcentrez&rendertype=abstract

14. Sajjan SU, Forstner JF. Characteristics of binding of Escherichia coli serotype O157:H7 strain CL-49 to purified intestinal mucin. Infect Immun. 1990;58(4):860–7.

15. Wanke C a., Cronan S, Goss C, Chadee K, Guerrant RL. Characterization of binding of Escherichia coli strains which are enteropathogens to small-bowel

mucin. Infect Immun. 1990;58(3):794–800.

16. Sun J, Le GW, Shi YH, Su GW. Factors involved in binding of Lactobacillus plantarum Lp6 to rat small intestinal mucus. Lett Appl Microbiol. 2007;44(1):79–85.

17. Doe WF. The intestinal immune system. Gut. 1989;30:1679–85.

18. Peterson DA, McNulty NP, Guruge JL, Gordon JI. IgA response to symbiotic bacteria as a mediator of gut homeostasis. Cell Host Microbe. 2007;2(5):328–39.

19. Levinson KJ, Jesus M De, Mantis NJ. Rapid effects of a protective O-polysaccharide-specific monoclonal IgA on Vibrio cholerae agglutination, motility, and surface morphology. Infect Immun. 2015;83(4):1674–83.

20. Hendrickx APA, Top J, Bayjanov JR, Kemperman H, Rogers MRC, Paganelli FL, et al. Antibiotic-driven dysbiosis mediates intraluminal agglutination and alternative segregation of enterococcus faecium from the intestinal epithelium. MBio. 2015;6(6):1–11.

21. Endt K, Stecher B, Chaffron S, Slack E, Tchitchek N, Benecke A, et al. The microbiota mediates pathogen clearance from the gut lumen after non-typhoidal salmonella diarrhea. PLoS Pathog. 2010;6(9).

22. Bunker JJ, Erickson SA, Flynn TM, Henry C, Koval JC, Meisel M, et al. Natural polyreactive IgA antibodies coat the intestinal microbiota. Science (80-) [Internet]. 2017;358(6361):eaan6619. Available from: http://www.sciencemag.org/lookup/doi/10.1126/science.aan6619

23. Moor K, Diard M, Sellin ME, Felmy B, Wotzka SY, Toska A, et al. High-avidity IgA protects the intestine by enchaining growing bacteria. Nature [Internet]. 2017;544(7651):498–502. Available from: http://www.nature.com/doifinder/10.1038/nature22058

24. Mantis NJ, Rol N, Corthésy B. Secretory IgA's complex roles in immunity and mucosal homeostasis in the gut. Mucosal Immunol [Internet]. 2011;4(6):603–11. Available from: http://www.nature.com/doifinder/10.1038/mi.2011.41

25. Donaldson GP, Ladinsky MS, Yu KB, Sanders JG, Yoo BB, Chou WC, et al. Gut microbiota utilize immunoglobulin A for mucosal colonization. Science (80-) [Internet]. 2018;800(May):eaaq0926. Available from: http://www.sciencemag.org/lookup/doi/10.1126/science.aaq0926

26. Bergström JH, Birchenough GMH, Katona G, Schroeder BO, Schütte A, Ermund A, et al. Gram-positive bacteria are held at a distance in the colon mucus by the lectin-like protein ZG16. Proc Natl Acad Sci [Internet]. 2016;113(48):13833–8. Available from: http://www.pnas.org/lookup/doi/10.1073/pnas.1611400113

27. Asakura S, Oosawa F. On interaction between two bodies immersed in a solution of macromolecules. J Chem Phys. 1954;22(1954):1255–6.

28. Asakura S, Oosawa F. Interaction between particles suspended in solutions of macromolecules. J Polym Sci. 1958;33:183–92.

29. Vrij A. Polymers at interfaces and the interactions in colloidal dispersions. Pure Appl Chem. 1976;48:471–83.

30. Gast AP, Hall CK, Russel WB. Polymer-induced phase separations in nonaqueous colloidal suspensions. J Colloid Interface Sci [Internet]. 1983 [cited 2018 Apr 19];96(1):251–67. Available from: https://ac.els-cdn.com/0021979783900279/1-s2.0-0021979783900279-main.pdf?_tid=92957995-976d-4b56-89e5-375e1f3503e6&acdnat=1524159252_a80a1a5abbd1c629ca137cfe2b85a79d

31. Prasad V. Weakly interacting colloid polymer mixtures. Harvard University; 2002.

32. Lu PJ, Conrad JC, Wyss HM, Schofield AB, Weitz DA. Fluids of clusters in attractive colloids. Phys Rev Lett. 2006;96(2):28306.

33. Ilett S, Orrock A, Poon W, Pusey P. Phase behavior or a model colloid-polymer mixtures. Phys Rev E. 1995;51(2):1344–53.

34. Valentine MT, Perlman ZE, Gardel ML, Shin JH, Matsudaira P, Mitchison TJ, et al. Colloid surface chemistry critically affects multiple particle tracking measurements of biomaterials. Biophys J. 2004;86(6):4004–14.

35. Wang Y-Y, Lai SK, Suk JS, Pace A, Cone R, Hanes J. Addressing the PEG mucoadhesivity paradox to engineer nanoparticles that “Slip” through the human mucus barrier. Angew Chemie-International Ed. 2008;47(50):9726–9.

36. Ensign LM, Cone R, Hanes J. Oral drug delivery with polymeric nanoparticles: the gastrointestinal mucus barrier. Adv Drug Deliv Rev. 2012;64(6):557–70.

37. Tirosh B, Rubinstein A. Migration of adhesive and nonadhesive particles in the rat intestine under altered mucus secretion conditions. J Pharm Sci. 1998;87(4):453–6.

38. Maisel K, Chattopadhyay S, Moench T, Hendrix C, Cone R, Ensign LM, et al. Enema ion compositions for enhancing colorectal drug delivery. J Control Release [Internet]. 2015;209:280–7. Available from: http://dx.doi.org/10.1016/j.jconrel.2015.04.040

39. Hasler W. Motility of the small intestine and colon. In: Alpers DH, Kalloo AN, Kaplowitz N, Owyang C, Powell DW, editors. Textbook of Gastroenterology, Fifth Edition. 5th ed. Blackwell Publishing; 2009. p. 231–263.

40. Lai SK, Wang YY, Hanes J. Mucus-penetrating nanoparticles for drug and gene delivery to mucosal tissues. Adv Drug Deliv Rev [Internet]. 2009;61(2):158–71. Available from: http://dx.doi.org/10.1016/j.addr.2008.11.002

41. Rubio-Tapia A, Barton SH, Rosenblatt JE, Murray JA. Prevalence of small intestine bacterial overgrowth diagnosed by quantitative culture of intestinal aspirate in celiac disease. J Clin Gastroenterol. 2009;43(2):157–61.

42. O'Hara AM, Shanahan F. The gut flora as a forgotten organ. EMBO Rep. 2006;7(7):688–93.

43. Simon GL, Gorbach SL. Intestinal flora in health and disease. Gastroenterology [Internet]. 1984;86(1):174–93. Available from: http://www.gastrojournal.org/article/0016508584906061/fulltext

44. Padmanabhan P, Grosse J, Asad ABMA, Radda GK, Golay X. Gastrointestinal transit measurements in mice with 99mTc-DTPA-labeled activated charcoal using NanoSPECT-CT. EJNMMI Res [Internet]. 2013;3(1):60. Available from: http://www.pubmedcentral.nih.gov/articlerender.fcgi?artid=3737085&tool=pmcentrez&rendertype=abstract

45. Royall CP, Poon WCK, Weeks ER. In search of colloidal hard spheres. Soft Matter. 2013;9(1):17–27.

46. Pusey PN, Van Megen W. Phase behaviour of concentrated suspensions of nearly hard colloidal spheres. Nature. 1986;320(6060):340–2.

47. Lekkerkerker HNW, Poon WCK, Pusey PN, Stroobants A, Warren PB. Phase behavior of colloid + polymer mixtures. Europhys Lett. 1992;20(6):559.

48. Lu PJ, Zaccarelli E, Ciulla F, Schofield AB, Sciortino F, Weitz DA. Gelation of particles with short-range attraction. Nature. 2008;453(7194):499–503.

49. Zaccarelli E, Lu PJ, Ciulla F, Weitz DA, Sciortino F. Gelation as arrested phase separation in short-ranged attractive colloid-polymer mixtures. J Phys Condens Matter. 2008;20(49).

50. Vincent B, Edwards J, Emmett S, Jones A. Depletion flocculation in dispersions of sterically-stabilised particles ("soft spheres"). Colloids and Surfaces. 1986;18(2–4):261–81.

51. Cowell C, Li-In-On R, Vincent B. Reversible flocculation of sterically-stabilised dispersions. J Chem Soc Faraday Trans 1 [Internet]. 1978;74(0):337. Available from: http://xlink.rsc.org/?DOI=f19787400337

52. Vincent B, Luckham PF, Waite FA. The effect of free Polymer on the stability of sterically stabilized dispersions. J Colloid Interface Sci. 1980;73(2):508.

53. Clarke J, Vincent B. Nonaqueous silica dispersions stabilized by terminally anchored polystyrene: The effect of added polymer. J Colloid Interface Sci. 1981;82(1):208–16.

54. Feigin RI, Napper DH. Depletion stabilization and depletion flocculation. J Colloid Interface Sci. 1980;75(2):525–41.

55. Vincent B, Clarke J, Barnett KG. The Flocculation of non-aqueous, sterically-stabilised latex dispersions in the presence of free polymer. Colloids and Surfaces. 1986;17(1):51–65.

56. Gast AP, Leibler L. Interactions of Sterically Stabilized Particles Suspended in a Polymer Solution. Macromolecules. 1986;19(3):686–91.

57. Jones A, Vincent B. Depletion flocculation in dispersions of sterically-stabilised particles 2. Modifications to theory and further studies. Colloids and Surfaces. 1989;42(1):113–38.

58. Napper DH. Polymeric stabilization of colloidal dispersions. 1983. 398-399 p.

59. Lindahl A, Ungell A-L, Knutson L, Lennernas H. Characterization of Fluids from the Stomach and Proximal Jejunum in Men and Women. Pharm Res. 1997;14(4):497–502.

60. Fuchs A, Dressman JB. Composition and physicochemical properties of fasted-state human duodenal and jejunal fluid: A critical evaluation of the available data.

J Pharm Sci. 2014;103(11):3398–411.

61. Yethiraj A, Van Blaaderen A. A colloidal model system with an interaction tunable from hard sphere to soft and dipolar. Nature. 2003;421(6922):513–7.

62. Jones RAL. Colloidal dispersions. In: Soft Condensed Matter. 1st ed. New York: OXford University Press; 2002. p. 52–62.

63. Rubinstein M, Colby RH. Polymer Physics. New York: OUP Oxford; 2003.

64. Cai L-H. Structure and Function of Airway Surface Layer of the Human Lungs and Mobility of Probe Particles in Complex Fluids. Vol. PhD, Chemistry. [Chapel Hill]: University of North Carolina; 2012.

65. Burchard W. Structure formation by polysaccharides in concentrated solution. Biomacromolecules. 2001;2(2):342–53.

66. Joanny JF, Leibler L, De Gennes PG. Effects of polymer solutions on colloid stability. J Polym Sci Polym Phys Ed. 1979;17:1073–84.

67. Verma R, Crocker JC, Lubensky TC, Yodh AG. Entropic colloidal interactions in concentrated DNA Solutions. Phys Rev Lett. 1998;81(18):4004–7.

68. Armstrong JK, Wenby RB, Meiselman HJ, Fisher TC. The hydrodynamic radii of macromolecules and their effect on red blood cell aggregation. Biophys J. 2004;87(6):4259–70.

69. Tanford C. Physical Chemistry of Macromolecules. New York: Wiley; 1961.

70. Lee H, Venable RM, Mackerell AD, Pastor RW. Molecular dynamics studies of polyethylene oxide and polyethylene glycol: hydrodynamic radius and shape anisotropy. Biophys J [Internet]. 2008;95(4):1590–9. Available from: http://dx.doi.org/10.1529/biophysj.108.133025

71. Flory PJ. Principles of Polymer Chemistry. Ithaca, New York: Cornell University Press; 1953.

72. Brandup J, Immergut E. Polymer Handbook. 2nd ed. John Wiley; 1975.

73. Weitz D, Huang J, Lin M, Sung J. Dynamics of diffusion-limited kinetic aggregation. Phys Rev Lett. 1984;53(17):1657–60.

74. Ball RC, Weitz DA, Witten TA, Leyvraz F. Universal kinetics in reaction-limited aggregation. Phys Rev Lett. 1987;58(3):274–7.

75. Smoluchowski M. Drei Vortrage uber Diffusion, Brownsche Bewegung und Koagulation von Kolloidteilchen. Phys Zeit. 1916;17:557–85.

76. Ermund A, Schütte A, Johansson ME V, Gustafsson JK, Hansson GC, Schuette A. Gastrointestinal mucus layers have different properties depending on location - 1. Studies of mucus in mouse stomach, small intestine, Peyer's patches and colon. Am J Physiol Gastrointest Liver Physiol [Internet]. 2013;305(5):ajpgi.00046.2013-. Available from: http://ajpgi.physiology.org/content/early/2013/07/05/ajpgi.00046.2013.reprint

77. Johansson ME V, Ambort D, Pelaseyed T, Schütte A, Gustafsson JK, Ermund A, et al. Composition and functional role of the mucus layers in the intestine. Cell Mol Life Sci. 2011;68(22):3635–41.

78. Ambort D, Johansson ME V., Gustafsson JK, Nilsson HE, Ermund a., Johansson BR, et al. Calcium and pH-dependent packing and release of the gel-forming MUC2 mucin. Proc Natl Acad Sci. 2012;109(15):5645–50.

79. Murphy K, Travers P, Walport M. Janeway's Immunobiology. 8th ed. Current Biology, Ltd.; 2004.

80. Kishimoto Y, Kanahori S, Sakano K, Ebihara S. The maximum single dose of

resistant maltodextrin that does not cause diarrhea in humans. J Nutr Sci Vitaminol (Tokyo) [Internet]. 2013;59(4):352–7. Available from: http://www.ncbi.nlm.nih.gov/pubmed/24064737

81. Fibersol-2 FAQ's [Internet]. Available from: http://www.fibersol.com/products/fibersol-2/faqs/

82. Dongowski G, Lorenz A, Anger H. Degradation of pectins with different degrees of esterification by Bacteroides thetaiotaomicron isolated from human gut flora. Appl Environ Microbiol. 2000;66(4):1321–7.

83. Thakur BR, Singh RK, Handa AK. Chemistry and Uses of Pectin - A Review. Crit Rev Food Sci Nutr. 1997;37(1):47–73.

84. Holloway W, Tasman-Jones C, Maher K. Pectin digestion in humans. Am J Clin Nutr. 1983;37(2):253–5.

85. Coenen M, Mosseler A, Vervuert I. Fermentative gases in breath indicate that Inulin and Starch start to be degraded by microbial fermentation in the stomach and small intestine of the horse in contrast to pectin and cellulose. J Nutr. 2006;136(May):2108–10.

86. Saha D, Bhattacharya S. Hydrocolloids as thickening and gelling agents in food: A critical review. J Food Sci Technol. 2010;47(6):587–97.

87. Grey H, Abel C, Zimmerman B. Structure of IgA proteins. Ann New York Acad Sci. 1971;190(1):37–48.

88. Kerr M. The structure and function of human IgA. Biochem J [Internet]. 1990;271(2):285–96. Available from: http://www.pubmedcentral.nih.gov/articlerender.fcgi?artid=1149552&tool=pmcentrez&rendertype=abstract

89. Secor PR, Michaels LA, Ratjen A, Jennings LK, Singh PK. Entropically driven aggregation of bacteria by host polymers promotes antibiotic tolerance in Pseudomonas aeruginosa. Proc Natl Acad Sci [Internet]. 2018;201806005. Available from: http://www.pnas.org/lookup/doi/10.1073/pnas.1806005115

90. Highgate D. Particle Migration in Cone-plate Viscometry of Suspensions. Nature. 1966;211:1390–1.

91. Michele J, Patzold R, Donis R. Alignment and aggregation effects in suspensions of spheres in non-Newtonian media. Rheol Acta. 1977;16(3):317–21.

92. Kim J, Helgeson ME. Shear-induced clustering of Brownian colloids in associative polymer networks at moderate Péclet number. Phys Rev Fluids [Internet]. 2016;1(4):43302. Available from: https://link.aps.org/doi/10.1103/PhysRevFluids.1.043302

93. Highgate DJ, Whorlow RW. Rheological properties of suspensions of spheres in non-Newtonian media. Rheol Acta [Internet]. 1970;9(4):569–76. Available from: https://doi.org/10.1007/BF01985469

94. Snijkers F, Pasquino R, Vermant J. Hydrodynamic interactions between two equally sized spheres in viscoelastic fluids in shear flow. Langmuir. 2013;29(19):5701–13.

95. USDA. The Food Supply and Dietary Fiber : Its Availability and Effect on Health. Nutrition Insight 36. 2007.

96. USDA. 2015 – 2020 Dietary Guidelines for Americans [Internet]. 2015 – 2020 Dietary Guidelines for Americans (8th edition). 2015 [cited 2018 Jun 11]. Available from: http://health.gov/dietaryguidelines/2015/guidelines/

97. Datta SS, Preska Steinberg A, Ismagilov RF. Polymers in the gut compress the colonic mucus hydrogel. Proc Natl Acad Sci U S A [Internet]. 2016 Jun 28 [cited

2016 Jul 22];113(26):7041–6. Available from: http://www.ncbi.nlm.nih.gov/pubmed/27303035

98. Leary S, Underwood W, Anthony R, Cartner S. AVMA Guidelines for the Euthanasia of Animals: 2013 Edition [Internet]. American Veterinary Medical Association. 2013 [cited 2018 Jun 11]. p. 98. Available from: https://www.avma.org/kb/policies/documents/euthanasia.pdf

99. Otsu N. A threshold selection method from gray-level histograms. IEEE Trans Syst Man Cybern. 1979;SMC-9(1):62–6.

100. Bois J. BE / Bi 103 : Data Analysis in the Biological Sciences [Internet]. 2015. Available from: http://bebi103.caltech.edu.s3-website-us-east-1.amazonaws.com/2017/lecture_notes/l06_frequentist_methods.pdf

101. Ward FW, Coates ME. Gastrointestinal pH measurement in rats: Influence of the microbial flora, diet and fasting. Lab Anim. 1987;21(3):216–22.

102. Smith HW. Observations on the flora of the alimentary tract of animals and factors affecting its composition. J Pathol Bacteriol. 1965;89:95–122.

103. McConnell EL, Basit AW, Murdan S. Measurements of rat and mouse gastrointestinal pH, fluid and lymphoid tissue, and implications for in-vivo experiments. J Pharm Pharmacol [Internet]. 2008;60(1):63–70. Available from: http://doi.wiley.com/10.1211/jpp.60.1.0008

104. de Gennes PG. Conformations of polymers attached to an interface. Macromolecules [Internet]. 1980;13(19):1069–75. Available from: http://pubs.acs.org/doi/abs/10.1021/ma60077a009

105. Israelachvili J. Intermolecular and Surface Forces. Intermolecular and Surface Forces. 2011.

106. Waters DJ, Engberg K, Parke-Houben R, Hartmann L, Ta CN, Toney MF, et al. Morphology of photopolymerized end-linked poly (ethylene glycol) hydrogels by small-angle X-ray scattering. Macromolecules. 2010;43(16):6861–70.

107. Kawaguchi S, Imai G, Suzuki J, Miyahara A, Kitano T, Ito K. Aqueous solution properties of oligo- and poly(ethylene oxide) by static light scattering and intrinsic viscosity. Polymer (Guildf). 1997;38(12):2885–91.

108. Arratia PE, Voth GA, Gollub JP. Stretching and mixing of non-Newtonian fluids in time-periodic flows. Phys Fluids. 2005;17(5):1–10.

109. Takahashi T. Flow Behavior of Digesta and the Absorption of Nutrients in the Gastrointestine. J Nutr Sci Vitaminol. 2011;57:265–73.

110. Arratia PE, Cramer LA, Gollub JP, Durian DJ. The effects of polymer molecular weight on filament thinning and drop breakup in microchannels. New J Phys. 2009;11(November).

Supplementary Information

*Supplemental **Figure**s*

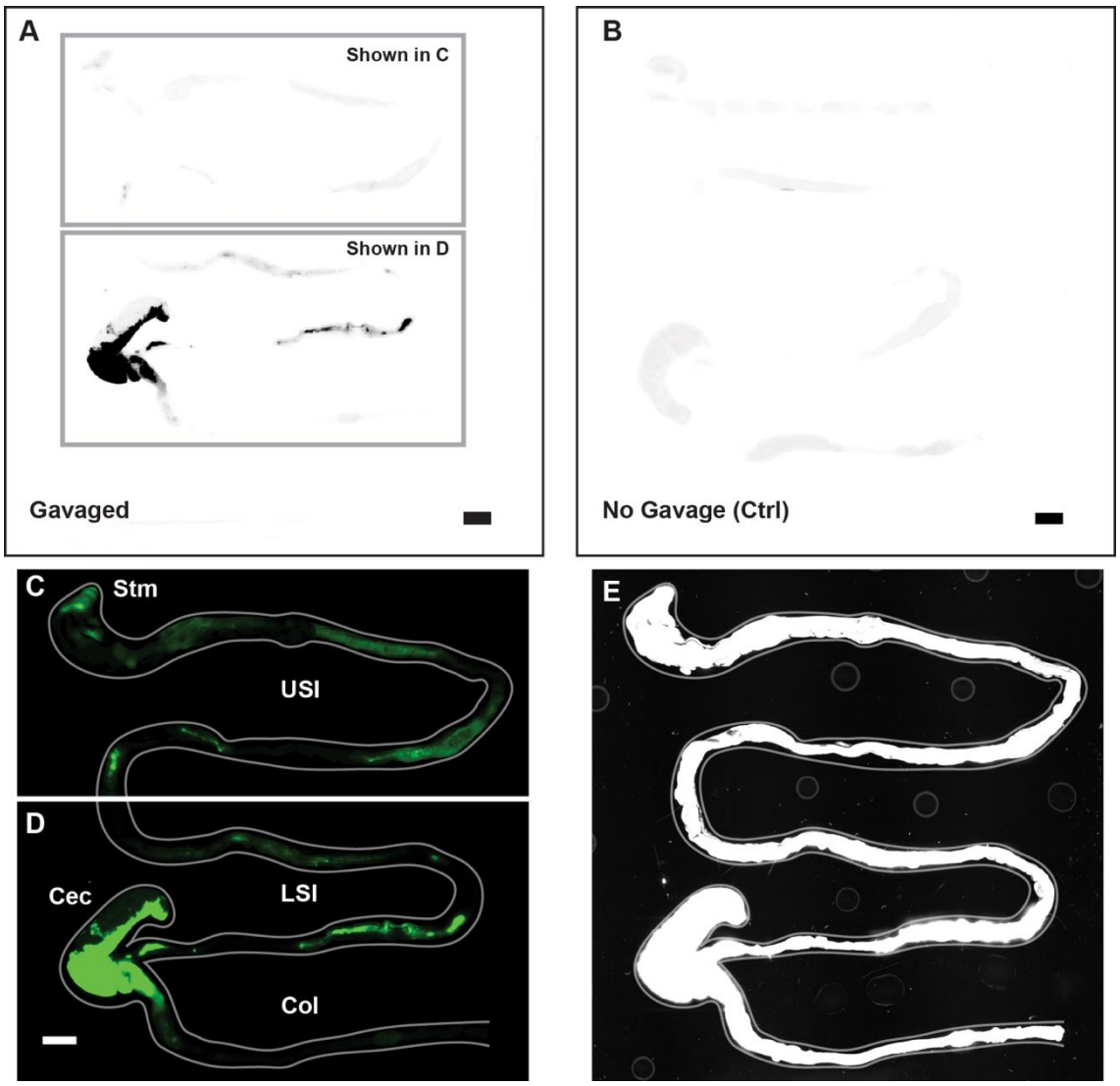

Figure 5.S1: Overview of image processing for fluorescent scanner images in **Figure** 5.1. (A) Unmodified fluorescent scanner images of the gastrointestinal tract of a mouse gavaged with 1 μm-diameter PEG-coated particles (prior to the contrast and color-adjustments shown in **Figure** 5.S1A–B). Scale bar is 0.5 cm. Boxes indicate the regions that are shown in panels C and D. (B) Unmodified fluorescent scanner image of the gut of a mouse that has not been gavaged with particles. Scale bar is 0.5 cm. (C and D). The contrast and color-adjusted images that appear in **Figure** 5.S1A–B. (E) Contrast-adjusted image of **Figure**s 5.S1A-B that was used to trace the outline of the gut shown in **Figure** 5.S1A–B (and panel C and D of this **Figure**). Outline of gut is shown in grey on both C, D, and E.

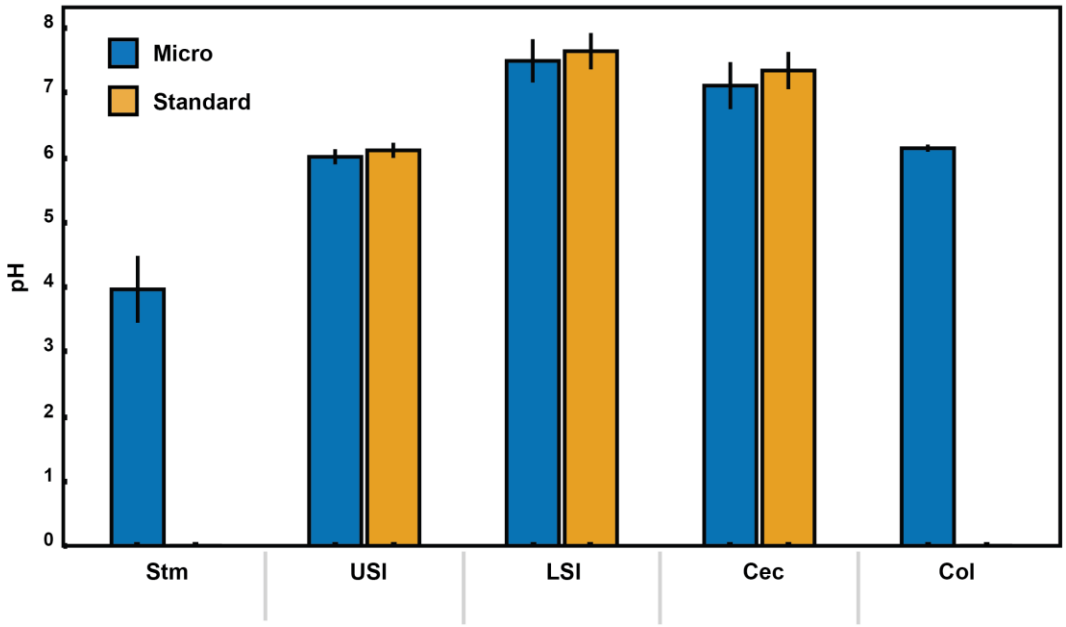

Figure 5.S2: pH measurements of luminal fluid from different sections of the gastrointestinal tract. Measurements were conducted on pooled samples of luminal fluid collected from two groups of mice. Each measurement was repeated three times, and the error bars are the standard deviation across the six trials (three trials per group). Micro (blue) indicates measurements that were conducted using a micro pH electrode. Standard (orange) indicates measurements that were conducted using a standard pH electrode. For the stomach and colon samples there was insufficient luminal fluid from both groups to submerge the tip of the standard pH electrode, so measurements were only taken with the micro pH electrode. Stm = stomach, USI = upper small intestine. LSI = lower small intestine, Cec = cecum, and Col = colon.

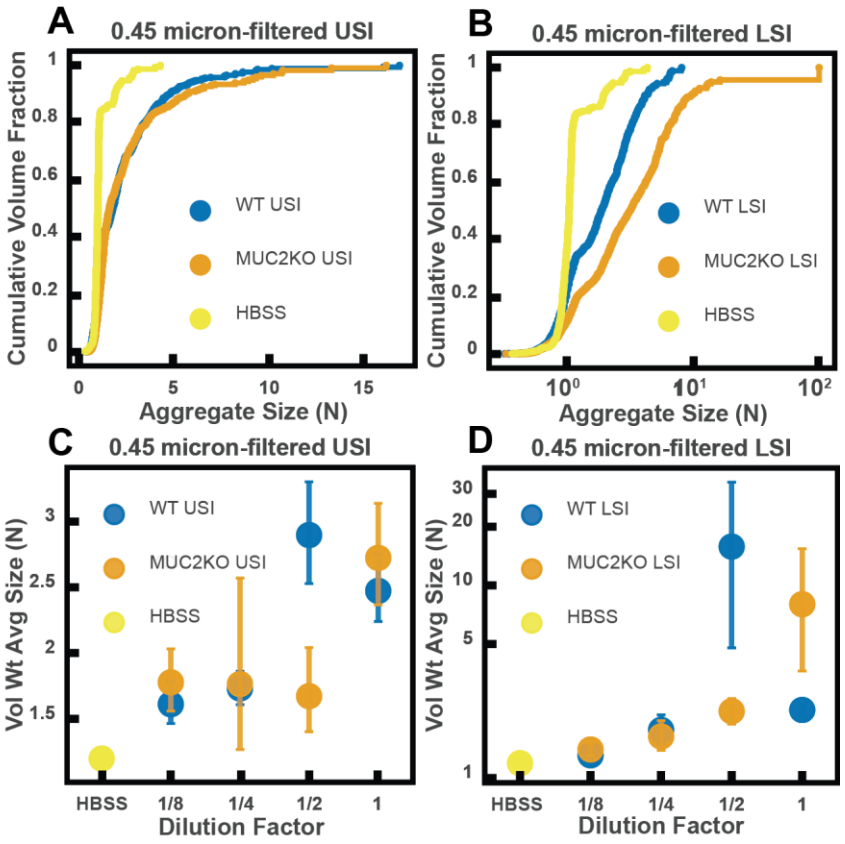

Figure 5.S3: *Ex vivo* aggregation in 0.45 µm-filtered luminal fluid from the small intestines (SI) of wild-type (WT) and MUC2 knockout (MUC2KO) mice. (**A** and **B**) Volume-weighted empirical cumulative distribution functions (ECDFs) comparing aggregation of the particles in undiluted, 0.45-µm-filtered samples from the upper (A) and lower (B) SI of two separate groups of WT and MUC2KO mice to the control (particles suspended in HBSS). The vertical axis is the cumulative volume fraction of the total number of particles in solution in an aggregate of a given size. The horizontal axis is aggregate size in number of particles per aggregate (N). (C and D) Volume-weighted average aggregate sizes (Vol Wt Avg Size) for serial dilutions of 0.45 µm-filtered samples from the upper (C) and lower (D) SI of two separate groups of WT and MUC2KO mice. Volume-weighted average sizes are plotted on the vertical axis in terms of number of particles per aggregate (N). The dilution factor is plotted on the horizontal axis, where a dilution factor of 1 is undiluted and ½ is a two-fold dilution. The control (particles suspended in HBSS) is plotted as a dilution factor of 0. The vertical error bars are 95% empirical bootstrap CI using the bootstrapping procedure described in *Materials and Methods*.

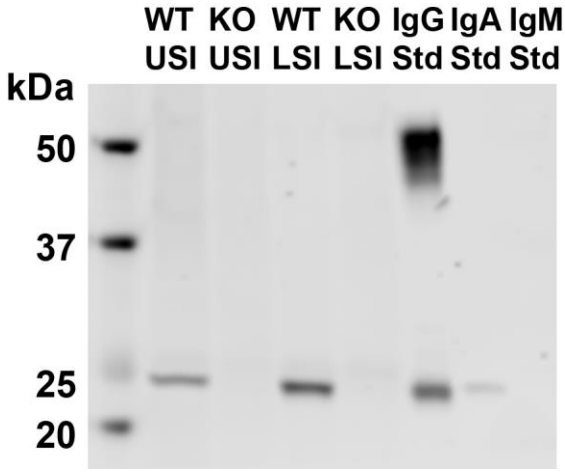

Figure 5.S4: Western blots of 30 µm-filtered samples from the small intestine (SI) of wild-type (WT) and Rag1 knockout (Rag1KO) mice. WT USI = WT upper SI; KO USI = KO lower SI; WT LSI = WT lower SI; KO USI = KO upper SI. For the detection of IgG, 1:10,000 dilutions of Li-Cor IRDye 800 CW Goat Anti-Mouse IgG was used. Because the Anti-IgG antibody appears to be binding to just the light chains (around 25 kDa), we suspect that it is mostly binding to IgA. Li-Cor's published validation (https://www.licor.com/bio/products/reagents/secondary_antibodies/irdye_800cw.html) found that the antibody binds to the heavy and light chains of IgG and just the light chains of IgA. Because we see binding of the antibody to both the heavy and light chains in the IgG standard, but only binding to a light chain in the SI samples and the IgA control, this suggests that we are detecting the light chains of IgA in the SI samples.

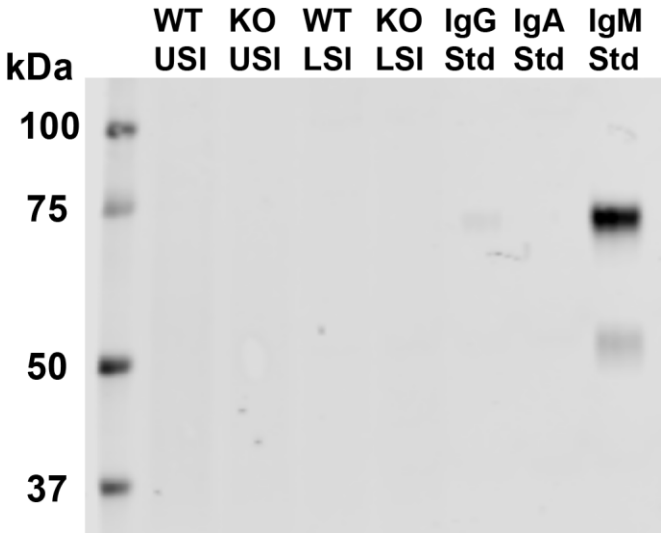

Figure 5.S5: Western blots of 30 µm-filtered samples from the small intestine (SI) of wild-type (WT) and Rag1 knockout (Rag1KO) mice. WT USI = WT upper SI; KO USI = KO lower SI; WT LSI = WT lower SI; KO USI = KO upper SI. For detection of IgM, 1:10,000 dilution of Li-Cor IRDye 800CW Goat Anti-Mouse IgM was used. We do not detect IgM in any of the SI samples.

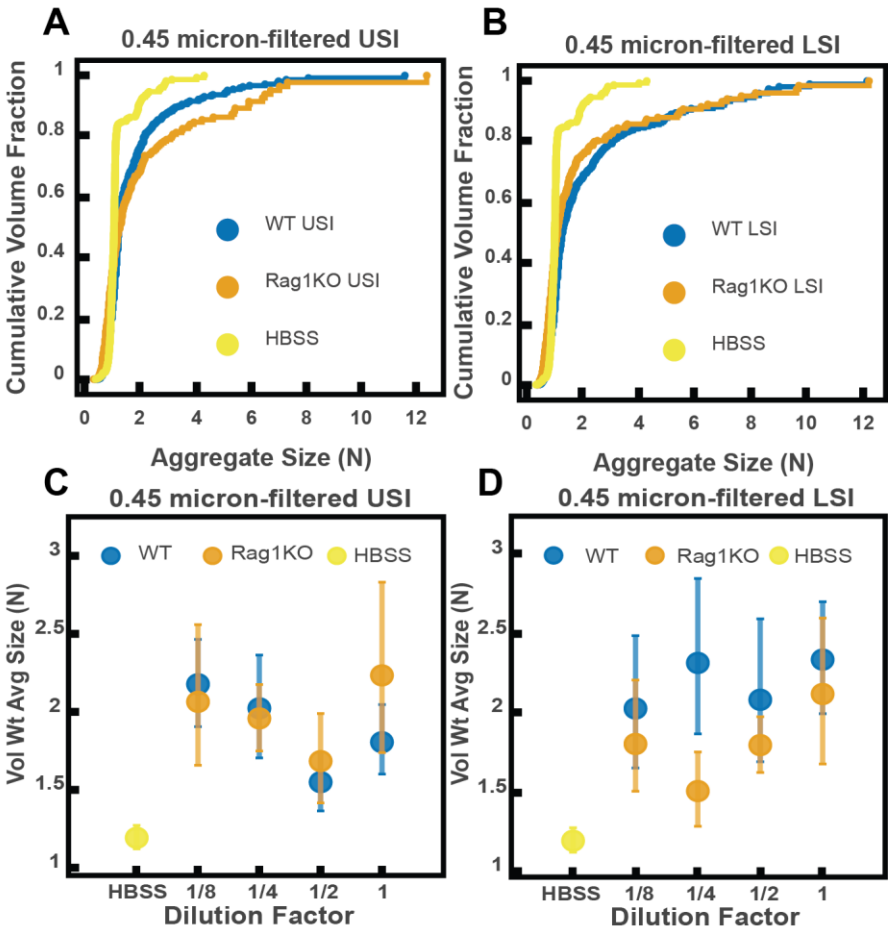

Figure 5.S6: *Ex vivo* aggregation in 0.45-µm-filtered luminal fluid from the small intestines (SI) of wild-type (WT) and Rag1 knockout (Rag1KO) mice. (A and B) Volume-weighted empirical cumulative distribution functions (ECDFs) comparing aggregation of the particles in undiluted, 0.45-µm-filtered samples from the upper (A) and lower (B) SI of two separate groups of WT and immunoglobulin-deficient (Rag1KO) mice to the control (particles suspended in HBSS). Plotted on the vertical axis is the cumulative volume fraction of the total number of particles in solution in an aggregate of a given size. Plotted on the horizontal axis are aggregate sizes in number of particles per aggregate (N). (C and D). Volume-weighted average aggregate sizes (Vol Wt Avg Size) for serial dilutions of 0.45-µm-filtered samples from the upper (C) and lower (D) SI of two separate groups of WT and Rag1KO mice. Volume-weighted average sizes are plotted on the vertical axis in terms of number of particles per aggregate (N). The dilution factor is plotted on the horizontal axis, where a dilution factor of 1 is undiluted and ½ is a two-fold dilution. The control (particles suspended in HBSS) is plotted as a dilution factor of 0. The vertical error bars are 95% empirical bootstrap CI using the bootstrapping procedure described in

Materials and Methods.

Supplemental Tables

Table 5.S1: Estimates of physical parameters of polymers from gel permeation chromatography for liquid fractions from the upper small intestine of MUC2 knockout (MUC2KO) and wild-type (WT) mice.

Retention volume (mL)	**11 to 16**		**16 to 20**		**>20**	
Mouse type	WT	MUC2KO	WT	MUC2 KO	WT	MUC2 KO
M_w (kDa)	3,560±410	5,420±620	162±20	147±17	4.05±0.46	2.96±0.34
M_w/M_n	1.36	1.59	2.16	2.43	3.59	10.9
R_h (nm)	49.1	45.5	6.31	5.95	1.18	1.02
Fract. Conc. (mg/mL)	2.52±0.29	1.18±0.13	24.6±2.8	21.9±2.5	88.7±10.1	86.0±9.8

We calculated values with both dn/dc = 0.185 (for proteins) and dn/dc = 0.147 (pullulan). When the value varied with dn/dc, it is reported in the table as the mid-range values ± the absolute deviation between the two calculated values. M_w = the weight-average molecular weight; M_w/M_n = the dispersity; R_h = hydrodynamic radius; Fract. Conc. = Concentration of a given molecular weight fraction.

Table 5.S2: Estimates of physical parameters of polymers from gel permeation chromatography for liquid fractions from the lower small intestine of MUC2 knockout (MUC2KO) and wild-type (WT) mice

Retention volume (mL)	**11 to 16**		**16 to 20**		**>20**	
Mouse type	WT	MUC2KO	WT	MUC2KO	WT	MUC2KO
M_w (kDa)	4,730±540	5,180±590	219±25	155±18	13.7±1.6	5.93±0.68
M_w/M_n	1.24	1.80	1.91	1.84	1.88	2.03
R_h (nm)	57.0	49.2	8.45	7.58	1.89	1.35
Fract. Conc. (mg/mL)	3.42±0.39	2.36±0.27	23.0±2.6	22.8±2.6	54.8±6.3	63.3±7.2

We calculated values with both dn/dc = 0.185 (for proteins) and dn/dc = 0.147 (pullulan). When the value varied with dn/dc, it is reported in the table as the mid-range values +/- the absolute deviation between the two calculated values. M_w = the weight-average molecular weight; M_w/M_n = the dispersity; R_h = hydrodynamic radius; Fract. Conc. = Concentration of a given molecular weight fraction.

Table 5.S3: Estimates of physical parameters of polymers from gel permeation chromatography for liquid fractions from the upper small intestine of immunoglobulin-deficient (Rag1KO) and wild-type WT mice.

Retention volume (mL)	**11 to 16**		**16 to 20**		**>20**	
Mouse type	WT	Rag1KO	WT	Rag1KO	WT	Rag1KO
M_w (kDa)	1,480±170	2,140±250	108±12	74.2±8.5	2.84±0.32	1.91±0.22
M_w/M_n	1.09	1.14	2.62	2.42	1.59	1.54
R_h (nm)	31.8	39.8	4.77	2.51	1.078	0.936
Fract. Conc. (mg/mL)	1.07±0.12	1.13±0.13	14.3±1.6	13.9±1.6	66.1±7.6	70.5±8.1

We calculated values with both dn/dc = 0.185 (for proteins) and dn/dc = 0.147 (pullulan). When the value varied with dn/dc, it is reported in the table as the mid-range value +/- the absolute deviation between the two calculated values. M_w = the weight-average molecular weight; M_w/M_n = the dispersity; Rh = hydrodynamic radius; Fract. Conc. = Concentration of a given molecular weight fraction.

Table 5.S4: Estimates of physical parameters of polymers from gel permeation chromatography for liquid fractions from the lower small intestine of immunoglobulin-deficient (Rag1KO) and wild-type WT mice.

Retention volume (mL)	**11 to 16**		**16 to 20**		**>20**	
Mouse type	WT	Rag1KO	WT	Rag1KO	WT	Rag1KO
M_w (kDa)	1,080±120	2,490±290	66.9±7.7	91.6±10.5	3.64±0.42	3.72±0.43
M_w/M_n	1.18	1.05	1.71	1.98	2.09	1.98
R_h (nm)	34.6	47.1	4.67	4.85	1.116	1.09
Fract. Conc. (mg/mL)	1.52±0.17	1.89±0.22	15.8±1.8	14.1±1.6	49.5±5.7	55.1±6.3

We calculated values with both dn/dc = 0.185 (for proteins) and dn/dc = 0.147 (pullulan). When the value varied with dn/dc, it is reported in the table as the mid-range values +/- the absolute deviation between the two calculated values. M_w = the weight-average molecular weight; M_w/M_n = the dispersity; R_h = hydrodynamic radius; Fract. Conc. = Concentration of a given molecular weight fraction.

Table 5.S5: Gel permeation chromatography of Fibersol-2 and pectin in phosphate-buffered saline

Sample	Fibersol-2	Pectin
M_w (kDa)	3.48	232
M_w/M_n	10.5	1.97
R_h (nm)	1.24	25.4

Both fiber types were analyzed with dn/dc = 0.147 for polysaccharides**.** M_w = weight-average molecular weight; M_w/M_n = the dispersity; R_h = hydrodynamic radius

Table 5.S6: Estimates of physical parameters of polymers from gel permeation chromatography for liquid fractions from upper small intestine of pectin and Fibersol-2 fed mice

Retention volume (mL)	**11 to 16**		**16 to 20**		**>20**	
Mouse type	Pectin	Fibersol-2	Pectin	Fibersol-2	Pectin	Fibersol-2
M_w (kDa)	267±31	686±79	40.0±4.5	35.3±4.0	1.39±0.16	1.67±0.19
M_w/M_n	1.50	1.08	2.15	2.64	2.45	1.48
R_h (nm)	31.8	N/C**	5.52	2.88	0.819	N/C**
Fract. Conc. (mg/mL)	1.62±0.19	0.516±0.059	9.00±1.03	23.3±2.7	53.7±6.1	77.0±8.8

We calculated values with both dn/dc = 0.185 (for proteins) and dn/dc = 0.147 (pullulan). When the value varied with dn/dc, it is reported in the table as the mid-range values +/- the absolute deviation between the two calculated values. M_w = the weight-average molecular weight; M_w/M_n = the dispersity; R_h = hydrodynamic radius; Fract. Conc. = Concentration of a given molecular weight fraction. N/C** denotes values for which the concentration was too low to calculate.

Table 5.S7: Estimates of physical parameters of polymers from gel permeation chromatography for liquid fractions from lower small intestine of pectin and Fibersol-2-fed mice

Retention volume (mL)	**11 to 16**		**16 to 20**		**>20**	
Mouse type	Pectin	Fibersol-2	Pectin	Fibersol-2	Pectin	Fibersol-2
M_w (kDa)	282±32	1680±190	30.2±3.5	18.8±2.2	1.12±0.13	2.32±0.27
M_w/M_n	7.37	1.64	1.70	2.78	2.89	1.14
R_h (nm)	29.0	26.4	5.28	2.16	0.724	1.06
Fract. Conc. (mg/mL)	2.48±0.28	0.839±0.096	9.43±1.1	53.6±6.1	42.7±4.9	88.3 ±10.1

We calculated values with both dn/dc = 0.185 (for proteins) and dn/dc = 0.147 (pullulan). When the value varied with dn/dc, it is reported in the table as the mid-range values +/- the absolute deviation between the two calculated values. M_w = the weight-average molecular weight; M_w/M_n = the dispersity; R_h = hydrodynamic radius; Fract. Conc. = concentration of a given molecular weight fraction.

Table 5.S8: Zeta potential and NMR measurements of PEG-coated particles

Surface Modification of PS particles	Zeta potential (mV)	Nanomoles PEG/mg particles
mPEG 5 kDa	-18.87 ±1.78	5.5
mPEG 5 kDa w/ mPEG 1 kDa backfill	-7.66 ±2.12	4.6
mPEG 5 kDa w/ mPEG 350 Da backfill	-9.99 ± 1.65	4.3
mPEG 5 kDa w/ mPEG 5 kDa backfill	-14.56 ± 1.78	4.0
mPEG 2 kDa	-39.59 ± 2.41	9.4
Carboxylate-coated (no PEG)	-61.36 ± 12.40	0.0

For the zeta potential measurements, each particle solution was 0.1 mg/ml of particles in 1 mM KCl. Measurements were done on a Brookhaven NanoBrook ZetaPALS Potential Analyzer. Three trials were done where each trial was 10 runs each and each run was 10 cycles. Values reported are the average zeta potential for the 30 runs. NMR measurements were performed as described in *Materials and Methods*. Values are estimates of the nanomoles of polyethylene glycol (PEG) per milligrams of particles. To calculate this, we have to assume all the PEG on the surface is a single MW. It is therefore assumed all the PEG on the surface is PEG 5 kDa.

Detailed contributions from non-corresponding authors

A.P.S. Co-designed all experiments and co-analyzed all experimental results; developed theoretical tools and performed all calculations; co-developed imaging analysis pipeline in

ImageJ; developed computational tools for bootstrapping procedure; co-developed microscopy assay for examining luminal contents from mice gavaged particles used in **Figure** 5.1C and 1D; Co-performed, designed, and analyzed data from experiments involving oral administration of particles in **Figure** 5.1; performed, designed, and analyzed data from all *ex vivo* aggregation experiments in SI fluid in **Figure**s 5.2, 5.3, 5.5-7, 5.S2, and 5.S5; performed, designed, and analyzed data from all GPC measurements in **Figure**s 5.3, 5.5-7, and Tables 5.S1-7; performed, designed, and analyzed data from all *in vitro* aggregation experiments with PEG solutions in **Figure** 5.4D, **Figure** 5.4 – **Figure** supplements 1-2, and with dietary fiber in **Figure** 5.7A; developed a computational approach for theoretical calculations in 5.4H and 5.4I and performed all calculations; performed, designed, and analyzed data from Western blots in **Figure**s 5.5E, 5.6E, 5.S3, and 5.S4; helped supervise animal husbandry of MUC2KO colony; performed animal husbandry for WT mice on autoclaved diets in **Figure** 5.6 and 5.S5; performed animal husbandry for mice on pectin and Fibersol-2 diets in **Figure** 5.7; performed, designed, and analyzed all zeta potential measurements in Table 5.S8; performed pH measurements on luminal fluid in **Figure** 5.S2; co-interpreted results; co-wrote the paper.

S.S.D. Conceived and co-planned the project; initially observed the aggregation phenomenon described in this work; co-designed and co-analyzed preliminary experiments; performed preliminary *ex vivo* and *in vitro* aggregation experiments; co-developed microscopy assay for examining luminal contents from mice gavaged particles used in **Figure** 5.1C and 5.1D; developed *ex vivo/in vitro* aggregation assay used in **Figure**s 5.2-7; co-developed approach to extract liquid fraction of murine intestinal contents; co-developed protocol for NMR measurements on PEG-coated particles; organized transfer and initial set up of MUC2KO colony; co-interpreted results; co-wrote the paper.

T.N. Co-developed imaging analysis pipeline in ImageJ; co-analyzed *ex vivo* aggregation data in **Figure** 5.2; co-designed and co-analyzed preliminary *ex vivo* aggregation experiments with MUC2KO mice; provided useful advice on design of bootstrapping procedure; co-interpreted results; co-wrote the paper.

J.C.R. Developed protocol for NMR measurements on PEG-coated particles; performed synthesis of particles; performed NMR measurements in Table 5.S8; co-wrote the paper.

S.R.B. Co-performed preliminary experiments; developed fluorescent laser scanning approach for examining luminal contents of mice gavaged with particles appearing in **Figure** 5.1A and 5.1B; Administered particles to mice in **Figure** 5.1; co-developed approach to extract liquid fraction of murine intestinal contents; co-organized transfer and initial set up of MUC2KO colony; setup genotyping of MUC2KO mice; helped supervise animal husbandry of MUC2KO colony; helped with interpretation of results; co-wrote the paper.

Chapter 6

QUANTITATIVE AND QUALITATIVE CHANGES IN THE UPPER GASTROINTESTINAL MICROBIOME CONTROLLED BY SELF-REINOCULATION IN MICE INFLUENCE BILE-ACID METABOLISM AND HOST PHYSIOLOGY

Said Bogatyrev, Justin C. Rolando, and Rustem F. Ismagilov

ABSTRACT

The composition and functional roles of the small-intestine microbiome in humans remains obscure primarily because it is difficult to access the upper gastrointestinal system in humans for sampling. Rodent models are used extensively in microbiome research and enable the spatial, compositional, and functional evaluation interrogation of the gastrointestinal microbiome and its effects on the host physiology and disease phenotype. However, important differences in rodent physiology can affect the relevance of these models to humans. Specifically, fecal microbial reinoculation (via coprophagy) in mice and rats is believed to transmit microbes among co-housed animals and is known to affect the composition and abundance of microbes in their upper gastrointestinal tracts. Coprophagy thus complicates investigations of the unique structure and function of the upper gastrointestinal microbiome, alterations of which are believed to be implicated in the disease pathogenesis (e.g., small intestinal bacterial overgrowth (SIBO) in non-alcoholic and alcoholic steatohepatitis (NASH) or inflammatory bowel conditions). Here, we evaluated the dependence of the structure and function of the small-intestine microbiome on repeated fecal microbial self-reinoculation in conventional specific pathogen-free laboratory mice using two methods: housing on wire floors and fitting mice with tail cups. We confirmed that only tail cups were truly effective at preventing self-reinoculation. When not completely prevented, the continuous self-exposure to the fecal microbiota in mice had substantial quantitative and qualitative effects on the upper gastrointestinal microbiome in these animals. These differences in microbial abundance and community composition resulted in altered microbial functions in the small intestine, specifically in relation to bile acid metabolism,

with detectable changes on host physiology. Our work highlights the importance of evaluating the structure and function of the upper gastrointestinal microbiome in relation to the effects of the gut microbiome on host physiology and disease phenotype and emphasizes the important role of microbial exposure on its structure and function.

INTRODUCTION

The small intestine is the primary site for nutrient uptake and immune sampling in the human gastrointestinal system. Its large surface area vastly exceeding that of the large intestine [1] and represents a broad interface for the host interaction with the microbial players in the external environment.

Normal microbial levels in the small intestine in healthy humans are orders of magnitude lower than those in the large intestine and generally the physiological role of the small-intestinal microbial colonization remains obscure.

Rodents (mice and rats) remain the predominant mammalian animal model organisms in the field of human microbiome research despite some well-recognized limitations of these model organisms associated with their anatomical and physiological differences with humans [2], [3]. Among these limitations is the persistent tendency of rodents to practice gastrointestinal auto- and allo-reinoculaiton with large-intestinal microbiota (via fecal ingestion, or coprophagy) in laboratory settings.

We hypothesized that this behavioral variable may have dramatic effects on the structure and function of the upper gastrointestinal microbiome (and the gastrointestinal microbiome in general), which in turn could have detectable effects on the model host organism physiology and disease modeling. Moreover, self-reinoculation in model mammalian organisms may have dramatic effects not only on their native complex microbiota (e.g., in SPF mice) but also on the individual microbial colonizers (e.g., gnotobiotic animals) and the xenomicrobiota (e.g., human microbiota-associated mice). By understanding and controlling these effects, the field will be able to refine mouse models of gastrointestinal microbial colonization and improve analyses of the related host physiological states and diseases.

In the past several decades, multiple studies have evaluated the effects of self-reinoculation on the structure of the upper gut microbiome [4]–[7] and the persistence of its selected

members [8] in rodents using classical microbiological techniques. Others suggested self-reinoculation has augmenting effects on establishing a stable microbial colonization in the mouse gut by Pseudomonas spp. [9] and other species via repeated self-exposure. However, the field is lacking precise and comprehensive evaluations of the effects of self-reinoculation on the spatial, structural and functional state of the gut microbiome and its effects on the mammalian host physiology and microbiome-associated disease modeling.

We evaluated two methods for preventing fecal microbial self-reinoculation in conventional specific pathogen-free (SPF) laboratory mice: housing on wire floors and fitting mice with "tail cups". We looked at the quantitative and compositional changes in the microbiome along the entire length of mouse gastrointestinal tract, evaluated the bile acid profile in the corresponding segments of the gut and other elements of the enterohepatic circulation system (bile, liver tissues, and plasma), and measured host blood cytokine response and gastrointestinal mucosal and liver gene expression.

METHODS

Reagents

TαMCA, TβMCA, TωMCA, THCA, αMCA, βMCA, ωMCA, HCA, HDCA, MCA, GCDCA, GDCA, and GCA were obtained from Steraloids (Newport, Rhode Island, USA).

TCA, CA, DCA, TCDCA, TDCA, TUDCA, TLCA, CDCA, UDCA, LCA, D_4-TCA, D_4-DCA, D_4-CA, D_4-TDCA, D_4-GLCA, D_4-GUDCA, D_4-GCDCA, D_4-GCA, and D_4-GDCA were obtained from Isosciences (Ambler, PA, USA).

Acetonitrile (Optima grade), Water (Optima grade) and Formic Acid were obtained from Fisher Scientific.

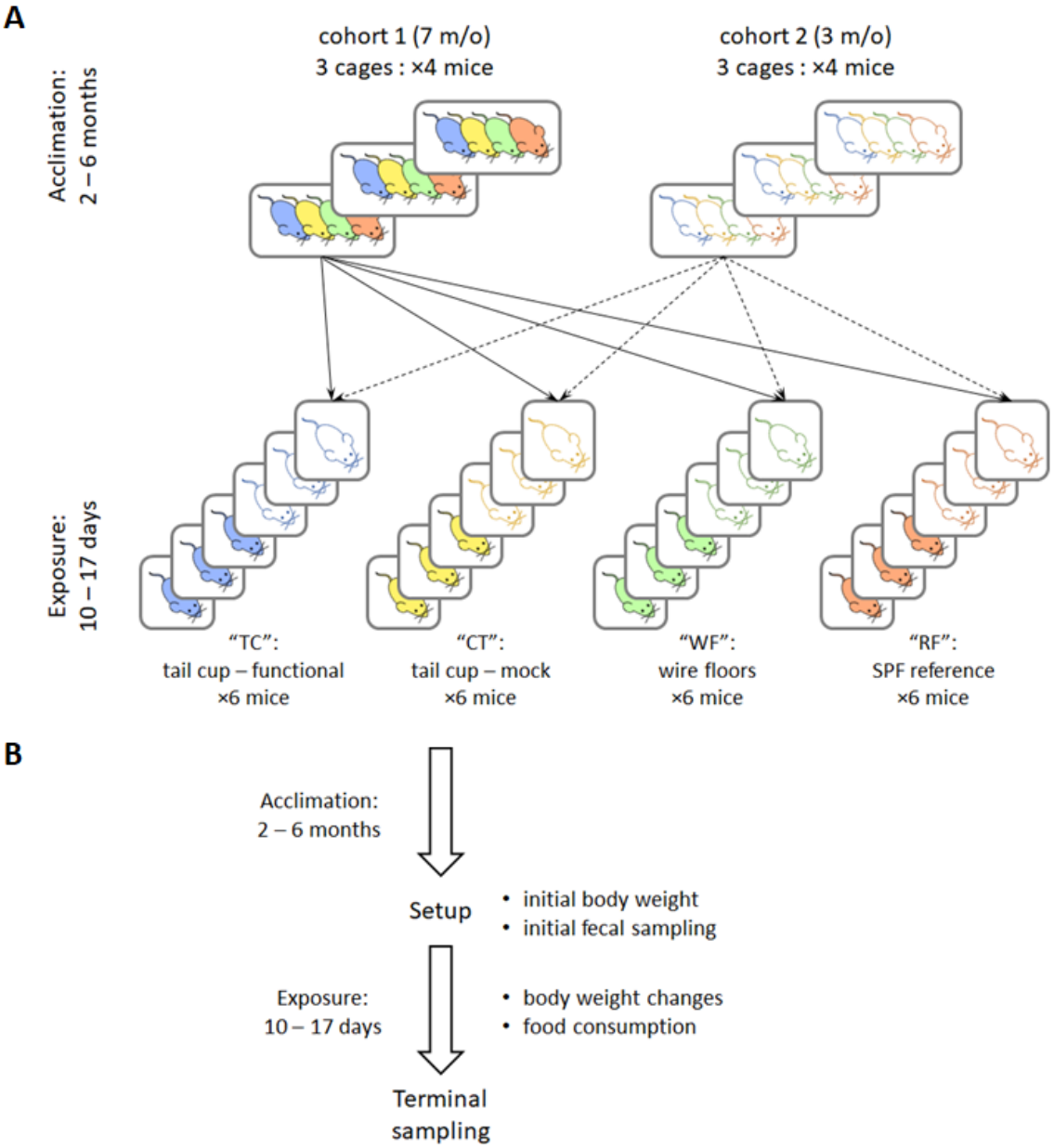

Fig. 6.1: Study layout, timeline, and logistics. A: Two cohorts of mice C57BL/J6 were used, 3 and 7 months of age. During the acclimation phase, mice were housed in groups of four animals per cage and then split into four different experimental groups. During the study, all animals were singly housed. Each experimental group consisted of six animals. The following groups of animals have been set up: RF: SPF reference animals maintained in standard conditions; WF: SPF animals maintained on wire floors; TC: mice fitted with functional "tail cups" to prevent self-reinoculation; CT: mice fitted with mock "tail cups" allowing self-reinoculation to control for the handling procedures and potentially higher stress levels in TC mice. B: Body weight and food intake were recorded during the "exposure" phase of the study. After the terminal sample collection, microbial loads and profiles were analyzed in gastrointestinal contents and mucosal samples along the

gastrointestinal tract. Metabolomic bile acids profiling was performed on gastrointestinal contents along the gastrointestinal tract, bile, liver tissues, blood plasma, and urine.

Sample preparation

To overcome sample buffering (pH issues), samples were extracted in 9x volumes of ethanol with 0.5% formic acid and nine different heavy isotope (D_4) internal standards at 5 µM. D_4 internal standards were Taurocholic acid (TCA), Cholic Acid (CA), Deoxycholic Acid (DCA), Taurodeoxycholic Acid (TDCA), Glycocholic acid (GCA), Glycolithocholic acid (GLCA), Glycoursodeoxycholic acid (GUDCA), Glycochenodeoxycholic acid (GCDCA), and Glycodeoxycholic acid (GDCA). Samples were heated for one hour at 70°C with gentle shaking (250 rpm). Solids were precipitated at 17,000 RCF for 15 minutes at 4°C. 10% of the original sample (e.g. 100 µL of a 1 mL extraction sample) was decanted and evaporated at approximately 100 mTorr without heating. The solids were reconsistuted at 100x dilution from the original sample (e.g. 100 µL decanted solution is resuspended at 1 mL) in 20% Acetonitrile, 80% water with 0.1% formic acid. Gall bladder samples were diluted 100x in water prior to extraction.

10 µL extracted and reconsistuted sample injections were analyzed on a Waters Acquity UPLC coupled to a Xevo-qTOF Mass Spectrometer (Waters, Manchester, UK) using an Acquity UPLC HSS T3 1.8 micron, 2.1 x 100 mm column (Part No 186003539) and Acquity UPLC HSS T3 1.8 micron Guard Column (Part No 186003976). Needle wash was two parts isopropanol, one part water, and one part acetonitrile. Purge solvent was 5% acetonitrile in water. A pooled quality control sample was run every 8 injections to correct for drift in response.

Mass spectrometer instrument parameters were as follows: 2.4 kV, Collision Energy 6.0 eV, Sampling Cone 90V, Source Offset 40, Source 120°C, desolvation 550°C, Cone Gas 50 L/Hr, and desolvation Gas 900 L/Hr.

A seven point external calibration curve was collected three times within the run from 0.05 to 30 µM of the bile acid standards [0.05, 0.1, 0.5, 1, 5, 10, 30 µM]. External standards were

Taurocholic acid (TCA), Tauro-alpha-Muricholic acid (TαMCA), Tauro-beta-Muricholic acid (TβMCA), Tauro-omega-Muricholic acid (TωMCA), Tauro-hyocholic acid (THCA), Tauro-Deoxycholic acid (TDCA), TauroUrsodeoxycholic acid (TUDCA), Tauro-Chenodeoxycholic acid (TCDCA), Taurolithocholic acid (TLCA), Glyco-Cholic acid (GCA), Glyco-Hyocholic acid (GHCA), Glyco-deoxycholic acid (GDCA), Glyco-hyodeoxycholic acid (GHDCA), Cholic acid (CA), alpha-muricholic acid (αMCA), beta-muricholic acid (βMCA), omega-muricholic acid (ωMCA), Hyocholic acid (HCA, also known as γ-Muricholic acid), Deoxy-cholic acid (DCA), ChenoDeoxycholic acid (CDCA), Ursodeoxycholic acid (UDCA), Hyodeoxycholic acid (HDCA), Murocholic acid (Murideoxycholic acid, MDCA), lithocholic acid (LCA), Glycolithocholic acid (GLCA), Glycourosodeoxycholic acid (GUDCA), and Glycochenodeoxycholic acid (GCDCA). It was not possible to resolve UDCA and HDCA and report the sum.

Elution Gradient

Samples were eluted using the following gradient of water with 0.1% formic acid ("A") and balance of acetonitrile with 0.1% formic acid:

1. 0 min, 0.55 mL/min at 68% A
2. 2 min, 0.55 mL/min at 60% A, 10 curve
3. 5 min, 0.55 mL/min at 40% A, 5 curve
4. 6 min, 1.1 mL/min at 0% A, 10 curve,
5. 6.2 min, 1.2 mL/min at 0% A, 6 curve;
6. 6.5 min, 1.47 mL/min at 0% A, 6 curve;
7. 8.9 min, 1.5 mL/min at 0% A, 6 curve;
8. 9.0 min, 0.9 mL/min at 68% A, 6 curve;
9. 10 min, 0.55 mL/min at 68% A, 6 curve;

RESULTS

- Self-reinoculation dramatically increases the microbial load in the upper gut in mice, but does not affect its levels in the large intestine.
- Self-reinoculation profoundly affects the microbial composition in the mouse upper gut and changes the absolute abundance of selected taxa in the large-intestine.
- Shifts in microbial loads and composition in the upper gastrointestinal tract in mice translate into differential microbial function resulting in the distinctive bile acid profile.
- Self-reinoculation exerts subtle effects on secondary bile acid metabolism.
- We hypothesize similar total levels of secondary bile acids are likely to have similar "dose-dependent" effects on the host.
- Reduced deconjugation of bile acids is known to increase reuptake by the host from the small intestine and reduce their availability for the large-intestinal microbiota to metabolize. This could be one of the explanations for the non-coprophagic mice to have a lower fraction of the secondary bile acids in the entire bile acid pool. Alternatively, eliminated re-ingestion of secondary bile acids in tail cup mice may be a reason for their lower fraction in the entire bile acid pool in these animals.
- Secondary bile acid metabolism is generally believed to be occurring in the large intestine of mammals. Based on the presence of some microbial secondary bile acid metabolism genes in the small intestine of non-"TC" mice the possibility of the secondary bile acid metabolism occurring in the small intestine of coprophagic mice rich in the deconjugated primary bile acid substrates cannot be ruled out.

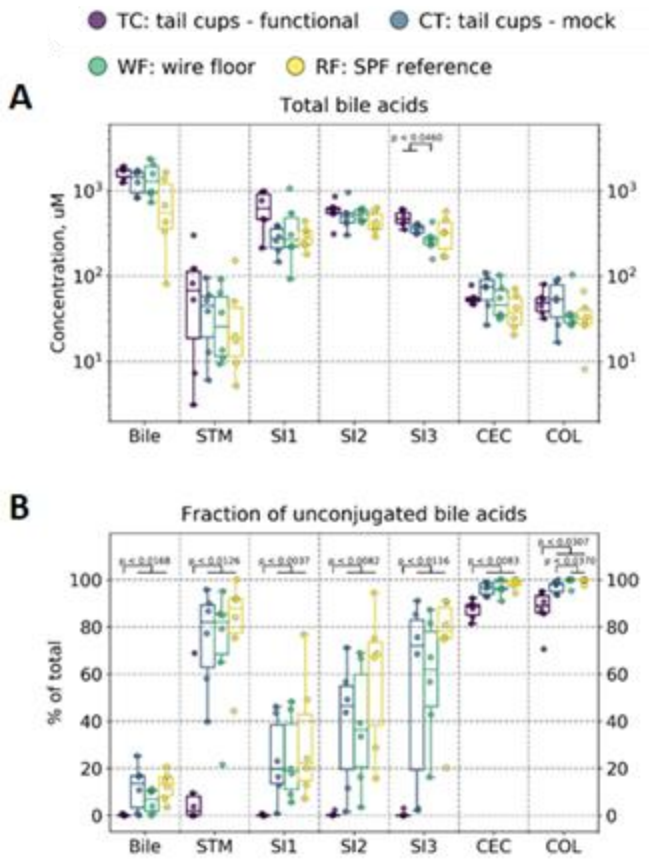

Fig. 6.2: Shifts in microbial loads and composition in the upper gastrointestinal tract in mice translate into differential microbial function resulting in the distinctive bile acid profile. A: Total bile acid (primary + secondary, conjugated + deconjugated) levels throughout the gastrointestinal tract or in bile are not affected by fecal ingestion and microbial self-reinoculation. B: Depletion of the small-intestinal microbiota in non-coprophagic mice results in a dramatically reduced rate of bile acid deconjugation: almost 100% of total bile acids remain in a conjugated form in the small intestine of TC mice, while in all other groups the fraction of deconjugated bile acids increases towards the distal small intestine. Additionally, TC mice carry a larger fraction of conjugated bile acids in the large intestine (CEC + COL) compared to all other groups of animals.

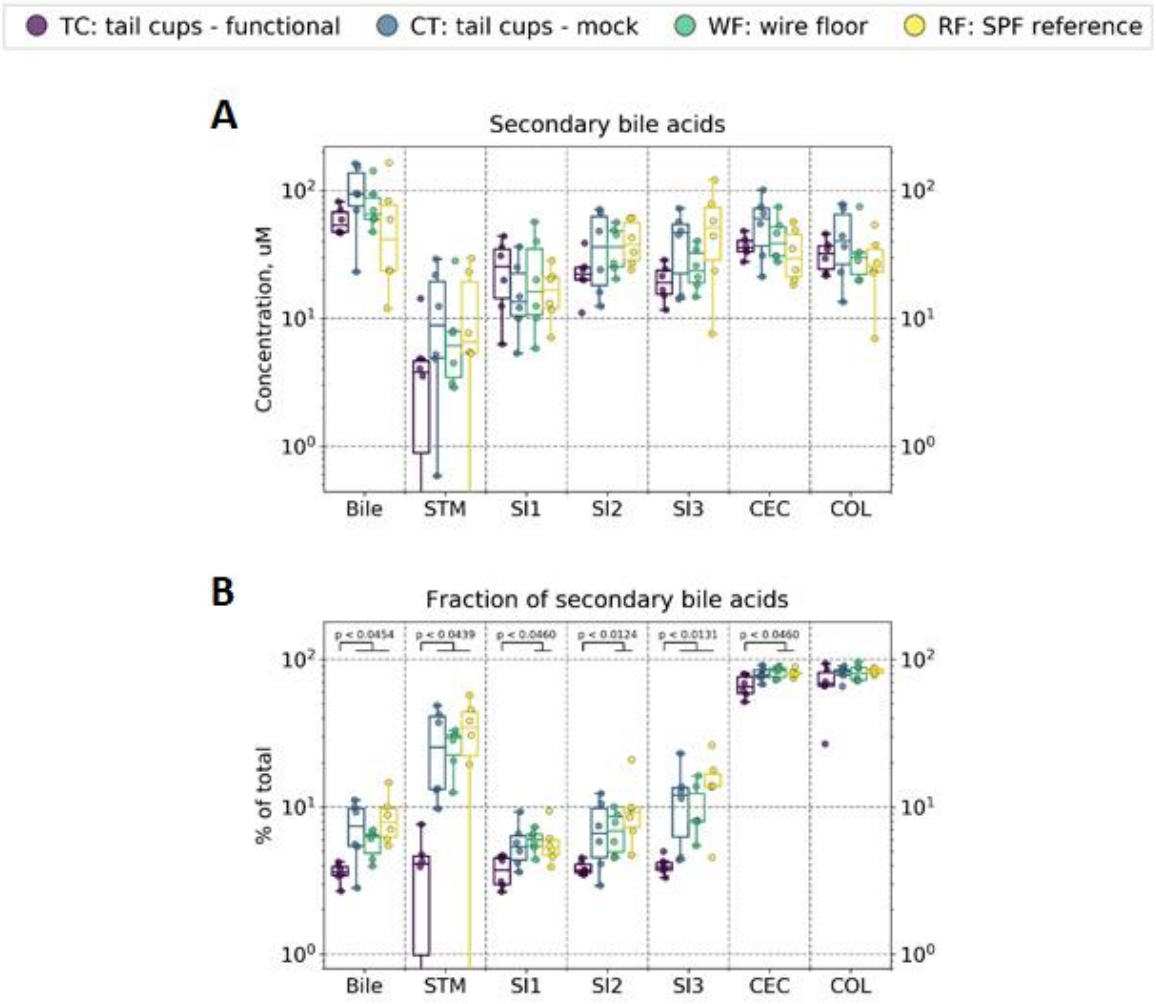

Fig. 6.3: Self-reinoculation exerts subtle effects on secondary bile acid metabolism. A: Plot of total levels of secondary bile acids (conjugated + deconjugated) in all parts of the gastrointestinal tract and in bile are similar among all groups. B: Plot of the fraction of total secondary bile acids (conjugated + deconjugated) in the entire bile acid pool in bile, small intestine, and cecum is few % lower in "TC" mice, suggesting a somewhat lower microbial contribution to the total bile acid pool in these animals

CONCLUSION

Consistent with a previous studies [10], we confirmed that only “tail cups” were truly effective for preventing self-reinoculation. Continuous self-exposure to the fecal microbiome in mice has dramatic quantitative and qualitative effects on the upper gastrointestinal microbiome in these animals. Such changes result in a differential microbial function in the small intestine in relation to the bile acid metabolism, which in turn leads to detectable changes in the host physiology (liver gene expression via FXR signaling/sterol metabolism; and mucosal gene expression – FXR signaling/FGF15-19/AMPs/etc.).

AUTHOR CONTRIBUTIONS

S.R.B. Conception, mouse tail cup development, animal study execution, animal study sample processing for microbial 16S quantification and 16S metagenomic sequencing, 16S quantification and sequencing data analysis, animal study sample processing for metabolomic analysis, bile acid data analysis, plasma ultrasensitive cytokine measurements and data analysis, mouse tissue gene expression quantification and data analysis, manuscript preparation.

J.C.R. Metabolomics method development and validation, animal study sample processing for metabolomic analysis, UPLC-MS instrument setup and sample analysis, chromatographic and mass spectra data analysis.

BIBLIOGRAPHY

[1] H. F. Helander and L. Fändriks, “Surface area of the digestive tract - revisited.,” *Scand. J. Gastroenterol.*, vol. 49, no. 6, pp. 681–9, Jun. 2014.

[2] T. L. A. Nguyen, S. Vieira-Silva, A. Liston, and J. Raes, “How informative is the mouse for human gut microbiota research?,” *Dis. Model. Mech.*, vol. 8, no. 1, pp. 1–16, Jan. 2015.

[3] F. Hugenholtz and W. M. de Vos, “Mouse models for human intestinal microbiota research: a critical evaluation.,” *Cell. Mol. Life Sci.*, vol. 75, no. 1, pp. 149–160, 2018.

[4] H. W. Smith, “Observations on the flora of the alimentary tract of animals and factors affecting its composition,” *J. Pathol. Bacteriol.*, vol. 89, no. 1, pp. 95–122, Jan. 1965.

[5] R. J. Fitzgerald, B. E. Gustafsson, and E. G. McDaniel, “Effects of Coprophagy Prevention on Intestinal Microflora in Rats,” *J. Nutr.*, vol. 84, no. 2, pp. 155–160, Oct. 1964.

[6] M. Lev, R. H. Alexander, and S. M. Levenson, “Stability of the Lactobacillus population in feces and stomach contents of rats prevented from coprophagy.,” *J. Bacteriol.*, vol. 92, no. 1, pp. 13–6, Jul. 1966.

[7] B. E. Gustafsson and R. J. Fitzgerald, “Alteration in Intestinal Microbial Flora of Rats with Tail Cups to Prevent Coprophagy,” *Exp. Biol. Med.*, vol. 104, no. 2, pp. 319–322, Jun. 1960.

[8] H. L. B. M. Klaasen, J. P. Koopman, P. M. Scholten, M. E. Van Den Brink, and A. G. M. Theeuwes, “Effect of Preventing Coprophagy on Colonisation by Segmented Filamentous Bacteria in the Small Bowel of Mice,” *Microb. Ecol. Health Dis.*, vol. 3, no. 2, pp. 99–103, Jan. 1990.

[9] S. E. George, M. J. Kohan, L. D. Claxton, and D. B. Walsh, “Acute colonization study of polychlorinated biphenyl-degrading pseudomonads in the mouse intestinal tract: Comparison of single and multiple exposures,” *Environ. Toxicol. Chem.*, vol. 8, no. 2, pp. 123–131, Feb. 1989.

[10] R. H. Barnes, G. Fiala, B. McGehee, and A. Brown, “Prevention of Coprophagy in the Rat,” *J. Nutr.*, vol. 63, no. 4, pp. 489–498, Dec. 1957.